VOLUME 11 NUMBER 3-4 2024 ISSN 2409-6121; eISSN 2522-1361

# Physical Sciences and Technology

National Nanotechnological Laboratory of Open Type
Institute of Experimental and Theoretical Physics

Physical Sciences and Technology is publishing two number in a year by al-Farabi Kazakh National University, al-Farabi ave., 71, 050040, Almaty, the Republic of Kazakhstan
website: http://phst.kaznu.kz/

Any inquiry for subscriptions should be send to:
Dr. Gauhar Mussabek, al-Farabi Kazakh National University
al-Farabi ave., 71, 050040, Almaty, the Republic of Kazakhstan
e-mail: journal.phst@gmail.com

# SCOPE AND AIM

*Physical Sciences and Technology* provides an original paperback for the publication of peerreviewed research and review articles in all fields of Physics and related Technology. The topics, included in the scope, especially emphasize understanding of the physics underlying modern technology.

Subject areas may include, but are not limited to the following fields: Astronomy and Space Research, Theoretical Physics and Astrophysics, Plasma Physics and Related Technology, Chemical Physics and Related Technology, Condensed Matter Physics and Related Technology, Thermal physics and Related Technology, Nuclear Physics and Related Technology, Nanomaterials and Nanotechnology, Applied Atomic and Molecular Physics, Material Sciences and Related Technology, Electronics and Related Technology, Instrumentation, Photonics and Quantum Electronics, Signal processing.

The Journal is issued under the auspices of the National Nanotechnological Laboratory of Open Type and Institute of Experimental and Theoretical Physics and is published two times a year by the «Kazakh University» Publishing House. The International Editorial Board of the Journal consists of leading researchers from different countries of the world. The Journal is wide open for contributions that both lie at the far frontiers of contemporary physics and are particularly aimed at applications of the scientific principles of physics to modern technological problems.

IRSTI 29.15.15; 34.49.23 https://doi.org/10.26577/phst2024v11i2b01

# Monitoring the distribution of radon isotopes and their decay products in Almaty

Yu. Zaripova*, A. Yushkov, N. Amangeldiyeva, K. Dyussebayeva and A. Shaidollina

Al-Farabi Kazakh National University, Almaty, Kazakhstan
*e-mail: zarypova.iulyiya1@kaznu.kz

*(Received September 5, 2024; received in revised form October 7, 2024; accepted October 16, 2024)*

This paper examines the relationship between indoor radon accumulation and the concentration of its decay products in the soil to comprehensively assess the impact on public health, as high indoor radon concentrations have been clearly shown to increase the risk of lung cancer, making it a serious public health problem. Indoor radon concentration, gamma and beta activity of soil samples were studied in Almaty at a distance of 27 m to 1500 m from the tectonic fault. It was found that indoor radon concentration $C_{Rn}$ decreases with increasing distance to the tectonic fault. The indoor radon activity concentration ranged from 6.23 to 405.21 Bq/m$^3$ with a geometric mean of 38.9 Bq/m$^3$. The specific activity in the selected soil samples was measured using the SPUTNIK-99 spectrometric setup. The results showed that beta activity varied in the range from 191.67±28.75 to 275.32±41.30 Bq/kg and gamma activity from 112.51±16.88 to 451.60±67.74 Bq/kg. Radon concentration also shows a good correlation with the gamma activity of the collected soil samples. The correlation coefficient was 0.79 for "$C_{Rn}$-Gamma" and 0.58 for "$C_{Rn}$-Beta", and the correlation analysis was done using Pearson's correlation tools.

**Key words:** indoor radon, radon concentration, radon decay products, exposure to radon, gamma radioactivity, beta radioactivity, radioecology.
**PACS number(s)**: 23.40.−s.

## 1. Introduction

The UN's 17 Sustainable Development Goals call for healthy lives and well-being for all at all ages. As part of task 3.4, monitoring radioactive gases (particularly radon) is recommended to assess their impact on public health [1].

The radioactive gas radon is a daughter product of natural uranium and thorium decay in the soil. It can spread from the source and accumulate in the air, water sources, and plants (flora) by molecular diffusion, gas diffusion, erosion, and dissolution processes [2, 3]. At the same time, its daughter products of decay are heavy metals, which pose the main danger when they enter the body. WHO and IARC classify radon as a Group I carcinogen [4, 5]. It has been clearly established that the impact of radon and its decay products on the human body increases the probability of developing lung and bronchial cancer, especially for non-smokers [6, 7]. And according to data [5], it ranges from 3% to 14%. Moreover, studies [8-10] show a correlation between radon levels and the probability of developing lung cancer. According to statistics for the Republic of Kazakhstan [11], mortality from lung cancer in the country is in first place. An analysis of global studies has shown that there are studies that radon exposure may be associated with other types of cancer [4, 12-14]. However, the results obtained in these studies were not so clear and convincing that further research in this area is relevant.

Radon is colorless and odorless, so it is not detected by the senses, which makes it dangerous for the population [5]. In open spaces, radon quickly dissipates in the air, while in closed spaces, it can accumulate and reach high values, creating a serious danger to human health [15]. This is especially true if we consider that according to data [16], the population spends more than 80% of its time in closed spaces every day.

In Almaty and the Almaty region, the problem of radon hazard in the territory, despite the presence of a large number of tectonic faults (while radon levels in rooms near and above faults can reach high values

[17, 18]), has not been sufficiently studied [19, 20], and comprehensive studies on the impact of radon on public health are not being conducted.

Although indoor radon exposure is the main contributor to the annual radiation dose from natural sources, it is also necessary to consider radon's ability to accumulate in the human environment. The decay of radon isotopes produces alpha, beta, and gamma radionuclides, which are easily absorbed by substances in various phase states [21]. Radionuclides can be found in air, water, and soil as a result of natural and artificial pollution [22], which can increase short-term and/or long-term effects on human health. Therefore, searching for and monitoring local radon "flares" in Almaty is a relevant area.

The relevance of the study in the direction of increasing the risk of cancer is associated with internal irradiation caused by inhalation and food consumption of radon and its decay products, which can cause damage to the respiratory tract, as well as the intestinal tract [12, 23, 24]. The ICRP [15] recommends that all countries establish a reference range for radon volume activity of 100÷300 Bq/m$^3$. In this regard, the need to monitor radon concentration measurements in residential and administrative buildings [25], where the population spends a lot of time, is becoming more urgent.

At the same time, 80% of the total radiation dose for the population is formed by natural long-lived radionuclides and their decay products, accumulating in soil, water, and air, making them an urgent research problem [26]. Soil plays a significant role in radioactive contamination of the environment, being one of the main sources of radiation exposure to the population, as it serves as the main means of transporting radionuclides into biological systems [27, 28]. When radon decays, radionuclides such as $^{210}$Po, $^{210}$Pb, $^{218}$Po, $^{214}$Pb, $^{214}$Bi, and $^{214}$Po are formed. $^{210}$Pb has a long residence time in the body and makes a large contribution to the radiation dose [29]. $^{210}$Pb and $^{210}$Po accumulate for decades in small air passages in the lungs (bronchioles) and gastrointestinal tract and are subsequently absorbed into the blood. Then, there is a transition to other organs and tissues, causing local radiation doses to these organs and tissues.

Since radon is characterized by seasonal, daily, and multi-day variations [30-33], which is associated with differences in pressure, temperature, and other environmental parameters, then in order to determine areas exposed to radon, it is recommended to establish patterns of concentration of its decay products in the soil in order to predict its accumulation in a given area depending on the physical and chemical characteristics. At the same time, according to [34], using the results of gamma studies of soil samples can improve the mapping of radon hazard zones. This is due to the fact that most gamma-emitting nuclides, as well as radon isotopes, are daughter products of decay in natural decay chains from $^{235}$U, $^{232}$Th, and $^{238}$U. Therefore, comprehensive radiation monitoring of environmental objects can be used to assess the expected annual dose from natural radiation sources and construct maps of radon potential in the areas under study.

## 2. Materials and methods

In this work, radiometric measurements of the equivalent equilibrium volumetric activity (EEVA) of radon in buildings located at different distances from tectonic faults and beta- and gamma-spectrometric measurements of soil samples were performed.

The measurements were carried out at different distances from tectonic faults using the radon radiometer "RAMON-02" in temporary and long-term buildings. Radiometers "RAMON-02" are used to measure the EEVA of radon in the range of 1÷5•10$^5$ Bq/m$^3$. The EEVA values of radon and its decay products were obtained by measuring the RAMON-02 device at the positions indicated in Figure 1. For this study, buildings located in Almaty, southeastern Kazakhstan, in the foothills of the Zailiyskiy Alatau, were selected. Radon monitoring measurements were carried out from January 2024 to July 2024 at different distances from tectonic faults. The latest seismic microzonation map, taking into account all known faults, was developed and approved in 2021 by the Institute of Seismology [35].

The Faculty of Physics and Technology (43°13'25.88"N 76°55'29"E) was identified as the first study object (No. 1), located 235 m from the nearest tectonic fault. The second study object (No.2) was the Student House (43°13'08.7"N 76°55'30.2"E), located 27 m from the tectonic fault. The third study object (No. 3) was the Student House (43°13'06"N 76°55'14"E), located 274 m from the fault.

The next object (No. 4) was the Student Service Center building (43°13'11.7"N 76°55'19.4"E), located 386 m from the fault. Measurements were taken in the basements. The fifth object (43°12'35.9"N 76°53'18.5"E) is 1,500 meters from

the nearest tectonic fault. The five-story building has four entrances, and the house is a privatized dormitory. The sixth object (43°13'56.7"N 76°57'34.4"E) is 917 m from the fault and is an office building of the Koktem Towers business center. The seventh object of study (No. 7, 465 m from the fault) was the Faculty of Biology and Biotechnology (43°13'25"N 76°55'15"E).

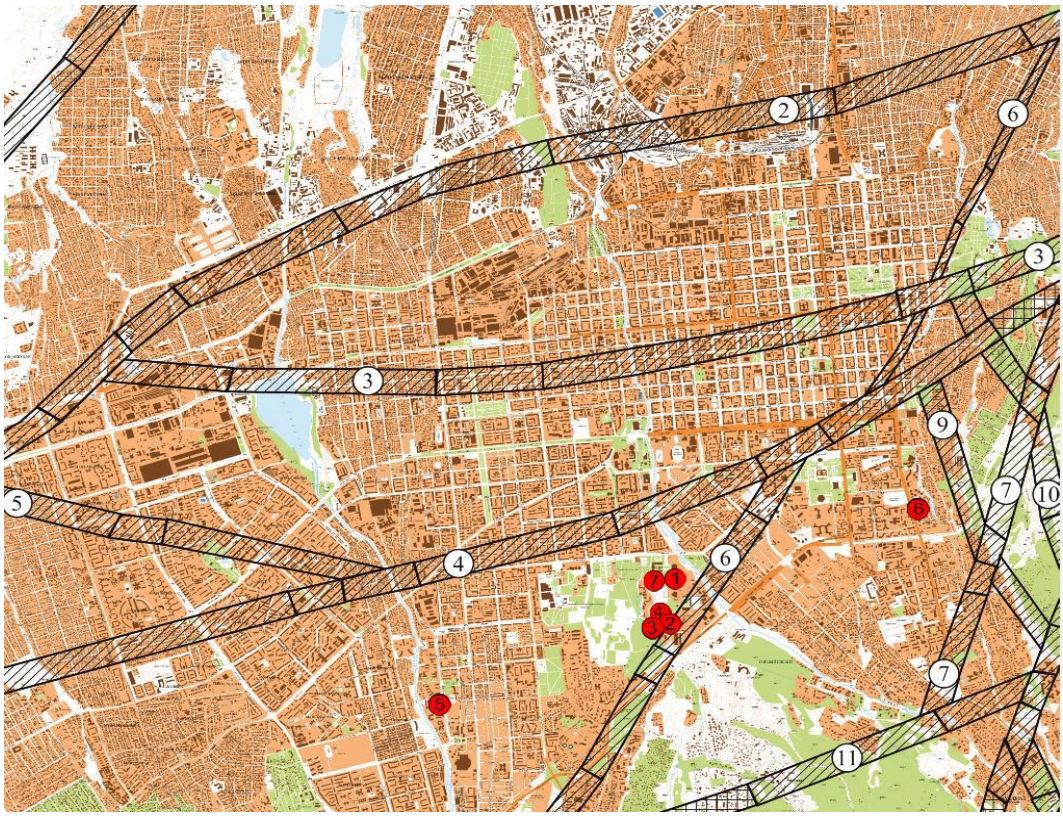



**Figure 1 –** Radon measurement positions (red dots) on the map of active tectonic faults [36]

All radon concentration measurements were taken in closed, unventilated rooms to determine the highest potential for radon exposure. This is because closed spaces without the influence of air flows have higher radon levels than rooms with good natural or artificial ventilation systems [5]. Three radon EEVA measurements were taken in each position using a RAMON-02 radiometer (exposure time for each measurement was 128 seconds) per day, with subsequent conversion to average daily values for each measurement position.

Despite the fact that radon isotopes are alpha emitters, most of their decay products are beta and gamma emitters with fairly long half-lives: $^{214}$Pb ($T_{1/2}$ = 26.8 min), $^{210}$Pb ($T_{1/2}$ = 22.2 years), $^{214}$Bi ($T_{1/2}$ = 19.9 min), $^{212}$Bi ($T_{1/2}$ = 61 min), $^{210}$Bi ($T_{1/2}$ = 5.01 days), $^{210}$Po ($T_{1/2}$ = 138 days). In this regard, within the framework of this work, beta and gamma spectrometry of soil samples taken at different distances from the fault was also carried out to search for a relationship between the level of accumulated activity and the level of radon concentration. The measurements were carried out on beta and gamma spectrometric installations SKS-99 "SPUTNIK" with scintillation types of detectors based on CsI (45x50 mm) for measuring the activity of gamma-emitting radionuclides and based on ZnS with plastic for measuring the flux density of beta particles.

Soil sampling for gamma and beta measurements was carried out in Almaty at the coordinates indicated in Table 1. Nine samples were collected at different positions located from the nearest tectonic fault between 144 m and 1190 m. About 1 kg of soil was collected for the soil samples by removing 5 cm of the surface soil layer. The measurement positions are shown schematically in Figure 2.

**Table 1 –** Spectrometric measurement positions of soil samples

| No. | Coordinates of measurement positions | Distance to fault, m |
|---|---|---|
| 1 | 43°13'09.8"N<br>76°55'12.6"E | 394 |
| 2 | 43°13'24.2"N<br>76°55'29.0"E | 233 |
| 3 | 43°13'20.7"N<br>76°55'30.5"E | 177 |
| 4 | 43°14'37.5"N<br>76°54'04.4"E | 371 |
| 5 | 43°13'08.8"N<br>76°52'49.9"E | 613 |
| 6 | 43°13'38.4"N<br>76°53'41.7"E | 144 |
| 7 | 43°13'38.8"N<br>76°53'06.8"E | 307 |
| 8 | 43°15'46.3"N<br>76°56'39.2"E | 913 |
| 9 | 43°15'58.5"N<br>76°56'38.6"E | 1190 |

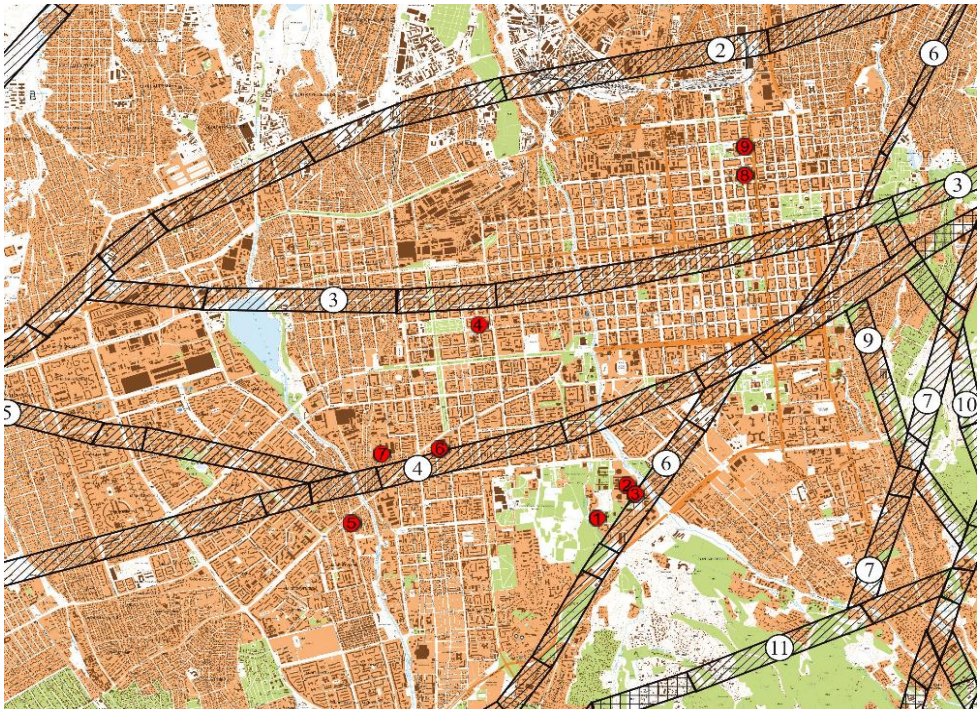


**Figure 2 –** Positions of beta and gamma activity measurements (red dots) on the map of active tectonic faults [36]

The beta spectrometer was calibrated using the Sr-Y-90 beta source, and the gamma spectrometer was calibrated using Cs-137 gamma sources. Figure 3 shows the calibration curve of the beta spectrometer using the Sr-Y-90 beta source.

After soil sample preparation, a quantitative assessment of the natural beta and gamma activity concentration in the selected samples was performed. Each sample was pre-dried for at least 24 hours (Figure 4a). Manual grinding was performed (Figures 4b and 4c) to increase the concentration of the samples and obtain a homogeneous mixture. Weighing the samples was performed using a digital scale SF-400 with an accuracy of ±0.01 g. Table 2 shows the net weight of the selected soil samples for beta and gamma spectrometry.

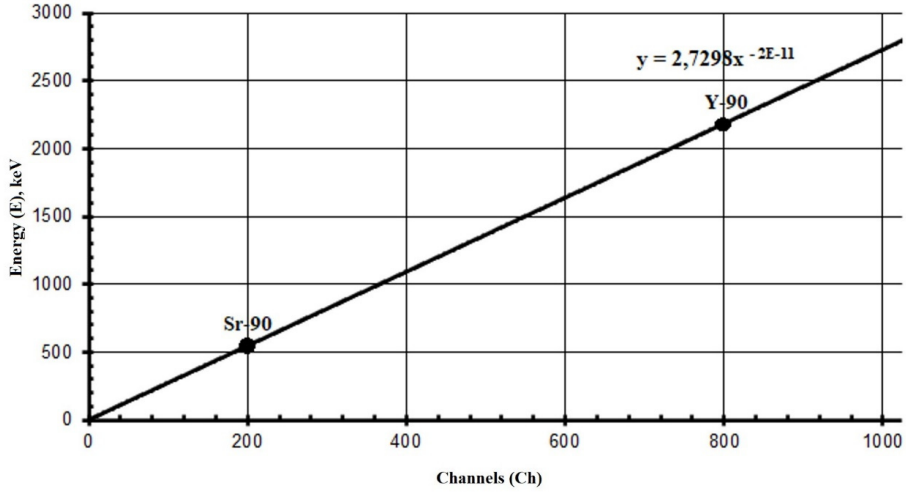



**Figure 3 –** Beta-spectrometer energy calibration curve



a) b) c)

**Figure 4 –** Soil sample preparation for spectrometric measurements:
a) preparation of soil samples for drying; b) the process of manual grinding of samples
for gamma-spectrometry analysis; c) the process of manual grinding of samples for beta-spectrometry analysis

**Table 2 –** Sample mass for beta and gamma spectrometry

| Sample Code | Position (coordinates) of sample selection | $m_\beta$, g | $m_\gamma$, g |
|---|---|---|---|
| 1 | 43°13'09.8"N 76°55'12.6"E | 22 | 632 |
| 2 | 43°13'24.2"N 76°55'29.0"E | 25 | 467 |
| 3 | 43°13'20.7"N 76°55'30.5"E | 22 | 416 |
| 4 | 43°14'37.5"N 76°54'04.4"E | 21 | 501 |
| 5 | 43°13'08.8"N 76°52'49.9"E | 17 | 376 |
| 6 | 43°13'38.4"N 76°53'41.7"E | 17 | 459 |
| 7 | 43°13'38.8"N 76°53'06.8"E | 16 | 456 |
| 8 | 43°15'46.3"N 76°56'39.2"E | 18 | 462 |
| 9 | 43°15'58.5"N 76°56'38.6"E | 19 | 503 |

The exposure of measurements on the SKS-99 "SPUTNIK" spectrometers was no less than 10,000 events per sample to reduce statistical uncertainty. Background measurements were performed before and after each sample measurement. The background spectra were used to correct the net areas of the measured samples' spectra.

The equipment used for measurements has been verified by SOLO LLP and the Almaty Certification Bureau (verification certificate No. BA.17-04-47195 dated September 28, 2023, and is valid until September 28, 2024).

## 3. Results and discussion

The analysis of the obtained results showed that the geometric mean value for the measured positions was 38.9 Bq/m$^3$. The radon concentration fluctuated between 6.13 and 405.21 Bq/m$^3$ (Figure 5). The analysis of the results showed that the radon EEVA decreases exponentially according to the following pattern: $C_{Rn}=499.85 \cdot e^{-0.0078 \cdot R}$, where $R$ is the distance to the nearest tectonic fault. In addition, for some measurement positions in rooms close to a tectonic fault, values exceeded the standard values for radon concentration in indoor air (200 Bq/m$^3$) [5].

Figure 5 shows that the highest radon concentration value was found at a distance of 27 m in building No. 2 (Figure 1). The results show the influence of the proximity of a tectonic fault on the level of radon concentration inside the premises, as in the works [37, 38]. This is most likely due to the fact that faults are a favorable migration path for radon gas since faults have higher permeability. Thus, if there are many cracks in tectonic faults, which form high permeability, radon from the depth can easily rise to the surface from the depth, leading to higher radon concentrations near the fault.

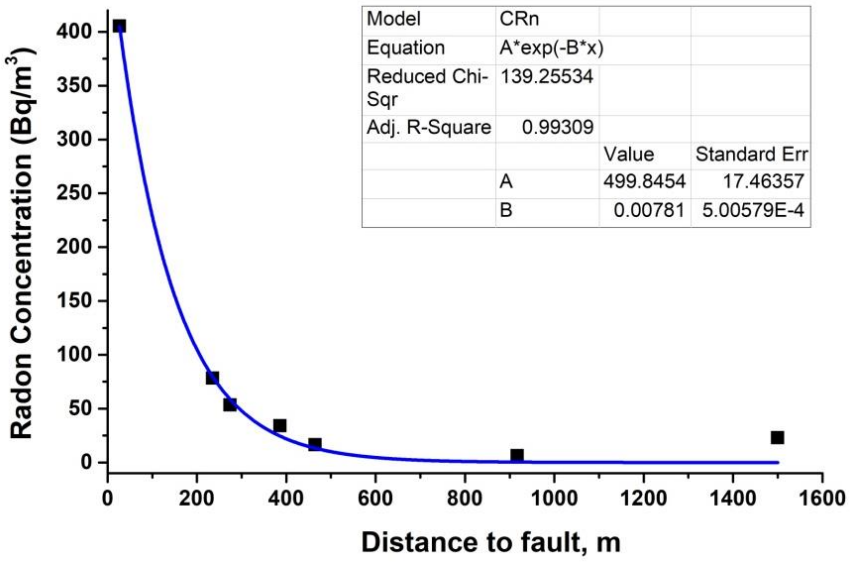
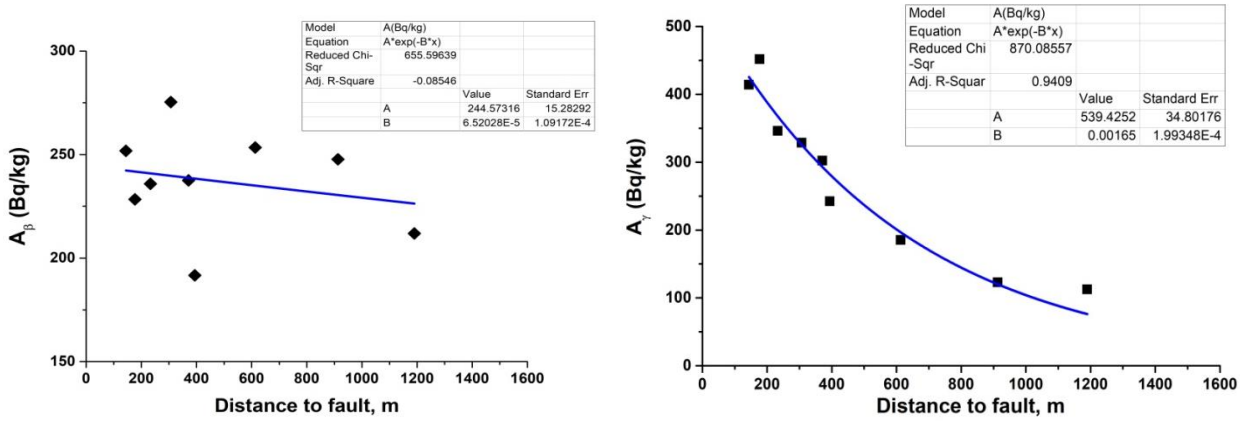



**Figure 5 –** Average indoor radon concentration depending on the distance from the tectonic fault

Based on the obtained experimental spectrometric data, the specific integral beta and gamma activities were assessed in the studied soil samples. The specific activity of the samples (Bq/kg) was calculated using the following formula [26]:

$$A = \frac{cps}{I_{\gamma,\beta} \cdot \varepsilon_{\gamma,\beta} \cdot m_{\gamma,\beta}} \quad (1)$$

where $cps = \frac{N}{t} - \frac{N_0}{t_0}$ – net counts per second; $I_\gamma$ and $I_\beta$ –the gamma and beta emission probabilities; $\varepsilon$ – is the detection efficiency; $m_\beta$ – the mass (dry weight) in kilogram of the beta sample (in kg), $m_\gamma$ – the mass (dry weight) in kilogram of the gamma sample (in kg). An exponential pattern of decrease in beta and gamma activities with distance to the tectonic fault $R$ was found (Figure 6): for beta – $A_\beta = 244.57 \cdot e^{-6.52E-5 \cdot R}$, for gamma – $A_\gamma = 539.43 \cdot e^{-0.00165 \cdot R}$.




a) b)

**Figure 6 –** Concentration of a) beta and b) gamma activities of samples depending on the distance from the tectonic fault

The concentrations of beta activity in soil samples varied from 191.67±28.75 to 275.32±41.30 Bq/kg, and gamma activity from 112.51±16.88 to 451.60±67.74 Bq/kg. The results obtained do not exceed the established world standard of 465 Bq/kg for the activity of natural gamma radionuclides [39] and are in the same ranges for the obtained beta and gamma activities as in the works [40-44]. However, it is worth noting that the maximum value for the gamma activity of the soil (451.60 Bq/kg) obtained in this work exceeds the standard established for the Republic of Kazakhstan (397 Bq/kg) [39].

Pearson correlation analysis was used to calculate correlation coefficients [45]:

$$r_{xy} = \frac{\Sigma(x_i - \bar{x}) \times (y_i - \bar{y})}{\sqrt{\Sigma(x_i - \bar{x})^2 \times \Sigma(y_i - \bar{y})^2}} \qquad (2)$$

where $x_i$ – values taken by variable X; $y_i$ – values taken by variable Y; $\bar{x}$– average by X; $\bar{y}$ – average by Y. Correlation analysis showed that the beta activity concentration weakly correlates with the radon concentration in the air (correlation coefficient – 0.58). A strong correlation was found between the concentrations of gamma activity in the soil and the radon concentrations in the air (correlation coefficient – 0.79). Interpretation of the results of the correlation analysis leads to the following conclusions: 1) beta-emitting radionuclides may have less penetrating ability than gamma radionuclides; 2) spectrometric gamma analysis of radon decay products can be used as an indirect method for measuring radon concentration.

## 4. Conclusions

The concentration of radon activity and its decay products was measured by spectroradiometric methods for soil and air samples collected in Almaty at a distance of 27 m to 1500 m from the tectonic fault. The results show that the higher the indoor radon concentration, the closer the building is to the tectonic fault. The average radon concentration in the basement of building No.2 in Figure 1 (located 27 m from the tectonic fault) exceeds by 305% the value of 100 Bq/m$^3$ defined by WHO as requiring action [5] and by 102.5% the value of 200 Bq/m$^3$ defined in the Republic of Kazakhstan for buildings in operation [46]. This demonstrates the need to take corrective measures, for example, by improving the building's ventilation system.

In the soil samples examined in this study, the average concentration of beta and gamma activities is approximately in the same range as in other countries [47-49]. At the same time, the positive correlation between the concentration of gamma activity and the indoor radon concentration showed that the content of gamma radionuclides in the soil has a similar pattern of decreasing with distance from the tectonic fault. In other words, a high concentration of gamma radionuclides in the soil is a harbinger of increased levels of radon gas in the premises at present or in the near future.

It is important to identify the presence of positions with higher concentrations of radon and its decay products, as well as the causes of their occurrence, for an accurate assessment of the corresponding radon risk. These results will allow the

development of protective measures to reduce the entry of radon into indoor air in the future. In particular, understanding the relationship between radon concentration and the activity of radon decay products will allow the development of risk maps and identify areas requiring constant radiation monitoring. This is especially true for areas with a high gamma background level, where urban planners can develop and implement radon-resistant construction methods associated with the potential danger of elevated radon levels.

## Acknowledgments

This research is funded by the Science Committee of the Ministry of Science and Higher Education of the Republic of Kazakhstan (Grant No. AP23486701).

### References

1. Sustainable Development Goals (SDGs).- 2024 – https://www.undp.org/sustainable-development-goals?gclid=EAIaIQobChMIvZCkqIq7gAMVD4RoCR1EBQXjEAAYASAAEgKy6fD_BwE
2. Li P., Zhang R., Gu M., Zheng G. Uptake of the natural radioactive gas radon by an epiphytic plant // Science of The Total Environment. – 2018. – Vol. 612. – P. 436-441. https://doi.org/10.1016/j.scitotenv.2017.08.253
3. Sun H., Semkow T.M. Mobilization of thorium, radium and radon radionuclides in ground water by successive alpha-recoils // J. Hydrol. – 1998. – Vol. 205. – P. 126-136. https://doi.org/10.1016/S0022-1694(97)00154-6
4. IARC Monographs on the evaluation of carcinogenic risks to humans. D Radiation. – Lyon: International Agency for Research on Cancer- 2012. – Vol.10.-P.341.
5. WHO Handbook on Indoor Radon: A Public Health Perspective. – Geneva: World Health Organization, 2009. – https://iris.who.int/bitstream/handle/10665/44149/9789241547673_eng.pdf
6. ICRP Publication 50. Lung cancer risk from exposures to Radon daughters // Ann. ICRP. – 1987. – Vol. 17.-N. 1. – P.60.
7. ICRP Publication 65. Protection against Radon-222 at home and at work // Ann. ICRP. – 1993. – Vol. 23. N.2. – P.45.
8. Schoenberg J.B., Klotz J.B., Wilcox H.B., Nicholls G.P., Gil-del-Real M.T., Stemhagen A. Case-control study of residential radon and lung cancer among New Jersey women // Cancer Research. – 1990. – Vol. 50.- No. 20. – P. 6520-6524.
9. Darby S., Hill D., Auvinen A., Barros-Dios J.M., Baysson H., Bochicchio F., Deo H., Falk R., Forastiere F., Hakama M., et al. Radon in homes and risk of lung cancer: Collaborative analysis of individual data from 13 European case-control studies // BMJ. – 2004. – Vol. 330. – P. 223-226. https://doi.org/10.1136/bmj.38308.477650.63
10. Coretchi L., Ene A., Ababii A. Control of the health risk of Radon exposure in the Republic of Moldova // Atmosphere. – 2021. – Vol. 12. Is. 10. – P.1302. https://doi.org/10.3390/atmos12101302
11. Kaidarova D.R., Shatkovskaya O.V., Zholdybay Zh.Zh., Zhylkaidarova A.Zh., Panina A.S. Lung cancer in Kazakhstan: age-gender features // Oncology and Radiology of Kazakhstan. – 2020. – Vol. 55, No. 1. – P. 3-8. https://doi.org/10.52532/2521-6414-2020-1-55-4-10
12. Kendall G.M., Smith T.J. Doses to organs and tissues from radon and its decay products // Journal of Radiological Protection: Official Journal of the Society for Radiological Protection. – 2002. – Vol. 22. – P. 389-406. https://doi.org/10.1088/0952-4746/22/4/304
13. Brauner E.V., Andersen Z.J., Andersen C.E., Pedersen C., Gravesen P., Ulbak K., Hertel O., Loft S., Raaschou-Nielsen O. Residential radon and brain tumour incidence in a Danish cohort // PloS One. – 2013. – Vol. 8. – P.74435. https://doi.org/10.1371/journal.pone.0074435
14. Turner M.C., Krewski D., Chen Y., Pope C.A., Gapstur S.M., Thun M.J. Radon and nonrespiratory mortality in the American Cancer Society cohort // American journal of epidemiology. – 2012. – Vol. 176. – P. 808-814. https://doi.org/10.1093/aje/kws198
15. ICRP Publication 126. Radiological Protection against Radon Exposure // Ann. ICRP. – 2014. – Vol. 43, No. 3. – P. 5-73.
16. ASHRAE Guideline 10P. Interactions Affecting the Achievement of Acceptable Indoor Environments, Second Public Review. – Atlanta: ASHRAE-2010.
17. Miklyaev P.S., Petrova T.B., Shchitov D.V., Sidyakin P.A., Murzabekov M.A., Marennyy A.M., Nefedov N.A., Sapozhnikov Y.A. The results of long-term simultaneous measurements of radon exhalation rate, radon concentrations in soil gas and groundwater in the fault zone // Applied Radiation and Isotopes. – 2021. – Vol. 167. – P.109460. https://doi.org/10.1016/j.apradiso.2020.109460
18. Drolet J.P., Martel R. Distance to faults as a proxy for radon gas concentration in dwellings // Journal of Environmental Radioactivity. – 2016. – Vol. 152. – P. 8-15. http://doi.org/10.1016/j.jenvrad.2015.10.023
19. Kobal I., Vaupotic J., Gregoric A., Uralbekov B. Comparison of approaches in Slovenia and Kazakhstan in managing exposure to radon // Uranium – Past and Future Challenges / in: Merkel, B., Arab, A. // Cham: Springer International Publishing - 2015. – P. 689-698. https://doi.org/10.1007/978-3-319-11059-2_79
20. Fedorov G.V., Kayukov P.G., Bensman V.A. Current issues of studying radon hazard of the territory of the Republic of Kazakhstan // Ekologiya i razvitie obshchestva. – 2012. - Vol. 2. Is. 4. – P. 73-79.
21. Tokonami S. Experimental verification of the attachment theory of radon progeny onto ambient aerosols // Health Phys. – 2000. – Vol. 78. – P. 74-79. https://doi.org/10.1097/00004032-200001000-00012
22. United Nations Scientific Committee on the Effects of Atomic Radiation (UNSCEAR). Radiation Effects and Sources. – United Nations Environment Programme: Nairobi, Kenya - 2016. https://wedocs.unep.org/20.500.11822/7790

23. Lorenzo-Gonzalez M., Torres-Duran M., Barbosa-Lorenzo R., Provencio-Pulla M., Barros-Dios J.M., Ruano-Ravina A. Radon exposure: A major cause of lung cancer // Expert Rev. Respir. Med. – 2019. – Vol. 13. No. 9. – P. 839-850. https://doi.org/10.1080/17476348.2019.1645599

24. Manna F., Pugliese M., Ambrosino F., Trifuoggi M., Giarra A., La Verde G. Radionuclides in italian drinking water and regulations: Data collection to improve risk assessment // Environments. – 2023. – Vol. 10. – P.193. https://doi.org/10.3390/environments10110193

25. Measurement protocol for Radon in dwellings // NRPA - 2013. – P.17

26. Dina N.T., Das S.C., Kabir M.Z., et al. Natural radioactivity and its radiological implications from soils and rocks in Jaintiapur area, North-east Bangladesh // J Radioanal Nucl Chem. – 2022. – Vol. 331. – P. 4457-4468. https://doi.org/10.1007/s10967-022-08562-0

27. Al-Hamarneh I.F., Awadallah M.I. Soil radioactivity levels and radiation hazard assessment in the highlands of northern Jordan // Radiation Measurements. – 2009. – Vol. 44, Is.1. – P.102-110. https://doi.org/10.1016/j.radmeas.2008.11.005

28. Ahmad N., Jaafar M.S., Bakhash M., Rahim M. An overview on measurements of natural radioactivity in Malaysia // Journal of Radiation Research and Applied Sciences. – 2015. – Vol. 8, Is.1. – P. 136-141. https://doi.org/10.1016/j.jrras.2014.12.008

29. Swift B. Dating human skeletal remains: investigating the viability of measuring the equilibrium between $^{210}$Po and $^{210}$Pb as a means of estimating the post-mortem interval // Forensic Sci. Int. – 1998. – Vol. 98. – P. 119-126. https://doi.org/10.1016/S0379-0738(98)00141-8

30. Otoo F., Darko E.O., Garavaglia M., Giovani C., Pividore S., Andam A.B., Amoako J.K., Adukpo O.K., Tandoh J.B., Inkoom S. Seasonal indoor radon studies in buildings of Accra metropolis of greater Accra region of Ghana // Radioprotection. – 2018. – Vol. 53, No. 3. – P. 199-206. https://doi.org/10.1051/radiopro/2018023

31. Duggal V., Rani A., Mehra R. A study of seasonal variations of radon levels in different types of dwellings in Sri Ganganagar district, Rajasthan // J. Radia. Res. Appl. Sci. – 2014. – Vol. 7. - Is. 2. – P. 201-206. . https://doi.org/10.1016/j.jrras.2014.02.007

32. Fujiyoshi R., Sakamoto K., Imanishi T., Sumiyoshi T., Sawamura S., Vaupotic J., Kobal I. Meteorological parameters controlling variability of $^{222}$Rn activity concentration in soil gas at a site in Sapporo Japan // Sci. Tot. Env. – 2006. – Vol. 370.- Is. 1. – P. 224-234. https://doi.org/10.1016/j.scitotenv.2006.07.007

33. Kitto M.E. Interrelationship of indoor radon concentrations, soil-gas flux, and meteorological parameters // J. Radio. Nucl. Chem. – 2005. – Vol. 264. – P. 381-385. https://doi.org/10.1007/s10967-005-0725-6

34. Wilford J. A Weathering intensity index for the Australian Continent using airborne gamma-ray spectrometry and digital terrain analysis // Geoderma. – 2012. – Vol. 183-184. – P. 124-142. https://doi.org/10.1016/j.geoderma.2010.12.022

35. Sadykova A.B., Silacheva N.V., Stepanenko N.P. Seismic micro zoning of the territory of Almaty on a new methodological basis // NEWS of the Academy of Sciences of the Republic of Kazakhstan. Series of Geology and Technical Sciences. – 2021. – Vol. 1.- No. 445. – P. 127-134. https://doi.org/10.32014/2021.2518-170X.18

36. Zhdanovich A.R., Stepanenko N.P., Uteuliev T.S., Shestakov V.V., Zhakupov N.S., Ashirov B.M., Kadyrkhanova N.Zh. Map of active fault zones (with possible manifestation of residual deformations in the soil in the territory of Almaty). – 2016 https://seismology.kz/

37. Yang S., Goyette Pernot J., Hager Jorin C., Niculita-Hirzel H., Perret V., Licina D. Radon investigation in 650 energy efficient dwellings in Western Switzerland: impact of energy renovation and building characteristics // Atmosphere. – 2019. – Vol. 10, Is. 12. – P.777. https://doi.org/10.3390/atmos10120777

38. Zaripova Y., Dyachkov V., Bigeldiyeva M., Gladkikh T., Yushkov A. Preliminary survey of exposure to indoor Radon in al-Farabi Kazakh National University, Kazakhstan // Atmosphere. – 2023. – Vol. 14.- No. 10. – P.1584. https://doi.org/10.3390/atmos14101584

39. UNSCEAR Sources and effects of ionizing radiation, vol. I. United Nations scientific committee on the effects of atomic radiation, New York -2000.

40. Amin S.A., Al-Khateeb M.A., Abd T.K. Gamma activity in Bu'Aitha soil, south Baghdad // Int. J. Environ. Sci. Technol. – 2019. – Vol. 16. – P. 4665-4670. https://doi.org/10.1007/s13762-018-2075-2

41. Shahzadi C., Jabbar A., Rafique M., Khan M., Dilband M., Hayat Satti K. Study of gross alpha, gross beta and natural radioactivity in soil samples of district Muzaffarabad // International Journal of Environmental Analytical Chemistry – 2020. – Vol. 102(17). – P. 5549-5566. https://doi.org/10.1080/03067319.2020.1800001

42. Hayat Satti K., Jabbar T., Dilband M., Chaudhry M., Jabbar A., Arshad W. Spatial distribution of radionuclides and major elements in soil of Murree and Kotli Sattian Punjab, Pakistan // Journal of Environment and Earth Science. – 2016. – Vol. 6.- No. 11. – P. 104-114.

43. Tahani M. Kadhim, et al. Measurement of the natural radiological activity of soil samples of some general education schools in Al-Qadisiyah Governorate // IOP Conf. Ser.: Mater. Sci. Eng. – 2020. – Vol. 928. –P. 072026. https://doi.org/10.1088/1757-899X/928/7/072026

44. Küçükönder E., Gümbür S., Söğüt Ö., et al. Natural radioactivity in soil samples taken from Kahramanmaraş provincial center // Environ Geochem Health. – 2023. – Vol. 45. – P. 5245-5259. https://doi.org/10.1007/s10653-023-01577-w

45. Berman J. Understanding Your Data. Chapter 4 in Data Simplification. – Boston: Morgan Kaufmann- 2016. – P. 135-187.

46. On approval of hygienic standards to ensure radiation safety. Order of the Minister of Health of the Republic of Kazakhstan-2022 https://adilet.zan.kz/rus/docs/V2200029012

47. Otoo F., Darko E.O., Garavaglia M. Correlation analysis of natural radionuclides, radon exposure, soil particles and moisture from quarry towns in greater Accra region, Ghana // Water, Air, & Soil Pollut. – 2022. – Vol. 233. – 338. https://doi.org/10.1007/s11270-022-05791-7

48. Farid S.M. Indoor radon in dwellings of Jeddah city, Saudi Arabia and its correlations with the radium and radon exhalation rates from the soil // Indoor Built Environ. – 2016. – Vol. 25. Is. 1. – P. 269-278. https://doi.org/10.1177/1420326X14536749

49. Otoo F., Kpordzro R., Amable A.S.K. Radon mapping, correlation study of radium, seasonal indoor radon and radon exhalation levels in communities around Ghana atomic energy commission // Heliyon. – 2023. – Vol. 9.-Is. 4. – P.15259. https://doi.org/10.1016/j.heliyon.2023.e15259

***Information about authors:***

*Zaripova Yuliya, PhD, Senior lecturer at al-Farabi Kazakh National University (Almaty, Kazakhstan) e-mail: zarypova.iulyiya1@kaznu.kz*

*Yushkov Alexandr, doctor of science, professor at al-Farabi Kazakh National University (Almaty, Kazakhstan) e-mail: yushkov.prof@kaznu.kz*

*Amangeldiyeva Nazerke. Laboratory assistant at al-Farabi Kazakh National University (Almaty, Kazakhstan) e-mail: amangeldiyeva.nazerke26@gmail.com*

*Dyussebayeva Kuralay, Senior lecturer at al-Farabi Kazakh National University (Almaty, Kazakhstan) e-mail: kuralay.diusebaeva@kaznu.kz*

*Shaidollina Aknur. 2nd year Master student, laboratory assistant at al-Farabi Kazakh National University (Almaty, Kazakhstan) e-mail: akojank02@gmail.com*

IRSTI 29.15.17; 29.15.19 https://doi.org/10.26577/phst2024v11i2b02

# Extraction of the radii of $^{9}$Be, $^{10}$B and $^{11}$B nuclei in the approximation of the strongly absorbing nucleus model in elastic scattering reactions of deuterons

V.V. Dyachkov

Voronezh State University, 1 Universitetskaya pl., Voronezh, 394018, Russia
e-mail: slava_kpss@mail.ru
*(Received September 5, 2024; received in revised form September 30, 2024; accepted October 10, 2024)*

To study the cluster states of light nuclei, in this work, the radii of $^{9}$Be, $^{10}$B and $^{11}$B nuclei were calculated using elastic scattering of deuterons with energies from 11 MeV to 28 MeV. The values of the free parameters from the complex angular momentum method were calculated using fits to the single-valued minimum Pearson values. The fits were carried out by describing the theoretical curve of the experimental data for the first two oscillations of the Fraunhofer-type nuclear diffraction of the differential cross sections of elastic scattering of deuterons. Moreover, the array of experimental data points was not always unambiguous, and this led to difficulties in the quality of fitting free parameters, which affected the results of radius calculations. The results of the radii are presented in the paper, the values of which were compared with the values of the world literature data. The obtained calculated values of the radii of nuclei for $^{9}$Be are in satisfactory agreement with the exception of some values. For $^{10}$B and $^{11}$B, there is a systematic excess of the obtained radii over the literature values. It is possible that such excess is due to the fact that when calculating the radii of the nuclei under study, the structure of the deuterons and their own radius, which increases the radius of interaction, were not taken into account.

**Key words:** elastic scattering; deuterons; light nuclei; Fraunhofer-type nuclear diffraction; root-mean-square radius of a nucleus.
**PACS number(s):** 25.60.Bx; 27.20.+n.

## 1. Introduction

Light nuclei, the structure of which is described by theoretical models of cluster states [1-4], are currently being actively studied. In most cases, such a theoretical approach describes the distribution of nuclear density quite well. This phenomenon, in turn, manifests itself in the form of anomalous sizes of mean-square radii, such as the halo in [5]. Nuclei in the cluster model approach have been studied for quite a long time; as an example, such studies can be traced in works [6-8]. Determining the root-mean-square radius of a nucleus, and if this value goes beyond classical concepts, then this allows us to draw conclusions about further study of the nuclei under study and the possible pronounced cluster configuration of these nuclei. The relevance and importance of studying differential, integral and total cross sections of light incident particles is, first of all, the solution of fundamental problems of nuclear astrophysics and applied problems of thermonuclear energy and radioecology.

In the present work, calculations of the radii of $^{9}$Be, $^{10}$B and $^{11}$B nuclei were performed. The radii of nuclei were calculated using the complex angular momentum method (CAMM). The CAMM was implemented in an analytical form by the authors of [9-11] from a rigorous quantum-mechanical expression for the elastic scattering amplitude expanded in partial waves.

## 2. Materials and methods

Basic information about the structure and properties of nuclei and the mechanisms of nuclear reactions is obtained primarily from elastic scattering reactions.

Studies on the structure of light nuclei based on the cluster approach, in particular in [12-22], show that the relevance of using the cluster model to describe light nuclei, up to 40-Ca, is very high. This

approach allows us to interpret such nuclei as a group of different clusters interacting with each other. In this case, the dynamic association in the ratio of one type of cluster to another from nucleus to nucleus, or even from isotope to isotope, can be radically different. Such a difference and the existence with a greater probability of certain cluster configurations affects the root-mean-square radius, the blurriness of the edge of the nucleus and the nuclear deformation. In turn, such nuclear parameters are extracted from various nuclear reactions. In particular, in this work, the root-mean-square radius is extracted from oscillations of differential cross sections of elastically scattered deuterons. Expansion of the scattering amplitude into the sum of partial scattered waves

$$\frac{d\sigma(\theta)}{d\Omega} = \left|A(\theta)\right|^2 = \\ = \frac{1}{2ik}\cdot\sum_{l=0}^{\infty}\left[2l+1\right]\cdot\left[e^{2i\eta_l}-1\right]\cdot P_l\left(\cos(\theta)\right), \quad (1)$$

where $\eta_l$ – scattering phase

$$\eta_l = \sigma_l + \delta_l . \quad (2)$$

$\sigma_l$ – Coulomb phase; $\delta_l$ – nuclear phase.

Scattering matrix has the form

$$S_l = e^{2i\eta_l} = e^{2i(\sigma_l+\delta_l)}, \\ S_l = 1-\left[1+\exp\frac{l-l_0}{\lambda}\right]^{-1}. \quad (3)$$

where $l$ is the angular momentum, λ is the diffuseness parameter of the edge of the nucleus. Section (1) taking into account (3) will have the following form

$$\frac{d\sigma(\theta)}{d\Omega} = \sigma_0(\theta) = \\ = \frac{8\pi}{k^2}|a|^2 l_0 \frac{b^2+\cos^2\left(\left(l_0+0{,}5\right)\theta+\gamma\right)}{\sin(\theta)\cdot e^{2\beta\theta}} \quad (4)$$

where $|a|, l_0, \beta, b, \gamma$ are the free parameters of the theory. The analytical form (4) with the corresponding restrictions in the paradigm of the strongly absorbing nucleus model is the method of complex angular momenta [9-11].

In elastic scattering, nuclear diffraction of different types can be observed in differential angular distributions depending on the properties of the incident wave from the beam of charged particles interfering with the properties of the target nucleus. The conditions for the occurrence of one or another type of nuclear diffraction are presented below.

1. $kR \sim 1$ – Rutherford scattering;
2. $\begin{cases} kR >> 1 \\ n \sim 1 \end{cases}$ – Fraunhofer type diffraction;
3. $\begin{cases} kR >> 1 \\ n >> 1 \end{cases}$ – Fresnel type diffraction. (5)

where $n = \frac{Z_1 Z_2 e^2}{\hbar \cdot v}$ – Coulomb parameter (Sommerfeld parameter); $k = \frac{\sqrt{2\cdot M\cdot E}}{\hbar}$ – wave number. Fraunhofer diffraction occurs when the wavelength of the incident particle is less than the radius of the nucleus. This resembles the passage of light through a narrow slit, where a characteristic interference pattern with alternating light and dark bands is observed on the screen. In the case of nuclear diffraction, these bands correspond to different scattering angles of the particle. For this process to occur, it is important that the Sommerfeld parameter is less than 1. This parameter characterizes the influence of the Coulomb field of the nucleus on the trajectory of the particle. The smaller the Sommerfeld parameter, the less the influence of the Coulomb field, and the clearer the diffraction pattern. Fresnel diffraction differs from Fraunhofer diffraction in that the Sommerfeld parameter in this case is greater than 1. This means that the Coulomb field of the nucleus strongly influences the motion of the particle. As a result, we observe interference between nuclear scattering (reflection from the nucleus) and scattering in the Coulomb field. This interaction leads to more complex diffraction patterns. Let's consider each type in more detail.

Fraunhofer diffraction: Imagine a beam of electrons directed at an atomic nucleus. This makes Fresnel diffraction more difficult to analyze, but also more informative in terms of studying the structure of the nucleus.

This paper presents a literature experimental analysis of differential angular cross sections of

elastic scattering of deuterons under Fraunhofer-type nuclear diffraction conditions.

The search for the optimal parameters of the CAMM (4) was carried out by minimizing the value $\chi 2$

$$\chi^2 = \frac{1}{N}\sum_{i=1}^{N}\left[\frac{(\sigma_i)_{teor} - (\sigma_i)_{\exp}}{\Delta(\sigma_i)_{\exp}}\right]^2, \qquad (6)$$

where $(\sigma_i)_{teor}$ and $(\sigma_i)_{\exp}$ – theoretical and experimental cross sections, $N$ – number of measured points.

Figure 1 shows the picture of the values of the $\chi^2$ isolines of the free parameters of the model (4) calculated for the reaction 11-B(d,d)11-B Ed=18 MeV. The search for optimal parameters was proposed in [23]. In this work, the parameters of the theory were adjusted to the experiment using this method.

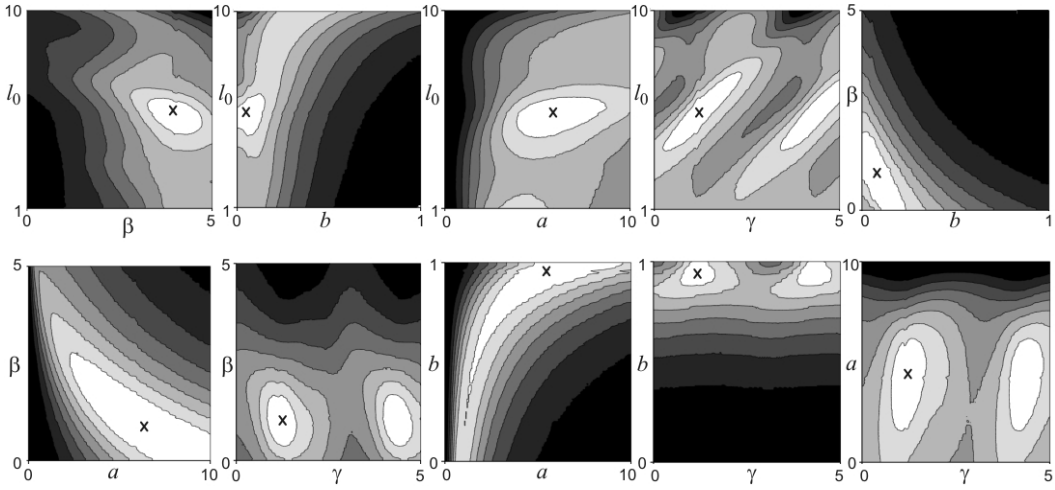



**Figure 1 -** $\chi 2$- distributions for five pairs of free parameters of the method of complex angular momenta of elastically scattered deuterons on $^{11}$B, $E_d$=18 MeV

Based on the found free parameters of the CAMM (4), the radius of interaction of the incident charged particles with the studied nuclei was calculated

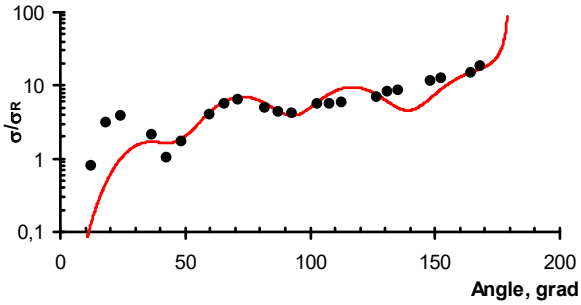
$$R_{\text{int}} = \frac{1}{k}\left[n + \sqrt{n^2 + l_0(l_0+1)}\right], \qquad (7)$$

where $k$ – wave number; $n$ – Coulomb parameter, $l_0$ – orbital momentum from (4).

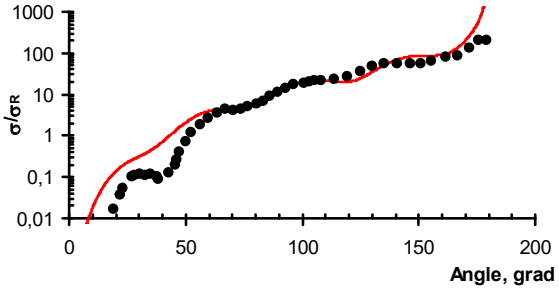
### 3. Results and discussion

In this work, using our own developed software for searching for optimal values, free parameters of the model (4) were found.

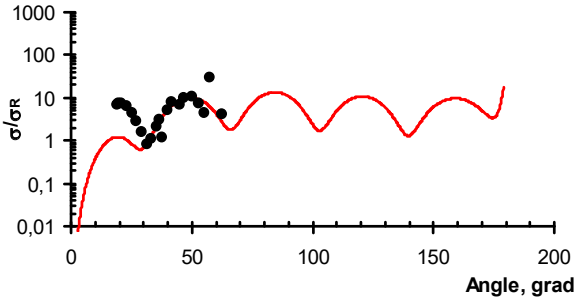
Figures 2-5 show the dependences of the angular distributions of differential cross sections of elastically scattered deuterons on $^{9}$Be, $^{10}$B and $^{11}$B with energies from 11 MeV to 27.7 MeV. The points in the angular dependences are experimental data taken from the international nuclear database NNDC. The criteria for finding the optimal free parameters were the following considerations. In the region of small angles, where Coulomb forces compete and in some cases prevail over nuclear forces, this method, the method of complex angular moments, describes the experimental data poorly. This is explained by the fact that the Coulomb component does not enter into the section (4) itself. At angles greater than 90 degrees, inelastic nuclear absorption begins to enter, as well as exchange processes that are not taken into account in the scattering matrix. Thus, in this model (method) the region of angles is investigated, in which nuclear scattering mechanisms prevail. The CAMM allows to reveal these regions, in which if the theory describes experimental data well, then strong discrepancies are observed beyond their boundaries. Such discrepancies are manifested in the discrepancy between the oscillation frequency, phase, slope of the envelope and the absolute value of the cross section. Table 1 presents the values of the free parameters of the model and the calculated interaction radii.



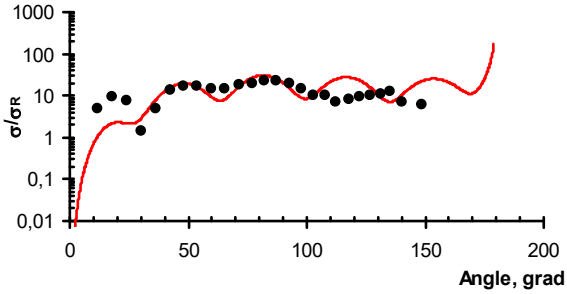

$E_d$=11 MeV (points – [24], curve – CAMM (4))




$E_d$=13.6 MeV (points – [25], curve – CAMM (4))

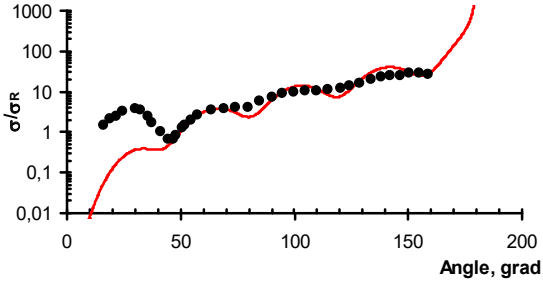



$E_d$=18 MeV (points – [26], curve – CAMM (4))



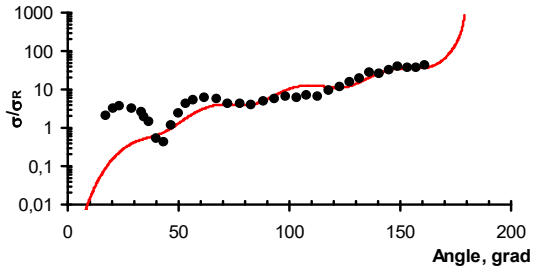

$E_d$=27.7 MeV (points – [27], curve – CAMM (4))

**Figure 2 -** Differential cross sections of elastically scattered deuterons on $^{9}$Be



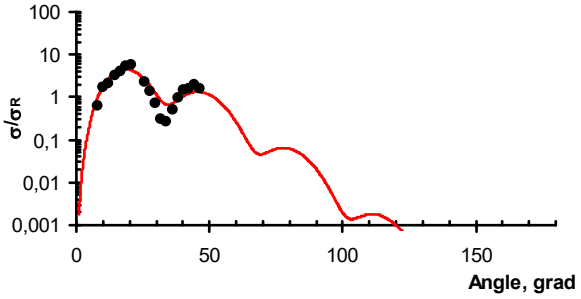

$E_d$=11.8 MeV (points – [28], curve – CAMM (4))

**Figure 3 -** Differential cross sections of elastically scattered deuterons on $^{10}$B

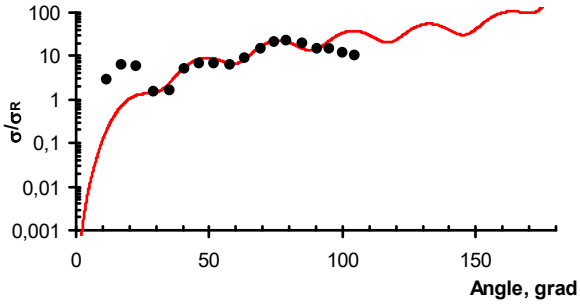



$E_d$=11.8 MeV (points – [28], curve – CAMM (4))

**Figure 4 -** Differential cross sections of elastically scattered deuterons on $^{11}$B




$E_d$=18 MeV (points – [26], curve – CAMM (4))




$E_d$=27.7 MeV (points – [27], curve – CAMM (4))

**Figure 5 -** Differential cross sections of elastically scattered deuterons on $^{11}$B

**Table 1 -** Values of free parameters of the CAMM (4)

| | E, MeV | k, 1/fm | n | $R_{int}$, fm | $l_0$ | β | b | \|a\| | γ |
|---|---|---|---|---|---|---|---|---|---|
| $^{9}$Be(d,d) | 11.00 | 0.84 | 0.24 | 4.91 | 3.40 | 0.80 | 0.90 | 0.70 | 1.50 |
| | 13.60 | 0.93 | 0.22 | 4.71 | 3.70 | 0.00 | 1.10 | 0.20 | 2.10 |
| | 18.00 | 1.07 | 0.19 | 4.72 | 4.40 | 1.10 | 0.40 | 1.20 | 2.20 |
| | 27.00 | 1.33 | 0.15 | 3.88 | 4.55 | 1.00 | 0.65 | 1.17 | 2.25 |
| $^{10}$B(d,d) | 11.80 | 0.89 | 0.30 | 5.54 | 4.20 | 0.10 | 0.70 | 0.30 | 1.20 |
| $^{11}$B(d,d) | 11.80 | 0.90 | 0.30 | 5.21 | 3.90 | 0.22 | 1.20 | 0.27 | 1.40 |
| | 18.00 | 1.11 | 0.24 | 4.97 | 4.80 | 4.00 | 0.50 | 5.80 | 1.60 |
| | 27.70 | 1.38 | 0.20 | 4.70 | 5.80 | 0.50 | 0.90 | 0.50 | 1.25 |

Thus, in Figure 2, during the interaction of deuterons with an energy of 11 MeV with $^{9}$Be, one maximum of Fraunhofer diffraction is well described, which stretched over the angular range of scattered deuterons from 50 to 100 degrees. The first maximum is not described due to the absence of Coulomb interaction in this model. At high energies, 13.6 MeV, 27.7 MeV, two maxima are described quite well. In the experimental data at the deuteron energy of 18 MeV, unfortunately, the authors of [26] did not obtain enough data. For $^{10}$B and $^{11}$B, similar trends were observed in the fitting of the free parameters of the model. However, when describing the angular distribution of elastically scattered 18 MeV deuterons on $^{11}$B, the envelope slope should most likely be different. At least not as different from the envelope slope as shown in the angular distributions of elastically scattered 27.7 MeV deuterons. Nevertheless, the description of the first maximum fits well into the overall picture of the interaction radii at different energies, as shown in Figure 6. Nevertheless, for one or two Fraunhofer-type oscillations, it is possible to select the parameter $l_0$, which is associated with the interaction radius (7).

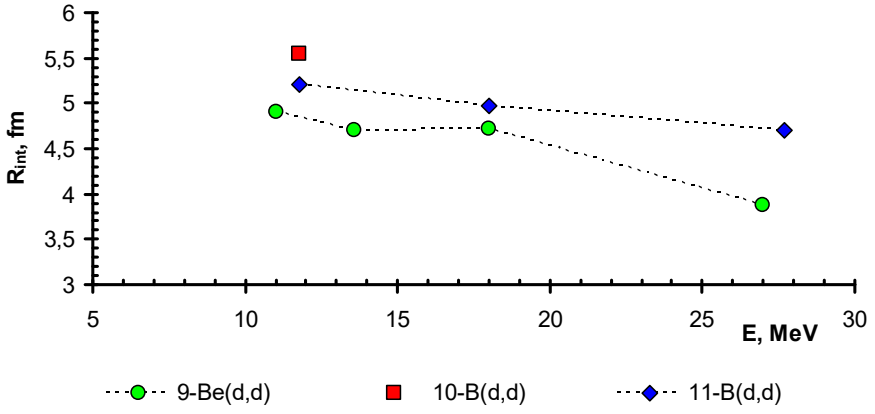



**Figure 6 -** Radii of interaction of deuterons with nuclei $^{9}$Be, $^{10}$B, $^{11}$B

To determine the radii of the nuclei under study, it is necessary to remove the energy dependence. As was shown in [21], the radius of the nucleus can be determined as

$$R = R_{\text{int}} - \lambda_d - r_{NN}, \qquad (8)$$

where $\lambda_d = 1/k$ – de Broglie wavelength of deuterons, $r_{NN} = 1,0\ Fm$ – nuclear force range. Figure 7 shows the radii of the studied nuclei, calculated using this CAMM method (dots), in comparison with literature data (straight lines) [29, 30].

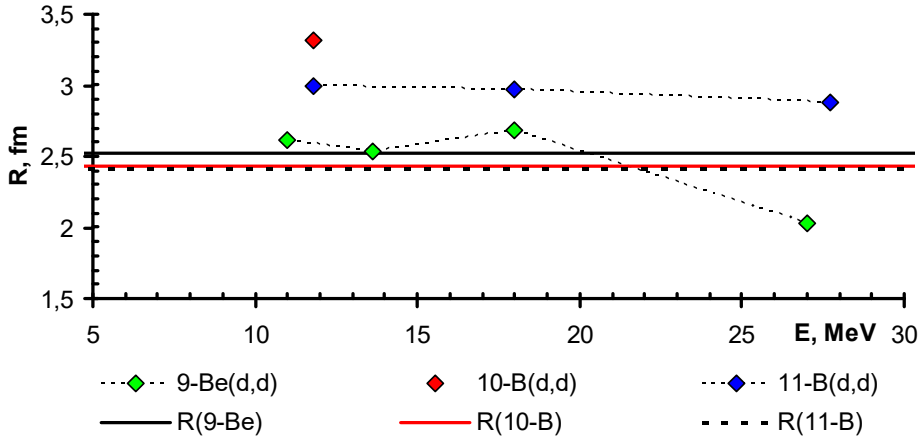



**Figure 7 -** Radii of nuclei $^{9}$Be, $^{10}$B, $^{11}$B

At energies up to 20 MeV, the calculated radii for $^{9}$Be agree satisfactorily with the literature data. However, at a deuteron energy of 27.7 MeV, the radius value is significantly smaller. Perhaps, it is necessary to conduct a more accurate analysis and study the reactions of elastic scattering of deuterons close to this energy, or this can be explained by the fact that at a given deuteron energy, the de Broglie wavelength is approximately equal to half the radius of the alpha particle; scattering may occur on a combination of nucleon associations representing alpha clusters in $^{9}$Be. For boron isotopes, the radius values are more. Perhaps, this is due to the internal structure of the deuteron, its large radius and, in this regard, the calculation of the radii by (8) will not be accurate, where the incoming components do not take into account the properties of deuterons.

## 4. Conclusions

Thus, as a result of calculations to extract the optimal free parameters of the complex angular momentum method, the interaction radii of deuterons with energies from 11 MeV to 28 MeV on $^{9}$Be, $^{10}$B and $^{11}$B nuclei were calculated. The optimal parameters were extracted from the differential cross sections of elastically scattered deuterons on the nuclei under study with energies in the above-mentioned ranges, at which Fraunhofer-type nuclear diffraction oscillations were clearly evident. The radii were calculated using the optimal free parameters of the CAMM. However, as a comparison with the literature values of the radii of the nuclei under study showed, there is a clear excess of the obtained values. For such an explanation, it is necessary to conduct an analysis on a large array of experimental data on elastic scattering of light ions, with good angular resolution and a wide angular range.

## Acknowledgments

The work was carried out within the framework of fundamental studies of the structure of alpha-cluster configurations of light nuclei in elastic nuclear interactions of light ions.

### References

1. Zhusupov M.A., Kabataeva R.S., Kopenbaeva A.S. Studying the Cluster Structure of the $^{11}$B Nucleus // Bulletin of the Russian Academy of Sciences: Physics. – 2020. – Vol. 84. – N. 10. – P. 1179-1182. https://doi.org/10.3103/S1062873820100329

2. Kasparov A.A., Konobeevski E.S., Zuyev S.V., Mordovskoy M.V., Afonin A.A., Mitcuk V.V. Simulation of the Inelastic Alpha-Particle Scattering Reaction for Investigating the Cluster Structure of Excited States of $^{9}$Be // Physics of Particles and Nuclei. – 2019. Vol. 50. – P. 605-607. https://doi.org/10.1134/S1063779619050125

3. Penionzhkevich Yu.E. Peculiarities of nuclear reactions with weakly bound cluster nuclei // Nuclear physics. – 2019. – Vol. 82. N. 3. – P. 208-217. (in Russian) https://doi.org/10.1134/S0044002719030140

4. Penionzhkevich Yu.E., Kalpakchieva R.G. Light nuclei at the boundary of neutron stability // JINR. – 2016. P. 383. (in Russian)

5. Demiyanova A.S., Ogloblin A.A., Ershov S.N., Gareev F.A., Kurmanov R.S., Svinareva E.F., Goncharov S.A., Adodin V.V., Burtebaev N., Bang J.M., Vaagen J.S. Rainbows in Nuclear Reactions and the Optical Potential // Physica Scripta. – 1990. – Vol. 32. – P. 89-106. https://doi.org/10.1088/0031-8949/1990/T32/015

6. Wheeler J.A. Molecular Viewpoints in Nuclear Structure // Physical Review. – 1937. – Vol. 52. – P. 1083-1106. https://doi.org/10.1103/PhysRev.52.1083

7. Helm R.H. Inelastic and Elastic Scattering of 187-Mev Electrons from Selected Even-Even Nuclei // Physical Review.– 1956. – Vol. 104. – N. 5. – P. 1466. https://doi.org/10.1103/PhysRev.104.1466

8. Gridnev K.A., Kartamyshev M.P., Vaagen J.S., Lukyanov V.K., Anagnostatos G.S. The role of linear alpha-cluster configuration for $^{12}$C // International Journal of Modern Physics E. – 2002. – Vol. 11. – No. 05. – P. 359-367. https://doi.org/10.1142/S0218301302000934

9. Inopin E.V., Shebeko A.V. Taking into account higher approximations for the nonsphericity parameter in the theory of inelastic diffraction scattering // Journal of Experimental and Theoretical Physics. – 1966. – Vol. 51. – P. 1761-1769.

10.Tishchenko B.I., Shebeko A.V. Contribution to the Theory of Diffraction Scattering of Particles by Nuclei, Based on the Method of Complex Angular Momenta // Journal of Experimental and Theoretical Physics. – 1966. – Vol. 23. – No. 6. – P. 1113-1117.

11. Inopin P.V., Tishchenko B.I., Shebeko A.V. Description of Inelastic Diffraction Scattering by the Complex Angular Momentum Method // Journal of Experimental and Theoretical Physics. – 1966. – Vol. 22. – No. 6. – P. 1247-1251.

12. Ikeda K, Tagikawa N. and Horiuchi H. The Systematic Structure-Change into the Molecule-like Structures in the Self-Conjugate 4n Nuclei // Progress of Theoretical Physics Supplement. – 1968. – Vol. 68(E). – P. 464-475. https://doi.org/10.1143/PTPS.E68.464

13. Kawabata T., Akimune H., Fujita H., Fujita Y., Fujiwara M., Hara K., Hatanaka K., Itoh M., Kanada-En'yo Y., Kishi S., Nakanishi K., Sakaguchi H., Shimbara Y., Tamii A., Terashima S., Uchida M., Wakasa T., Yasuda Y., Yoshida H.P., Yosoi M. 2α+t cluster structure in $^{11}$B // Physics Letters B. – 2007. – Vol. 101(1). – P. 6-11. https://doi.org/10.1016/j.physletb.2006.11.079

14. Gridnev K.A., Dyachkov V.V., Yushkov A.V. Determining the Statistical Weight of Multicluster Wave Functions for Light Nuclei in a Parametrized Phase Analysis // Bulletin of the Russian Academy of Sciences. Physics. – 2014.– Vol. 78.– No. 7.– P. 640–642. https://doi.org/10.3103/S1062873814070132

15. Gridnev K.A., Dyachkov V.V., Yushkov A.V. Phenomenon of the diffraction rise of cross sections in the forward angular hemisphere as an effect of nuclear and cluster interference // Bulletin of the Russian Academy of Sciences: Physics. – 2015. – Vol. 79. – No. 7. – P. 856-857. https://doi.org/10.3103/S1062873815070126

16. Dyachkov V.V., Zaripova Yu.A., Yushkov A.V. Accelerator beam measurements of kinematic tracks as a direct method for determining multicluster intranuclear amplitudes // Recent Contributions to Physics. –2015. – Vol .4(55). – P. 80-84. (in Russian)

17. Dyachkov V.V., Zaripova Yu.A., Yushkov A.V., Zholdybayev T.K., Kerimkulov Zh.K. Kinematic Method for Separating Dominant Types of Cluster Configurations in a Complex Nucleus // Bulletin of the Russian Academy of Sciences: Physics. – 2017. – Vol. 81. – No. 10. – P. 1174–1178. https://doi.org/10.3103/S1062873817100124

18. Zaripova Yu.A., Dyachkov V.V., Yushkov A.V., Zholdybayev T.K., Gridnev D.K. Direct experimental detection of spatially localized clusters in nuclei on alpha-particle beams // International Journal of Modern Physics E. – 2018. – Vol. 27. – No. 2. – P. 1850017-185001716. https://doi.org/10.1142/S0218301318500179

19. Torilov S.Yu., Maltsev N.A., Goldberg V.Z., Gridnev K.A., Zherebchevsky V.I., Lönnroth T., Novatskii B.G., Slotte J.M.K., Sobolev Yu.G., Trzaska W.H., Tyurin G.P., Khlebnikov S.V. Quasimolecular states in a reaction with carbon isotopes // JETP Letters. – 2015. – Vol. 102. – P. 69–72. https://doi.org/10.1134/S0021364015140118

20. Ogloblin A., Danilov A., Demyanova A., Goncharov S., Belyaeva S., Trzaska W. Nuclear States with Abnormal Radii // KnE Energy.– 2018. – P. 10–20. https://doi.org/10.18502/ken.v3i1.1716

21. Yushkov A.V. Surface B(Z,N) of nuclear deformation for nuclei with Z=2-102 // Physics of elementary particles and atomic nucleus. – 1993. – Vol.24. – No. 2. – P. 348-408.

22. Nassurlla M., Burtebayev N., Sakuta S., Nassurlla M., Khojayev R., Alimov D., Baimbetova G., Dyachkov V., Zazulin D., Sabidolda A., Mukanov Y., Issayev D., Makhmut A. Study of Alpha- Particle Scattering on $^{10}$B Nuclei at an Energy of 29 MeV // Universe. – 2024. – Vol. 10. – No. 51. https://doi.org/10.3390/universe10010051

23. Gonchar V.Yu. Study of the uniqueness of parameters in the phase shift method // Nuclear physics. – 1969. – Vol. 9. – No. 5. – P. 987-996. (in Russian)

24. Generalov L.N., Abramovich S.N., Zvenigorodskii A.G. $^{9}$Be(d,p0,1) and $^{9}$Be(d,t0) reaction cross sections // Bull. Russian Academy of Sciences – Physics. – 2000. – Vol. 64. – P. 440. (in Russian))

25. Matusevich V.A., Solovyev V.A., Chernov I.P. Backward scattering of deuterons by light nuclei // Journal of nuclear physics. – 1972. – Vol. 15. – P. 670. (in Russian)

26. Dyachkov V.V., Burtebaev N.T., Yushkov A.V. Measuring Elastically Scattered 18 MeV Deuterons and the Shape of Nuclei // Bulletin of the Russian Academy of Sciences. Physic. – 2012. – Vol. 76. – No. 8. – P. 895–900.

27. Slobodrian R.J. Scattering of 27.2 MeV deuterons on beryllium and boron // Journal of nuclear physics. – 1962. – Vol. 32. – P. 684.

28. Fitz W., Jahr R., Santo R. Scattering and pick-up reactions with deuterons on Be, B, C, N and O at 11.8 MeV // Journal of nuclear physics A. – Vol. 101. – P. 449-459.

29. Chart of nucleus shape and size parameters. Centre for photonuclear experiments data http://cdfe.sinp.msu.ru/

30. Angeli I., Marinova K.P. Table of experimental nuclear ground state charge radii: An update // Atomic Data and Nuclear Data Tables. – 2013. – Vol. 99. – P. 69-95 https://doi.org/10.1016/j.adt.2011.12.006

***Information of authors:***

*Dyachkov Vyacheslav, candidate of science, associate professor at the Voronezh State University. e-mail: slava_kpss@mail.ru*

IRSTI 34.49.31 https://doi.org/10.26577/phst2024v11i2b03

# STM32F407 microcontroller based multichannel analyzer for spectroscopy

A. Temirzhanov[1,2*], B. Sadykov[2], T. Zholdybayev[2], B. Duisebayev[2], G. Ussabayeva[2,3] and Zh. Kerimkulov[2]

[1]Satbayev University, Almaty, Kazakhstan
[2]Institute of Nuclear Physics, Almaty, Kazakhstan
[3]Abai University, Almaty, Kazakhstan
*e-mail: alik-25.01.97@mail.ru

*(Received August 2, 2024; received in revised form October 12, 2024; accepted November 6, 2024)*

The multichannel analyzer (MCA) is a crucial device for recording and analyzing radiation energy spectra to ascertain energy and intensity. It can be implemented via FPGA with a fast ADC and digital algorithm or a microcontroller with a peak detector circuit using an analog electrical circuit. MCA is widely applied in field work, nuclear medicine, and accelerator experiments. This work focuses on developing a low-cost alpha and gamma spectrometric system for experimental physics and field work, such as recording radiation and monitoring nuclear facility surroundings. Modern microcircuits, with small size and low power consumption, enable simpler and cheaper analog signal processing circuits that process signals in real-time without digital conversion delays. The spectrometric amplifier (SA) and peak detector (PD) were modeled and prototyped. A Python-based real-time data acquisition program was developed. Signals are recorded on the STM32F407 microcontroller's ADC and transmitted via USB to a PC. An experiment obtaining the Ra226 alpha source spectrum verified the MCA's functionality. It is valuable for environmental radioactivity field work and student teaching.

**Key words:** Multichannel analyzer, alpha spectroscopy, gamma spectroscopy, nuclear electronics.
**PACS number(s):** 29.30.−h; 06.60.Jn; 07.05.Hd; 07.77.Ka; 07.50.Qx

## 1. Introduction

Modern integrated circuits, which possess small dimensions and low power consumption, open up the possibility of fabricating portable nuclear radiation detection systems. These systems are constructed using an electrical circuit that includes a charge sensitive preamplifier, a spectrometric amplifier (shaper), and a multichannel analyzer (MCA), as reported in references [1, 2, 3]. The MCA is a device that enables the registration and analysis of the energy spectra of diverse types of radiation and can determine their energy and intensity. It can be based on FPGA integrated circuits, which incorporate fast ADCs and digital signal processing algorithms, or on a microcontroller with a peak detector circuit. In the latter case, the signal is processed entirely by an analog electrical circuit, as described in [2, 4, 5, 6]. MCAs find application in various fields, such as nuclear medicine, accelerator experiments, and the detection of radioactive emissions for radiation monitoring over large areas in field conditions, among others, as documented in [7 – 10].

A multichannel analyzer based on the commercially available STM32F407 – Discovery microcontroller series is proposed. This microcontroller is characterized by fast multichannel ADCs with a sampling rate ranging from 2.5 to 5 million samples per second. Such a sampling rate is not sufficient for accurately measuring the signal peak when using digital signal processing methods, in contrast to digitizers where the ADC speed can reach 250 – 500 million samples per second, as noted in [11]. However, by employing an analog peak detector circuit, the signal peak can be preserved prior to being recorded by the ADC, thereby allowing any ADC and microcontroller to be utilized, as indicated in [9, 12].

The objective of the article was to develop a low-cost and portable system dedicated to alpha and gamma spectrometry. This system is designed to be applicable in experimental physics and fieldwork

scenarios, particularly for detecting radioactive background levels during the monitoring of areas in the vicinity of nuclear facilities. To achieve this, suitable microchips were carefully chosen, and an analog signal processing circuit was devised. The simulation of the analog signal processing circuits was carried out with the utilization of NI MultiSim 14 software, as detailed in references [13 – 15].

## 2. Methodology

Figure 1 presents the overall operational framework of the alpha spectrometry system. The detector is furnished with a bias voltage via the Bias block. Signals originating from the surface barrier detector (manufactured by Ortec) that has a thickness of 300 microns are amplified by a charge-sensitive preamplifier (CSA, Ortec 142B). Subsequently, the signal is transformed into a semi-Gaussian shape by the spectrometric amplifier (SA). A single-channel analyzer (Discr) functions as a comparator. It compares the signal emerging from the amplifier block with a predetermined threshold and generates a TTL signal. The TTL signal from the single-channel analyzer prompts the microcontroller's ADC to commence recording the signal from the output of the peak detector (PD). Thereafter, the microcontroller gathers the data and transmits it to a PC. On the PC, the data is processed by a program developed in Python.

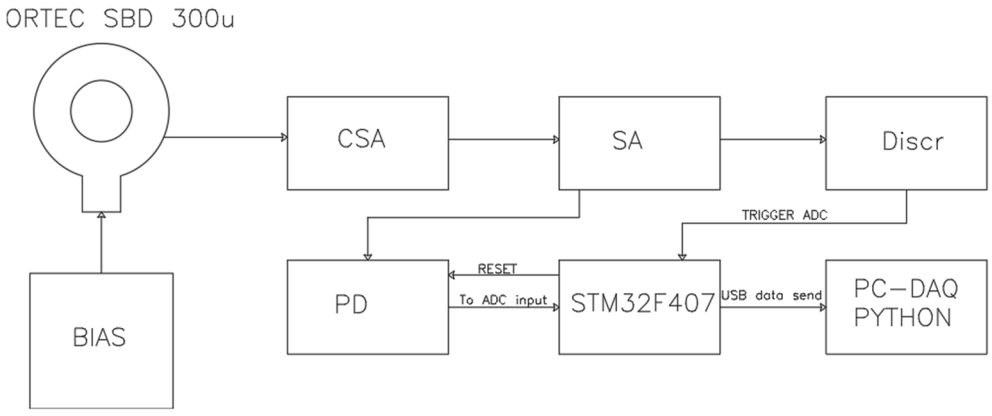



**Figure 1 –** Block Diagram of the MCA

The analog signal processing circuit is composed of several essential components. Firstly, the **SA**, which is the Spectrometric amplifier, is responsible for shaping the incoming signal to a more suitable form for further analysis. Secondly, the **Discr**, or discriminator, also known as the single-channel analyzer, functions by comparing the signal to a preset threshold. This comparison is crucial in determining certain characteristics of the signal. Lastly, the **PD**, or peak detector, plays a vital role in holding the peak value of the signal, which is then made available for subsequent processing. These components are all constructed using operational amplifiers.

The operational amplifiers (OAs) are the key determinants of the speed and resolution of the MCA. Specifically, they must possess specific characteristics. A high slew rate of at least 10 volts per microsecond is required to ensure rapid signal processing. Additionally, a low noise level at the nanovolt per hertz level is essential to maintain the integrity of the signal. Moreover, a wide bandwidth of no less than 20 MHz is necessary for handling a broad range of signal frequencies. Based on these requirements, the OPA354 and AD8616 operational amplifiers were selected as they meet these criteria.

For the discriminator (Discr), the TLV3201 and LM339N comparators were chosen. This selection is due to the fact that the pulse width of the signal from the SA output is 2 microseconds. In such a scenario, the speed of the comparator becomes a critical factor for the proper and efficient operation of the entire circuit. It ensures that the signal is accurately and promptly processed and analyzed within the required time frame.

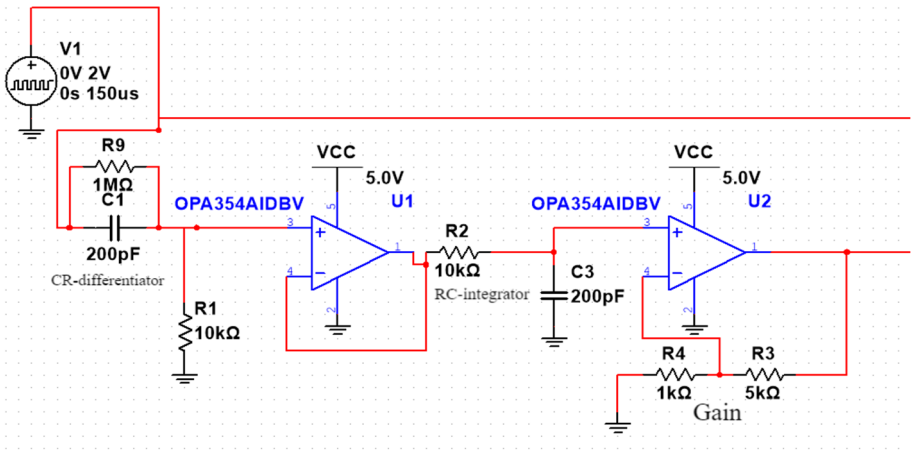



**Figure 2** – Schematic diagram of the **SA** spectrometric amplifier

**SA** is designed using two operational amplifiers, OPA354AIDVDR. The circuit is a CR-RC chain of discriminator and integrator circuits. C1C3 – 200 pF and R1R2 – 10k, converts a long signal from the preamplifier 100–150 microseconds long into a Gaussian signal 10 microseconds long. By changing the values of the resistor and capacitor CR-RC, you can achieve a change in the signal width, as well as its height. In Figure 3, the signal from the preamplifier is shown in turquoise, and the signal from the SA output is shown by yellow line. In the first case, C1C3 – 200 pF and R1R2 – 10k; in the second, C1C3 – 400 pF and R1R2 – 10k.

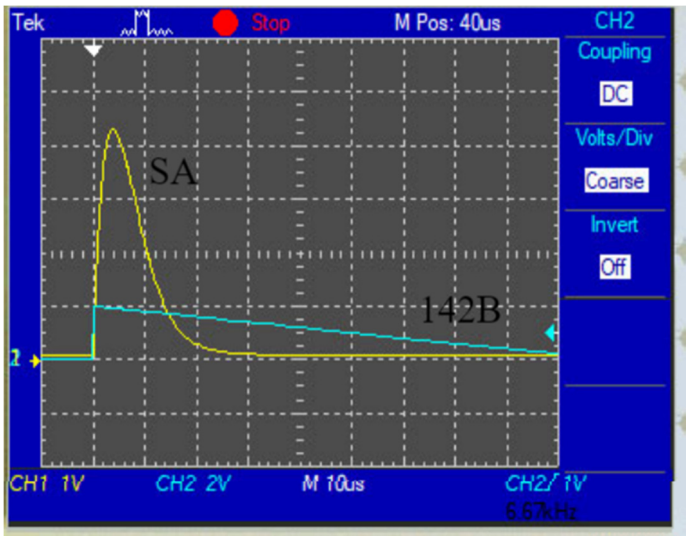



**Figure 3** – Signal from preamplifier and **SA**

Figure 4 shows the **Discr** discriminator circuit and the output TTL signal of the comparator with a width equal to the signal from the **SA**. The signal from the comparator starts the operation of the ADC of the microcontroller and allows reading the number of events from the detector.

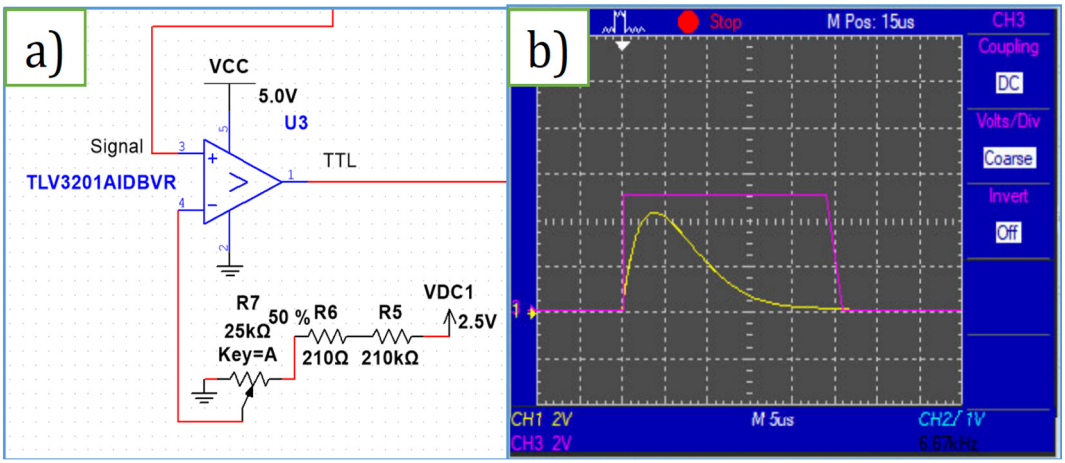



**Figure 4** – a) **Discr** discriminator circuit and b) **Discr** output signal

Figure 5 presents the circuit diagram of the peak detector that is based on the operational amplifier AD8616. This particular circuit diagram of the peak detector is sourced from [16]. A basic circuit diagram of a peak detector typically comprises diodes and a capacitor. The signal, when passing through the diodes, charges the capacitor to the value of the signal peak. In the event that the capacitor is not grounded, the signal gets stored in the capacitor for a duration equal to the product of the capacitor capacitance and the resistor resistance. The ADG701 analog CMOS switch discharges the capacitor C5 subsequent to recording the signal from the ADC. In this scenario, the signal from the comparator arrives with a 10-microsecond delay and then discharges the capacitor. As a result, the peak detector is then primed and prepared to handle the next signal that emanates from the detector.

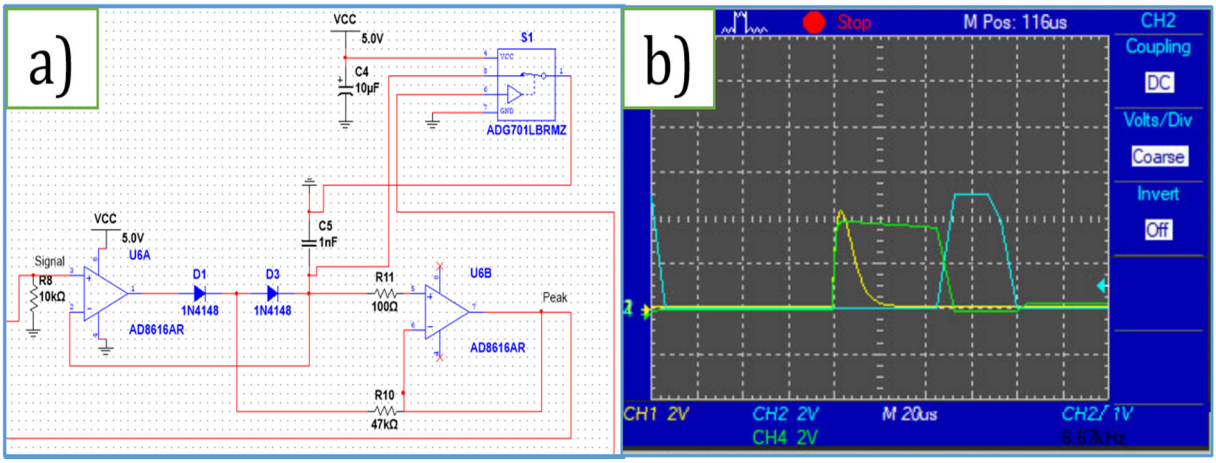



**Figure 5** – a) Peak detector circuit and b) signals from the oscilloscope

## 3. Results and discussion

After modeling and simulating the electrical circuits in the NI MultiSim program, prototypes of **SA**, **Discr**, **PD** were created. The created circuits were tested in real conditions on an Ortec 300 micron thick surface barrier silicon detector and an Ortec 142B preamplifier [17-19]. In Figure 6a, you can see the telescope with the detector installed inside and the $Ra^{226}$ alpha source [20-22].

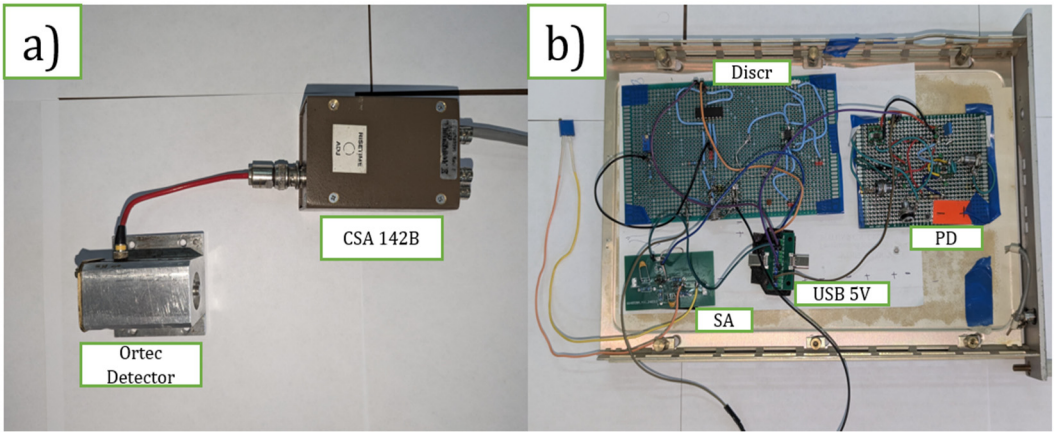



**Figure 6** – a) Detector in the telescope connected to the preamplifier and b) prototype of analog frontend of MCA

Figure 6b shows the designed prototype of analog frontend consisting of SA, PD and Discr. PD and Discr were developed on double sided solder boards. The prototype of SA was designed in the EasyEda environment and manufactured as a two-layer board.

In Figure 7 you can see the signals from the preamplifier and the converted signal by the SA. The amplitude of the converted signal corresponds to the amplitude of the signal from the preamplifier linearly.

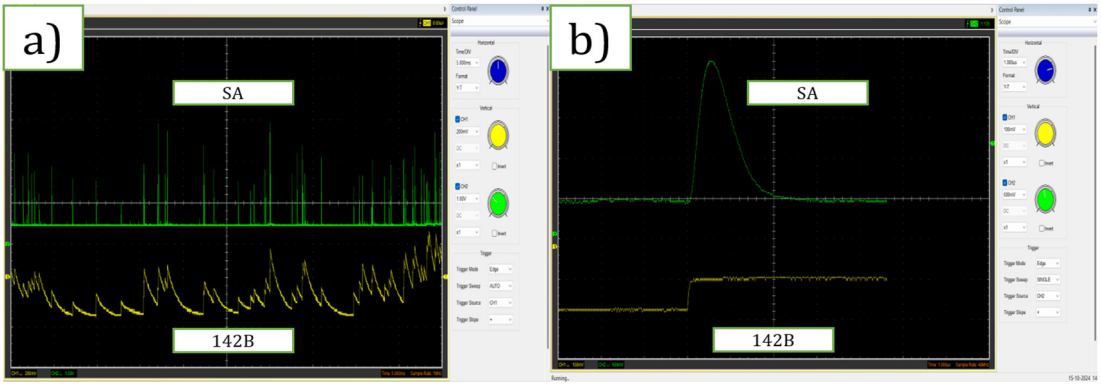



**Figure 7** – a) series of signal from the preamplifier and **SA** b) scaled signals

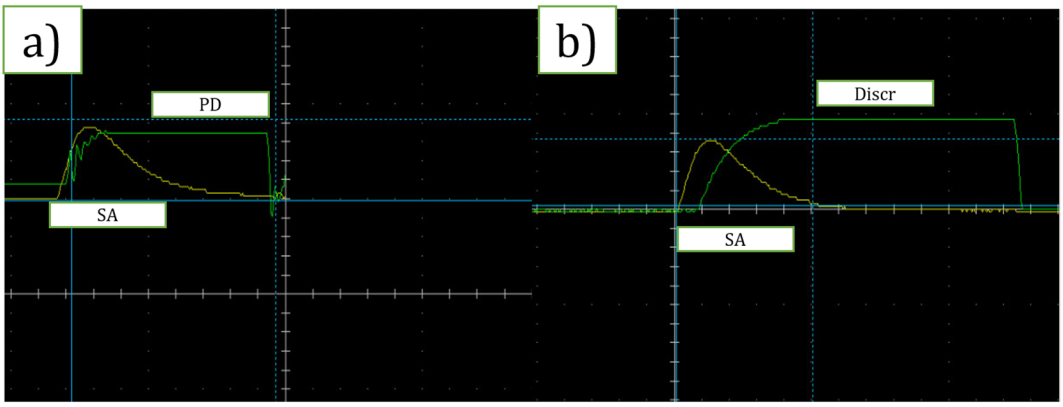



**Figure 8** – a) Peak detector signal b) Discr signal

Figure 8 illustrates the signals originating from the peak detector (8a) and the discriminator (8b), which are employed to activate the microcontroller's ADC. The Discr prototype was implemented by utilizing the LM339N comparator, which exhibits a latency of approximately 1.3 microseconds.

The peak detector signal is fed to the input of the microcontroller's ADC, which is configured for 1024 channels and operates in ADC Direct Memory Access (ADC_DMA) mode [23]. This mode allows the ADC to start quickly and store values in the microcontroller's RAM. The ADC is triggered by an external signal from the discriminator. After signal from PD detected and stored microcontroller sends TTL signal to ADG701 switch and resets PD.

Data transfer occurs via USB at a speed of 12 Mbps. On the PC side, a Python-based PC-DAQ program was created for real-time data processing and storage. The program uses the Matplotlib library [24] for visualization and processes the data, saving it in CSV format.

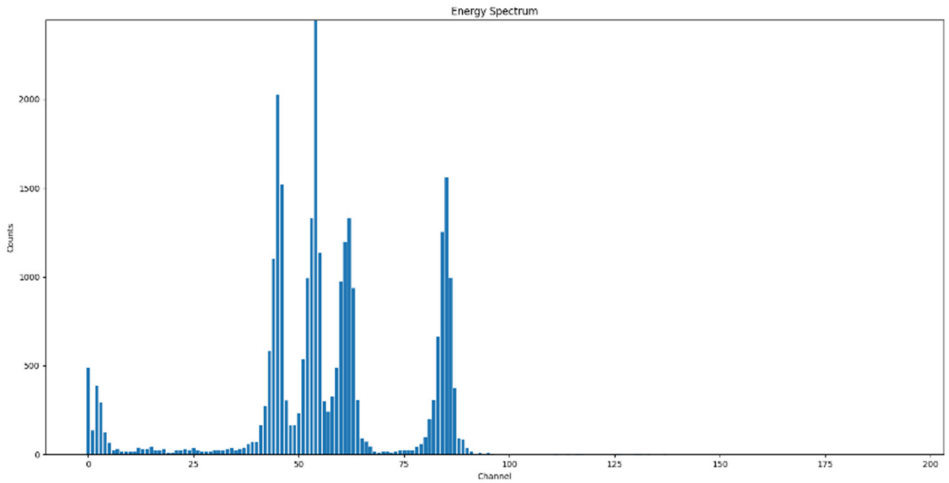



**Figure 9** – Python DAQ Program

Figure 10 shows the spectrum from an alpha source [25]. The native resolution of the Ortec detector with a thickness of 300 microns is 15-20 KeV when measuring the energy of alpha particles in a vacuum. In this case, the measurement was performed in air. Despite this, it is possible to reliably identify 4 peaks of the $Ra^{226}$ alpha source, which corresponds to an energy resolution of 200-250 KeV and is comparable to the energy resolution of NaI and CsI scintillation crystals [26].

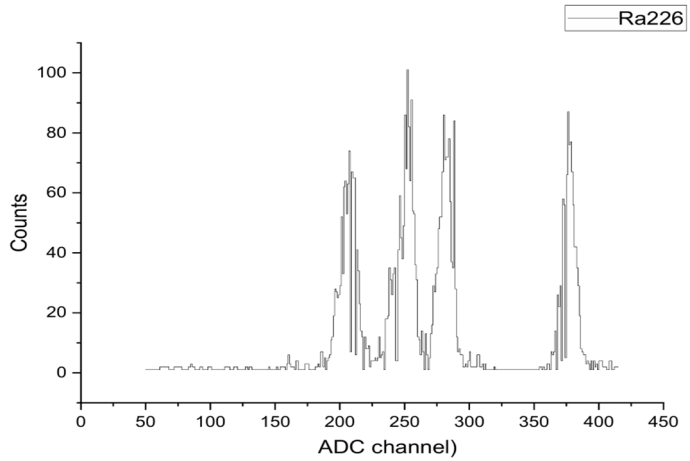



**Figure 10** – Spectrum of the alpha source of radium 226 collected from the MCA

## 4. Conclusions

In this academic paper, a novel methodology for fabricating electronic units dedicated to nuclear spectroscopy, leveraging contemporary microcircuits, was put forward. This innovative approach is anticipated to curtail the size and cost of such units while concurrently retaining all essential characteristics. At the present developmental stage, electrical circuits for the SA spectrometric amplifier were successfully devised. Additionally, a multichannel analyzer, founded on the STM32F407 microcontroller in combination with the PD peak detector circuit, was meticulously designed. A program was authored in the Python programming language, endowing the system with the capacity to amass data in real-time and archive the data array in CSV format. The Ra226 alpha source was measured using a surface barrier detector, thereby validating the functionality and viability of the proposed data collection system.

Looking ahead, efforts will be directed towards constructing a system for gauging charged particles, predicated on these advancements and employing the EdE method. In this envisioned setup, a two- or three-detector system will be deployed to accurately ascertain the type of particle engendered as a byproduct of nuclear reactions during the operation of the U-150M accelerator.

## Acknowledgements

This research was funded by the Science Committee of the Ministry of Science and Higher Education of the Republic of Kazakhstan, grant BR20280986.

### References

1. Kleczek R., Grybos P. Szczygiel R. Low power analog readout front-end electronics for time and energy measurements // Nuclear Instruments and Methods in Physics Research Section A: Accelerators, Spectrometers, Detectors and Associated Equipment. – 2014. – Vol. 748. – P. 54-60. https://doi.org/10.1016/j.nima.2014.02.018

2. Dornelas T. I. et al. Front-end design and characterization for the ν-angra nuclear reactor monitoring detector // Journal of Instrumentation. – 2016. – Vol. 11. – №. 07. – P. P07018. https://doi.org/10.1088/1748-0221/11/07/P07018

3. Sriskaran V. et al. New architecture for the analog front-end of Medipix4 //Nuclear Instruments and Methods in Physics Research Section A: Accelerators, Spectrometers, Detectors and Associated Equipment. – 2020. – Vol. 978. – P. 164412. https://doi.org/10.1016/j.nima.2020.164412

4. Li G. et al. Development of high-performance multichannel analyzer by using traditional pulse forming method and high-speed waveform sampling technology //Journal of Instrumentation. – 2019. – Vol. 14. – №. 05. – P. T05003. https://doi.org/10.1088/1748-0221/14/05/T05003

5. Chierici A. et al. A high-performance gamma spectrometer for unmanned systems based on off-the-shelf components //Sensors. – 2022. – Vol. 22. – №. 3. – P. 1078. https://doi.org/10.3390/s22031078

6. Carminati M. et al. Handheld magnetic-compliant gamma-ray spectrometer for environmental monitoring and scrap metal screening //Sensors. – 2022. – Vol. 22. – №. 4. – P. 1412. https://doi.org/10.3390/s22041412

7. Susanto A. T. et al. A systematic literature reviews of multichannel analyzer based on FPGA for gamma spectroscopy //Journal of Physics: Conference Series. – IOP Publishing, 2020. – Vol. 1528. – №. 1. – P. 012016. https://doi.org/10.1088/1742-6596/1528/1/012016

8. Thuraka E. R. et al. Digital Multi-Channel analyzer for detection and analysis of radiation in nuclear spectroscopy // Materials Today: Proceedings. – 2021. – Vol. 38. – P. 3160-3167. https://doi.org/10.1016/j.matpr.2020.09.580

9. Sengupta S., Johnston M. L. A multichannel analyzer with programmable energy bins for gamma ray spectroscopy // IEEE International Midwest Symposium on Circuits and Systems (MWSCAS).-2021. – P. 121-124. https://doi.org/10.1109/MWSCAS47672.2021.9531801

10. Dyachkov V. V. et al. Estimated measurements of natural background radiation in the surface atmospheric layer of the Almaty region // Physical Sciences and Technology. – 2021. – Vol. 8. – №. 3-4. – P. 4-9. https://doi.org/10.26577/phst.2021.v8.i2.01

11. Zhang J., Yang Z., Li Y. Research on gamma spectroscopy system while drilling based on DSP and FPGA // Journal of Physics: Conference Series, IOP Publishing – 2023. – Vol. 2418. – №. 1. – P. 012024. https://doi.org/10.1088/1742-6596/2418/1/012024

12. Chierici A. et al. Resource constrained electronics and signal processing for UAV radiation sensors // EPJ Web of Conferences. – EDP Sciences – 2023. – Vol. 288. – P. 10019. https://doi.org/10.1051/epjconf/202328810019

13. Atiea H. M., Rashid J. M. Simulation of charge sensitive preamplifier to improve nuclear pulse detecting using Multisim software // Journal of Physics: Conference Series, IOP Publishing – 2021. – Vol. 1999. – №. 1. – P. 012125. https://doi.org/10.1088/1742-6596/1999/1/012125

14. Guo S. et al. Design and verification of a radiation detector's electronics system // The Journal of Engineering. – 2019. – Vol. 2019. – №. 23. – P. 8527-8530. https://doi.org/10.1049/joe.2018.9047

15. Patil A. T., Siddavatam A. P. I., Vaidya P. P. A novel way of uniform amplitude generation for calibration and testing of high-resolution nuclear spectroscopy systems // 2nd International Conference on Intelligent Computing, Instrumentation and Control Technologies (ICICICT), IEEE – 2019. – Vol. 1. – P. 660-664. https://doi.org/10.1109/ICICICT46008.2019.8993201

16.Nebesniy A. F. et al. USB-analyzer for nuclear radiation spectroscopy // Pribory i Tekhnika Eksperimenta. – 2021. – №. 2. – P. 157-159. https://doi.org/10.31857/S003281622102018X

17.Torrisi L. et al. SiC and Si detectors comparison for high carbon energy spectrometry // Journal of Instrumentation. – 2024. – Vol. 19. – №. 07. – P. P07005. https://doi.org/10.1088/1748-0221/19/07/P07005

18.Scarduelli V. et al. A method to optimize mass discrimination of particles identified in Δ E–E silicon surface barrier detector systems // The European Physical Journal A. – 2020. – Vol. 56. – №. 1. – P. 24. https://doi.org/10.1140/epja/s10050-020-00021-2

19.Nandi J. et al. Enhancement in energy resolution of silicon surface barrier detector at low temperature //Proceedings of the 28th national symposium on cryogenics and superconductivity: book of abstracts. – 2022. https://inis.iaea.org/search/search.aspx?orig_q=RN:55001881

20.Liu S. et al. Development of a novel method for rapid and accurate determination of Ra-226 activity in soil by NaI (TI) spectrometer //Radiation Physics and Chemistry. – 2024. – Vol. 218. – P. 111654. https://doi.org/10.1016/j.radphyschem.2024.111654

21.Mahmood Z. et al. Sediment distribution of Ra-226 and Ra-228 in the East Coast of Peninsular Malaysia //AIP Conference Proceedings, AIP Publishing -2020. – Vol. 2295. – №. 1. https://doi.org/10.1063/5.0031492

22.Zhumabaeva, K., et al. Human teeth enamel as a test for assessing the consequences of radiation pollution of the environment // Isvestiya NAN RK. Seriya Biologisheskaiya I Medicinskaiya-2021.-Vol.-5-6.-P.13-18. https://doi.org/10.32014/2021.2519-1629.96

23.Ünsalan C., Gürhan H. D., Yücel M. E. Embedded system design with ARM cortex-M microcontrollers. // Springer International Publishing – 2022. https://link.springer.com/book/10.1007/978-3-030-88439-0

24.Moruzzi G., Moruzzi G. Plotting with matplotlib // Essential Python for the Physicist. – 2020. – P. 53-69. https://link.springer.com/chapter/10.1007/978-3-030-45027-4_3

25.El Afifi E. M., Hilal M. A., Attallah M. F. Performance characteristics and validation of alpha particle spectrometers for radiometric analysis of natural and anthropogenic radionuclides of environmental impacts //Applied Radiation and Isotopes. – 2021. – Vol. 168. – P. 109548. https://doi.org/10.1016/j.apradiso.2020.109548

26.Suzart K. F. et al. Development and characterization of CsI (Tl) crystal for use as a radiation detector //Brazilian Journal of Radiation Sciences. – 2021. – Vol. 9. – №. 1A. https://doi.org/10.15392/bjrs.v9i1A.1586

***Information about the authors:***

*Temirzhanov Alisher Alibekuly, Junior Researcher at the Institute of Nuclear Physics, studying for a PhD in Robotics at KazNITU named after K. Satpayev. e-mail: alik-25.01.97@mail.ru*

*Sadykov Bakhtiyar Madenuly, Senior Researcher at the Institute of Nuclear Physics, Candidate of Physical and Mathematical Sciences. e-mail: sadykovbm@inp.kz*

*Zholdybayev Timur Kadyrzhanovich, Senior Researcher at the Institute of Nuclear Physics, Candidate of Physical and Mathematical Sciences. e-mail: zholdybayev@inp.kz*

*Duisebayev Bek Alnurovich, Senior Researcher at the Institute of Nuclear Physics, Candidate of Physical and Mathematical Sciences. e-mail: mr.alnurov@mail.ru*

*Usabaeva Gulnaz, Junior Researcher at the Institute of Nuclear Physics, completed a PhD in Nuclear Physics at KazNU. e-mail: gulnazim85@inbox.ru*

*Kerimkulov Zhambul Kuanyshbekovich, Senior Researcher at the Institute of Nuclear Physics, Candidate of Physical and Mathematical Sciences. e-mail: zhambul-k@yandex.ru*

IRSTI 29.19.04 https://doi.org/10.26577/phst2024v11i2b04

# Effect of Ca dopant concentration on the change in properties of $ZrO_2$ ceramics

K. Samarkhanov[1*] and S. Askerbekov[2]

[1]Institute of Atomic Energy Branch of the National Nuclear Center, Kurchatov, Kazakhstan
[2]Satbayev University, Almaty, Kazakhstan
*e-mail: samarkhanovkuanysh21@gmail.com

*(Received October 15, 2024; received in revised form November 4, 2024; accepted November 10, 2024)*

The work is devoted to the study of effects associated with polymorphic transformations in $ZrO_2$ ceramics stabilized by 0.1 M $CaCO_3$, with variations in the temperature of thermal annealing. Interest in this topic of research is due to the possibilities of determining the kinetics of structural changes caused by the addition of a stabilizing dopant, alongside thermal action, the change of which causes the initialization of the polymorphic transformation processes characteristic of $ZrO_2$ ceramics. Annealing of the samples was carried out in the temperature range from 1000 to 1500 °C, the choice of which was determined by the possibilities of initializing the processes of polymorphic transformations in ceramics due to thermal processes and dopant. According to the conducted studies, it was determined that the addition of 0.1 M $CaCO_3$ at annealing temperatures of 1000 – 1100 °C results in initialization of polymorphic transformation processes of the type monoclinic – $ZrO_2$ → tetragonal – $ZrO_2$, however, complete transformation is not observed, which in turn makes it possible to obtain two-phase ceramics. The annealing temperature growth to 1200 °C and above results in formation of a cubic $Zr(Ca)O_2$ phase, with tetragonal – $ZrO_2$ impurity inclusions, the presence of which leads to the dislocation hardening effect formation due to the filling of the intergranular space with finely dispersed particles and the buffer zone formation. The results of the analysis of the structural parameters of the studied ceramics demonstrated that the annealing temperature elevation leads to the emergence of substitution effect, manifesting itself in the form of the $Zr(Ca)O_2$ phase formation, the crystal lattice parameters of which indicate that part of the zirconium ions are substituted by calcium ions in octo- and tetrahedral positions.

**Key words:** doping, structural changes, optical properties, zirconium ceramics, deformation distortions.
**PACS number(s):** 61.72.Ww; 61.82.Fk.

## 1. Introduction

Today, much attention in practical applications is paid to ceramic materials based on oxide compounds such as $ZrO_2$, $Al_2O_3$, MgO, BeO, $CeO_2$, etc. Interest in this type of ceramics is due to their strength and high melting point (for most ceramics, the melting point is higher than 1500 – 2000 °C), which creates possibilities of their use in extreme conditions, which includes operation at high temperatures [1-3]. The possibility of using $ZrO_2$ ceramics, which have fairly good compatibility with most different materials, as well as degradation resistance during interaction with acidic and alkaline environments, opens up great prospects for this type of ceramics in alternative energy. In particular, these ceramics are considered as candidate materials for the creation of inert matrices for dispersed nuclear fuel, possessing sufficiently high resistance to radiation damage [4-6]. Good indicators of resistance to radiation exposure while maintaining thermal physical parameters also allow these ceramics to be used as thermal insulation materials. The mixed conductivity type opens up great prospects for this type of ceramics when used as materials for the creation of solid oxide fuel cells used to produce hydrogen [7, 8]. Interest in ceramic materials based on zirconium dioxide when used as solid oxide fuel cells is primarily due to their high resistance to thermal expansion, typical for high-temperature operating conditions, as well as their mixed type of conductivity, which ensures good capacity and, as a consequence, performance [9-11].

However, despite the great prospects of this class of materials as solid oxide fuel cells, the problem of deformation-induced polymorphic transformations

of the m – $ZrO_2$ → t –$ZrO_2$, t – $ZrO_2$ → c – $ZrO_2$ type can have a dual effect on the change in the thermophysical and capacitive characteristics of this type of ceramics [12,13]. To restrain the polymorphic transformation processes, various additives in the form of magnesium, yttrium or calcium oxide dopants are usually used, allowing stabilization of the crystal structure of zirconium dioxide due to partial substitution of zirconium by a dopant. The latter results in formation of stable phases in the composition of ceramics that are not subject to polymorphism, the main reason for the occurrence of which, in addition to the deformation effect, is the presence of a large number of oxygen vacancies in the composition [14-16]. In this case, the use of stabilizing dopants is usually not only due to the possibility of initializing the polymorphic transformation processes in zirconium dioxide, but also to a decrease in the temperature at which these transformations are initiated, which in turn makes it possible to reduce the effect of thermal agglomeration of grains at high temperatures, which plays a very important role in determining the effects associated with size factors, and the size of the specific surface area [17, 18].

The aim of this study is to determine the prospects of using $CaCO_3$ as a stabilizing dopant for the initialization of polymorphic transformation processes in $ZrO_2$ ceramics, and to establish the effect of annealing temperature on the phase formation processes associated with polymorphic transformations of the m – $ZrO_2$ → t –$ZrO_2$, t – $ZrO_2$ → c – $ZrO_2$ type, alongside the possibility of controlling them by varying the synthesis conditions. An important role in the research is played by the study of the influence of synthesis conditions not only on the processes of phase formation, but also on changes in strength characteristics, which play an important role in determining the potential for using this type of ceramics as structural materials. Interest in this research topic is due to the possibilities of controlling the polymorphic transformation processes in zirconium dioxide by adding stabilizing dopants, the use of which allows not only to initiate the polymorphic transformation processes, but also to reduce the temperature of these transformations, the reduction of which allows reduction of the production cost of ceramics, possessing strong potential for application both in structural materials and as fuel cells used to produce hydrogen, viewed as one of the auspicious alternative fuel types.

## 2. Materials and methods

The synthesis of ceramics was carried out using the method of mechanical activation combined with thermal annealing, the change in temperature of which allows initiating processes of change of both morphological properties and structural ones, associated with the variation of structural parameters and processes of polymorphic transformations, the occurrence of which in $ZrO_2$ ceramics can be initiated both by changing the sintering temperature and in the case of variation of the concentration of the stabilizing dopant. Calcium carbonate ($CaCO_3$) was used as a stabilizing dopant in a molar ratio of 0.1 M of the total mass of powders used for the synthesis of ceramics using the mechanical activation method. The mechanical activation process itself was carried out using a PULVERISETTE 6 planetary mill (Fritsch, Berlin, Germany), the use of which allows obtaining ceramics that are homogeneous in size and uniform in composition by mechanically grinding the initial components in a given volume in a special tungsten carbide grinding cup, in which 10 mm tungsten carbide balls are used as grinding media. The volume of balls in relation to the ground powders is 3 to 1, the total volume of the glass is 80 ml. Grinding is carried out at a grinding speed of 300 rpm for 30 minutes, after which the ground powders are removed from the glass and subjected to thermal annealing at various temperatures. Annealing of samples is carried out in a PM-1700 muffle furnace (Rusuniverstal, Chelyabinsk, Russia) using an annealing program that includes heating the samples to a given temperature at a rate of 20 °C/min, holding the samples at a given temperature for 5 hours and then cooling for 12 hours until the samples reach room temperature, which remain in the chamber the entire time until complete cooling. The range of variable annealing temperatures was from 1000 to 1500 °C, the choice of this range is based on the possibilities of initializing the polymorphic transformation processes in $ZrO_2$, the control of which using stabilizing dopants is one of the important methods of monitoring the phase transformation processes in zirconium dioxide.

To determine the grain sizes, the laser optical diffraction method was used, which was implemented on the ANALYSETTE 22 NeXT Nano particle analyzer (Fritsch, Berlin, Germany). The

measurements were carried out in several parallels, which made it possible to establish not only the dynamics of grain size changes depending on the annealing temperature, but also to determine the convergence of the results obtained in various experiments aimed at identification of the synthesis method repeatability.

The morphological features of the synthesized ceramics depending on the annealing temperature were obtained using the scanning electron microscopy method implemented on a Phenom™ ProX microscope (Thermo Fisher Scientific, Eindhoven, The Netherlands). Before analyzing the morphological features, the samples were dispersed on holders using a Nebula disperser (Thermo Fisher Scientific, Eindhoven, The Netherlands).

The ceramics' phase composition was established through the X-ray diffraction method, which consists in establishment of the main and impurity phases in the composition of the powders under study, and the change in structural parameters subject to the synthesis conditions. X-ray diffraction patterns were obtained on a D8 ADVANCE ECO powder diffractometer (Bruker, Karlsruhe, Germany). The diffraction patterns were recorded in the Bragg-Brentano geometry, in the angular range of 2θ=20 – 70°, the measurement step was 0.03°, the spectrum acquisition time at a point was 1 sec. The DiffracEVA v.4.2 software was used to determine the structural parameters and their change depending on the phase transformations associated with a change in the annealing conditions. The structural parameters were refined by comparing the reference values with the experimental data, as a result of which the main parameters of the crystal lattice, as well as the degree of structural ordering, were established. The synthesized ceramics were also studied using the Raman spectroscopy method, the use of which made it possible to establish the kinetics of polymorphic transformations, since, unlike X-ray diffraction, the Raman spectroscopy method is more sensitive to structural changes and deformations that occur as a result of external influences or variations in synthesis conditions. The spectra were obtained on an Enspectr M532 Raman microscope (Spectr-M LLC, Chernogolovka, Russia).

To gauge the hardness of $ZrO_2$ ceramics contingent upon the annealing temperature, the microindentation method, implemented using a Duroline M1 microhardness tester (Metkon, Bursa, Turkey), was applied. The measurements were conducted using a Vickers pyramid, with a constant load on the indenter of 100 N. The choice of load range is determined by the standard hardness measurement procedure.

## 3. Results and discussion

Figure 1 illustrates the grain distribution assessment results in $ZrO_2$ ceramics stabilized by $CaCO_3$, contingent upon the annealing temperature, and reflects the annealing temperature effect on the grain agglomeration processes associated with both polymorphic transformations and thermal sintering of samples, resulting in formation of large agglomerates of large sized grains. The general form of the presented dependencies of the grain distribution diagrams is for trends that clearly depend on the annealing temperature, associated with the coarsening of grains and the formation of fairly large agglomerates that are not amenable to dispersion in ultrasound. At annealing temperatures of 1000 – 1200 °C, the particle distribution has weakly expressed maxima in the region of 1-5 μm, which indicates fairly small grains, as well as a fairly large dispersion of particle size distribution associated with thermal exposure and phase transformation processes. In the case of the annealing temperature growth above 1200 °C, a sharp shift in the size distribution to the region above 10 μm is observed. This indicates agglomeration processes, which can be caused by both the effects of sintering at high temperatures and processes caused by phase transformations, the initialization of which occurs at high temperatures and, as a rule, is accompanied by coarsening of grains, resulting in compaction of ceramics. Moreover, the observed effects of asymmetry in the distribution of grains at temperatures of 1400 – 1500 °C may be associated with the formation of a finely dispersed fraction in the structure, the presence of which is due to the processes of phase formation and their enlargement.

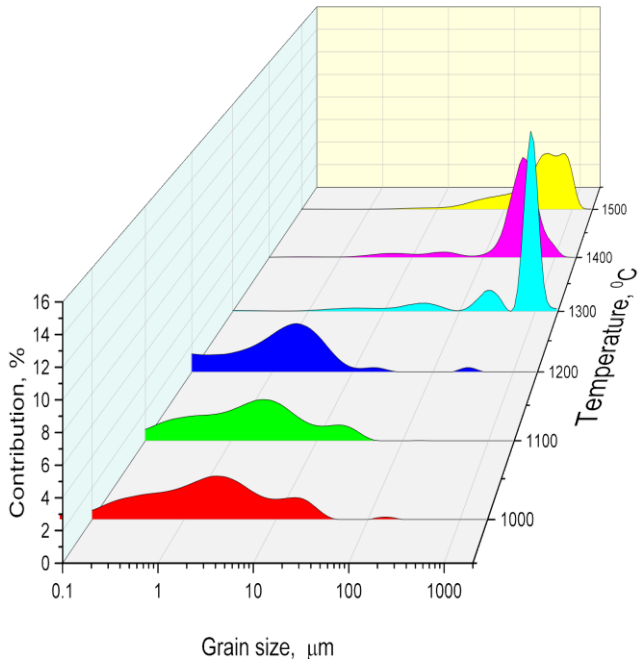



**Figure 1 –** Results of the evaluation of grain distribution in the composition of ceramics using the optical laser diffraction method for the studied samples depending on the variation of the annealing temperature

Figure 2 shows the results of the morphological features of the synthesized ceramics obtained using the scanning electron microscopy method. The overall view of the presented changes in the morphology of the ceramics indicates the annealing temperature effect on the agglomeration processes, which can also be caused by the phase transformation effects associated with polymorphic transformations. Moreover, the overall appearance of the provided morphological features of ceramics contingent upon the annealing temperature has an analogous trend established during the particle size analysis through the optical laser diffraction method, the results of which are demonstrated in Figure 1. In the case of annealing temperatures of 1000 – 1200 °C, the morphology of the ceramics is represented by a finely dispersed fraction of spherical particles, characteristic of the monoclinic phase of $ZrO_2$ used for synthesis. From this, it can be concluded that during thermal annealing of $ZrO_2$ at temperatures below 1200 °C, morphological changes associated with the coarsening of grains due to their fusion or agglomeration are not observed. At an annealing temperature of 1200 °C, the initialization of the processes of agglomeration of grains into dendrite-like formations, alongside their compaction, is observed. The latter indicates that with an elevation in the annealing temperature, the particles become larger, which can also be caused by the processes of polymorphism, which was established using the X-ray diffraction method. In the case of annealing temperatures of 1400 – 1500 °C, the formation of large agglomerates of grains, in which a finely dispersed fraction is present, especially manifested at a temperature of 1500 °C, is observed. Moreover, the finely dispersed fraction is located at the boundary of large grains, thereby filling the intergranular space, forming a buffer zone, the presence of which can have a positive effect on strength properties. The nature of these grains, as well as changes in their concentration, may be due to the effects of polymorphic transformations that occur during the heat treatment of ceramics stabilized with $CaCO_3$, the addition of which can lead to a shift in the temperature of polymorphic transformations in zirconium dioxide.

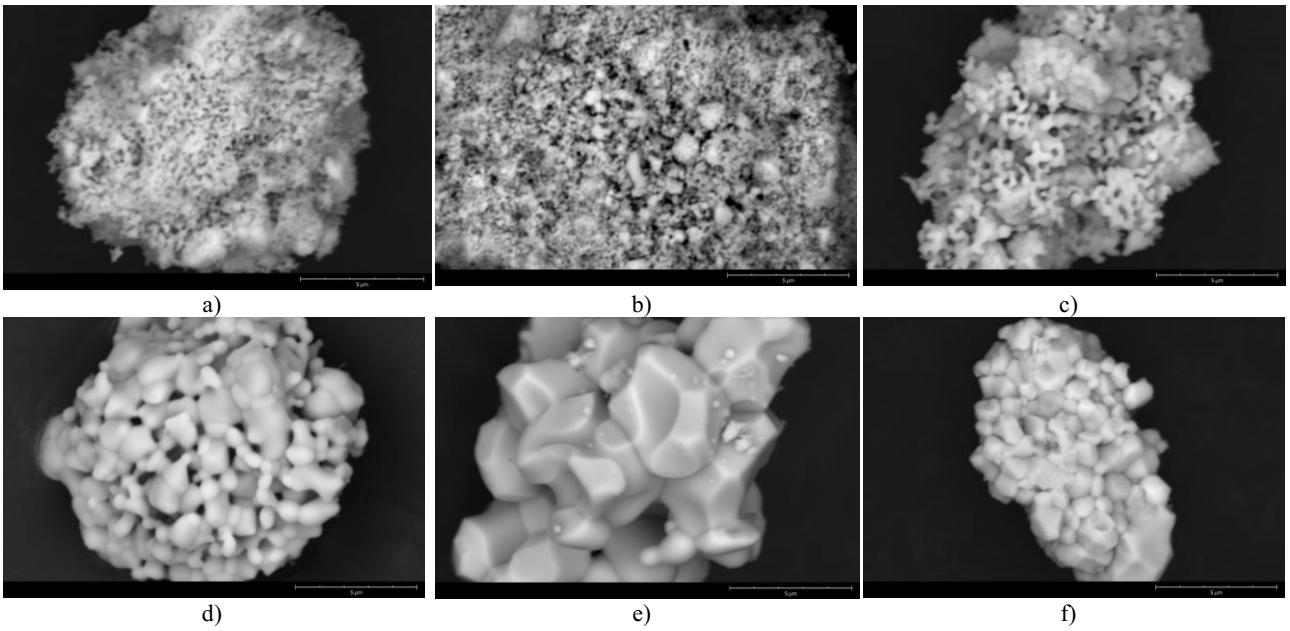
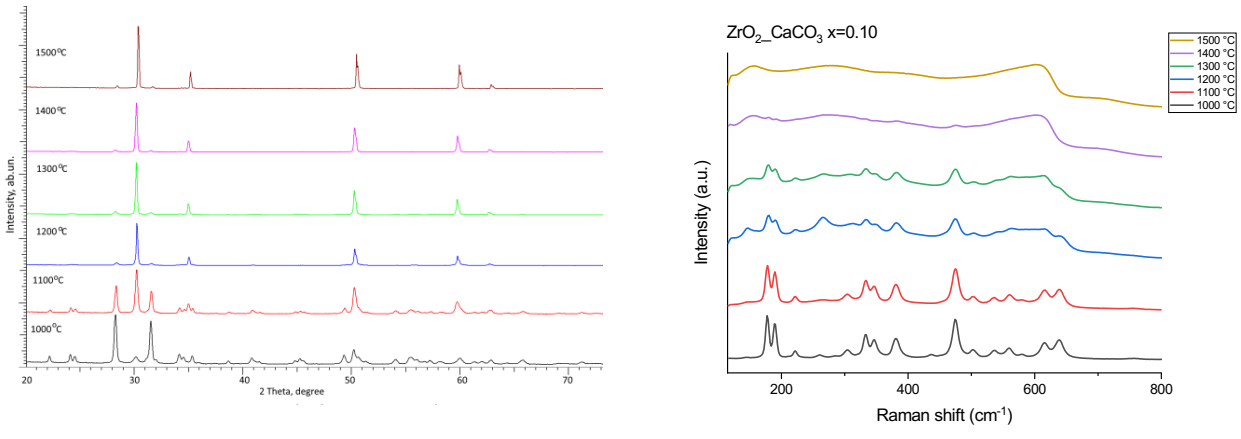



**Figure 2** – Results of morphological features of synthesized $ZrO_2$ ceramics stabilized with 0.1 M $CaCO_3$ at variation of annealing temperature: a) 1000 °C; b) 1100 °C; c) 1200 °C; d) 1300 °C; e) 1400 °C; f) 1500 °C

Figure 3a illustrates the results of X-ray diffraction of the studied ceramic samples depending on the change in the annealing temperature of the ceramic samples, the variation of which allows for the initiation of phase transformation processes associated with polymorphic transformations. The dynamics of changes in the phase composition of ceramics with variations in the annealing temperature were determined by comparative analysis of the obtained X-ray diffraction patterns with the data of the PDF-2 database, which allows determination of the main and impurity phases in the composition of ceramics by comparison of card and experimental values, alongside determination of the type of polymorphic transformations that arise when the synthesis conditions change.

The general view of the provided X-ray diffraction patterns when considering changes contingent upon the annealing temperature indicates a change in the phase composition of the ceramics, which clearly confirms the effect of adding the stabilizing dopant $CaCO_3$ on the processes of phase transformations of the m – $ZrO_2$ → t-$ZrO_2$ type and the t – $ZrO_2$ → c-$ZrO_2$ type, which are characteristic of zirconium dioxide.




a) b)

**Figure 3** – a) X-ray diffraction results of $ZrO_2$ ceramic samples obtained at temperatures from 1000° C to 1500 °C; b) Raman spectra of ZrO2 ceramic samples obtained at temperatures from 1000 ° C to 1500 °C

Figure 3b shows the Raman spectra of $ZrO_2$ samples with a concentration of 0.1 M $CaCO_3$ at different annealing temperatures. The spectra of the samples obtained at temperatures of 1000 and 1100 °C contain only modes associated with the monoclinic $ZrO_2$ phase. At annealing temperatures of 1200 and 1300 °C, a background appears in the spectra, the peaks of the monoclinic phase become less pronounced, which is associated with a rise in the content of the cubic $ZrO_2$ phase in the samples. At a temperature of 1500 °C, the modes related to the monoclinic $ZrO_2$ phase disappear, while three very broad peaks are visible in the spectra at 154, 280 and 604 $cm^{-1}$, indicating the presence of the cubic phase of $ZrO_2$ [19].

Figure 4 demonstrates a diagram of the change in the phase ratio in the composition of ceramics depending on the annealing temperature. The phase composition of the ceramics, as well as the weight of each specific phase depending on the component ratio, was determined using expression (1):

$$V_{\text{admixture}} = \frac{RI_{\text{phase}}}{I_{\text{admixture}} + RI_{phase}}, \qquad (1)$$

where $I_{phase}$ is the intensity of the main phase, $I_{admixture}$ is the intensity of the impurity phase, the presence of which is associated with phase transformations, R=1.45.

As is evident from the presented phase analysis data, at temperatures higher than 1200 °C, the c-$ZrO_2$ phase dominates in the ceramics, while the t-$ZrO_2$ phase content varies from 5 to 3 wt. % subject to the annealing temperature. Analyzing the observed reduction in the contribution of the t-$ZrO_2$ phase with an increase in the annealing temperature, it can be concluded that a further increase in temperature can result in complete transformation of t-$ZrO_2$ → c-$ZrO_2$, however, the decrease rate less than 1 % with the annealing temperature growth by 100 °C (with a change in temperature from 1400 °C to 1500 °C) indicates a low efficiency of the proposed increase in the annealing temperature for completing the processes of polymorphic transformations. In turn, the analysis of the shape of the diffraction reflections, alongside the data of the morphological features presented in Figures 1 and 2, indicate an increase in particle size with an increase in the annealing temperature, which in turn indicates that with a further growth in temperature to complete the processes of polymorphic transformations, the effect of uncontrolled sintering of particles into larger agglomerates can be observed. In turn, the observed alterations in the morphological characteristics of ceramics at temperatures of 1400 – 1500 °C indicate that larger particles represent the c-$ZrO_2$ phase, while smaller particles may represent the t-$ZrO_2$ phase, the proportion of which corresponds to the amount of finely dispersed fraction filling the intergranular space. Such filling, in turn, can lead to the effect of dispersion hardening associated with the filling of the intergranular space with small particles, which in turn inhibit the spread of microcracks under external mechanical influences.

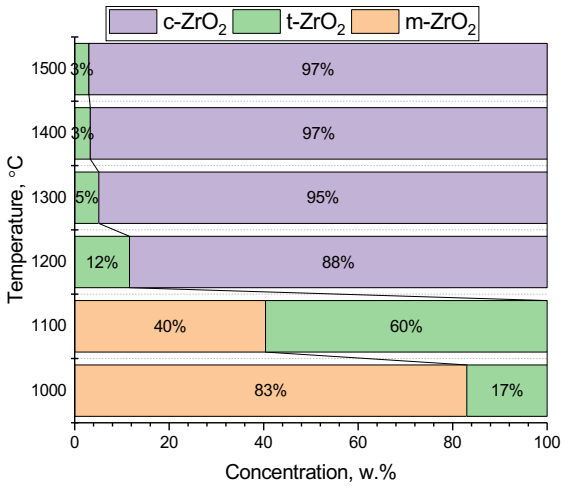



**Figure 4** – Phase analysis results of the studied ceramics under variation in synthesis conditions associated with annealing temperature alterations

The data on the phase ratio alteration in the composition of ceramics with a variation in the annealing temperature, allows formulation of the basic formula reflecting the polymorphic phase transformation processes in ceramics stabilized by $CaCO_3$. This formula can be written as follows:

$$\text{monoclinic} - ZrO_2 \xrightarrow{1100\,℃} \text{tetraconal} - ZrO_2 \xrightarrow{1200-1500\,℃} \text{cubic} - Zr(Ca)O_2(\text{tetragonal} - ZrO_2)$$

Table 1 demonstrates the structural parameters of the studied $ZrO_2$ ceramics subject to the samples' annealing temperature.

According to the tabular data, the ionic radius of $Zr^{4+}$ is about 79 pm, the ionic radius of $Ca^{2+}$ is about 99 pm. In this case, the difference in ionic radii of about 20 pm causes the growth effect of the parameters of the crystalline cubic $ZrO_2$ phase, observed with the annealing temperature elevation from 1200 to 1500 °C. From which it follows that the formed c-$ZrO_2$ phase can be represented as c – $Zr(Ca)O_2$, characteristic of the effect of partial substitution of zirconium ions by calcium ions in octo- and tetrahedral positions.

**Table 1 –** Structural parameter data of $ZrO_2$ ceramics

| **Phase** | **Temperature, °C** | | | | | |
|---|---|---|---|---|---|---|
| | **1000** | **1100** | **1200** | **1300** | **1400** | **1500** |
| **m-$ZrO_2$** | a=5.2781±0.0013 Å, b=5.1871±0.0015 Å, c=5.1315±0.0021 Å, β=99.425° | a=5.2802±0.0024 Å, b=5.1895±0.0014 Å, c=5.1317±0.0023 Å, β=99.424° | - | - | - | - |
| **t-$ZrO_2$** | a=3.5834±0.0026 Å, c=5.1701±0.0024 Å | a=3.5837±0.0023 Å, c=5.1705±0.0027 Å | a=3.5841±0.0026 Å, c=5.1714±0.0014 Å | a=3.5846±0.0013 Å, c=5.1725±0.0025 Å | a=3.5861±0.0023 Å, c=5.1731±0.0028 Å | a=3.5867±0.0021 Å, c=5.1734±0.0014 Å |
| **c-$ZrO_2$** | - | - | a=5.0831±0.0015 Å | a=5.0834±0.0012 Å | a=5.0835±0.0029 Å | a=5.0843±0.0023 Å |
| **Crystallinity degree, %** | 91.1 | 91.6 | 92.5 | 94.5 | 95.4 | 95.7 |

Based on the data obtained, the structural ordering degree (crystallinity degree) of the studied ceramic samples depending on the annealing temperature, the data on the change of which are presented in Table 1, was evaluated. According to the assessment conducted, the annealing temperature increase leads to the structural ordering degree growth, which implies that the phase composition alteration results in perfection of the crystal structure, due to its ordering, alongside alterations in structural features. At the same time, the broadening of the crystal lattice parameters as the crystallinity degree increases is due to substitution effects, resulting in formation of the c –$Zr(Ca)O_2$ phase.

Figure 5 reveals the hardness assessment results of the studied $ZrO_2$ ceramics depending on the annealing temperature. Hardness measurements were carried out by indenting the surface in different areas in order to determine the hardness and isotropy of the strength parameters.

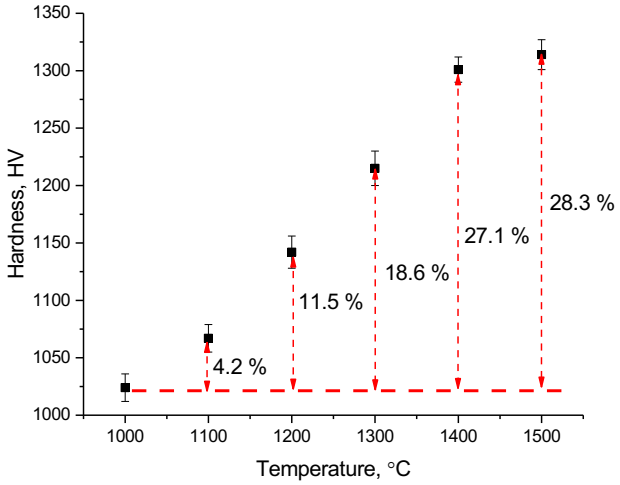



**Figure 5** – Evaluation results of alterations in the hardness of $ZrO_2$ ceramics contingent upon the annealing temperature (the dotted lines indicate the hardening effect of ceramics obtained at temperatures of 1100 – 1500 °C in comparison with samples obtained at an annealing temperature of 1000 °C)

The overall trend of alterations in the hardness of ceramics with changes in the annealing temperature, which, as has been established, results in phase polymorphic transformations, implies a positive effect of polymorphic transformations on the ceramics' hardening. Moreover, the displacement of the monoclinic phase from the composition of ceramics due to the increase in the contribution of the tetragonal phase and subsequently the cubic phase causes a growth in hardness by more than 10-28 %. At the same time, in the case of dominance of the cubic phase, the hardening effect is caused by the dispersion effect associated with the filling of the intergranular space with a finely dispersed fraction of t-$ZrO_2$, which has a positive effect on enhancement of resistance to external mechanical influences (in particular, enhancement of resistance to external pressure created by an indenter during hardness measurements).

## 4. Conclusion

During the conducted studies of the influence of annealing temperature on the polymorphic transformation processes in $ZrO_2$ ceramics during their stabilization with 0.1 M $CaCO_3$, the following results were obtained:

1. An analysis of the morphological features of the obtained ceramics revealed that polymorphic transformations of the m – $ZrO_2$ → t-$ZrO_2$ type lead to the formation of a finely dispersed fraction with a porous structure, while at annealing temperatures above 1200 °C, the resulting polymorphic transformations of the m – $ZrO_2$ → c –$Zr(Ca)O_2$ type result in grain coarsening with the formation of large particle agglomerates.

2. According to the evaluation results of the phase composition of ceramics, it was established that the addition of 0.1 M $CaCO_3$ to the $ZrO_2$ ceramics' composition at temperatures higher than 1200 °C makes it possible to exclude polymorphic transformations associated with the tetragonal phase formation, while the main alterations are associated with the m – $ZrO_2$ → c –$Zr(Ca)O_2$ type polymorphic transformations, which are accompanied by the formation of a partial substitution phase of $Zr(Ca)O_2$, the formation of which leads to an elevation in structural ordering and, as a consequence, a reduction in the concentration of oxygen vacancies in the composition.

3. Analysis of structural parameter alterations confirmed the presence of the $Zr(Ca)O_2$ substitution phase, the formation of which occurs due to partial substitution of $Zr^{4+}$ ions by $Ca^{2+}$ ions, which leads to a rise in the crystal lattice parameters.

4. It has been determined that the formation of the t-$ZrO_2$ impurity phase in the composition of $Zr(Ca)O_2$ ceramics obtained at thermal annealing temperatures of 1400 – 1500 °C results in formation of an interphase hardening effect associated with the formation of a finely dispersed fraction in the interboundary space, leading to the

containment of microcracks under external mechanical influences.

Based on the conducted studies and analysis of structural changes, a general conclusion can be made that the addition of a stabilizing dopant $CaCO_3$ at a concentration of 0.1 M results in initialization of phase transformation processes of the m – $ZrO_2$ → t-$ZrO_2$ type at a temperature of 1000 – 1100 °C with the possibility of obtaining composite ceramics consisting of two phases, the ratio of which varies depending on the annealing temperature. At annealing temperatures above 1200 °C, the addition of $CaCO_3$ leads to the initialization of the m – $ZrO_2$ → c –$Zr(Ca)O_2$ processes, which makes it possible to obtain ceramics in which the dominant phase is c – $Zr(Ca)O_2$, and the finely dispersed fraction, the presence of which enhances the resistance of ceramics to external influences, is t-$ZrO_2$ grains.

**Acknowledgements**

This work was carried out within the framework of program-targeted funding (program No. BR21882237 «Development and research of advanced composite materials for energy and the fuel cycle») with the support of the Science Committee of the Ministry of Science and Higher Education of the Republic of Kazakhstan.

**References**

1 Sadiq I., Asim Ali S., Ahmad T. Advanced Hybrid Ceramics for Nuclear and Hydrogen Energy Applications // ChemistrySelect. – 2023. – Vol. 8. – №. 27. – P. e202300837. https://doi.org/10.1002/slct.202300837

2 Zhou X. W., Hou M. D., Liu R., Liu B. Fabrication of beryllium oxide based fully ceramic microencapsulated nuclear fuels with dispersed TRISO particles by pressureless sintering method //Journal of Nuclear Materials. – 2024. – Vol. 588. – P. 154798. https://doi.org/10.1016/j.jnucmat.2023.154798

3 Evarts J. S., Chong S., Oshiro J. M., Riley B. J., Asmussen R. M., McCloy, J. S. Ceramic–Metal (Cermet) Composites: A Review of Key Properties and Synthesis Methods Focused on Nuclear Waste Immobilization //Industrial & Engineering Chemistry Research – 2024. – Vol. 63. – №. 14. – P. 6003-6023. https://doi.org/abs/10.1021/acs.iecr.3c04450

4 Güler S. H., Güler Ö., Kavaz E., Almisned, G., Albayrak M. G., Issa, B., Tekin, H. O. Fabrication and structural, physical, and nuclear radiation shielding properties for Oxide Dispersion-Strengthened (ODS) alloys through Erbium (III) oxide, Samarium (III) oxide, and Praseodymium (III) oxide into 316L matrix //Ceramics International. – 2024. – Vol. 50.- №. 3. – P. 5443-5452. https://doi.org/10.1016/j.ceramint.2023.11.295

5 Fu L., Wang B., Zhu Y., Shen T., Deng Y., Xu G., Xia W.Structural integrity and damage of glass-ceramics after He ion irradiation: Insights from ZrO2-SiO2 nanocrystalline glass-ceramics //Journal of the European Ceramic Society. – 2023. – Vol. 43. №. 6. – P. 2624-2633. https://doi.org/10.1016/j.jeurceramsoc.2023.01.043

6 Ugolkov V. L., Koval'chuk N. A., Osipov A. V., Mezentseva L. P., & Akatov A. A. Ceramic Composites Based on Zircon and Zirconium Dioxide // Refractories and Industrial Ceramics. – 2024. – Vol. 64.- №. 5. – P. 492-496. https://doi.org/10.1007/s11148-024-00877-7

7 Bekheet M. F., Schlicker L., Popescu R., Riedel W., Grünbacher, M., Penner S., Gurlo A. A quantitative microscopic view on the gas- phase- dependent phase transformation from tetragonal to monoclinic ZrO2. // Journal of the American Ceramic Society. – 2024. – Vol. *107*(7). – P. 5036-5050. https://doi.org/10.1111/jace.19749

8 Alhindawy I. G., Sayyed M. I., Aloraini D. A., Almuqrin A. H., Alomar M. S., Elawadi G. A., Mahmoud K. A. A multi-phase investigation to understand the function of lanthanum and neodymium in the zirconia ceramics' synthesis, structural, and gamma-ray protective ability //Radiation Physics and Chemistry. – 2024. – Vol. 215. – P. 111336. https://doi.org/10.1016/j.radphyschem.2023.111336

9 Li Z., Cui Y., Yan W., Zhang D., Fang Y., Chen Y., Wang Y. M. Enhanced strengthening and hardening via self-stabilized dislocation network in additively manufactured metals //Materials Today. – 2021. – Vol. 50. – P. 79-88. https://doi.org/10.1016/j.mattod.2021.06.002

10 Li, S., Jin, P., Zhu, Y., Chai, J., Niu, L., Shen, T., & Wang, Z. Effects of He irradiation on the microstructures and mechanical properties of Al2O3–ZrO2–ZrC ceramic composites //Ceramics International. – 2024. – Vol. 50, №. 9. – P. 15633-15641. https://doi.org/10.1016/j.ceramint.2024.02.043

11 Alhindawy I. G., Mahmoud K. A., Rashad M., & Sayyed M. I. Zirconium tungstate (Zr4W8O32)-doped zirconium dioxide (ZrO2) for gamma ray shielding: an in-depth examination of fabrication, characterizations, and gamma ray attenuation properties //Journal of Materials Science. – 2024. – Vol. 59. №. 27. – P. 12285-12304. https://doi.org/10.1007/s10853-024-09851-7

12 Kozlovskiy A.L., Kabyev M., Shlimas D.I., Uglov V.V. Study of the effect of the formation of two-phase ceramics based on neodymium zirconate due to doping with MgO and Y2O5 on the stability of strength and thermophysical parameters under irradiation //Eurasian Physical Technical Journal. – 2024. – Vol. 21.- №. 2 (48). – P. 5-13. https://doi.org/10.31489/2024No2/5-13

13 ALMisned G., Baykal D. S., Ilik, E. R. K. A. N., Kilic, G. Ö. K. H. A. N., & Tekin, H. O. The role of ZrO2 as glass-network former on radiation transmission properties of aluminoborosilicate (ABS) glasses: A glass type for nuclear waste immobilization //Ceramics International. – 2023. – Vol. 49. – №. 23. – P. 39124-39133. https://doi.org/10.1016/j.ceramint.2023.09.252

14 Al-Amin M., Mumu H. T., Sarker S., Alam M. Z., Gafur M. A. Effects of sintering temperature and zirconia content on the mechanical and microstructural properties of MgO, TiO2 and CeO2 doped alumina–zirconia (ZTA) ceramic //Journal of the Korean Ceramic Society. – 2023. – Vol. 60.- №. 1. – P. 141-154. https://doi.org/10.1007/s43207-022-00194-0

15 Kozlovskiy A. L., Konuhova M., Borgekov D. B., Anatoli P. Study of irradiation temperature effect on radiation-induced polymorphic transformation mechanisms in ZrO2 ceramics. // Optical Materials – 2024. – Vol. 156. – P. 115994. https://doi.org/10.1016/j.optmat.2024.115994

16 Ouyang J., Peng Y., Zhou W., Liang X., Wang G., Zhang, Q., Yuan B. The Role of Oxygen Vacancies in Phase Transition and the Optical Absorption Properties within Nanocrystalline ZrO2.// Nanomaterials. – 2024. – Vol. 14(11). – P. 967. https://doi.org/10.3390/nano14110967

17 Kogler M., Köck E. M., Vanicek S., Schmidmair D., Götsch T., Stöger-Pollach M., Penner S. Enhanced kinetic stability of pure and Y-doped tetragonal ZrO2.// Inorganic Chemistry. – 2014. – Vol. 53(24). – P. 13247-13257. https://doi.org/10.1021/ic502623t

18 Serena S., Caballero A., Sainz M. A. Analysis of the polymorphic transformation of nano-and microcrystalline zirconia doped with CaO and MgO during reaction-sintering process by neutron thermodiffraction. A thermodynamic approach. // Journal of the European Ceramic Society – 2013. – Vol. 33(8). – P. 1413-1424. https://doi.org/10.1016/j.jeurceramsoc.2012.12.026

19 Kumar A., Kumar P., Dhaliwal A. S. Phase transformation behavior of Ca-doped zirconia sintered at different temperatures // Journal of the Korean Ceramic Society. – 2022. – Vol. 59(3). – P. 370-382. https://doi.org/10.1007/s43207-021-00183-9

***Information about authors:***

*Samarkhanov Kuanysh K, researcher at the Institute of Atomic Energy Branch of the National Nuclear Center of the Republic of Kazakhstan (Kurchatov, Kazakhstan) e-mail: samarkhanovkuanysh21@gmail.com*

*Askerbekov Saulet K., PhD, associate professor, senior researcher at the Satbayev University (Almaty, Kazakhstan) e-mail: askerbekov@physics.kz*

IRSTI 59.14.25 https://doi.org/10.26577/phst2024v11i2b05

# Modeling and calibration of electrical features of p-n junctions based on Si and GaAs

J. Sh. Abdullayev[1]* and I. B. Sapaev[1,2]

[1]National Research University TIIAME, Tashkent, Kari Niyazov Street 39, 100000, Uzbekistan
[2]Western Caspian University, Scientific researcher, Baku, Azerbaijan
*e-mail: j.sh.abdullayev6@gmail.com
*(Received August 7, 2024; received in revised form October 28, 2024; accepted November 22, 2024)*

This study provides a detailed analysis of the temperature-dependent electrophysical properties and current-voltage (I-V) characteristics of p-n junction structures based on Silicon (Si) and Gallium Arsenide (GaAs). The investigation spans a temperature range of 0–1000 K, examining key parameters such as bandgap, mobility, intrinsic carrier concentration, and I-V characteristics. Advanced modeling and calibration techniques were employed to reveal intricate thermal dependencies of these parameters and their impact on device behavior. The results demonstrate that recombination currents dominate at low forward biases (0.1–0.3 V), characterized by an ideality factor near 2, while diffusion currents prevail between 0.3–0.7 V, with an ideality factor approaching 1. At higher voltages, high-injection conditions emerge. In Si, diffusion mechanisms dominate from 0.4–0.7 V, while in GaAs, recombination remains the primary mechanism up to 1.2 V. These findings are corroborated by semi-logarithmic I-V curves, illustrating the distinct transitions between current mechanisms. This comprehensive study highlights the robustness of the proposed models in accurately capturing the temperature-dependent behavior of these materials. The insights gained offer valuable implications for optimizing p-n junction-based devices across a wide temperature range. Future research will extend these models to explore more advanced semiconductor structures and operational scenarios.

**Key words:** p-n junction, Si, GaAs, calibration, cryogen temperature, bandgap, mobility, intrinsic concentration, I(V) curve, ideality factor.
**PACS number(s):** 73.40. Lq, 73.61.C w, 73.61. E y, 72.20. Jv

## 1 Introduction

Semiconductor devices, particularly p-n junctions, are integral components of modern electronic systems. Accurate modeling and calibration of the electrophysical properties of Si and GaAs are essential for optimizing device performance. Temperature is one of the most important parameters that externally affect the electrophysical properties of semiconductor materials. This article details the methodologies for modeling and calibration, offering insights into the unique characteristics exhibited by Si and GaAs p-n junctions. These methodologies enable a thorough exploration of temperature-dependent behaviors, enhancing our understanding of semiconductor physics and influencing the design of electronic systems. The use of these simulation tools allows for a more nuanced understanding of the complex interactions within semiconductor materials. Semiconductor materials are selected based on their wide application in semiconductor devices. The most crucial electrophysical parameters include the band gap, intrinsic carrier concentration, and the mobility of electrons and holes, along with current-voltage characteristics. In this paper, we focus on analyzing the features of semiconductor materials such as Si and GaAs. The mechanisms within the p-n junction are examined through the analysis of the I(V) characteristic and ideality factor. As is known, the band gap of semiconductor materials depends on several factors, such as temperature [1-3], geometric size [4, 5], and particle size in semiconductor nanomaterials [6]. The p-n junctions of Si and GaAs are well-studied, and the I(V) characteristics under forward bias are explained both experimentally and through modeling [7-12]. Investigating the ideality factor of p-n junctions is an established method for explaining current mechanisms [13-16]. However, many formulas for calculating the ideality factor in p-

n junctions are not well-explained across a wide range of both reverse and forward voltages. By studying existing models and developing new ones, we aim to address these shortcomings more effectively. Semiconductor devices can be modified in terms of geometry, materials, and structure. The subsequent sections of this article outline the methodologies employed for modeling and calibration, present the results of the temperature-dependent analysis, and discuss the implications for the broader field of semiconductor electronics. We also discuss the temperature dependence of band gap, mobility of electrons and holes, intrinsic conductivity, and the I(V) current and ideality factor m(V) as a function of forward voltage.

## 2. Methods and theoretical background

In this section, we conduct a comprehensive analysis of both the material characteristics and the methodologies employed. The study delves into the temperature dependence of electrophysical parameters, including band gap, intrinsic carrier concentration, electrical conductivity, and mobility. Our investigation specifically aims to clarify the current transport mechanisms in Si and GaAs-based p-n junctions, using a method that calculates the ideality factor by considering drift-diffusion and generation-recombination current mechanisms.

### *2.1 Bandgap and intrinsic concentration*

As previously mentioned, the Band Gap emerges as the most crucial parameter in semiconductor materials. Therefore, the equation (1) enables the calculation of the varying temperature of the bandgap for *Si* and *GaAs*. The formula for calculating the temperature dependence of the bandgap in semiconductor materials is typically described by the Varshni equation. It's expressed as:

$$E_g(T) = E_g(T=0) - \frac{\alpha \cdot T^2}{T+\beta} \quad (1)$$

where $E_g(T)$ and $E_g(T=0)$ are band gap at T and 0 K respectively, $\alpha$ and $\beta$ are material-specific constants. This equation shows how the bandgap energy varies with temperature. The parameters $\alpha$ and $\beta$ are experimentally determined constants for a particular semiconductor material. The results of our new model and the corresponding equation are depicted in Figure 1. The intrinsic concentration serves as a fundamental electrophysical parameter of semiconductor materials. The intrinsic carrier concentration $n_i$ in a semiconductor is given by the equation:

$$n_i(T) = \sqrt{N_C(T) \cdot N_V(T)} \cdot \exp\left(-\frac{E_g(T)}{2kT}\right) \quad (2)$$

where: $N_C(T)$ and $N_V(T)$ are the effective density of states in the conduction band and the effective density of states in the valence band. $E_g(T)$ is the energy band gap, $k$ is the Boltzmann constant and $T$ is the absolute temperature. The values of $N_C(T)$ and $N_V(T)$ depend on the material and are often expressed as functions of temperature.

### *2.2 Mobility and intrinsic electrical conductivity*

The significance of carrier mobility in semiconductors is at a high level, especially when working with semiconductor devices. Carrier mobility refers to the ability of charge carriers (electrons or holes) to move through a semiconductor material in response to an electric field. The mobility $\mu_{n,p}$ is expressed in units of *cm²/V·s* and is given by the formula (3a) and (3b): Semiempirical formulas (3a) and (3b) do not match the experimental results at temperatures below 50K.

$$\mu_n = \mu_{n_0}\left(\frac{T}{300}\right)^{-0.57} + \frac{7.4\cdot 10^8 T^{-2.33}}{1+0.88\left[\dfrac{N_D}{1.26\cdot 10^{17}\cdot\left(\dfrac{T}{300}\right)^{2.4}}\right]\cdot\left(\dfrac{T}{300}\right)^{-0.146}} \quad (3a)$$

$$\mu_n = \mu_{p_0}\left(\frac{T}{300}\right)^{-0.57} + \frac{1.36\cdot 10^8 T^{-2.33}}{1+0.88\left[\frac{N_A}{1.26\cdot 10^{17}\cdot\left(\frac{T}{300}\right)^{2.4}}\right]\cdot\left(\frac{T}{300}\right)^{-0.146}} \quad (3b)$$

Where $N_A$ and $N_D$ are acceptor and donor concentrations respectively, incomplete ionization has been considered in several studies [17, 18], but in this work, we assume that all $N_A$ and $N_D$ acceptor and donor ions are fully ionized. T is the temperature, $\mu_{p0}$ and $\mu_{n0}$ are constant values for material *Si* and *GaAs*. Several factors affect carrier mobility such as temperature [19-21], Masetti [22]. However, in this study, we exclusively utilized model mobility dependent on temperature. Materials with high charge carrier mobility are crucial for faster and more efficient electronic devices. Si and GaAs are commonly used semiconductors with relatively high carrier mobility. Carrier mobility plays a vital role in the design and optimization of semiconductor devices, such as transistors, diodes, and integrated circuits. At high electric fields, carrier velocity may saturate due to scattering effects. Understanding carrier mobility is essential for designing semiconductor devices that operate efficiently and reliably. Different operating modes and factors affecting mobility are key to optimizing semiconductor technology for various applications. Ordinarily, multiple sources of scattering, such as impurities and lattice phonons, are present concurrently. A widely used approximation is "Matthiessen's Rule, " which was originally formulated by Augustus Matthiessen in [23]. This rule combines the effects of different scattering mechanisms and is expressed as (4): The graphical representation of the result from expressions (3a) and (3b) are depicted in Figure 4, illustrating intrinsic electrical conductivity as a function of temperature.

$$\frac{1}{\mu_{total}(T)} = \frac{1}{\mu_{lattice}(T)} + \frac{1}{\mu_{impurity}(T)} + \frac{1}{\mu_{defect}(T)}\cdots \quad (4)$$

Another electrophysical parameter influenced by temperature is intrinsic conductivity. intrinsic electrical conductivity in semiconductors is strongly temperature-dependent. At low temperatures, very few electrons have enough energy to jump from the valence band to the conduction band, leading to low conductivity. As temperature increases, more electrons gain sufficient thermal energy to overcome the band gap, moving into the conduction band, and creating electron-hole pairs. This increase in charge carriers (both electrons and holes) causes the intrinsic conductivity to rise exponentially with temperature. Although this mathematical model was analyzed over a wide temperature range, the effects of incomplete ionization at low temperatures were not considered. This approach was chosen to first examine the model without accounting for incomplete ionization as an initial step, with plans to incorporate incomplete ionization in subsequent studies. The relationship is typically modeled as (5): Thus, the intrinsic conductivity increases with temperature as more carriers are thermally excited across the band gap. For the materials we have chosen, expression (5) corresponds to the equation for electrical conductivity as a function of temperature:

$$\sigma(T) = \sigma_0(T)\cdot\exp(-\frac{E_g(T)}{2kT}) \quad (5)$$

$\sigma(T)$ is the conductivity, $\sigma_0(T)$ is determined by expression (6), which indicates a linear dependence on temperature, and we have also considered that this expression is temperature-dependent. This expression (5) was analyzed in two cases: Case A, where $\sigma_0(T)$ is assumed to have a strong linear dependence on temperature, and Case B, where $\sigma_0(T)$ is considered temperature-independent. The difference between Cases A and B is presented and analyzed in Figure 3.

$$\sigma_0(T) = q \cdot (n(T) \cdot \mu_n(T) + p(T) \cdot \mu_p(T)) \quad (6)$$

Here, $n(T)$ and $p(T)$ are the electron and holes concentration, $\mu_n(T)$ and $\mu_p(T)$ are the electrons and hole mobility which represents the temperature dependence. If we consider equal intrinsic electrons and holes concentration $n_i(T) = p_i(T)$, expression (5) can be substituted with expression (7).

$$\sigma_i(T) = \sigma_{0i}(T) \cdot \exp(-\frac{E_g(T)}{2kT}) \quad (7)$$

The graphical representation of the result from expression (7) is depicted in Figure 3, illustrating intrinsic electrical conductivity as a function of temperature. The obtained results were derived by considering the temperature dependence of the electrophysical parameters in our model.

*2.3 I(V) curve and ideality factor*

The forward voltage curve can be divided into three distinct regions. At low voltage, the recombination mechanism predominantly influences the behavior. In the middle voltage range, the diffusion current mechanism takes precedence, while at high voltage, the high injection mechanism becomes dominant. The Shockley diode equation describes the current-voltage characteristic of an ideal p-n junction diode. The equation is given by:

$$J(T) = J_0(T) \cdot (\exp(\frac{qV_{p-n}}{mkT}) - 1) \quad (8)$$

Where J(T) is the diode current, $J_0$(T) is the reverse-bias saturation current. $V_{p-n}$ is the applied voltage across the p-n junction, $m$ is the ideality factor and unitless quantity, which is typically between 1 and 2, q is the charge of an electron. This equation provides a mathematical representation of the current-voltage relationship in a semiconductor diode under different bias conditions. The ideality factor of *p-n* and *p-i-n* junctions is determined by equation (9), but this expression is reliable and accurate only at voltages higher than 0.1 V.

$$m = \frac{q}{kT} \cdot \frac{dV}{d\ln(I)} \quad (9)$$

The barrier height $\varphi_k(T)$ of a p-n junction, also known as the built-in potential or contact potential, can be determined using the following formula:

$$\varphi_k(T) = \frac{kT}{q} \ln(\frac{N_A \cdot N_D}{n_i^2(T)}) \quad (10)$$

Where $N_A$ and $N_D$ are the acceptor and donor concentrations, respectively, $n_i(T)$ is the intrinsic carrier concentration. This equation characterizes the equilibrium state of a *p-n* junction, wherein no external bias is applied. The barrier height is contingent upon doping concentrations and temperature.

## 3. Simulation results and discussion

This section presents graphical representations of the formulas and results analyzed above, derived from our new model, accompanied by a thorough analysis and comparisons. Figure 1 illustrates the results obtained from our model, which accurately represents the temperature-dependent bandgap width of Si and GaAs. Modeling the variation of the bandgap width with temperature over a wide range is crucial for understanding material behavior. Similar to Si, the bandgap of GaAs decreases with temperature; however, GaAs retains its direct bandgap nature, while Si exhibits an indirect bandgap. The temperature-dependent bandgap significantly impacts carrier generation, intrinsic carrier concentration, and overall device performance, including applications in solar cells, diodes, and transistors. Silicon is widely preferred for most electronic applications due to its abundance and indirect bandgap, while GaAs is commonly employed in optoelectronic devices such as LEDs and lasers, thanks to its direct bandgap.

In the next steps, the expressions for intrinsic concentration (2). As a result, this becomes very important in our new model, which can explain these properties as functions of temperature. Figure 2 presents results from our new model and outcomes derived from expression (2), accurately depicting the temperature-dependent intrinsic concentration with of *Si* and *GaAs*. The intrinsic concentration at 300 K for *Si* and *GaAs* signifies the equilibrium concentration of charge carriers (electrons and holes) in these materials.

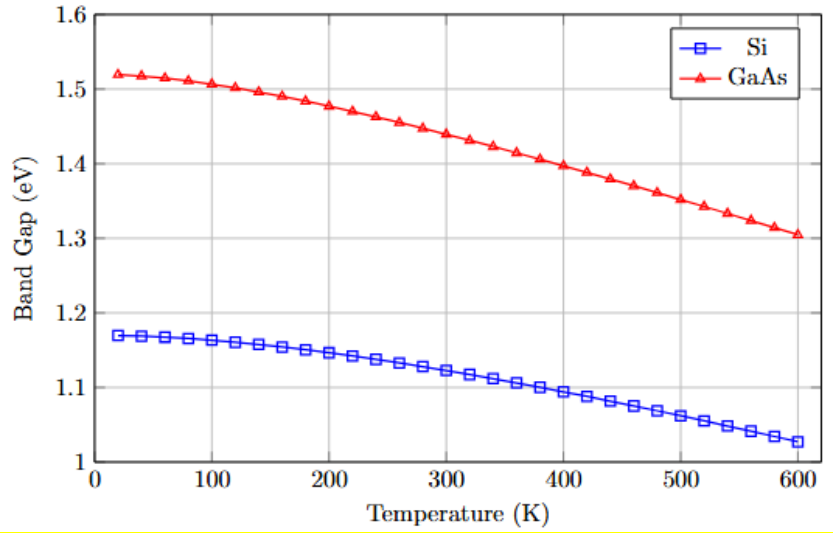



**Figure 1 –** Bandgap of a semiconductor as a function of temperature

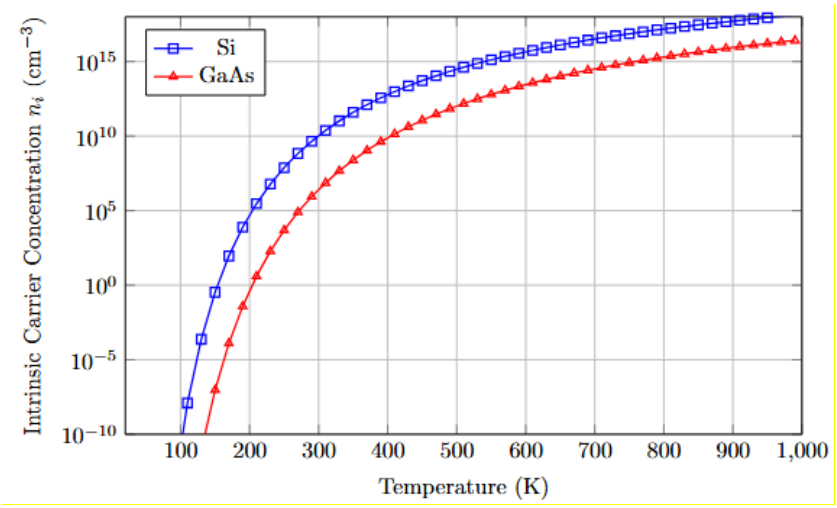



**Figure 2 –** The intrinsic carrier concentration of a semiconductor as a function of temperature

This intrinsic concentration, a characteristic property of semiconductors, is influenced by factors like the energy bandgap, temperature, and material-specific parameters. Understanding, intrinsic concentration is critical to analyzing the electrical behavior of semiconductors, particularly in devices like diodes and transistors. At low temperatures, not all dopant atoms are ionized, leading to incomplete ionization. Conversely, at high temperatures, full ionization occurs as all dopant atoms are ionized. Figure 2 shows at 300 K, $n_i = 1.5 \cdot 10^{10} [\frac{1}{cm^3}]$ for Si and $n_i = 2 \cdot 10^{6} [\frac{1}{cm^3}]$ for GaAs indicate the intrinsic carrier concentration.

By knowing the intrinsic concentration from expression (2), the intrinsic electrical conductivity can be determined using expression (7), which is shown as a function of temperature in Figure 3. The difference between state A and state B (6) lies in the value of the intrinsic conductivity, which reflects the strong temperature dependence of the expression. In state A, it takes a greater value compared to state B.

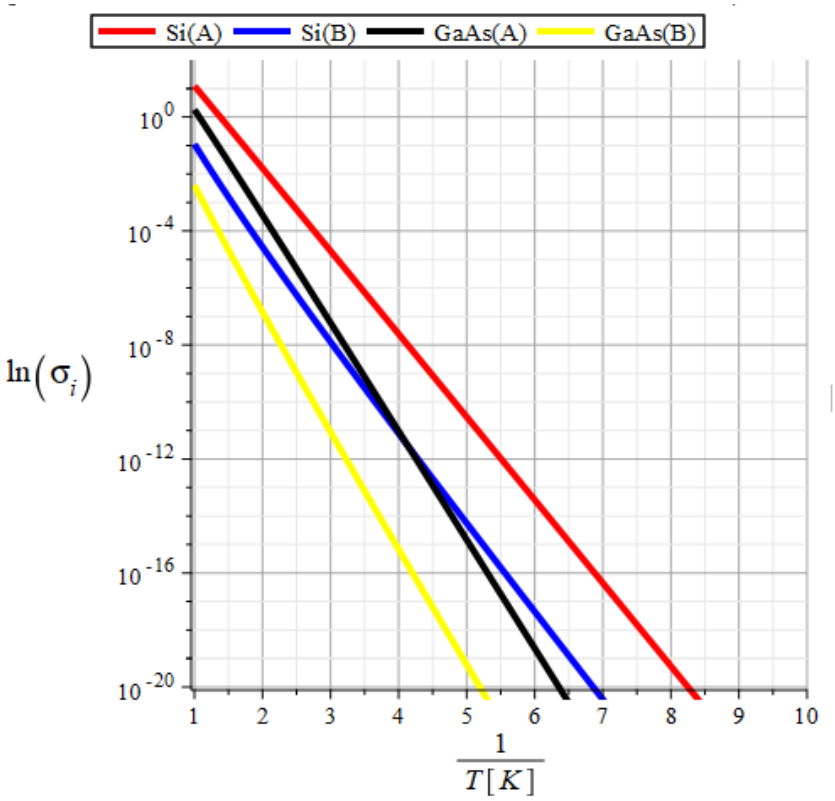



**Figure 3 –** Intrinsic conductivity of *Si* and *GaAs* as a function of temperature: In case (A) a strong temperature dependence was considered, while in case (B) a weak temperature dependence was taken into account

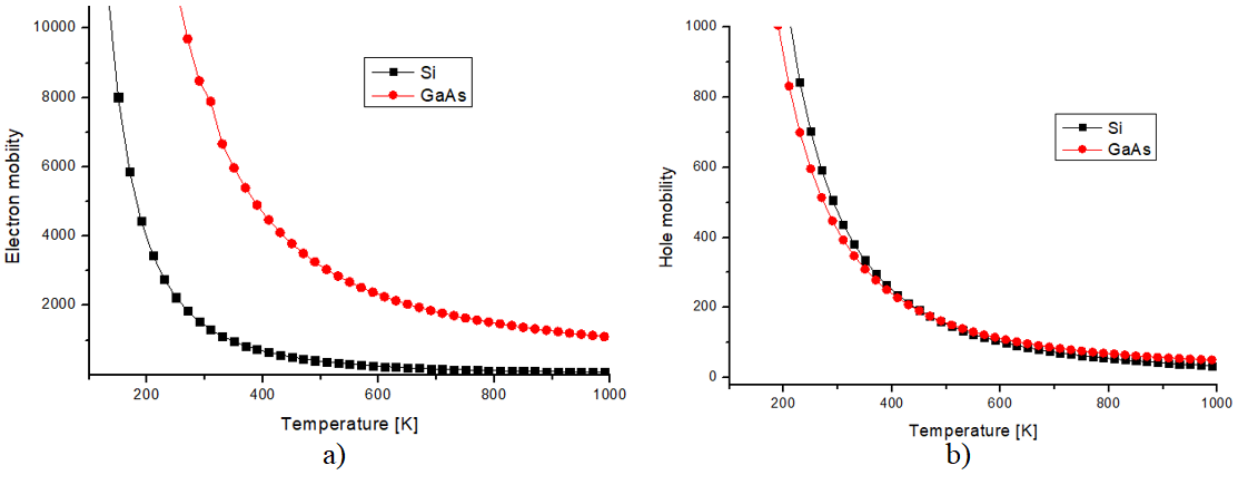



**Figure 4 –** The temperature dependence of carrier mobility for a) electrons and b) holes

Figure 4 illustrates a clear agreement between the mobility values derived from our new model and those obtained from reputable literature. Specifically, the electrons and holes mobilities $\mu_n = 1500[\frac{cm^2}{V \cdot s}]$ and $\mu_p = 450[\frac{cm^2}{V \cdot s}]$ for silicon (Si) and the electrons and holes mobilities $\mu_n = 8500[\frac{cm^2}{V \cdot s}]$ and $\mu_p = 400[\frac{cm^2}{V \cdot s}]$ for (GaAs) align closely with their respective literature values [24]. This indicates the reliability and accuracy of our new model in characterizing the mobility of electrons and holes in these materials.

Figures 5 and 6 showcase the I(V) characterristics of *Si* and *GaAs* materials, as determined by our new model. The drift-diffusion and generation-recombination models were incorporated into the simulation as current transport mechanisms. The temperature dependence of the band gap was calculated using the *Old Slotboom* mechanizm [25] and calibrated against experimental results for the selected Si material, as shown in Figure 5(a) [26]. By including the material parameters for GaAs, the new model produced the graph shown in Figure 5(b).

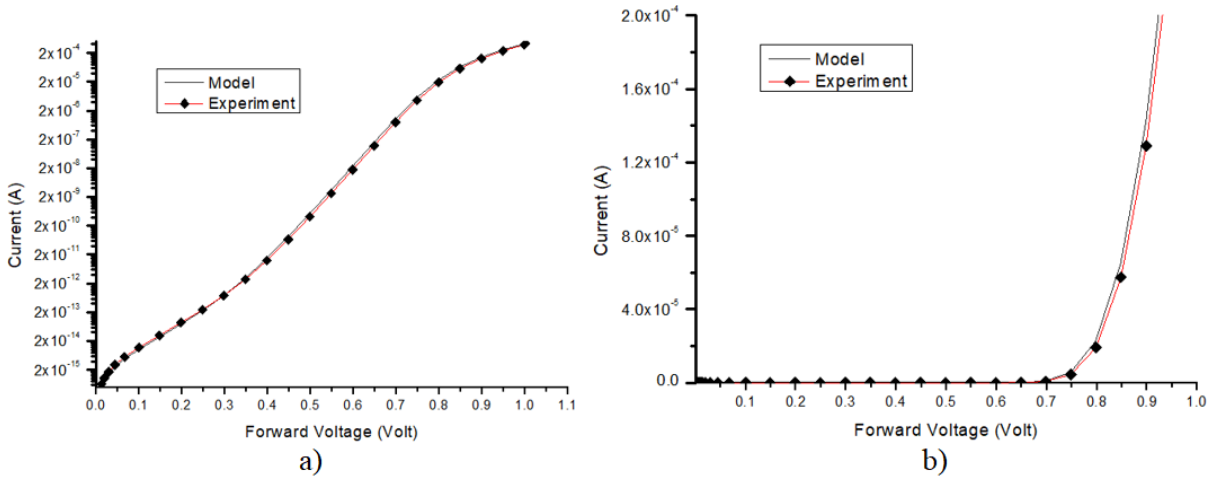



**Figure 5 –** a) Semilogarithmic I-V characteristics for the p-n junction based on Si, b) linear I-V characteristics for the p-n junction based on Si

Figure 5 illustrates that at low voltages, recombination current dominates up to 0.3 V, followed by diffusion current dominating up to 0.8 V. Beyond 0.8 V, the scenario shifts to high injection. Current (A) and voltage (V) characteristics are crucial for determining the current transfer mechanism and electrophysical processes in p-n junction structures. In the semi-logarithmic graph, the curvature of the curve between 0.1 and 0.3 V, and between 0.3 and 0.7 V at low voltage in forward bias, is explained by the current transfer mechanism. In this case, the ideality factor between 0.1 and 0.3 V takes a value close to 2, indicating a recombination mechanism. The ideality factor from 0.3 to 0.7 V is close to 1, signifying a diffusion mechanism.

Figure 6 depicts the *I(V)* characteristic of *GaAs* material, highlighting the series resistance effect above 1.3 V. Figure 5 and 6 a) the dominant region of the semi-logarithmic graph is commonly used to explain the current transport mechanism at low voltages. In the model, temperature dependence is considered for the strong A and weak B states. The voltage dependence of the ideality factor for both cases A and B is presented in Figure 7. It's important to note that this equation assumes ideal conditions and does not consider factors such as surface states or non-idealities present in real-world devices. In this paper, we calculated for Si $\varphi_k(T) = 0.823$ volt, for GaAs $\varphi_k(T) = 1.34$ volt by our model.

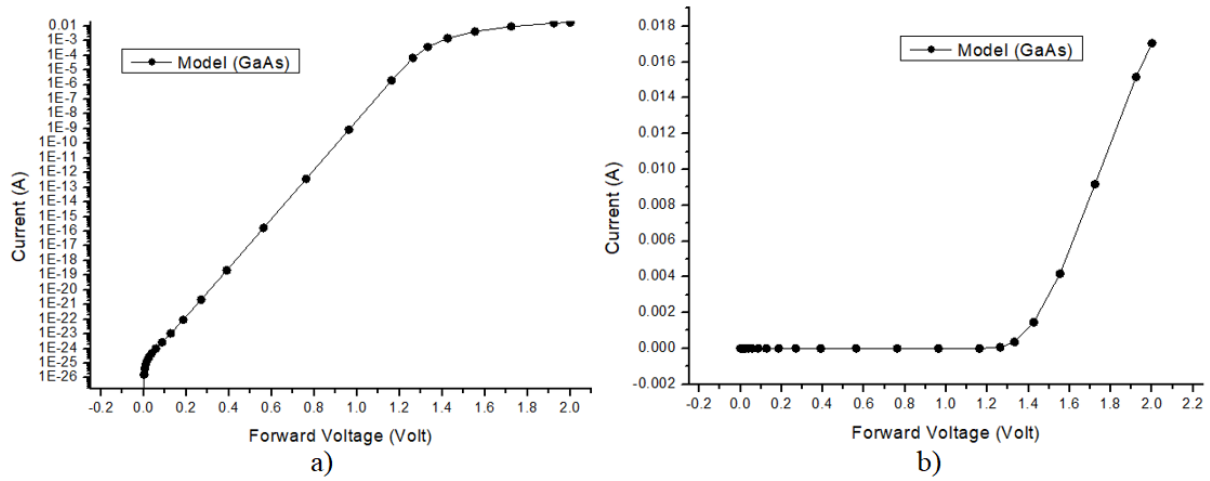



**Figure 6 –** a) Semilogarithmic I-V characteristics for the p-n junction based on *GaAs*, b) linear I-V characteristics for the p-n junction based on *GaAs*

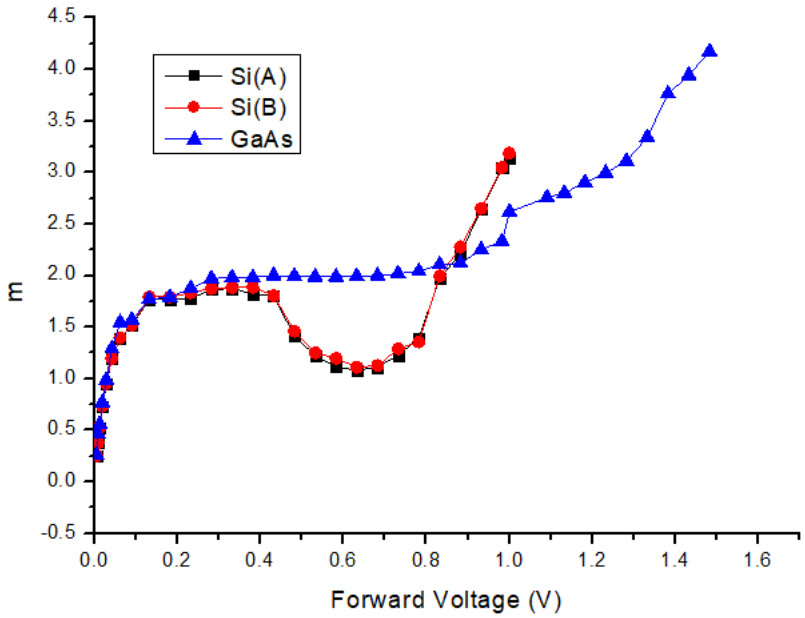



**Figure 7 –** Forward bias voltage dependent ideality factor for the p-n junction based on *Si(A), Si(B)* and *GaAs*

The ideality factor m is a dimensionless parameter that represents the deviation of the diode from ideal behavior. In an ideal diode, m would be equal to 1. However, in real-world diodes, m is often greater than 1, indicating non-ideal behavior such as recombination currents, series resistance, and other imperfections. Typically, m values range from around 1 to 2 for most diodes, but it can vary depending on the type of diode and its characteristics. Understanding and accurately determining the ideality factor is important in the analysis and modeling of diode circuits. Figure 7 displays the experimental results for *Si(A)* alongside the model results for *Si(B)* and our new model, as well as the results from the *GaAs* model. Analyzing the results for silicon (Si), it can be inferred that recombination mechanisms were predominant up to 0.4 V, while diffusion mechanisms prevailed up to 0.8 V. Due to GaAs's large band gap of 1.43 eV, the recombination mechanism was the dominant current mechanism from 0 V to 1.5 V.

## 3. Conclusion

In conclusion, our comprehensive investigation into the temperature-dependent properties of silicon (Si) and gallium arsenide (GaAs), achieved through meticulous modeling, calibration, and theoretical analysis, has yielded highly accurate findings. In the semi-logarithmic graph, the curvature of the curve between 0.1 and 0.3 V, and between 0.3 and 0.7 V, at low voltage in forward bias, is explained by the current transfer mechanism. In this context, the ideality factor between 0.1 and 0.3 V approaches 2, indicating a recombination mechanism. Conversely, the ideality factor from 0.3 to 0.7 V is close to 1, signifying a diffusion mechanism. We found that the temperature dependence of the internal electrical conductivity is stronger in case A than in case B. Furthermore, it was shown that in Si, the recombination mechanism dominates at low voltages between 0.1 and 0.3 V, while the diffusion mechanism prevails at higher voltages between 0.4 and 0.7 V. In GaAs, the recombination mechanism is dominant across the voltage range of 0.1 to 1.2 V. The robustness of our model is evident in its ability to accurately capture and predict the intricate behavior of these materials across a broad temperature range. Consequently, we envision utilizing this model in our future research endeavors.

**References**

1. Rahmouni S., Boubekri, H., Bendjeffal, H. et al. The temperature effect on the photoluminescence of porous silicon films obtained from an n-type silicon substrate // Silicon. – 2024. – Vol.16. – P. 4253–4261 https://doi.org/10.1007/s12633-024-02996-9.

2. Katelyn J. Baumler, Raymond E. Schaak. Tutorial on describing, classifying and visualizing common crystal structures in nanoscale materials systems // ACS Nanoscience. – 2024. – Vol.4 (5). – P. 290-316. https://doi.org/10.1021/acsnanoscienceau.4c00010

3. Shin J. C., Chanda D., Chern W., Yu K. J., Rogers J. A., Li X. Experimental study of design parameters in silicon micropillar array solar cells produced by soft lithography and metal-assisted chemical etching // IEEE Journal of Photovoltaics – 2012. – Vol.2. – № 2. – P.129–133. https://doi:10.1109/JPHOTOV.2011.2180894

4. Botan Jawdat Abdullah., Size effect of band gap in semiconductor nanocrystals and nanostructures from density functional theory within HSE06 // Materials Science in Semiconductor Processing. – 2022. – Vol. 137. – P. 106214. https://doi.org/10.1016/j.mssp.2021.106214

5. Yao B., Shaopeng W., Jun H., Shuitao G. Size and temperature effects on bandgap analysis of a defective phononic crystal beam // Crystals. – 2024. – Vol.14(2). – P.163. https://doi.org/10.3390/cryst14020163

6. Saeed M., Ur Rehman S., Khan M. M., Uddin Z. Computation of characteristics of C IV transitions // East European Journal of Physics. – 2023. – Vol. 2. – P. 165-172. https://doi.org/10.26565/2312-4334-2023-2-16

7. Ayoub R., AL-Timimi M. H., Abdullah M. Enhancements of structural and optical properties of MgO: SnO2 nanostructure films // East European Journal of Physics. -2023. -Vol. 3. – P. 546-554. https://doi.org/10.26565/2312-4334-2023-3-64.

8. Borblik V.L. Analytic theory for current-voltage characteristic of a nanowire radial p-i-n diode // Semiconductor Physics, Quantum Electronics Optoelectronics. – 2021. – Vol.24(4). – P. 419-424. https://doi.org/10.15407/spqeo24.04.419

9. Ibeh G., Lawani C., Emmanuel J., Oyedare P., Danladi E., Ige O. Enhanced performance of CuIn1-xGxSe2 solar cell through optimization of absorber and buffer layer properties using SCAPS-1D // East European Journal of Physics. – 2021. – Vol.(3). – P.67-76. https://doi.org/10.26565/2312-4334-2022-3-09

10. Parida M. K., Sundari S. T., Sathiamoorthy V., Sivakumar S. Current-voltage characteristics of silicon PIN diodes irradiated in KAMINI nuclear reactor // Nuclear Instruments and Methods in Physics Research Section A: Accelerators, Spectrometers, Detectors and Associated Equipment. – 2018. – Vol. 905. – P. 129-137. https://doi.org/10.1016/j.nima.2018.07.014

11.Kolesnikova I., Lozinskaya A., Mihaylov T., Novikov V., Shemeryankina A., Sherbakov I., Zarubin A. Temperature dependencies of current-voltage characteristics of GaAs:Cr // Journal of Instrumentation. – 2016. – Vol. 11(3). – P. 03059–03059. https://doi.org/10.1088/1748-0221/11/03/C03059

12.Kurucova N., Šagátová A., Pavlovič M., Zaťko B., Kováčová E., Boháček P., Predanocy M. Experimental analysis of the electric field distribution in semi-insulating GaAs detectors via alpha particles // Journal of Instrumentation. – 2024. – Vol.19(3). – P.03049. https://doi.org/10.1088/1748-0221/19/03/C03049

13.Fahad O. A., Al-Rawi B. K., Ramizy A. Performance evaluation of multi layered ZnO/Ge/Si photodetector: the effect of pulses laser. Optical and Quantum Electronics. – 2024. – Vol. 56(8). – P. 1392. https://doi.org/10.1007/s11082-024-07309-3.

14.Borblik V.L., Electrostatics of the nanowire radial p-i-n diode // Semiconductor Physics, Quantum Electronics & Optoelectronics – 2019. Vol.22 (2). – P. 201-205. https://doi.org/10.15407/spqeo22.02.201

15.Su Q., Lin H., Wang G., Tang H., Xue C., Li Z., Gao P. Theoretical limiting□efficiency assessment on advanced crystalline silicon solar cells with Auger ideality factor and wafer thickness modifications. Progress in Photovoltaics: Research and Applications – 2024.- Vol. 32. № 9. P. 587-598. https://doi.org/10.1002/pip.3790

16. Liu Y., Zhang K., Feng F., Chan K. W., Yeung S. Y., Kwok H. S., Liu Z. The size and temperature effect of ideality factor in GaN/InGaN multiple quantum wells micro□light□emitting diodes // Journal of the Society for Information Display-2021.Vol. 29(12). – P. 948-960. https://doi.org/10.1002/jsid.1070

17. Borblik V.L., Concerning the depletion width of a radial p-n junction and its influence on electrical properties of the diode // Semiconductor Physics, Quantum Electronics & Optoelectronics. – 2017. – Vol. 20(2). – P. 168-172. https://doi.org/10.15407/spqeo20.02.168

18.Abdullayev J. Sh., Sapaev I. B. Optimization of the influence of temperature on the electrical distribution of structures with radial p-n junction structures // East Eur. J. Phys. – 2024. – Vol. 3. – P. 344 https://doi.org/10.26565/2312-4334-2024-3-39

19.Wong H. Y. Calibrated Si mobility and incomplete ionization models with field dependent ionization energy for cryogenic simulations // International Conference on Simulation of Semiconductor Processes and Devices (SISPAD) Kobe, Japan. – 2020. – P. 193-196. https://doi.org/10.23919/SISPAD49475.2020.9241599

20.Abdullayev J. Sh., Sapaev I. B. Optimizing the influence of doping and temperature on the electrophysical features of p-n and p-i-n junction structures // Eurasian Physical Technical Journal – 2024. – Vol. 21. – № 3(49). – P. 21–28. https://doi.org/10.31489/2024No3/21-28

21.Habibe B., Sertap A. Exact analytical solution of the diode ideality factor of a p-n junction device using Lambert W-function model // Turkish Journal of Physics. – 2007. – Vol. 31(1). – P.7-10. https://journals.tubitak.gov.tr/physics/vol31/iss1/2

22. Gyubong K. Multiscale calculation of carrier mobility in organic solids through the fine-tuned kinetic Monte Carlo simulation // Computational Materials Science. – 2023. – Vol. 218. – P. 111957 https://10.1016/j.commatsci.2022.111957

23.Tobehn-Steinhäuser I., Reiche M., Schmelz M., Stolz R., Fröhlich T., Ortlepp T. Carrier mobility in semiconductors at very low-temperatures // Engineering Proceedings. – 2021. – Vol. 6(1). – P. 86. https://doi.org/10.3390/I3S2021Dresden-10086

24.Pathak P., Deb D., Nath D. et al. Incomplete ionization-dependent carrier mobility in silicon-on-insulator n-p-n double-gate tunnel field-effect transistors // J. Electron. Mater. – 2024. – Vol.53. – P. 1142–1160. https://doi.org/10.1007/s11664-023-10852-6

25.Ma J., Nissimagoudar A. S., Li W. First-principles study of electron and hole mobilities of Si and GaAs // Physical Review B. – 2018. – Vol.97(4). – P.045201. https://doi.org/10.1103/PhysRevB.97.045201

26.Ramya M., Nagarajan K.K. Investigation of single event transients on RingFET using 3D TCAD simulations // Silicon – 2023. – Vol. 15. – P. 875–886. https://doi.org/10.1007/s12633-022-02055-1

27. Cai X.-Y., Yang J.-H., Wei Y. Suppression of the drift field in the p-type quasineutral region of a semiconductor p-n junction // Chinese Physics Letters. – 2012. Vol. 29(9). – P. 097202. https://doi.org/10.1088/0256-307X/29/9/097202

***Information about authors:***

*Abdullayev Jo'shqin Shakirovich, Senior teacher at the Tashkent Institute of Irrigation and Agricultural Mechanization Engineers, National Research University. e mail: j.sh.abdullayev6@gmail.com*

*Sapaev Ibrokhim Bayramdurdievich, PhD, associate professor at the Tashkent Institute of Irrigation and Agricultural Mechanization Engineers, National Research University. e mail: sapaevibrokhim@.gmail.com*

IRSTI 29.19.31 https://doi.org/10.26577/phst2024v11i2b06

# Auto-oscillations of current in injection structures p+-p (Si<Mn>) based on heavily compensated silicon

K.S. Ayupov[1], H.F. Zikrillaev[1], E.B. Saitov[2]*, N.U. Abdullaeva[3], Z.N. Umarkhojayeva[1] and M.M. Yakhyayev[1]

[1]Tashkent State Technical University, Tashkent, 100095, Uzbekistan
[2]University of Tashkent for Applied Sciences, Str. Gavhar 1, Tashkent 100149, Uzbekistan
[3]Tashkent regional branch of Astrakhan State Technical University. Tashkent 100164, Uzbekistan
4Tashkent Medical Academy, Tashkent 100095, Uzbekistan
*e-mail: elyor.saitov@utas.uz
*(Received May,21, 2024; received in revised form November 20,2024; accepted November 28, 2024)*

This paper presents the findings of a study on the current-voltage characteristics (IVC) and current self-oscillations in n++-p(Si)-p+ structures made from heavily compensated silicon. We observed that the self-oscillations in manganese-doped silicon are linked to the injection of holes. During our examination of the I-V characteristics in p*-p(Si)-p* structures, we discovered that certain voltage levels can trigger self-oscillations in injection current, which are related to unipolar hole injection. Moreover, these current self-oscillations consistently promote vertical current growth within the IVC region. Initially, before stabilizing into fixed current self-oscillations, we noted chaotic fluctuations that transitioned to regular oscillations with a slight increase in voltage. We identified the characteristics of highly compensated silicon in an extremely nonequilibrium state and highlighted the unique functional capabilities of this material, which differ from those of conventional semiconductors. This discovery paves the way for developing innovative types of photoelectric, optoelectrical, and magnetoelectrical devices, as well as sensors for physical parameters and classical semiconductor devices that demonstrate high resistance to radiation and thermal effects.

**Key words:** silicon, current, injection, structure, compensation, self-oscillations, hole, trap.
**PACS number(s):** -61.72.jd.

## 1. Introduction

The modern development of electronics and microelectronics would be unimaginable without advancements in the contact properties of semiconductor devices [1, 2]. This necessitates the formulation of various contact types, such as ohmic, injection, or barrier contacts, each with specific parameters, optimized technological processes, and reduced production costs [3-5]. To achieve this, technologies are being developed to replace expensive materials, such as gold and silver, with more affordable alternatives. In this context, the aim is to align laboratory technologies for producing contacts in semiconductor devices with factory conditions. Many physical effects and phenomena remain underutilized due to the limitations of current technological methods in large-scale semiconductor device production.

The study of injection currents in compensated semiconductors, particularly in silicon that contains impurity atoms with deep energy levels, provides valuable insights into the nature of these levels and the physical mechanisms underlying current flow [6]. The analysis of current-voltage (I-V) characteristics of such structures enables researchers to determine the injection properties and potential barrier heights that arise at contact boundaries. This evaluation is crucial for assessing the influence of injection contacts on the observed physical effects [7, 8]. In this regard, structures based on compensated silicon are of considerable interest to researchers, as they display several intriguing physical phenomena that could have wide-ranging applications in semiconductor electronics.

Developing $p^+$-p-$p^+$ and $n^+$-n-$n^+$ structures based on compensated silicon presents significant challenges. For instance, when fabricating structures

from compensated silicon doped with atoms such as Mn, Zn, or S, thermal processing is necessary, which can alter the material's electrophysical properties [9-13]. Moreover, forming these contacts through melting various alloys or using diffusion techniques is not feasible due to the high diffusion coefficients of the materials typically used for contacts. To overcome this limitation, we have adopted an unconventional technological approach to create injection contacts. This method not only enables the formation of injection contacts but also brings the production technology closer to standard factory conditions.

## 2. Materials and methods for obtaining injection structures

To create injection contacts, industrial-grade silicon wafers, designated KDB-2 and KDB-10 (boron-doped dislocation silicon), with a diameter of 76 mm were selected as the starting material. The silicon was sliced into wafers with a thickness of 1 mm, followed by mechanical grinding to eliminate the damaged surface layer. This grinding process used a suspension of silicon carbide, grade M-14, and approximately 100 μm was removed from each side of the wafer.

After polishing and a preliminary chemical cleaning, the diffusion of boron or phosphorus impurity atoms was carried out under factory conditions. The diffusion of boron and phosphorus in silicon was executed in two stages using solid sources. Boron nitride (BN) and phosphorus pentoxide ($P_2O_5$) served as the diffusing agents. The initial boron diffusion was performed at a temperature of 1353 K for 40 minutes in a nitrogen atmosphere to develop an enriched layer. As is well known, BN is stable and prevents the oxidation of the source, leading to the formation of boron oxide ($B_2O_3$) on the silicon wafer. This method results in a high concentration of boron in silicon, achieving a doping uniformity of approximately 5%. Following the initial diffusion, boron atoms were further diffused at a temperature of 1473 K for 6.5 hours in a nitrogen atmosphere. The thickness of the resulting p+-layers varied from a few micrometers to 30-40 μm, depending on the diffusion temperature and duration.

To create n-type contacts, $P_2O_5$ was utilized as the diffusant. Phosphorus diffusion was carried out in a nitrogen atmosphere at a temperature of 1393 K for 40 minutes, followed by additional diffusion at 1473 K. By carefully controlling the diffusion time, we achieved an n+ injection layer with a thickness ranging from a few microns to 35-40 μm, with a doping uniformity of ±5%.

The solid sources BN and $P_2O_5$ create diffusion layers within silicon wafers that exhibit a high surface concentration, $N_s = 10^{20}$ cm$^{-3}$. In our experiments, surface resistivity measurements indicated that the boron and phosphorus concentrations were approximately $N_s \approx 10^{19}$ cm$^{-3}$. This level of concentration was influenced by lower temperatures and relatively short diffusion durations.

To fabricate structures based on compensated silicon doped with manganese impurity atoms, a gas-phase diffusion method was employed. For doping purposes, the $p^+$-p-$n^+$ and $n^+$-p-$n^+$ structures were cut into parallelepiped crystals measuring (1-10) x (1-5) x 0.8 mm³. To remove mechanical defects, the crystals were ground on four sides while leaving the injection layer intact, followed by chemical etching. Subsequently, these structures were placed in quartz ampoules along with a manganese diffusant. The ampoules were evacuated to a vacuum of about $10^{-5}$ mmHg before being sealed. The diffusion annealing of the structures was conducted in a vacuum tube furnace at 1973°C, which allowed for temperature control with an accuracy of ±1 K. Table 1 presents the parameters of the resulting $p^+$-p-$\rho^+$ structures, which were dependent on the diffusion conditions of the manganese impurity atoms.

**Table 1 –** Diffusion process conditions and parameters of the obtained structures

| № | T, K | D см$^2$/sec | t, hour | $N_p^+$,cm$^{-3}$ | $N_p$,cm$^{-3}$, base | $N_p^+$,cm$^{-3}$ |
|---|---|---|---|---|---|---|
| 1. | 1473 | $5{,}1\cdot10^{-12}$ | 1 | $2{,}2\cdot10^{16}$ | $1{,}5\cdot10^{15}$ | $2{,}2\cdot10^{16}$ |
| 2. | 1473 | $5{,}1\cdot10^{-12}$ | 2 | $2{,}36\cdot10^{17}$ | $1{,}5\cdot10^{15}$ | $2{,}36\cdot10^{17}$ |
| 3. | 1473 | $5{,}1\cdot10^{-12}$ | 3 | $2{,}3\cdot10^{18}$ | $1{,}5\cdot10^{15}$ | $2{,}3\cdot10^{18}$ |
| 4. | 1473 | $5{,}1\cdot10^{-12}$ | 4 | $3{,}7\cdot10^{18}$ | $1{,}5\cdot10^{15}$ | $3{,}7\cdot10^{18}$ |
| 5. | 1473 | $5{,}1\cdot10^{-12}$ | 6 | $3{,}4\cdot10^{19}$ | $1{,}5\cdot10^{15}$ | $3{,}4\cdot10^{19}$ |

*Continuation of the table*

| № | T, K | D см$^2$/sec | t, hour | $N_p^+$,cm$^{-3}$ | $N_p$,cm $^{-3}$, base | $N_p^+$,cm$^{-3}$ |
|---|---|---|---|---|---|---|
| 6. | 1473 | $5{,}1\cdot10^{-12}$ | 10 | $9{,}5\cdot10^{19}$ | $1{,}5\cdot10^{15}$ | $9{,}5\cdot10^{19}$ |
| 7. | 1473 | $5{,}1\cdot10^{-12}$ | 12 | $1{,}26\cdot10^{20}$ | $1{,}5\cdot10^{15}$ | $1{,}26\cdot10^{20}$ |
| 8. | 1473 | $5{,}1\cdot10^{-12}$ | 15 | $2{,}0\cdot10^{20}$ | $1{,}5\cdot10^{15}$ | $2{,}0\cdot10^{20}$ |
| 9. | 1473 | $5{,}1\cdot10^{-12}$ | 17 | $2{,}6\cdot10^{20}$ | $1{,}5\cdot10^{15}$ | $2{,}6\cdot10^{20}$ |
| 10. | 1473 | $5{,}1\cdot10^{-12}$ | 20 | $3{,}41\cdot10^{20}$ | $1{,}5\cdot10^{15}$ | $3{,}41\cdot10^{20}$ |
| 11. | 1473 | $5{,}1\cdot10^{-12}$ | 24 | $3{,}6\cdot10^{20}$ | $1{,}5\cdot10^{15}$ | $3{,}6\cdot10^{20}$ |
| 12. | 1473 | $5{,}1\cdot10^{-12}$ | 30 | $4{,}2\cdot10^{20}$ | $1{,}5\cdot10^{15}$ | $4{,}2\cdot10^{20}$ |
| 13. | 1473 | $5{,}1\cdot10^{-12}$ | 40 | $4{,}9\cdot10^{20}$ | $1{,}5\cdot10^{15}$ | $4{,}9\cdot10^{20}$ |

The diffusion temperature was monitored using a thermocouple placed directly next to the quartz ampoule. This setup allowed for precise control over the manganese diffusion temperature in silicon, which is crucial for defining the various diffusion technological modes. Such control facilitates the development of a reproducible technology for producing structures based on silicon that is compensated with manganese impurity atoms.

To differentiate compensating impurities from various uncontrolled defects, control samples were simultaneously annealed under the same technological conditions. The high diffusion coefficient of manganese impurity atoms in silicon enabled uniform doping of the structure bases within a short annealing time. This approach effectively prevents the deep penetration of boron or phosphorus impurity atoms into the silicon.

**Table 2 –** The parameters of the obtained structures depending on the diffusion temperature of manganese impurity atoms in silicon.

| The brand of the initial sample | The concentration of boron $N\cdot10^{16}$, cm$^{-3}$ | Diffusion temperature - °C | Diffusion time, t | Type of conductivity of the base after diffusion | Sheet resistance of the base after diffusion ρ, Ω·cm | Mobility μ, cm$^2$/B·sec |
|---|---|---|---|---|---|---|
| 1 | 2 | 3 | 4 | 5 | 6 | 7 |
| CDB-2 | 1,7 | 1100 | 1,5 | p | $6{,}3\cdot10^3$ | 230 |
| CDB-2 | 1,7 | 1130 | 1,5 | n | $2{,}0\cdot10^5$ | 970 |
| CDB-7,5 | 0,3 | 1080 | 1,5 | p | $7{,}0\cdot10^4$ | 184 |
| CDB-7,5 | 0,3 | 1110 | 1,5 | n | $6{,}0\cdot10^4$ | 1010 |
| CDB-10 | 0,2 | 1030 | 1,5 | p | $8{,}0\cdot10^2$ | 196 |
| CDB-10 | 0,2 | 1035 | 1,5 | p | $3{,}6\cdot10^3$ | 208 |
| CDB-10 | 0,2 | 1040 | 1,5 | p | $7{,}4\cdot10^4$ | 200 |
| CDB-10 | 0,2 | 1045 | 1,5 | p | $1{,}4\cdot10^5$ | 195 |
| CDB-10 | 0,2 | 1050 | 1,5 | n | $1{,}5\cdot10^5$ | 980 |
| CDB-10 | 0,2 | 1060 | 1,5 | n | $7{,}1\cdot10^4$ | 910 |
| CDB-10 | 0,2 | 1080 | 1,5 | n | $2{,}8\cdot10^4$ | 1020 |

By controlling the diffusion temperature, we were able to obtain structures with bases that exhibited both hole and electron conductivity, each with varying resistivity values. This process resulted in the production of structures such as $p^+$-p(Si)-p, $p^+$-n(Si)-$p^+$, $n^+$-p(Si)-$n^+$, and $n^+$-n(Si)-$n^+$. Once the diffusion process was completed, we ground the surfaces of the samples to 100 μm on all four sides. This was done to remove the enriched layer of manganese atoms, except on the sides where the specially created injection layers were located. The resistivity of the bases of these structures was measured through conductivity assessments while obtaining the voltage-current characteristics (I-V characteristics).

## 3. Results and discussion

The I-V characteristics of the structures were investigated in darkness at room temperature. The study revealed a sharp increase in current at certain applied voltage values. To elucidate the mechanism

of current conduction in the injection structures and demonstrate that this increase is associated with unipolar injection, we examined the I-V characteristics of the initial samples KDB-2; 10 before and after thermal annealing, as well as structures with injection contacts and control samples (see Fig. 1). Additionally, for comparison, we investigated current conduction in injection structures that were compensated with manganese impurity atoms.

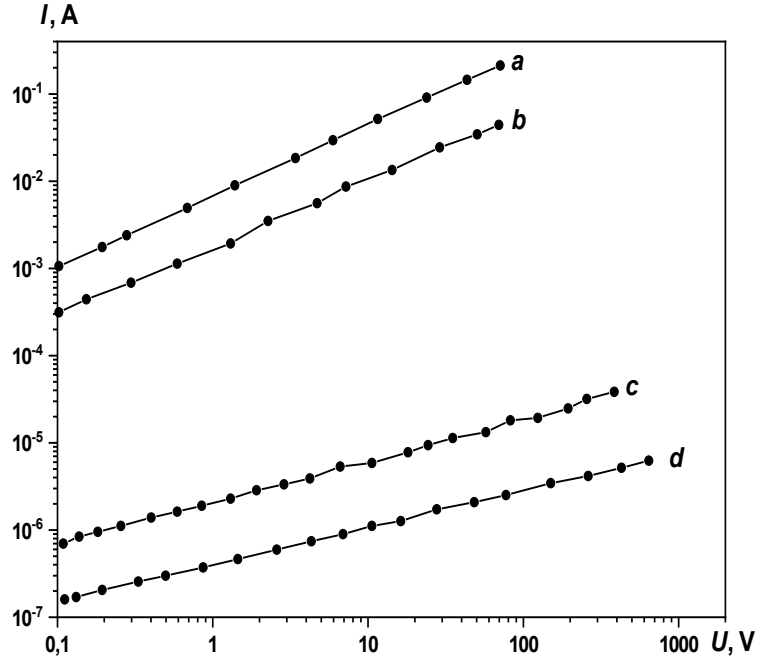



**Figure 1** – The I-V characteristics of the initial and control annealed structures of $p^+$-p-$p^+$ at a temperature of 300 K in darkness: a) $p^+$ -p- $p^+$ before annealing; b) $p^+$-p-$p^+$ after annealing; c) KDB before annealing; d) KDB after annealing.

To confirm that the sharp increase in current is indeed related to the unipolar injection of holes, we examined the I-V characteristics of several structures: $p^+$-p(Si)-$p^+$, $p^+$-n(Si)-$p^+$, $n^+$-p(Si)-$n^+$, and $n^+$-n(Si)-$n^+$, all based on compensated silicon doped with manganese (see Figure 2). These investigations showed that unipolar injection of holes specifically occurs in the $p^+$-p(Si)-$p^+$ structures, which are responsible for the emergence of current injection instabilities.

The I-V characteristics of the structures were assessed under dark conditions and at room temperature. Our analysis revealed a sharp increase in current at specific voltage values. To demonstrate that this increase is linked to unipolar injection, we evaluated the I-V characteristics of the initial samples KDB-2 and KDB-10, both before and after thermal annealing, as well as in structures containing manganese impurity atoms and control samples (see Fig. 2). A comparison of the obtained I-V characteristics confirmed that the sharp increase in current is indeed associated with the injection of charge carriers into the base of the structures doped with manganese impurity atoms. In contrast, other structures (see Fig. 2 curves 2, 3, 4) did not exhibit such a sharp increase in current.

To demonstrate that the sharp increase in current is specifically related to the unipolar injection of holes, we investigated the I-V characteristics of various structures: $p^+$-p(Si)-$p^+$, $p^+$-n(Si)-$p^+$, $n^+$-p(Si)-$n^+$, and $n^+$-n(Si)-$n^+$. These structures are based on compensated silicon doped with manganese impurity atoms (see Fig. 2, curve 1). Our studies revealed that unipolar injection of holes occurs predominantly in the $p^+$-p(Si)-$p^+$ structures, which contribute to the emergence of current injection instabilities.

The examination of the I-V characteristics of these injection structures with varying concentrations in the injecting layer allowed us to identify the specific boron concentration at which the sharp increase in current is observed. The I-V characteristics from these investigations are illustrated in Fig.

3. As shown in the figure, an increase in boron concentration in the injecting layer, within the range of $N_B=10^{15}$ to $10^{20}$ $cm^{-3}$, leads to a rise in current when the concentration of boron atoms reaches approximately $10^{17}$ $cm^{-3}$ or higher.

It is important to note that the increase in boron concentration in the p+-layer results in a shift towards lower voltages, where the degree of current increase becomes noticeable. At concentrations below $N_B \leq 10^{17} cm^{-3}$, there is no significant effect on the I-V characteristics in the $p^+$–p(Si)–$p^+$ structures. However, at injecting contact concentrations of $N_B=10^{17}$ $cm^{-3}$ to $10^{20}$ $cm^{-3}$, after the sharp increase in current, oscillations in the circuit current start to appear.

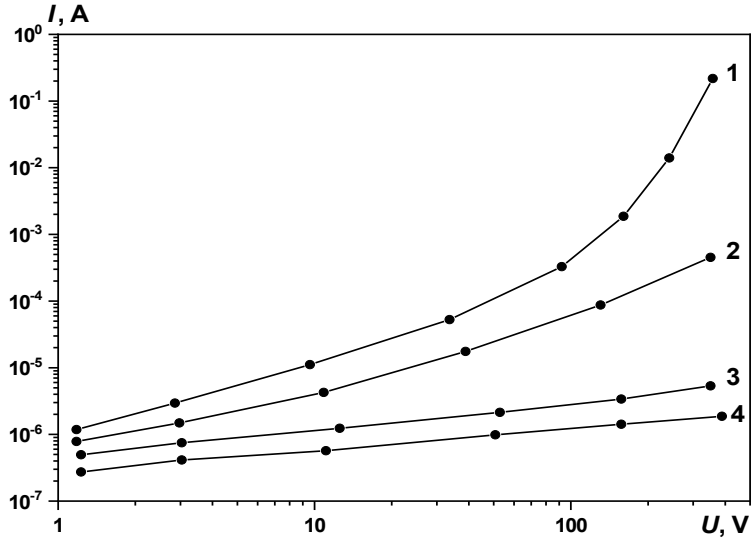



**Figure 2** – I-V characteristics of the structures: curve 1: $p^+$-p(Si<Mn>)$p^+$; curve 2: $p^+$-n(Si<Mn>)-$p^+$; curve 3: $n^+$-n(Si<Mn>); curve 4: $n^+$-p(Si<Mn>)-$n^+$.

At a temperature of 300 K, the specific resistance of the base measured $\rho = 5 \times 10^4$ Ω·cm. Analyzing the voltage-current characteristics of the $p^+$-p(Si)-$p^+$ structures provided valuable insights into unipolar hole injection. According to existing literature [14-20], unipolar carrier injection occurs in semiconductor materials that contain deep energy levels, which serve as traps for the primary charge carriers.

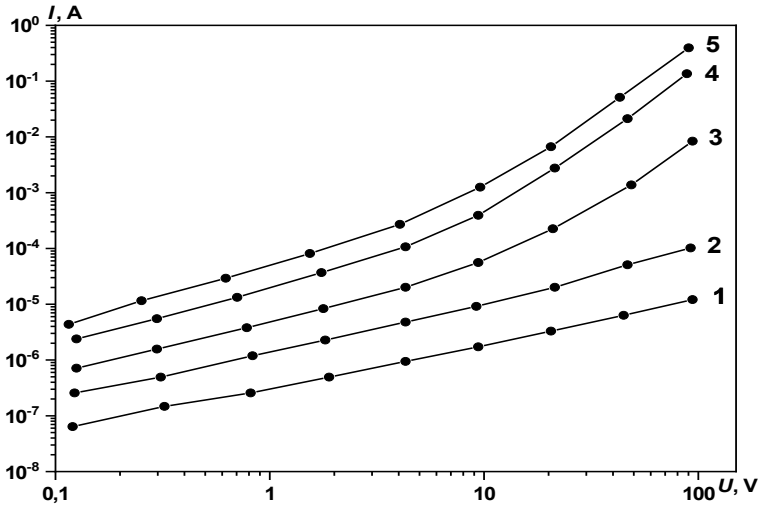



**Figure 3 –** I-V characteristics of $p^+$-p(Si<Mn>)-$p^+$ structures with different concentrations of $p^+$ layer: curve 1 – $10^{15}$ $cm^{-3}$; curve 2 – $10^{16}$ $cm^{-3}$; curve 3 – $10^{17}$ $cm^{-3}$; curve 4 – $10^{18}$ $cm^{-3}$; curve 5 – $10^{19}$ $cm^{-3}$ at T=300K

The quadratic section of the I-V characteristics of the structures corresponds to the monopolar injection of holes. The voltage at which the sharp increase in current begins, known as $V_{fct}$ (where 'fct' stands for field charge of traps), indicates the point at which the traps are fully charged. This allows for a clear determination of the complete filling of the energy level of the manganese impurity atom by these traps, which are responsible for the excitation of current oscillations in the studied structure. The results from the I-V characteristic studies of the structures at various illumination intensities provide valuable information regarding the total concentration and ionization energy of the manganese impurity atoms in compensated silicon.

If the value of $V_{fct}$ is known, the concentration of impurity atoms at the energy level can be determined using the appropriate formula:

$$N_t = \frac{\varepsilon V_{fct}}{ed^2} \quad (1)$$

where ε is dielectric constant of silicon, e is charge of the electron, d is thickness of the base of the structures. This, in turn, allows for the determination of the ionization energy from the energy equation at a given temperature.

$$E_v - E_t = kT\, ln \frac{N_S}{QgN_t} \quad (2)$$

where Q is a coefficient, which shows the ratio of the concentration of free charge carriers to the concentration of carriers trapped at energy levels, is defined by the expression:

$$Q = \frac{n_0 L^2}{\varepsilon V_X} \quad (3)$$

The calculation results show that for compensated silicon doped with manganese impurity atoms, this value is approximately Q ≈ (1 to 3)$^{(1/2)}$ 10, while the maximum values of concentration and activation energy of the manganese level are $N_t = 2.4 \times 10^{10}$ cm$^{-3}$ and Et = (0.14 to 0.16) eV, respectively. Knowing the experimental values of $V_{fct}$ and Q at various light intensities for compensated Si<Mn> samples with different degrees of compensation, it is possible to determine the concentration of the energy level in the structures $p^+$-p(Si<Mn>)-$p^+$ that are responsible for the excitation of current oscillations.

The results from the I-V characteristics studies allow us to determine the mobility of charge carriers. This mobility is a crucial parameter for understanding not only the mechanism behind injection instability but also the changes in carrier mobilities under conditions of strong compensation [17]. To calculate the mobility, the following formula was employed:

$$\mu = Id^2/EV \quad (4)$$

The mobility of holes was found to be in the range of μ = 100 to 300 cm²/V·s, depending on temperature, the degree of compensation of the base structures, and light intensity.

The results of the I-V characteristics study conducted on various structures based on compensated silicon revealed that a noticeable sharp increase in current, referred to as the bulk field charge current (BFCC), along with associated current oscillations, is only evident in the $p^+$-p(Si)-$p^+$ structures. In contrast, the $p^+$-n(Si)-$p^+$, $n^+$-n(Si)-$n^+$, and $n^+$-p(Si)-$n^+$ structures did not show any signs of BFCC or current oscillations. This suggests that the phenomena observed, particularly the vertical increase in current and the current oscillations, are linked to hole injection into the base of the $p^+$-p(Si)-$p^+$ structures.

From the analysis of the literature data [21-25], it is clear that the injection current oscillations in the $p^+$-p(Si)-$p^+$ structures are particularly important for gaining additional insights to develop a unified model of current instability in compensated silicon.

The studies on the I-V characteristics of the $p^+$-p(Si)-$p^+$ structures demonstrate that injection current oscillations occur at specific voltage levels, which are linked to the unipolar injection of holes. The research findings indicate that current oscillations in these structures are consistently triggered following a vertical increase in current within the I-V characteristic region. Notably, before stable current oscillations are established, chaotic oscillations can be observed. These chaotic oscillations transition into regular oscillations with only a slight increase in voltage. Figure 4 illustrates the various forms of current oscillations.

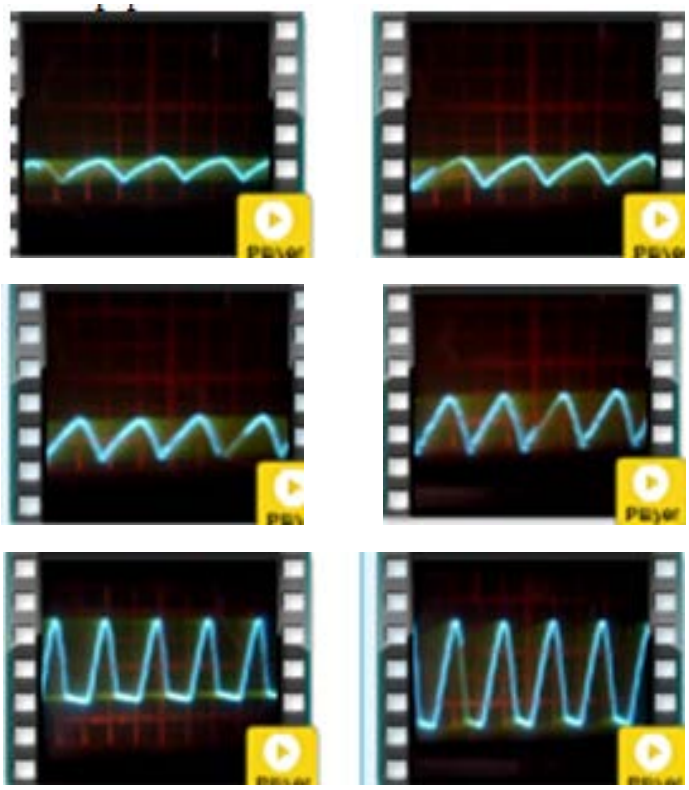


**Figure 4** – Forms of injection current oscillations in structures $p^+$-p(Si<Mn>)-$p^+$.

To determine the dependence of the conditions for excitation and parameters of current oscillations on the degree of compensation of the base, structures $p^+$-p(Si<Mn>)-$p^+$ with base resistivities $\rho_e = 10^2$ to $10^5$ Ω•cm was obtained. The studies showed that oscillations in the structures are observed at room temperature and in the dark, starting with base resistivities $\rho_e \geq 3 \cdot 10^2$ Ω•cm.

The research findings demonstrate that injection current self-oscillations in $p^+$-p(Si)-$p^+$ structures are observed across a wide range of base resistivity, ranging from 100 to 100,000 Ω•cm. The magnitude of these oscillations depends on the concentration of electroactive manganese dopant atoms. Additionally, it has been established that these injection current self-oscillations exhibit bulk characteristics. The experimental results provide an opportunity to select $p^+$-p(Si)-$p^+$ structures with optimal base electrophysical parameters for further investigations.

## 4. Conclusion

The study of auto-oscillations in $p^+$-p(Si<Mn>) injection structures, based on heavily compensated silicon, reveals significant insights into the dynamics of current instability. During unipolar injection, within particular voltage intervals, current oscillations are observed. These oscillations are of great significance as they reveal the complex interaction among compensation, base resistivity, and dopant concentration. Notably, as the voltage rises, the oscillations transition from chaotic to regular forms, opening up avenues for a more profound comprehension of their fundamental mechanisms.

Experimental investigations have firmly established that injection current oscillations occur over a wide range of base resistivity, spanning from $10^2$ to $10^5$ Ω·cm. Moreover, they are strongly influenced by the concentration of manganese atoms. This research emphasizes the bulk nature of these oscillations and their stability at room temperature in the absence of illumination. Consequently, $p^+$-p(Si<Mn>) structures emerge as a highly promising platform for further exploration and hold potential for applications in semiconductor devices.

The findings not only contribute to the evolution of a unified model of current instabilities in compensated silicon but also lay the groundwork for

optimizing the electrophysical parameters of such structures, thereby advancing semiconductor technologies.

**Acknowledgments**

The work was financially supported by the Ministry of Innovative Development of the Republic of Uzbekistan within the framework of the project F-OT-2021-497 – "Development of the scientific foundations for the creation of solar cogeneration plants based on photovoltaic thermal batteries.

The authors express their gratitude to the professors of Tashkent State Technical University N.F. Zikrillayev and Kh.M. Iliyuev for his scientific and practical help in writing this article.

**References**

1. Liu X.F., Xing K., Tang Ch.S., Sun Sh., Chen P., Qi D.-Ch., Breese M. B.H., Fuhrer M.S., Wee A.T.S., Yin X. Contact resistance and interfacial engineering: Advances in high-performance 2D-TMD based devices // Progress in Materials Science. – 2025. -Vol.148. – P.101390. https://doi.org/10.1016/j.pmatsci.2024.101390

2. Kim K. S., Kwon J., Ryu H., Kim Ch., Kim H., Lee E.-K., Lee D., Seo S., Han N. M., Suh J. M., Kim J., Song M.-K., Lee S., Seol M., Kim J. The future of two-dimensional semiconductors beyond Moore's law // Nature Nanotechnology. – 2024. – Vol. 19. – P. 895–906. https://doi.org/10.1038/s41565-024-01695-1

3. Zheng Y., Gao J., Han Ch., Chen W. Ohmic contact engineering for two-dimensional materials // Cell Reports Physical Science. – 2021. – Vol. 2(1). – P. 100298. https://doi.org/10.1016/j.xcrp.2020.100298

4. Pourtois R. D., Houssa G., Afzalian M. A. Fundamentals of low-resistive 2D-semiconductor metal contacts: an ab-initio NEGF study // npj 2D Materials and Applications. – 2023. – Vol.7. -№. 38. https://doi.org/10.1038/s41699-023-00402-3

5. Kao K. C. Charge carrier injection from electrical contacts, in book Dielectric phenomena in solids. With emphasis on physical concepts of electronic processes – 2004. – P. 327-380. Academic Press. Elsevier Inc. UK. London. https://doi.org/10.1016/B978-012396561-5/50016-5

6. Markku T. Petzold M., Teruaki Motooka. Handbook of silicon based MEMS materials and technologies. // A volume in micro and nano technologies. Third Edition 2020 Elsevier Inc. UK. London. https://doi.org/10.1016/C2018-0-01845-9

7. Meng J., Lee Ch., Li Zh. Adjustment methods of Schottky barrier height in one- and two-dimensional semiconductor devices // Science Bulletin. – 2024. – Vol.69. – P. 1342-1352. https://doi.org/10.1016/j.scib.2024.03.003

8. Divya S., Kallatt S., Chenniappan V., Nair S., Gupta G., Kiran J. Karmakar D., Majumdar K. Nature of carrier injection in metal/2D-semiconductor interface and its implications for the limits of contact resistance // Phys. Rev. B. -Vol. 96. -P. 205423. https://doi.org/10.1103/PhysRevB.96.205423

9. Fauveau A., Martel B., Veirman J., Dubois S., Kaminski-Cachopo A., Ducroquet F. Comparison of characterization techniques for measurements of doping concentrations in compensated n-type silicon // Energy Procedia. – 2016. -Vol. 92. – P. 691-696. https://doi.org/10.1016/j.egypro.2016.07.045

10. Zhang W.J., Chen J.S., Li S., Wu Y.H., Zhang P.L., Yu Z.S., Yue Z.H., Chun Y., Lu H. Electronic and mechanical properties of monocrystalline silicon doped with trace content of N or P: A first-principles study // Solid State Sciences. – 2021. – Vol. 120. – P. 106723. https://doi.org/10.1016/j.solidstatesciences.2021.106723

11. Lee M. Doped silicon's challenging behaviour // Nature Physics. – 2023. – Vol. 19. -P. 614–615. https://doi.org/10.1038/s41567-022-01918-z

12. Nasriddinov S.S., Esbergenov D.M. A Study of complex defect formation in silicon doped with nickel // Russ. Phys. J. – 2023. – Vol. 65. -P. 1559–1563. https://doi.org/10.1007/s11182-023-02801-x

13. Zhang X., Brynda M., Britt R.D., Carroll E.C., Larsen D.S., Louie A.Y., Kauzlarich S.M. Synthesis and characterization of manganese-doped silicon nanoparticles: Bifunctional paramagnetic-optical manomaterial // J. Am. Chem. Soc. – 2007. -Vol. 129. – P. 10668–10669. https://doi.org/10.1021/ja074144q

14. Neumann F., Genenko Y. A., Melzer C., von Seggern H. Self-consistent theory of unipolar charge-carrier injection in metal/insulator/metal systems // J. Appl. Phys. – 2006. -Vol. 100. -P. 084511. https://doi.org/10.48550/arXiv.0704.2322

15. Koehler M., Biaggio I.. Influence of diffusion, trapping, and state filling on charge injection and transport in organic insulators // Phys. Rev. B. – 2003. – Vol. 68. – P. 075205. https://doi.org/10.1103/PhysRevB.68.075205

16. Chen Y., Wang Y., Wang Z. et al. Unipolar barrier photodetectors based on van der Waals heterostructures // Nat Electron. – 2021. – Vol.4. – P. 357–363. https://doi.org/10.1038/s41928-021-00586-w

17. Zhang Q., Li N., Zhang T. et al. Enhanced gain and detectivity of unipolar barrier solar blind avalanche photodetector via lattice and band engineering // Nat Commun. – 2023. – Vol. 14. – P. 418. https://doi.org/10.1038/s41467-023-36117-8

18. Mussabek G., Mirgorodskij I., Kharin A., Taurbayev T., Timoshenko V. Formation and optical properties of nanocomposite based on silicon nanocrystals in polymer matrix for solar cell coating // Journal of Nanoelectronics and Optoelectronics. – 2015. – Vol. 9(6). – P. 738–740. https://doi.org/10.1166/jno.2014.1670

19. Talkenberg F., Illhardt S., Zoltán Radnoczi G., Béla P., Schmidl G., Schleusener A.,Dikhanbayev K., Mussabek G., Gudovskikh A., Sivakov V. Atomic layer deposition precursor step repetition and surface plasma pretreatment influence on semiconductor–insulator–semiconductor heterojunction solar cell // Journal of Vacuum Science and Technology A (JVS A). – 2015. -Vol. 33. -P. 041101-1-5. https://doi.org/10.1116/1.4921726

20. Markhabayeva A.A., Dupre R., Nemkayeva R., Nuraje N. Synthesis of hierarchical $WO_3$ microspheres for photoelectrochemical water splitting application // Physical Sciences and Technology. – 2023. – Vol. 10(3-4). – P.33-39. https://doi.org/10.26577/phst.2023.v10.i2.04

21. Mussabek G.K., Yermukhamed D., Dikhanbayev K.K., Mathur S., Sivakov V.A. Self-organization growth of Ge-nanocolums // Materials Research Express. – 2017. – Vol. 4. – P. 035003. https://doi.org/10.1088/2053-1591/aa5ed6

22. Tsukuda M., Imaki H., Omura I. Ultrafast lateral 600 V silicon SOI PiN diode with geometric traps for preventing waveform oscillation // Solid-State Electronics. – 2014. -Vol. 104. – P. 61-69. https://doi.org/10.1016/j.sse.2014.11.011

23. Razak N. H. A., Amin N. et al. Influence of pulsed Nd:YAG laser oscillation energy on silicon wafer texturing for enhanced absorption in photovoltaic cells // Results in Physics. – 2023. – Vol.48. – P.106435, https://doi.org/10.1016/j.rinp.2023.106435

24. Liu F., Cheng Y., Yang F., Chen X.. Quantum conductance oscillation in linear monatomic silicon chains // Physica E: Low-dimensional Systems and Nanostructures. – 2014. – Vol. 56. – P. 96-101. https://doi.org/10.1016/j.physe.2013.08.029

25. Patzauer M., Hueck R., Tosolini A., Schönleber K., Krischer K. Autonomous oscillations and pattern formation with zero external resistance during silicon electrodissolutio // Electrochimica Acta. – 2017. – Vol. 246. – P. 315-321. https://doi.org/10.1016/j.electacta.2017.06.005

***Information about authors:***

*Kutub Ayupov, doctor of science, professor at the Tashkent State Technical University (Tashkent, Republic of Uzbekistan) e-mail:ksayupov@gmail.com*

*Hayrulla F. Zikrillaev, doctor of science, professor at the Tashkent State Technical University (Tashkent, Republic of Uzbekistan) e-mail: zikrillayev_khayrulla@tdtu.uz*

*Elyor Saitov, PhD, associate professor at the Tashkent University for Applied Sciences, (Tashkent, Uzbekistan), e-mail: elyor.saitov@utas.uz*

*Nigora Abdullaeva, associate professor at the Tashkent Medical Academy (Tashkent, Uzbekistan), e-mail abnigorka@gmail.com*

*Zabarjad Umarkhojayeva, Senior lecturer at the Tashkent State Technical University (Tashkent, Uzbekistan), e-mail: zabarjad.umarxojayeva@tdtu.uz*

*Mirafzal Yakhyayev, PhD, Senior lecturer at the Tashkent State Technical University (Tashkent, Uzbekistan), e-mail: radiaretv@gmail.com*

IRSTI 29.19.37 https://doi.org/10.26577/phst2024v11i2b07

# Modeling the resistance of plate-like heat exchangers made of 06khn28mdt alloy (analogous to aisi904l steel) to crevice corrosion in recycled water enterprises

A.V. Dzhus*, S.O. Subbotin, T.V. Pulina and G.V. Snizhnoi

Zaporizhzhia Polytechnic National University, Zaporizhzhia, Ukraine
*e-mail: Anna-92@ukr.net

*(Received October 12, 2024; received in revised form October 31, 2024; accepted November 27, 2024)*

This study investigates the mechanisms and patterns of crevice corrosion in heat exchangers made from 06KhN28MDT alloy (analogous to AISI 904L steel) in model water systems of industrial enterprises. Using mathematical models, the relationship between activation potentials ($E_{crev}$), repassivation potentials ($E_{rep}$), and free corrosion potentials ($E_{cor}$) with the alloy's chemical composition and structural components was established. It was found that $E_{crev}$ shifted positively with increasing levels of Mn, Cr, Cu and $d_g$ (mean austenite grain diameter), and decreasing levels of C, Si, Ni, Ti, Mo, $V_S$ (sulfide volume), and $V_N$ (titanium nitride volume). Cr, Mo, and $d_g$ were identified as having the most significant influence on $E_{crev}$, $E_{rep}$ and $E_{cor}$. The study also highlights the importance of chromium in improving the protective properties of the oxide film, and the reduction of local corrosion damage near titanium carbonitrides intersecting austenite grain boundaries. The study concludes that the alloy's resistance to crevice corrosion in recycled water systems improves with higher concentrations of Cr, Mo, and $d_g$. The mathematical models developed in this research can be applied to predict the corrosion resistance of heat exchangers made from 06KhN28MDT alloy in industrial water systems.

**Key words:** 06KhN28MDT alloy heat exchanger, crevice corrosion, recycled industrial water, selective metal dissolution.
**PACS number(s):** 75.20.En.

## 1. Introduction

Plate heat exchangers made of 06KhN28MDT alloy are often used for the production of acids, such as sulfuric, hydrofluoric, stearic, phosphoric, etc. [1]. To cool process products, which are solutions of these acids, water from the recycling systems of enterprises is used. It contains chloride ions and other activators of local corrosion of passivated steels and alloys [2, 3]. This can cause pitting and crevice corrosion of heat exchange equipment in such media. Many studies have been devoted to determining and predicting the resistance of heat exchangers to pitting corrosion in recycled water [4-8]. In particular, the authors of [5] modeled the corrosion behavior of austenitic steels in chloride-containing media during the operation of plate-like heat exchangers, papers [6,7] are devoted to establishing the patterns and mechanisms of pitting corrosion of heat exchangers during its operation in chloride-containing media, and [9] to the influence of specific magnetic susceptibility on the corrosion losses of steel from pitting. And in [10, 11], the authors investigated the relationship between corrosion losses of the 06KhN28MDT alloy in model reservoir waters of oil and gas fields in Kazakhstan, depending on its chemical composition and structure components. Academician L.I. Rosenfeld determined the similarity of pitting and crevice corrosion patterns [12], but the latter has some characteristic features. That is, in the paper investigated the patterns and mechanisms of crevice corrosion of plate-like heat exchangers made of 06KhN28MDT alloy in the recycled water of enterprises, using the analysis of the developed mathematical models that establish the relationship between the alloy's ultimate electrochemical performance and its chemical composition within the standard and the structure components.

## 2. Materials and methods of research

Five industrial melts of the 06KhN28MDT alloy, which is used to produce heat exchanger plates with a thickness of 0.3- 1.2 mm, were studied. The chemical composition of the alloy and the components of its structure (table 1) have been determined in [8].

**Table 1 –** Real sample based on sample research results

| № swimming trunks | x1 | x2 | x3 | x4 | x5 | x6 | x7 | x8 | x9 | x10 | x11 | Ecor, V | Ecrev-V | Err, V | ДЕ, V |
|---|---|---|---|---|---|---|---|---|---|---|---|---|---|---|---|
| 1 | 0,05 | 0,32 | 0,6 | 24,31 | 27,39 | 0,79 | 2,9 | 2,75 | 0,1711 | 0,0091 | 11 | -0,4 | 1,1 | 0,8 | 1,2 |
| 2 | 0,067 | 0,46 | 0,57 | 22,68 | 27,65 | 0,59 | 2,78 | 2,68 | 0,1427 | 0,0036 | 24 | -0,43 | 0,58 | 0,5 | 0,93 |
| 3 | 0,068 | 0,54 | 0,55 | 21,84 | 27,45 | 0,55 | 2,55 | 2,6 | 0,1918 | 0,0043 | 29 | -0,42 | 0,58 | 0,22 | 0,64 |
| 4 | 0,048 | 0,57 | 0,62 | 22,67 | 27,73 | 0,67 | 2,56 | 2,53 | 0,1692 | 0,0043 | 31 | -0,4 | 1,1 | 0,55 | 0,95 |
| 5 | 0,05 | 0,31 | 0,57 | 23,46 | 27,51 | 0,89 | 2,51 | 2,78 | 0,0931 | 0,0036 | 15 | -0,38 | 1,13 | 0,6 | 0,98 |
| min | 0.048 | 0.31 | 0.55 | 21,84 | 27,39 | 0,55 | 2,51 | 2,53 | 0,0931 | 0,0036 | 11 | -0.5 | 0.4 | 0.1 | |
| max | 0.068 | 0.57 | 0.62 | 24,31 | 27,73 | 0,89 | 2,9 | 2,78 | 0,1918 | 0,0091 | 29 | -0.1 | 1.2 | 0.7 | |
| multiplicity | 0.001 | 0.01 | 0.01 | 0,01 | 0,01 | 0,01 | 0,01 | 0,01 | 0,0001 | 0,0001 | 1 | 0,01 | 0,01 | 0,01 | 0,01 |

where: $x_1$ – C, carbon content in steel, wt. %;
$x_2$ – Mn, manganese content in steel, wt. %;
$x_3$ – Si, silicon content in steel, wt. %;
$x_4$ – Cr, chromium content in steel, wt. %;
$x_5$ – Ni, nickel content in steel, wt. %;
$x_6$ – Ti, titanium content in steel, wt. %;
$x_7$ – Mo, molybdenum content in steel, wt. %;
$x_8$ – Cu, copper content in steel, wt. %;
$x_9$ – volume of nitrides, %. V = 0.0931 – 0.1918, vol. %;
$x_{10}$ – Volume of sulfides, %. V = 0.0036 – 0.0091, vol. %;
$x_{11}$ – $d_g$, μm, mean austenite grain diameter: d = 11-31μm;
$E_{cor}$ – free corrosion potential, V;
$E_{crev}$ – activation potential, V;
$E_{rep}$ – repassivation potential, V;
ΔE is the criterion defined as $E_{rep} – E_{cor}$, V.

The variance of deviations in the content of the alloy components is: for carbon ± 0.002, silicon ± 0.004, manganese ± 0.01, chromium ± 0.02, nickel ± 0.03, molybdenum ± 0.02, copper ± 0.02, titanium ± 0.02, phosphorus ± 0.02, sulfur ± 0.003 wt.%.

Polished samples 30x20x10mm with a hole 06 mm were collected in bags. A gap of 0.3 mm was set between the sample and the counterbody (the size of the gap between adjacent plates of plate-like heat exchangers, which was fixed with fluoroplastic washers). Electrochemical studies were performed on a P5848 potentiostat. The setup consisted of test samples made of 06KhN28MDT alloy with a thickness of 1 mm, a counter body made of the same alloy, a saturated chlorosilver comparison electrode, a Lugin capillary, an auxiliary electrode made of platinum, a fluoroplastic bolt and nut, cathode voltmeter (input resistance not less than 5 mV, measuring range not less than ±1V, counting accuracy not less than 5 mV), microammeter (current measuring range from 0.1 MA to 10 MA) and thermostat for maintaining the temperature in the range of ±1°C (Fig. 1).

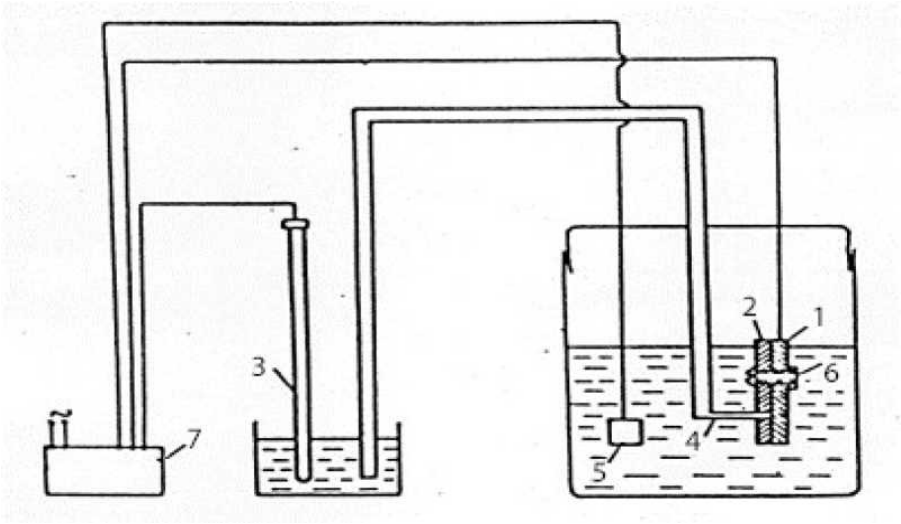



**Figure 1** – Schematic diagram of the setup for electrochemical studies of 06KhN28MDT alloy in a chloride-containing solution of 3% NaCl: 1 – sample; 2 – counterbody; 3 – comparison electrode; 4 – Lugin capillary; 5 – auxiliary electrode; 6 – fluoroplastic bolt and nut; 7 – potentiostat P 5848.

The sample was immersed for 30 minutes in the solution, which was repeatedly passed through a Lugin capillary and a gap. Prior to polarization, the samples were kept in the solution for 10 minutes until the steady-state potential was established and anodically polarized at a rate of 1.8 V/hour. The forward and reverse potentiodynamic curves were taken until the current density (30 mA/cm$^2$), and the reverse curves until the minimum cathodic currents (0.005 mA/cm$^2$) were recorded. The deviation of the activation potentials $E_{crev}$ and repassivation potentials $E_{rep}$ in the crevice did not exceed ±0.01 V. The crevice corrosion resistance of 06KhN28MDT alloy was evaluated by ΔE, a criterion determined by the difference between the repassivation potential $E_{rep}$ and the free corrosion potential $E_{cor}$. The alloy was considered to be resistant to crevice corrosion if ΔE>0.05V [13]. The alloy's $E_{crev}$ potential in the crevice was used as an additional criterion for assessing the alloy's crevice corrosion resistance in model recycled water. The electrochemical parameters of the 06KhN28MDT alloy are shown in Table 1. The generated variable ($x_1$...$x_{11}$) and output factors ($E_{cor}$, $E_{rep}$, $E_{crev}$, and ΔE) are shown in Table 2.

Multivariate linear regressions were used as the basis for constructing mathematical models [14]. The first-order multivariate linear regression equation is as follows:

$$y^S=\sum_{j=1}^{N} B_j x_j^s, y = 1, 2, \dots, S, \quad (1)$$

where $y^S$ is the value of the initial characteristic for the s-th observation of the sample

($E_{cor}$, $E_{rep}$, $E_{crev}$), °C,

Bj is the weight of the j-th feature,

S is the number of sample instances.

The quality of the model was assessed by the sum of squared instantaneous mistakes (2):

$$E = \sum_{s=1}^{S} (y^s - y^{s*})^2 , \quad (2)$$

where: $y^s$ is the actual value of the output feature for the s-th observation of the training sample;

$y^{s*}$ is the estimated value of the output feature for the s-th observation of the training sample.

**Table 2** – Generated sample

| s | x1 | x2 | x3 | x4 | x5 | x6 | x7 | x8 | x9 | x10 | x11 | $E_{cor}$, V | $E_{crev}$, V | $E_{rp}$, V |
|---|---|---|---|---|---|---|---|---|---|---|---|---|---|---|
| 1 | 0.0500 | 0.3200 | 0.6000 | 24.3100 | 27.3900 | 0.7900 | 2.9000 | 2.7500 | 0.1711 | 0.0091 | 11.0000 | -0.4000 | 1.1000 | 0.8000 |
| 2 | 0.0670 | 0.4600 | 0.5700 | 22.6800 | 27.6500 | 0.5900 | 2.7800 | 2.6800 | 0.1427 | 0.0036 | 24.0000 | -0.4300 | 0.5800 | 0.5000 |
| 3 | 0.0680 | 0.5400 | 0.5500 | 21.8400 | 27.4500 | 0.5500 | 2.5500 | 2.6000 | 0.1918 | 0.0043 | 29.0000 | -0.4200 | 0.5800 | 0.2200 |
| 4 | 0.0480 | 0.5700 | 0.6200 | 22.6700 | 27.7300 | 0.6700 | 2.5600 | 2.5300 | 0.1692 | 0.0043 | 31.0000 | -0.4000 | 1.1000 | 0.5500 |
| 5 | 0.0500 | 0.3100 | 0.5700 | 23.4600 | 27.5100 | 0.8900 | 2.5100 | 2.7800 | 0.0931 | 0.0036 | 15.0000 | -0.3800 | 1.1300 | 0.6000 |
| 6 | 0.0570 | 0.3100 | 0.5900 | 23.3300 | 27.6100 | 0.6700 | 2.7000 | 2.7100 | 0.1807 | 0.0039 | 13.0000 | -0.4100 | 0.6600 | 0.3300 |
| 7 | 0.0610 | 0.5100 | 0.6200 | 22.1500 | 27.5100 | 0.7800 | 2.6600 | 2.7500 | 0.1219 | 0.0043 | 23.0000 | -0.4300 | 0.3900 | 0.3200 |
| 8 | 0.0520 | 0.5400 | 0.6000 | 22.8800 | 27.3900 | 0.6000 | 2.6200 | 2.7500 | 0.1524 | 0.0054 | 16.0000 | -0.4100 | 0.6800 | 0.3600 |
| 9 | 0.0570 | 0.5400 | 0.6100 | 23.0900 | 27.6000 | 0.7900 | 2.5200 | 2.6700 | 0.0977 | 0.0059 | 19.0000 | -0.3900 | 1.0000 | 0.5400 |
| 10 | 0.0480 | 0.3300 | 0.6100 | 23.1600 | 27.5100 | 0.6700 | 2.5700 | 2.5700 | 0.1277 | 0.0054 | 25.0000 | -0.3800 | 1.2700 | 0.7300 |
| … | | | | | | | | | | | | | | |
| 40 | 0.0550 | 0.4300 | 0.5800 | 23.5200 | 27.5800 | 0.7700 | 2.7000 | 2.6300 | 0.1402 | 0.0040 | 18.0000 | -0.4000 | 1.0300 | 0.6500 |
| 41 | 0.0670 | 0.5100 | 0.6000 | 23.7300 | 27.6500 | 0.8400 | 2.8100 | 2.7700 | 0.1041 | 0.0058 | 20.0000 | -0.4000 | 1.1000 | 0.8700 |
| 42 | 0.0530 | 0.3200 | 0.6200 | 23.6300 | 27.4400 | 0.6000 | 2.7800 | 2.6300 | 0.1006 | 0.0059 | 14.0000 | -0.4000 | 0.9000 | 0.7300 |
| 43 | 0.0640 | 0.5500 | 0.5500 | 23.4500 | 27.6200 | 0.6400 | 2.8400 | 2.6000 | 0.0958 | 0.0041 | 25.0000 | -0.4100 | 1.1000 | 0.9500 |
| 44 | 0.0620 | 0.5100 | 0.5900 | 23.8800 | 27.4000 | 0.6900 | 2.6100 | 2.6500 | 0.1800 | 0.0051 | 22.0000 | -0.3700 | 1.6300 | 0.8500 |
| 45 | 0.0490 | 0.3500 | 0.6100 | 22.3200 | 27.6700 | 0.6600 | 2.7700 | 2.5400 | 0.1656 | 0.0063 | 28.0000 | -0.4400 | 0.5000 | 0.4200 |
| 46 | 0.0540 | 0.4100 | 0.5600 | 24.2200 | 27.5400 | 0.5800 | 2.7900 | 2.6600 | 0.1255 | 0.0077 | 26.0000 | -0.3700 | 1.7600 | 1.2200 |
| 47 | 0.0530 | 0.4500 | 0.5800 | 22.2300 | 27.5900 | 0.8700 | 2.5500 | 2.7500 | 0.1474 | 0.0060 | 14.0000 | -0.4300 | 0.1500 | 0.0300 |
| 48 | 0.0530 | 0.4300 | 0.5900 | 22.7200 | 27.6500 | 0.8500 | 2.8000 | 2.6300 | 0.1527 | 0.0071 | 13.0000 | -0.4500 | 0.1100 | 0.1800 |
| 49 | 0.0580 | 0.3900 | 0.5900 | 24.1700 | 27.5400 | 0.5600 | 2.8700 | 2.7600 | 0.1285 | 0.0050 | 25.0000 | -0.3900 | 1.5900 | 1.1900 |
| 50 | 0.0580 | 0.4600 | 0.6000 | 22.0700 | 27.6900 | 0.8700 | 2.5500 | 2.7400 | 0.1829 | 0.0037 | 20.0000 | -0.4300 | 0.2400 | -0.0200 |

### 3. Research results and discussion

A multifunctional mathematical model (3) was developed using Equation (1) and the generated sample of events (Table 2). It establishes the relationship between the repassivation potential of the 06KhN28MDT alloy ($E_{rep}$ ) and its chemical composition ($x_1$ ... $x_9$ ) and structure components ($x_9$ ... x ):

$$E_{rep} = -0.8136x_1 - 0.031x_2 + 0.0763x_3 + 0.3664x_4 - 0.3319x_5 - 0.0991x_6 + 0.2813x_7 + 0.1055x_8 - 1.8513x_9 + 1.3326x_{10} + 0.027x_{11}, \quad (3)$$

The quality of the constructed mathematical model (3) was evaluated using Formula 2, in particular, SSE is 0.0915 and MSE is 0.0018V. Thus, it adequately describes the relationship between the repassivation potential of the 06KhN28MDT alloy and its chemical composition and structure components and can be used to assess and predict the resistance of heat exchangers to crevice corrosion.

According to the results of the analysis of the constructed mathematical model (3), it can be noted that the repassivation potential $E_{rep}$ of the studied alloy shifts in a positive direction with an increase in the content of silicon, chromium, molybdenum, copper, the volume of titanium sulfides, the mean grain diameter of austenite, and a decrease in the content of carbon, manganese, nickel, titanium, and the volume of titanium nitrides. It should be noted that the variables ($x_1$ ... $x_{11}$) of the mathematical model (3) have a different effect on the potential $E_{rep}$ of the alloy in the gap. In particular, according to model (3) and data (Table 1), it was found that it shifts to the positive side by 0.005; 0.905; 0.11; 0.03; 0.007; and 0.54V with an increase in the content of Si, Cr, Mo, Cu, the volume of titanium sulfides, and the mean austenite grain diameter in the intervals given in (Table 1). At the same time, it was found that the potential $E_{rep}$ of the 06KhN28MDT alloy shifts by 0.016; 0.0002; 0.113; 0.034; 0.046V in the negative direction with an increase in the content of C, Mn, Ni, Ti, and the volume of titanium nitrides in the intervals given in Table 1. It should be noted that C, Mn, Si, and the volume of titanium sulfides practically do not affect the repassivation potential $E_{rep}$ of the studied alloy in the gap, since it can change within the measurement mistake (±0.01V) when these parameters change in the mentioned intervals (Table 1). Thus, it can be noted that the intensity of the influence of the parameters of the 06KhN28MDT alloy on its potential $E_{rep}$ in the gap increases in the following order: Cu; Ti; volume of titanium nitrides ($V_N$); Mo; mean austenite grain diameter ($d_g$); Cr. At the same time, it should be noted that Mo, Cr, and the mean austenite grain diameter of the alloy have an order of magnitude greater effect on the potential $E_{rep}$ than Cu, Ti, and the volume of titanium nitrides. This is consistent with the data from [15-19] on the ability of Cr and Mo to form mixed oxide films on the surface of stainless steels and alloys that actively counteract its local activation by chloride ions. Rosenfeld I.L. [12] and Todt F. [15] believed that Cr and Mo are the most effective alloying elements that increase the corrosion resistance of steels in chloride-containing media. It is believed [20] that Mo increases the resistance of passive films to "breakdown" in chloride-containing media, improves passivation characteristics, and reduces the rate of metal dissolution in pitting [21]. Papers [22-24] found that in model recycled waters where plate heat exchangers are operated, the critical pitting temperature of AISI321 and AISI304 steels increases with an increase in their chromium content, while the other chemical elements in its composition do not affect it. Paper [7] found that the pitting resistance of the 06KhN28MDT alloy depends on the parameters of the chloride-containing media, its structure components, and the content of chromium, and the effect of Mo on the critical temperature of its pitting was not found. However, it is believed in [16] that Mo improves the protective properties of passive films in neutral solutions due to the adsorption of $MoO_4^{-2}$ ions on them, which are formed as a result of the oxidative dissolution of molybdenum from steel and displacement chloride ions from its surface. In our opinion, the mechanisms of local corrosion of the 06KhN28MDT alloy described in [22-24] are inherent in low- mineralized chloride-containing media, such as recycled water from enterprises. Indeed, under such conditions, the number of metastable pitting on the alloy surface decreases, which can contribute to the transformation of the remaining ones that have not been repassivated into stable ones due to the redistribution of the anode current density. Thus, we believe that under such conditions, Mo does not increase the resistance of the oxide film on the surface of the 06KhN28MDT alloy to the activating effect of chloride ions, but it promotes the repassivation of localized corrosion damage on its surface in the crevice, shifting the

repassivation potential to the positive side by 0.11V, as mentioned above. This increases the ΔE- criterion of the alloy, which indicates its resistance to crevice corrosion. However, it should be noted that chromium has an 8.2-fold stronger effect on the repassivation potential of the alloy under study than Mo. It is known [2, 3] that localized corrosion damage on the surface of steels and alloys originates and develops in the vicinity of inclusions. In addition, stable pitting occurs and develops in the vicinity of inclusions of a certain nature [26-28] and size [29], which are in contact with the boundaries of austenite grains [2, 3]. Therefore, according to dependence (3), the potential $E_{rep}$ of the 06KhN28MDT alloy shifts to the positive side with an increase in the mean diameter of the austenite grain and a decrease in the volume of titanium nitride inclusions in the vicinity of which pitting in the gap mainly originated. After all, the bigger $d_g$ and the smaller the size of these inclusions, the less likely they are to intersect.

A multidimensional mathematical model (4) was constructed that establishes the relationship between the free corrosion potential $E_{cor}$ of the 06KhN28MDT alloy in the crevice and its chemical composition ($x_1$ ... $x_8$) and structure components ($x_9$ ... $x_{11}$).

$$E_{cor} = 0.285x1 - 0.0032x2 + 0.0304x3 + 0.0325x4 - 0.0324x5 - 0.0026x6 - 0.1131x7 + 0.0002x_8 - 0.0301x_9 - 0.1464x_{10} + 0.0013x_{11}; \quad (4)$$

The quality of the mathematical model (4) was evaluated using formula (2), in particular, SSE=0.0028282 and MSE=0.0000057B. Thus, it adequately establishes the relationship between the potential $E_{cor}$ of the studied alloy and its chemical composition and structure components. According to the results of the analysis of the mathematical model (4), it can be noted that the free corrosion potential $E_{cor}$ of this alloy shifts to the positive side with an increase in the content of C($x_1$); Si($x_3$); Cr($x_4$); Cu($x_8$) and the mean austenite grain diameter ($x_{11}$) and a decrease in Mn($x_2$), Ni($x_5$); Ti($x_6$); Mo($x_7$) and the volume of nitrides ($x_9$) and titanium sulfides ($x_{10}$). However, the intensity of the influence of these factors on the potential $E_{cor}$ of the alloy under study is very different. In particular, it was found that it shifts to the positive side by 0.0057, 0.021, 0.0803, 0.00005, and 0.026 V with an increase in the content of C, Si, Cr, Cu, and the mean diameter of the austenite grain in the intervals indicated in Table 1. In particular, this potential ($E_{cor}$) of the alloy shifts to the negative side by 0.0008, 0.011, 0.0009, 0.044, 0.003, 0.0008 V with an increase in the content of Mn; Ni; Ti and the volume of titanium nitrides and sulfides in the intervals indicated in (Table 1). It was found that the intensity of the influence of the chemical composition and the structure components of the studied alloy on its free corrosion potential ($E_{cor}$) increases in the following order: $d_g$, Mo, Cr. It can be noted that these alloying elements and the mean austenite grain diameter have the greatest effect on the potentials $E_{cor}$ and $E_{rep}$ of the 06KhN28MDT alloy in the gap. At the same time, the influence of Cr, Mo, and $d_g$ on the alloy repassivation potential in the gap $E_{rep}$ is 11.3, 2.5, and 20.8 times, respectively, greater than on the free corrosion potential $E_{cor}$. It should be noted that ΔE, a criterion by which the resistance of steels and alloys to crevice corrosion is evaluated [13], of the 06KhN28MDT alloy increases by 0.15 V with an increase in its Mo content (Table 1). Thus, it turns out that Mo effectively increases the resistance of 06KhN28MDT alloy to crevice corrosion in model recycled water, contributing to a shift in the repassivation potential of the alloy ($E_{rep}$) to the positive side and free corrosion $E_{cor}$ to the negative side. At the same time, the alloying of the studied alloy with Cr has a more effective effect on its resistance to crevice corrosion in a chloride-containing medium, since its ΔE criterion increases by 0.825 V with an increase in its Cr content from 21.84 to 24.34 wt.% (Table 1).

Summarizing the above, it can be noted that the 06KhN28MDT alloy is resistant to crevice corrosion in model recycled water. It is due to high content of Cr and Mo.

The activation potential of the 06KhN28MDT alloy in the gap ($E_{crev}$), according to [13], is proposed as an additional criterion for assessing its resistance to crevice corrosion in model recycled water. For this purpose, a multidimensional mathematical model (5) was constructed, which establishes the relationship between this potential ($E_{crev}$) of the alloy under study and its chemical composition ($x_1$ ... $x_9$) and structure components ($x_9$ ... $x_{11}$) (Table 1).

$$\Delta E_{crev} = -4.1448x_1 + 0.0198x_2 - 1.0528x_3 + 0.5981x_4 - 0.3620x_5 - 0.4513x_6 - 0.9145x_7 + 0.1009x_8 - 1.3369x_9 - 9.811x_{10} + 0.0325x_{11}; \quad (5)$$

The quality of the constructed mathematical model (5) was estimated by formula (2), in particular, SSE = 0.6497 and MSE = 0.0130 V. Consequently,

this model adequately establishes the relationship between the potential $E_{crev}$ of the 06KhN28MDT alloy in the gap and its chemical composition and structural components. According to the results of the analysis mathematical model (5), it was found that the potential $E_{crev}$ of the studied alloy shifts to the positive side with an increase in the content of Mn($x_2$); Cr($x_4$); Cu($x_8$) and the mean austenite grain diameter ($x_{11}$) and decreasing – C($x_1$); Si($x_3$); Ni($x_5$); Ti($x_6$); Mo($x_7$), the volume of nitrides($x_9$) and titanium sulfides ($x_{10}$). It should be noted that they affect this potential with different intensities, since it shifts to the positive side by 0.108, 1.477, 0.025, and 0.65 V with an increase in the content of Mn($x_2$); Cr($x_4$); Cu($x_8$) and the mean austenite grain diameter ($x_{11}$), respectively, in the intervals indicated (in Table 1). At the same time, it was found that the $E_{crev}$ potential shifts to the negative side by 0.082, 0.074, 0.123, 0.153, 0.357, 0.132, and 0.054 V with an increase in the content of C($x_1$) in the alloy; Si($x_3$); Ni($x_5$); Ti($x_6$); Mo($x_7$), the volume of nitrides ($x_9$) and titanium sulfides ($x_{10}$), respectively, in the intervals indicated in (Table1). It was found that the intensity of the influence of the chemical composition of the 06KhN28MDT alloy ($x_1$ ... $x_8$) and its structure components ($x_9$ ... $x_{11}$) on the potential $E_{crev}$ increases in the following order: Cu content ($x_6$), volume of titanium sulfides ($x_{10}$); Si content ($x_3$); C ($x_1$); Mn ($x_2$); Ni ($x_5$); volume of titanium nitrides ($x_9$); Ti content ($x_6$); Mo ($x_7$), mean austenite grain diameter ($x_{11}$), Cr content. It should be noted that Cr, Mo, and the mean austenite grain diameter have the greatest effect on the repassivation potential ($E_{rep}$), free corrosion ($E_{cor}$), and activation of the 06KhN28MDT alloy in the crevice ($E_{crev}$). At the same time, Cr has a 1.6 and 18.5 times more intense effect on the $E_{crev}$ potential than $E_{rep}$ and $E_{cor}$, respectively. At the same time, it should be noted that the mean austenite grain diameter has a 1.2 and 25 times more intense effect on $E_{crev}$ than $E_{rep}$ and $E_{cor}$, respectively. Taking into account the above, it can be noted that the probability of local corrosion damage in the vicinity of titanium nitrides at the intersection with the boundaries of austenite grains has almost the same effect on the $E_{crev}$ and $E_{rep}$ potentials of the 06KhN28MDT alloy in a chloride-containing media. This is due to the fact that the resistance of the oxide film to activation by chloride ions in these areas of the alloy and the influence of its structure imperfections on the repassivation of local corrosion damage are equivalent factors. But it should be noted that the effect of Mo on the potential repassivation $E_{rep}$ of the alloy is twice as high as Cr, which is consistent with the data from [21, 22].

It was found that the activation potential $E_{crev}$ of the 06KhN28MDT alloy in the crevice noticeably shifts to the negative side with an increase in the content of C (-0.008 V), Si (-0.07 V), Mo (-0.357 V), and Ti (-0.451 V) in the interval indicated in (Table 1). This is most likely due to the precipitation of Mo and Ti carbides in the vicinity of titanium nitrides, where pittings were born. This is consistent with the data of [29], which states that an increase in the Ti content in stainless steels reduces the potential region corresponding to the passive state. Under such conditions, an increase in current density was recorded on the anode polarization curves. This is attributed [30] to the ability of carbides, especially Ti, Mo, and Nb, to accelerate the ionization of hydrogen ions on them, which helps to accelerate anodic processes associated with the ionization of metals in localized corrosion damage. Taking into account the data from [31], the facilitated activation of the 06KhN28MDT alloy in the gap is most likely due to the promotion of Si to precipitate carbides from the solid solution of the alloy austenite. A noticeable shift in the potential $E_{crev}$ of the studied alloy to the negative side (-0.13V) with an increase in titanium nitride inclusions in the interval indicated in (Table 1) is most likely due to the precipitation of Mo and Ti carbides in their vicinity. After all, it shifts to the negative side by 0.082 V with an increase in the C content in the alloy, which created carbides with Mo and Ti. Obviously, the effect of Ti and especially Mo dissolved in a solid solution of austenite on the potential $E_{crev}$ is stronger than that of its carbides. This, taking into account the data in [2], may be due to the acceleration of the solid-phase diffusion of Fe atoms to the surface of local corrosion damage on the surface of the 06KhN28MDT alloy in the gap. It is likely that the shift of the potential $E_{crev}$ of this alloy in the negative direction (-0.12 V) with an increase in its Ni content is also associated with the acceleration of the solid-phase diffusion of Fe atoms to the surfaces of local corrosion damage, which contributed to their growth. The analysis of the mathematical model (5) also shows that the effect of titanium sulfides on the potential $E_{crev}$ of the alloy in the gap is close to Ti and Mo carbides in the vicinity of nitrides titanium, but half as much as these nitrides themselves. This is due to the fact that Mo and Ti sulfides are generally insoluble in acidic media [32], which are formed in the gap and localized corrosion

damage due to hydrogenation of alloy corrosion products.

Summarizing the above, it can be noted that the potential $E_{crev}$ of the 06KhN28MDT alloy, unlike $E_{cor}$ and $E_{rep}$, depends on many chemical composition and structure elements. It shifts to the positive side with an increase in the content of Mn, Cr, Cu, $d_g$ and a decrease in C, Si, Ni, Ti, Mo, and the volume of titanium sulfides and nitrides. This dependence is due to the improvement of the protective properties of chromium-containing oxide films on the surface of the studied alloy and reducing the likelihood of local corrosion damage pitting carbonitrides titanium carbonitrides, where the overvoltage of hydrogen ionization in acidic media formed in the crevice is reduced. It was found that the potential $E_{cor}$ of the studied alloy shifts to the positive side with an increase in the content of Si, Cr, Mo, Cu, $V_S$, $d_g$ and a decrease in C, Mn, Ni, Ti and $V_N$, but the influence of the parameters C, Mn, Si and $V_S$ is very low. It has been established that the potential $E_{rep}$ of the 06KhN28MDT alloy shifts to the positive side with an increase in the content of C, Cr, Cu, $d_g$ and a decrease in Mn, Ni, Ti, Mo, $V_N$, $V_S$. It has been found that Cr, Mo and $d_g$ have the greatest influence on the potentials $E_{crev}$, $E_{rep}$ and $E_{cor}$. At the same time, the higher they are, the higher the resistance of the alloy to crevice corrosion in model recycled water. The constructed mathematical models can be used for to evaluate i prediction resistance of heat exchangers made of 06KhN28MDT alloy to crevice corrosion during their operation in recycled water of enterprises.

## 4. Conclusion

Multifactorial mathematical models have been built that establish the relationship between the activation potentials $E_{crev}$, repassivation $E_{rep}$, and free corrosion $E_{cor}$ of the 06KhN28MDT alloy depending on its chemical composition and structure components in model recycled water. It has been found that the potential $E_{crev}$ of the alloy shifts to the positive side with an increase in the content of Mn, Cr, Cu, $d_g$ and a decrease in C, Si, Ni, Ti, Mo, $V_S$, $V_N$. It was found that the potential $E_{cor}$ potential of the alloy shifts to the positive side with an increase in the content of Si, Cr, Mo, Cu, $V_S$, $d_g$ and a decrease in C, Mn, Ni, Ti, and $V_N$, but the influence of C, Mn, Si, and $V_S$ is very low. It has been shown that the potential $E_{rep}$ of the alloy shifts to the positive side with an increase in the content of C, Si, Cr, Cu, $d_g$ and a decrease in Mn, Ni, Ti, Mo, $V_N$ and $V_S$.

At the same time, it was found that Cr is 1.6 and 1.8 times and $d_g$ is 1.2 and 25 times more intensively affected by the $E_{crev}$ potential than by $E_{rep}$ and $E_{cor}$, respectively. However, the effect of Mo on the $E_{rep}$ potential is twice as large as that of Cr. It is shown that Cr, Mo and $d_g$ have the greatest influence on the potentials $E_{crev}$, $E_{rep}$, and $E_{cor}$. At the same time, it was found that the influence of Cr, Mo, and $d_g$ on $E_{crev}$ is 1.6 and 143.5; Mo is 3.2 and 8.1; and $d_g$ is 1.2 and 2.5 times greater than on $E_{rep}$ and $E_{cor}$, respectively. It is shown that the resistance of the 06KhN28MDT alloy to crevice corrosion increases with an increase in the content of Cr, Mo, and the mean diameter of the austenite grain.

**References**

1. Vorob'jova G. Ja. Korrozionnaja stojkost' materialov v agressivnyh sredah himicheskih proizvodstv. Himija. Moscow, Russia. – 1985, 815 p. (In Russian).
2. Narivs'kyi O.E. Corrosion fracture of plate-like heat exchanger // Materials Science. – 2015. – Vol. 1 (41). – P. 122-128. https://doi.org/10.1007/s11003-005-0140-8
3. Narivs'kyi O.E. Micromechanism of corrosion fracture of the plates of heat exchangers // Materials Science. – 2017. – Vol.43(1). – P. 124-132. https://doi.org/10.1007/s11003-007-0014-3.
4. Narivskyi O.E., Subbotin S.O., at al. Modeling of pitting of heat exchangers made of 18/10 type steel in circulating waters // Materials Science. – 2023. – Vol. 58(5). – P.1-7. https://doi.org/10.1007/s11003-023-00725-y .
5. Narivskyi O.E., Subbotin S.O., at al. Corrosion behaviour of austenitic steels in chloride-containing media during the operation of plate-like heat exchangers // Physical Sciences and Technology. – 2023. -Vol. 10(3-4). – P. 48-56. https://doi.org/10.26577/phst.2023.v10.i2.06
6. Narivskyi O.E., Subbotin S.O., at al. Mechanism of pitting corrosion of austenitic steels of heat exchangers in circulating waters and its prediction // Materials Science. – 2024. – Vol. 59 (5). – P. 275-282. http://dx.doi.org/10.1007/s11003-024-00773-y
7. Dzhus A. V., Narivskyi O. E., Subbotin S. A., at al. Influence of components of 06ХН28МДТ alloy (analogue of AISI904L steel) and parameters of model chloride-containing recycled water of enterprises on its pitting resistance // Metallophysics and Advanced Technologies. – 2024. – Vol. 46 (4). – P. 371-383.
8. Narivs'kyi O.E., Belikov S.B. Pitting resistance of 06KhN28MDT alloy in chloride-containing media. Materials Science. – 2018. – Vol. 44 (4). – P. 573-580. https://doi.org/10.1007/s11003-009-9107-5

9. Narivs'kyi O.E., Snizhnoi G.V., et al. Effect of specific magnetic susceptibility of AISI 304 and 08Kh18N10 steels on their limiting potentials in chloride-containing environments // Materials Science. – 2024. – Vol. 59 (3). – P. 649-657. https://doi.org/10.1007/s11003-024-00824-4

10. Narivskyi A., Yar-Mukhamedova G., Temirgaliyeva E., Mukhtarova M., Yar-Mukhamedov Y. Corrosion losses of alloy 06KhN28MDT in choride-containing commercial waters // International Multidisciplinary Scientific GeoConference Surveying Geology and Mining Ecology Management. SGEM – 2016. – Vol.1. – P.63-70.

11. Narivskiy A., Atchibayev R., Muradov A., Mukashev K., Yar-Mukhamedov Y. Investigation of electrochemical properties in chloride-containing commercial waters // International Multidisciplinary Scientific GeoConference Surveying Geology and Mining Ecology Management, SGEM – 2018. Vol. 18(6.1). – P. 267–274. https://doi.org/10.5593/sgem2018/6.1/S24.036

12. Rosenfeld L.I. Corrosion and protection of metals. M.: Metallurgy – 1970. – P. 448. (In Russian).

13. GTM-26-01-88 Guiding technical material. Methods of corrosion tests of metallic materials. Basic requirements. Evaluation of results. Moscow: VNIIkhimmash – 1989. P.22 (In Russian).

14. Freedman D.A. Statistical models: theory and practice. Cambridge University Press – 2009. – P.412. https://doi.org/10.1017/CBO9780511815867

15. Todt F. Corrosion and protection against corrosion of metals. M.: Chemistry – 1996. – P. 848. (In Russian).

16. Pyschin L.M., Balvas N.I., Tsikman A.I. Effect of molybdenum alloying on pitting of stainless steels in vinegar solutions containing iodine. Metal Protection – 1982. – №. 12. – P. 910-913.

17. Kolotyrkin, Ya.M., Freiman L.I., Reformatskaya I.I., Panshin E.A. On the mechanism of increasing pitting resistance of stainless steels by molybdenum addition // Metal Protection. – 1994. -Vol. 30. – № 5. – P. 453 – 462.

18. Nenastina T., Sakhnenko M., Oskak S., Yar-Mukhamedova G., Zellele D., Mussabek G., Imanbayeva A. Study of complexation patterns in the system $Ni^{2+}$, $MoO_4^{2-}$, $P_2O_7^{4-}$, $Cit^{3-}$ for the development of poly-ligand electrolytes // Eurasian Chem.-Technol. J. -2024. -Vol. 26. -P. 155–160. https://doi.org/10.18321/ectj1638

19. Markhabayeva A.A., Anarova A. S., Abdullin Kh. A, Kalkozova Zh. K., Tulegenova A.T., Nuraje N. A hybrid supercapacitor from nickel cobalt sulfide and activated carbon for energy storage application // Physica Status Solidi – Rapid Research Letters. – 2024. – Vol. 18. – P. 2300211. https://doi.org/10.1002/pssr.202300211

20. Szklarska-Smialowska Z. Pitting corrosion of metals / Z. Szklarska-Smialowska. National Association of Corrosion Engineers, Houston – 1986. – P. 147 – 170.

21. Hazza M.I., El-Dahchan M. The effect of molybdenium on the localized corrosion behaviour of some steel alloy // Desalination. – 1994. – Vol. 95. – № 2. – P. 199 – 209. https://doi.org/10.1016/0011-9164(94)00014-X

22. Narivskyi O.E., Belikov S.B., Subbotin S.A., Pulina T.V. Influence of chloride-containing media on the pitting resistance of AISI 321 steel // Materials Science. – 2021. – Vol.57(2) – P. 291-297. https://doi.org/10.1007/s11003-021-00544-z

23. Narivs'kyi O., Atchibayev R., Kemelzhanova A., Yar-Mukhamedova G., Snizhnoi G., Subbotin S., Beisebayeva A. Mathematical modeling of the corrosion behavior of austenitic steels in chloride-containing media during the operation of plate-like heat exchangers // Eurasian Chemico-Technological Journal. – 2022. – Vol. 24(4). – P. 295-301. https://doi.org/10.18321/ectj1473

24. Narivskyi O.E., Subbotin S.A., at al. Assessment and prediction of the pitting resistance of plate-like heat exchangers made of AISI304 steel and operating in circulating waters // Materials Science. – 2022. -Vol.58. – P. 41–46. https://doi.org/10.1007/s11003-022-00628-4

25. Narivs'kyi O.E. Corrosion fracture of plate-type heat exchangers. Fiz.-Khim. Mekh. Mater – 2005. – Vol.41. – №1. – P. 104-108.

26. Mishchenko V. G., Snizhnoi G. V., Narivs'kyy O. Eh. Magnetometric investigations of corrosion behaviour of AISI 304 steel in chloride-containing environment // Metallofizika i noveishie tekhnologii. – 2011. – Vol. 33. – №. 6. – P. 769–774. (In Russian).

27. Narivs'kyi O.E. The influence of heterogeneity steel AISI321 on its pitting resistance in chloride – containing media // Materials Science. – 2007. – Vol.2(43). – P. 256-264. https://doi.org/10.1007/s11003-007-0029-9

28. Mussabek G.K., Yermukhamed D., Dikhanbayev K.K., Mathur S., Sivakov V.A. Self-organization growth of Ge-nanocolums //Materials Research Express – 2017. – Vol. 4. – P. 035003. https://doi.org/10.1088/2053-1591/aa5ed6

29. Freiman L.I., Reformatskaya I.I., Markova T.P. Relationship of influence of alloying elements and sulfide inclusions on passivability and pitting resistance of stainless steels // Metal Protection. – 1991. – Vol. 27. – №4. – P. 617-625.

30. Reformatskaya I.I., Sulzhenko A.N. Influence of chemical and phase composition of iron on its pitting resistance and passivability // Metal Protection. – 1998. – Vol.34. – №5. – P. 503-506.

31. Babakov A.A., Novokreschenova S.M., Levin F.L. Silicon as an alloying element in steel OOOX20H20 // Metal Protection. – 1974. – Vol.10. – №5. – P. 552-554.

32. Wranglen G. Pitting and sulphide inclusions in steel // Corrosion. – 1974. – Vol.14 (4). – P. 331 – 349.

**Information about authors:**

*Dzhus Anna, PhD student at the Zaporizhzhia Polytechnic National University, Zaporizhzhia, Ukraine, e-mail: Anna-92@ukr.net*

*Subbotin Sergey, doctor of science, professor at the Zaporizhzhia Polytechnic National University, Zaporizhzhia, Ukraine, e-mail: subbotin.csit@gmail.com*

*Pulina Tatiana, doctor of science, professor at the Zaporizhzhia Polytechnic National University, Zaporizhzhia, Ukraine, e-mail: pullina@ukr.net*

*Snizhnoi Gennadii, doctor of science, professor at the, Zaporizhzhia Polytechnic National University, Zaporizhzhia, Ukraine, e-mail: snow@zp.edu.ua*

IRSTI 29.27.51 https://doi.org/10.26577/phst2024v11i2b08

# Interaction of atmospheric pressure plasma with a liquid electrode

A.Kh. Toremurat[1,2*], A.I. Ashirbek[1,2], A.K. Akildinova[2] and S.A. Orazbayev[1,2]

[1]NNLOT, Al-Farabi Kazakh National University, Almaty, Kazakhstan
[2]Institute of Applied Sciences and IT, Almaty, Kazakhstan
*e-mail: aiymgultoremurat.13@gmail.com
*(Received September 12, 2024; received in revised form October 28, 2024; accepted November 14, 2024)*

This research focuses on the interaction between liquid electrode (water) and atmospheric discharge streamers in air. It elucidates water surface deformations due to electrohydrodynamic effects in high-voltage discharge-distilled water interaction. The aim is to comprehensively study processes in the water layer under electrical discharges, with research areas covering discharge parameter measurement, water surface deformation control, and electrode change analysis. The study holds scientific significance in enhancing understanding of electrohydrodynamic effects and plasma-liquid interaction mechanisms. Practically, it has potential applications in water treatment, liquid purification, and materials science. Research methods involve analyzing electrical characteristics of the discharge and surface properties of a metal grounded electrode in water. Key results show water surface deformation, electrolysis, and discharge electrical property changes at a fixed liquid thickness, characterizing plasma-liquid interaction dynamics and enabling optimization of related technologies. The results can enhance water treatment and purification, assist in new material and coating development. In water treatment and liquid purification, they can boost pollutant decomposition via plasma and electrolysis. In materials science, they can guide new anticorrosive coating development on metals by studying oxidation and deposition under plasma discharge. The data also benefits other plasma-technology-related fields.

**Key words:** plasma-liquid interactions, discharge in water, streamer dynamics, deformed water surfaces.
**PACS number(s):** 79.60.Cn.

## 1. Introduction

The non thermal gas discharges plasmas are the source of various charged species, metastable atoms, active radicals, UV photons and widely applied in the field of nanomaterial synthesis, surface treatment, gas conversion, agriculture, medicine and wastewater treatment [1-5]. The atmospheric pressure non thermal plasma sources are attracting more attention due to the high versatility, scalability and exhibit various interesting physical phenomena such as microdischarge [6,7] and self-organized pattern formation. In the field of plasma-liquid interaction, many studies have addressed various aspects of this physical phenomenon. Cavendish's work [8] was one of the first in this area, focusing on the production of nitric acid using electric sparks in air. These experiments were crucial for understanding the chemical reactions that occur in plasma-liquid interactions ("Experiments on Air"). Subsequently, scientists shifted their attention to a deeper understanding of chemical processes [9-11], the study of electrolysis [12-14], electrical destruction of dielectric liquids for high-voltage switching, and the interaction of plasma with liquids for applications in environmentally friendly technologies [15].

Some more recent works focus on effects such as various deformations of the water surface and electrohydrodynamic effects, which are widely used in various applications and electrospray technologies.

The work of Kawamoto and Umezu [16] provided a deeper understanding of the effects of corona discharge on the pressure and deformation of the water surface, emphasizing the importance of linking these effects to the so-called "ionic wind" generated by the discharge. Research in the field of electrohydrodynamic instability conducted in [17] proposed a new method for analyzing the data of

instabilities generated by corona discharge in dielectric liquids. This research explores their effect on surface and volume deformations and considers the properties of the discharge and its potential for application in technical devices.

The changes in the water surface in metal-water discharges have been carefully studied in [18], allowing the determination of different deformation modes depending on the discharge parameters. These studies provided key insights into the behavior of discharges and their potential in various applications.

Other research, such as [19], has provided important data on the effects of corona discharge on the surface characteristics of thin films of various liquids, as well as on the study of the self-sustaining plasma Moses effect. The results of [20] represent a detailed study of a discharge in the atmosphere and above the surface of water under conditions of exposure to nanosecond pulses of high voltage. The study of the decomposition of polystyrene upon contact with water in [21] also provided valuable insights into the applicability of the discharge in chemical synthesis processes.

Although the field of plasma-liquid interaction research is promising and broad, it includes many unresolved aspects that require further study and attention. In particular, it is important to understand the processes that occur during the interaction of a discharge with a liquid and the changes that occur in both the plasma and the liquid during this interaction. Some processes at the plasma-liquid interface remain unknown. Therefore, these studies are also important in fields such as medicine, environmental science, materials synthesis [2,22], and analytical chemistry [12,23].

In this context, our research aims to study the physical processes involved in the exposure of atmospheric pressure plasma to liquid electrodes (with low conductivity) and their influence on the physical properties of the discharge. Particular attention is paid to the occurrence of electrical breakdown at the air-liquid interface, the physical phenomena that occur during these interactions, and their features and mechanisms of formation. These aspects are key to understanding the mechanisms of interaction between atmospheric pressure discharges and liquid electrodes.

In previous studies on the interaction of plasma with water, in many cases the emphasis was placed on explaining chemical processes, and some works like ours used plasma flow in their research.

Unlike the above-mentioned works, our research focuses on the interaction of atmospheric pressure plasma with low-conductivity liquid electrodes and explains the deformations that occur on the water surface during this interaction without the use of plasma flow. In addition, electrical breakdown and electrolysis processes in such a system are being investigated, which expands the understanding of the mechanism of interaction in the plasma-liquid system.

Thus, our work contributes to the deepening of knowledge about the physical processes occurring at the plasma-water interface and their effect on discharge characteristics.

The purpose of our research is to study the physical processes involved when atmospheric pressure plasma interacts with a low-conductivity liquid electrode (a layer of distilled water) and the mechanisms of plasma action on the surface of a metal grounded electrode in a liquid medium.

To achieve this goal, we used experimental methods to analyze the electrical characteristics of the discharge at a fixed thickness of a low-conductivity liquid electrode. We also examined changes on the surface of a copper electrode in a liquid medium to understand the processes resulting from the propagation of a discharge through a “discharge-liquid-metal” medium.

## 2. Methods

The experimental setup shown in Figure 1. It consists of an electrode system including an upper and lower electrode, a power supply, oscilloscope, voltage divider, and resistor.

At the bottom of a quartz vessel with a closed window, there is a grounded lower electrode covered with aluminum. On top of this, a copper plate with a thickness of 2.9 mm and a diameter of 25 mm is placed, serving as the cathode.

The upper electrode is located 9 mm above the surface of the copper plate ($l_{u.e.} = 120\ mm, d_{u.e.} = 3.75\ mm, r_{tip} = 0.27\ mm$), made of stainless steel (AISI 304) with a pointed tip, which serves as an anode for high voltage discharge.

The upper electrode is connected to a sinusoidal high-voltage power supply (PVM-500), after which

the voltage signal is fed through a divider Tektronix P6015A (1000× 3.0pF 100MΩ) to the SIGLENT SDS 1204X-E (200MHz, Dual 1GSa/s, Quad 500MSa/s) for measuring current and voltagewaveforms. One of the oscilloscope probes is connected to a low-inductance resistor (R=57Ω, 10W) for further data processing and analysis of data based on the measured current and voltage values.

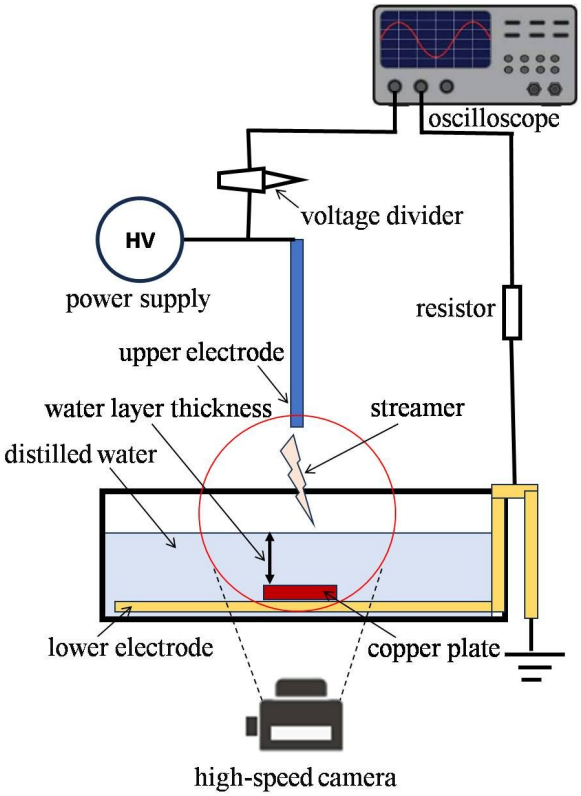



**Figure 1** – Schematic of the experimental setup

A 5 mm thick layer of distilled water is poured into a quartz vessel measuring 4.5 × 4.9 × 4.5 cm. Distilled water, with its low conductivity of 18.2 µS/cm, acts as a good insulator.

A photographic image of the discharge was captured using the PhantomVEO710S high-speed camera, operating at a frequency of 20,000 frames per second. The exposure time for each frame is 49 µs.

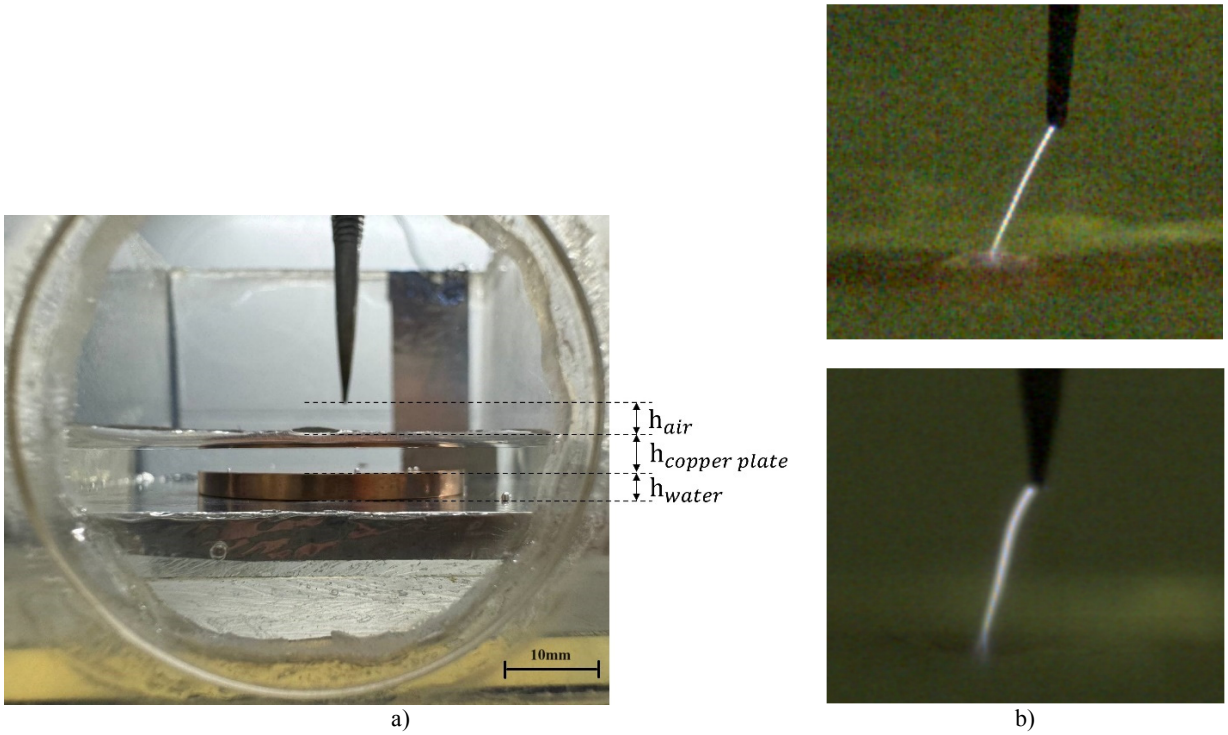
Using an TOPDON ITC629 infrared thermographic camera (Frame Rate of Thermal Images 9Hz), the temperature of the liquid and the top electrode is measured.

The main parameters of the experiment: $p = p_{atm}$, $f = 27$ kHz, $t_{d.i} = 5\ min$ (discharge ignition time) (Table 1). Water thickness: $h_{water} = 5\ mm$, interelectrode distance: $h_{air} = 4mm$, $h_{\text{copper plate}} = 2.9\ mm$ (Figure 2).

Raman spectroscopy was used to analyze the surface of the copper electrode after the experiments. The measurements were carried out using a laser with a wavelength of 473 nm, which provides high sensitivity to fluctuations in copper-oxygen bonds. The spectral resolution of the device was 4 $cm^{-}$ 1, which makes it possible to accurately identify peaks and their correspondence to certain vibrational modes.

**Table 1** – Parameters before and after the experiment

| Parameters | $h_{water}$, мм | $t_{\text{water}}$, $^0$C | $t_e$, $^0$C |
|---|---|---|---|
| Before the experiment | 5 | 22.3 | 22 |
| After the experiment | 4.6 | 39 | 48 |




a) b)

**Figure 2** – a) electrode location, b) type of plasma

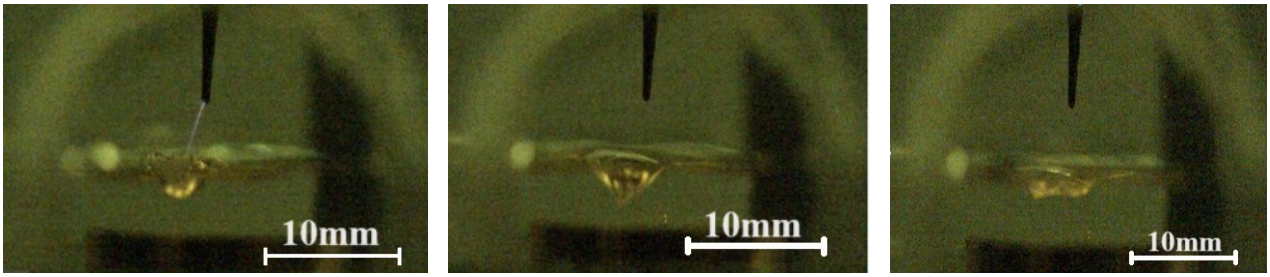
## 3. Results and discussion

During the experiment, voltage was applied to the upper electrode. This resulted in the formation of an electric field between the tip of the upper electrode and the surface of the water, within the layer of air. We will refer to this distance as the interelectrode distance.

We can visually observe the occurrence and propagation of a discharge within a layer of air, and the deformation of the water surface was captured using a high-speed camera.

As a result of the experiments, several processes were discovered: deformation of the water surface, the formation of sediment on the copper electrode and electrical breakdown. Let's consider these phenomena separately.

One of the observed phenomena during the experiment is the deformation of the water surface during the interaction with discharge streamers. Figure 3 displays photographs of experiments with water at a fixed thickness. As depicted in the figure, the deformation of the water surface is evident: the discharge induces depressions on the surface of the water.




a) the start b) 150th frame, 7500 μs c) 260 th frame, 13000 μs

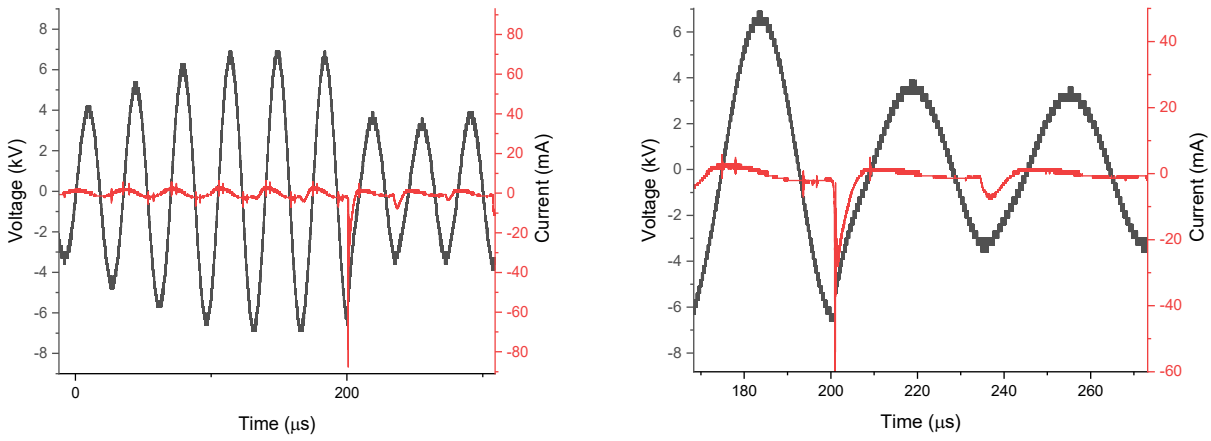
**Figure 3** – Deformation of the water surface obtained with the PhantomVEO710S high-speed camera sample rate 20000 f/s, exposure time 49 μs, $t_{d.i} = 5\ min$ (discharge ignition time), $h_{water} = 5\ mm$, $h_{air} = 4mm$, $h_{\text{copper plate}} = 2.9\ mm$

The deepening of the water surface occurs due to the electrohydrodynamic force [9,10]. In our discharge, ions are accelerated in one direction under the influence of an electric field. As they collide with neutral atoms in the air, and neutral atoms subsequently collide with the surface of the water, deformation occurs. This phenomenon is known as the electrohydrodynamic effect [24].

Deformation of the water surface commences upon the application of voltage. As the discharge voltage gradually increases, the intensity of the electromagnetic field rises, reaching a peak, resulting in a maximum deformation depth of about 2-3 mm (Figure 3a). However, as the discharge or voltage decreases, the electromagnetic effect diminishes, and the water molecules on the surface return to their original positions due to surface tension. This gradual process leads to the surface calming down and the disappearance of deformation (Figure 3b, c).

Figure 4a displays an oscillogram depicting the variation of voltage and current in time at a fixed thickness of the distilled water layer. This graph covers the whole process, starting from the very beginning of the experiment, and allows us to observe the general character of the changes, as well as to identify the moment of electrical breakdown.

Figure 4b shows the part of the graph focused on the moment of electrical breakdown. This plot shows sections of the half-periods at which the electrical breakdown occurs, and three half-periods near the breakdown are obtained. This allows us to examine the breakdown process and the changes in voltage and current in the vicinity of the breakdown point. According to the obtained data, electrical breakdown occurs at $t = 201\mu c$, with a breakdown voltage of $U_{br} = 6{,}5\ kV$ ($I = 87{,}7mA$).




a) b)

**Figure 4** – Instantaneous current and voltage waveforms
$p = p_{atm}, f = 27\ kHz, t = 22^0C$

Another process discovered after the experiment is the deposition of thin film on the surface of the copper plate. A solid dark spot formed in the center of the copper disk, and small spots were observed along the edges. Analysis by optical spectroscopy revealed that between the black spots in the center of the copper plate, there were slightly concave yellow spots. Additionally, black spots were observed all over the surface, except for the center of the plate, among which yellow spots were also present in the middle (Figure 5). These stains are the result of electrolytic processes, so we will further discuss their nature and analysis.

When a high voltage is applied, air ionization occurs between the tip of the upper electrode and the surface of the water. This process leads to the formation of a plasma channel, which serves as a conductor for charged particles (ions and electrons), allowing them to pass between the electrode and water. Once the plasma channel is installed, the

electrons moving through it reach the surface of the water and initiate the electrolysis process. At the moment of discharge, a local electric field is formed on the surface of the water [25], which leads to charge separation between the cathode and the anode, thereby contributing to electrolytic reactions.

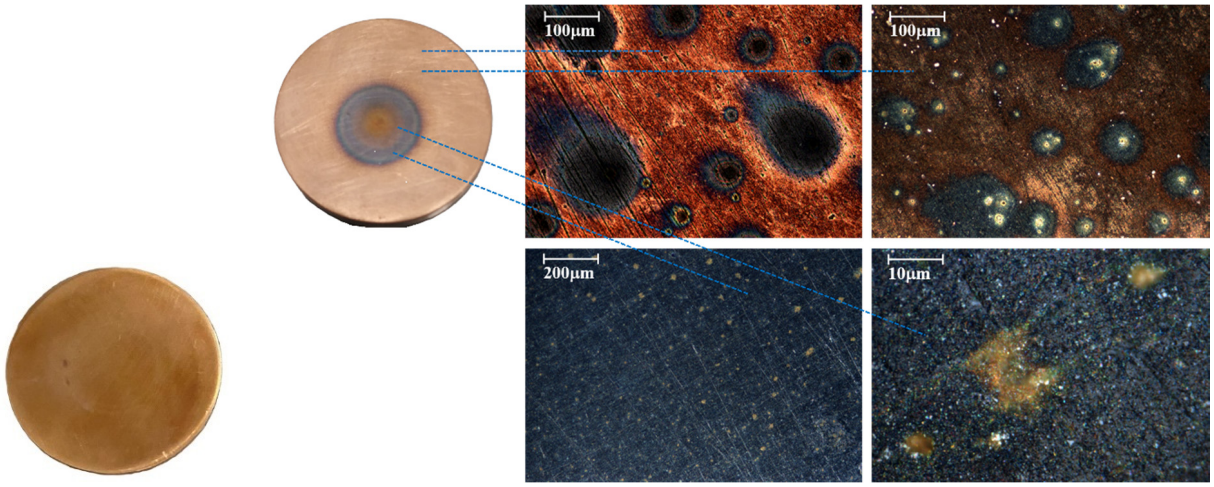



**Figure 5** – Edge and centre of the copper plate (after the experiment)
$t_{d.i} = 5\ min$ (discharge ignition time), $h_{\text{copper plate}} = 2.9\ mm$, $d_{\text{copper plate}} = 25$ мм, $d_{spot} \approx 10$ мм

Under normal conditions, plasma-liquid interaction induces a sequence of chemical reactions [4], including the electrolysis of water, leading to the formation of hydrogen and oxygen at the electrodes. Therefore, this system can be characterized as water electrolysis with sufficiently high potential, involving electrolytic reactions at the cathode and anode. Electrolysis of water involves two primary reactions: reduction process at the cathode (-) (1) and oxidation process at the anode (+) (2):

$$2H^+ + 2e^- \rightarrow H_2\ [12], \quad (1)$$

$$2H_2O \rightarrow O_2 + 4H^+ + 4e^-\ [12]. \quad (2)$$

During the electrolysis of water, the copper surface reacts with oxygen to form various compounds such as copper oxides or hydroxides can be formed. This is due to reactions of copper with products of water electrolysis such as oxygen or hydrogen. The reaction at the anode produces oxygen, which can interact with the copper surface, leading to the formation of copper (II) oxide:

$$4Cu + O_2 \rightarrow 2Cu_2O. \quad (3)$$

Thus, the formation of copper (II) oxide can lead to changes in the color and structure of the surface, which appears as stains.

To fully understand the processes occurring and determine the nature of the resulting compounds or structures, the surface of the copper plate was analyzed using Raman spectroscopy. In the spectra taken from the center and edges of the copper plate, characteristic peaks at 147.7, 213.7 and 642.7 cm$^-$ 1 were revealed, which correspond to copper oxide(I) – cuprite (Cu2O). These peaks indicate the presence of fluctuations in copper-oxygen bonds in the cuprite structure:

- 147.7 cm$^-$ 1 is the peak corresponding to the oscillation of the copper–oxygen bond in the cuprite structure (oscillatory mode A□G);
- 213.7 cm$^-$ 1 is a peak that indicates symmetrical oscillations in octahedral clusters characteristic of Cu2O(Eg);
- 642.7 cm$^-$ 1 – indicates deformation fluctuations of the Cu–O (T□G) bond.

The spectrum (Figure 6) indicates the presence of copper (I) oxide or cuprite ($Cu_2O$) with an oxidation state of +1 (I), both at the edges and in the center of the plate. This indicates that

each copper atom in this compound carries a positive charge of +1. The presence of cuprite on the surface of the copper plate was confirmed by comparing the peaks of the Raman spectra with those from other studies, including those provided in the cited article [26].

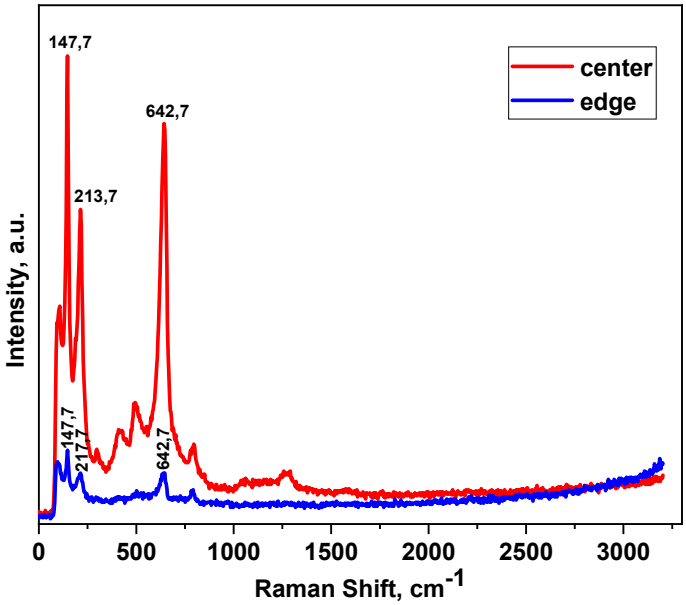



**Figure 6** – Results of Raman spectroscopy

Thus, the results of Raman spectroscopy and visual observations show that cuprite (CuO) and, probably, copper (II) oxide (CuO) are formed on the surface of the copper electrode. Their distribution and quantity depend on the intensity and duration of the discharge. With prolonged discharge, the accumulation of electrolysis products and the interaction of copper with plasma on the surface of the plate increases, which contributes to the formation of more cuprite and other oxidized compounds. In addition, at higher voltage and discharge intensity, more active particles are generated, which enhances the oxidation of copper. In the center of the plate, where the discharge conditions are most intense, deeper oxidation processes are observed, which is confirmed by the appearance of dark spots. These results demonstrate that changes in the composition and structure of deposition on the electrode are directly related to the duration and parameters of the discharge.

## 4. Conclusion

In this paper, we offer an explanation regarding the observed phenomena that occur during the interaction of atmospheric pressure plasma and distilled water. It has been determined that the deformation of the water surface during the operation of a discharge is related to the action of the electrohydrodynamic force. As the voltage rises, the depth of the water surface deformation also increases, and this deformation vanishes when the discharge is switched off. A graph illustrating the electrical breakdown during the interaction of water and discharge was presented. At a discharge time of $t = 201\mu c$, an electrical breakdown takes place; through the use of an oscillogram, it was established that the breakdown voltage is 6.5 kV.

During the experiment, a distinct spot appeared on the surface of a copper plate following the application of a discharge. This phenomenon is attributed to electrolysis. The series of reactions resulting from the interaction between water and discharge is described: it involves cathodic reduction and anodic oxidation reactions, which ultimately lead to the formation of copper oxide when the copper surface interacts with the reaction products. Raman spectral analysis of the copper plate surface confirmed the presence of copper oxide, as indicated by prominent peaks. This observation indirectly

validates that the characteristic spots on the copper plate surface are a consequence of electrolysis rather than the direct propagation of discharge through an aqueous medium.

The observed effects define the dynamics of the interaction between plasma and liquid. The results obtained enable us to gain a more profound understanding of the interaction between plasma and liquid and to develop novel technologies based on these interactions.

**Acknowledgements**

All authors are grateful to the Committee of Science of the Ministry of Science and Higher Education of the Republic of Kazakhstan (Program No. BR18574080 and Grant No. AP22786960)

We would like to express our special gratitude to PhD Ussenov Yerbolat for his valuable advice in planning the study and invaluable assistance in writing this article

**References**

1. Ussenkhan S., Kyrykbay B., Yerlanuly Y., Zhunisbekov A., Gabdullin M., Ramazanov T., Orazbayev S., Utegenov A. Fabricating durable and stable superhydrophobic coatings by the atmospheric pressure plasma polymerisation of hexamethyldisiloxane // Heliyon. – 2024. – Vol. 10. – No. 1. – P.e23844. https://doi.org/10.1016/j.heliyon.2023.e23844

2. Orazbayev S., Gabdullin M., Ramazanov T., Zhunisbekov A., Rakhymzhan Z. Obtaining hydrophobic surfaces in atmospheric pressure plasma // Mater. Today Proc. – 2020. – Vol. 20. – P. 335–341. https://doi.org/10.1016/j.matpr.2019.10.071

3. Orazbayev S., Utegenov A., Zhunisbekov A., Slamyiya M., Dosbolayev M., Ramazanov T. Synthesis of carbon and copper nanoparticles in radio frequency plasma with additional electrostatic field // Contrib. Plasma Phys. – 2018. – Vol. 58. – No. 10. – P. 961–966. https://doi.org/10.1002/advs.201700146

4. Orazbayev S., Zhumadilov R., Zhunisbekov A., Gabdullin M., Yerlanuly Y., Utegenov A., Ramazanov T. Superhydrophobic carbonous surfaces production by PECVD methods //Applied Surface Science. – 2020. – Vol. 515. – P.146050. https://doi:10.1016/j.apsusc.2020.146050

5. Orazbayev A., Jumagulov M., Dosbolayev M., Silamiya M., Ramazanov T., Boufendi L. Optical spectroscopic diagnostics of dusty plasma in RF discharge // In Dusty/Complex Plasmas: Basic and Interdisciplinary Research.– 2011. – Vol. 1397. – No. 1. – P. 379-380. https://doi:10.1063/1.3659852

6. Usenov E.A., Akishev Yu., Petryakov A. V., Ramazanov T. S., Gabdullin M. T., Ashirbek A., Akil'dinova A. K.The memory effect of microdischarges in the barrier discharge in airflow // Plasma Physics Reports. – 2020. – Vol. 46. – P. 459-464. https://doi:10.1134/S1063780X20040145

7. Ussenov Y., Ashirbek A., Dosbolayev M., Gabdullin M., Ramazanov T. Microdischarge dynamics of volume DBD under the natural convection airflow // Physica Scripta. – 2024. – Vol. 99. – No. 3. – P.035608. https://doi:10.1088/1402-4896/ad28a3

8. Cavendish H. XXIII. Experiments on air //Philosophical Transactions of the Royal Society of London. – 1785. – No. 75. – P. 372-384. https://doi.org/10.1098/rstl.1785.0023

9. Liu Z.C., Liu D.X., Chen C., Li D., Yang A.J., Rong M.Z., Chen H.L, Kong M.G. Physicochemical processes in the indirect interaction between surface air plasma and deionized water // Journal of Physics D: Applied Physics. – 2015. – Vol. 48. – No. 49. – P.495201. https://doi:10.1088/0022-3727/48/49/495201

10. Dubinov A.E., Kozhayeva J.P., Lyubimtseva V.A., Selemir V.D. Hydrodynamic and physicochemical phenomena in liquid droplets under the action of nanosecond spark discharges: A review //Advances in Colloid and Interface Science. – 2019. – Vol. 271. – 101986. https://doi:10.1016/j.cis.2019.07.007

11. Delgado H.E., Brown G.H., Bartels D.M., Rumbach P., Go D.B. The scaling of kinetic and transport behaviors in the solution-phase chemistry of a plasma–liquid interface //Journal of Applied Physics. – 2021. – Vol. 129(8). – No. 8. – 083303. https://doi:10.1063/5.0040163

12. Witzke M., Rumbach P., Go D., Sankaran M. Evidence for the electrolysis of water by atmospheric-pressure plasmas formed at the surface of aqueous solutions //Journal of Physics D: Applied Physics. – 2012. – Vol. 45. – No. 44. – 442001. https://doi:10.1088/0022-3727/45/44/442001

13. Rumbach P., Witzke M., Sankaran M., Go D. Plasma-liquid interactions: Separating electrolytic reactions from plasma/gas phase reactions //Proc. ESA Annual Meeting on Electrostatics. – 2013. – Vol. 130. – No. 20. – 200401. https://doi:10.1063/5.0078076

14. Hickling A., Ingram M. D. Glow-discharge electrolysis //Journal of Electroanalytical Chemistry. – 1964. – Vol. 8. – No. 1. – P. 65-81. https://doi.org/10.1016/0022-0728(64)80039-5

15. Bruggeman P. J. et al. Plasma–liquid interactions: a review and roadmap //Plasma sources science and technology. – 2016. – Vol. 25. – No. 5. – 053002. https://doi:10.1088/0963-0252/25/5/053002

16. Kawamoto H., Umezu S. Electrohydrodynamic deformation of water surface in a metal pin to water plate corona discharge system //Journal of Physics D: Applied Physics. – 2005. – Vol. 38. – No. 6. – 887. https://doi:10.1088/0022-3727/38/6/017

17. Mohamed M., Shahbaznezhad M., Dehghanghadikolaei A., Haque A., Sojoudi H. Deformation of bulk dielectric fluids under corona-initiated charge injection //Experiments in Fluids. – 2020. – Vol. 61. – No. 5. – 116. https://doi:10.1007/s00348-020-02951-5

18. Liu F. Deformation of water surface with different metal-water discharge modes //2021 IEEE 2nd China International Youth Conference on Electrical Engineering (CIYCEE). – IEEE, 2021. – https://doi:10.1109/CIYCEE53554.2021.9676923

19. Dekhtyar V. A., Kolesov H. N., Dubinov A. E. Plasma Moses Effect: Production of Stationary Circular Holes in the Liquid Films by a DC Corona Discharge //IEEE Transactions on Plasma Science. – 2023. – Vol. 51. – No. 2. – P. 451-455. https://doi.org/10.1109/TPS.2023.3234639

20. Herrmann A., Margot J., Hamdan A. Experimental and 2D fluid simulation of a streamer discharge in air over a water surface //Plasma Sources Science and Technology. – 2024. – Vol. 33. – No2. – 025022 https://doi.org/10.1088/1361-6595/ad286f

21. Zamo A., Rond C., Hamdan A. Polystyrene (PS) Degradation Induced by Nanosecond Electric Discharge in Air in Contact with PS/Water //Plasma. – 2024. – Vol. 7. – No. 1. – P. 49-63. https://doi:10.3390/plasma7010004

22. Orazbayev S., Muratov M., Ramazanov T., Dosbolayev M., Silamiya M., Jumagulov M., Boufendi L. The Diagnostics of Dusty Plasma in RF Discharge by Two Different Methods //Contrib. Plasma Phys. – 2013. – Vol. 53. – No. 4-5. – P. 436-441. https://doi:10.1002/ctpp.201200123

23. Li D. E., Lin C. H. Modeling and Experimental Validation on The Ionic Strength and Charge Effect in Plasma-Induced Liquid Mobility. – 2024. https://doi:10.21203/rs.3.rs-3779393/v1

24. Park S., Choe W., Lee H., Park J.Y., Kim J., S.Y. Moon., Cvelbar U. Stabilization of liquid instabilities with ionized gas jets //Nature. – 2021. – Vol. 592 (7852). – P. 49-53. https://doi:10.1038/s41586-021-03359-9

25. Fedoseev A., Salnikov M., Sukhinin G. Influence of an external electric field on plasma parameters around an isolated dust particle // Physical Sciences and Technology. – 2021. – Vol. 8. – No. 3-4. – P. 41-47. https://doi.org/10.26577/phst.2021.v8.i2.05

26. Zhakypov A. S. et al. Synthesis and in situ oxidation of copper micro-and nanoparticles by arc discharge plasma in liquid // Scientific Reports. – 2023. – Vol. 13. – No. 1. – P.15714. https://doi.org/10.1038/s41598-023-41631-2

***Information about authors:***

*Toremurat Aiymgul, PhD student at Al-Farabi Kazakh National University; Institute of Applied Science and IT, (Almaty, Kazakhstan), e-mail: aiymgultoremurat.13@gmail.com*

*Ashirbek Azamat, PhD student at Al-Farabi Kazakh National University; Institute of Applied Science and IT, (Almaty, Kazakhstan), e-mail:azamatjan97@gmail.com*

*Akildinova Ainur, PhD, Institute of Applied Science and IT, (Almaty, Kazakhstan), e-mail: akildinova@physics.kz*

*Orazbayev Sagi, PhD, associate professor at Al-Farabi Kazakh National University (Almaty, Kazakhstan), e-mail sagi.orazbayev@gmail.com*

IRSTI 29.27.51 https://doi.org/10.26577/phst2024v11i2b09

# Effects of increasing applied voltage and frequency on plasma parameters in dielectric barrier discharge plasma

Ibrahim K. Abbas

Department of Physics, College of Science, University of Baghdad, Baghdad, Iraq
e-mail: Ibrahim.kareem1104a@sc.uobaghdad.edu.iq

*(Received August 17, 2024; received in revised form November 21, 2024; accepted November 30, 2024)*

The dielectric barrier discharge (DBD) plasma is one of the branches of plasma produced at atmospheric pressure. It is easy to use in the laboratory, where the dielectric barrier discharge was built from a copper electrode with a glass insulator in front of one of the electrodes. The plasma was generated between the two electrodes at a high applied voltage ranging between (5-9) kV using a high voltage power supply and at a (7) kHz frequency. To perform the spectral characterization of the plasma produced by the dielectric barrier discharge (DBD) system and calculate the plasma parameters, a gradually increasing voltage (5-9) kV was used with a fixed frequency of (7) kHz in the first case, and in the other case, the frequency was changed (5-9) kHz with a constant applied voltage of (8) kV. The results showed that the increased applied voltage and frequency value led to an increase in the spectral intensity of ($N_2$) of the plasma generated between the two electrodes, ranging from (296.44 - 715) nm. As well as an increase in the plasma electron temperature ($T_e$) (0.895-1.436) eV and (0.922-0.522) eV, and the resulting plasma number density ($n_e$) (5.485-9.541) x$10^{16}$ $cm^{-3}$ and (4.856-8.090) x$10^{16}$ $cm^{-3}$ in both cases, respectively, as well as the rest of the other plasma parameters.

**Key words**: DBD system, plasma parameters, Stark broadening, electron temperature, plasma spectrum intensity.
**PACS number(s):** 79.60.Cn.

## 1. Introduction

Gas discharge plasmas, sometimes referred to as low-temperature plasmas, have garnered significant interest in recent decades due to their crucial role in numerous technological advancements. Subsequently, plasma technologies have applications in other technological and research domains, such as microelectronics, gas lasers, and polymer processing [1, 2]. Dielectric barrier discharge (DBD) is considered one of the most cost-effective producers of non-thermal plasma among various plasma sources [3, 4]. This discharge is recognized for its efficacy in beginning chemical and physical gas processes [5–7]. Consequently, the majority of plasma-generating systems are considered to be fundamental and essential systems because they are utilized in a considerable number of technological and research applications [5, 8]. Microelectronics, lasers, and related areas are included. The voltage discharge barrier is one system that can be utilized to process food, fruits, meat, vegetables, and other foods [9–11]. Plasma-generating systems are crucial in simplifying complex tasks in laboratory circumstances, such as dealing with atmospheric pressure and forming plasma between the poles. This efficiency reassures us of their potential in various applications, including cancer cell treatment, wound healing, and environmental purification [12]. To facilitate the handling of the dielectric barrier discharge, an insulator must be used between the two poles made of a specific material [13]. The air jet plasma and the dielectric barrier discharge continue to be at the top of the list of instruments that are considered to be among the most versatile, simple to run, and straightforward to deploy plasma generators [14, 15]. DBD has undergone thorough examination in recent years due to its prospective utilization in various domains [8]. It encompasses both material processing and applications in the energy and environment sectors [16]. It can generate highly reactive plasma at nearly ambient temperature, with low energy consumption, utilizing a straightforward reactor setup under atmospheric pressure settings [5,

9]. The domain of diagnostics in created plasma is extensive and varied, with diagnostic instruments serving as a crucial component for comprehending the behavior of the produced plasma [17]. Numerous diagnostic techniques are available, contingent upon the type of plasma produced and the requisite information, and are commonly utilized in academic settings; the analysis of the waveforms of the driving current and voltage is crucial for understanding the primary processes occurring during the discharge [17, 18]. The second instrument signifies an electrical probe utilized in low-pressure and low-temperature plasma environments. The third tool signifies mass spectrometry, conducted at the substrate borders, and does not significantly impact the plasma. The fourth instrument is optical emission spectroscopy, which is appropriate for application with a dielectric barrier discharge to analyze the spectral response produced during plasma generation between the two electrodes [19]. Various techniques are employed to quantify plasma characteristics, such as plasma electron temperature and electron density. However, optical emission is the most commonly utilized method [18], [19]. The optical emission spectroscopy (OES) method is frequently employed for optical characterization[20]. Most of the processes occurring in plasma are the result of collisional, radiational, excitational, and de-excitational processes that are in equilibrium with each other [14]. Therefore, at thermodynamic equilibrium (TE), all processes are balanced within the plasma, and its temperature can be determined. While at local thermal equilibrium (LTE), this means that the emission is generated somewhere in the plasma and absorbed somewhere else. Therefore, in such equilibrium, the energy loss through radiation (unabsorbed radiation) is slight compared to the energy involved in other processes (collisions), so local thermal equilibrium (LTE) can be assumed, and the plasma parameters for this case can be calculated. The LTE's electron temperature (Te eV) is calculated using the following equation [1,2].

$$ln\left[\frac{\lambda_{ji}I_{ji}}{hcA_{ji}g_j}\right] = -\frac{1}{KT}\left(E_j\right) + \ln\left|\frac{N}{U(T)}\right| \quad (1)$$

Where g denotes the statistical weight, λ denotes the wavelength, E is the excited state energy in eV, $I_{ji}$ denotes the intensity, $A_{ji}$ denotes the transition probability, N denotes the density of the state's population, and k denotes the Boltzmann constant [21, 22]. In plasma spectrum research, stark broadening is crucial in widening spectral lines [23]. It provides information on the electron density at a specific plasma electron temperature [24, 25]. The electron density can be determined by applying the following equation.

$$n_e = \left[\frac{\Delta\lambda}{2\omega_s}\right] N_r \ (cm^{-3}) \quad (2)$$

Where Δλ the full width at half maximum (FWHM) nm of the line ωs is the Stark broadening parameter in the standard tables, and $N_r$ is the reference electron density [21, 23]. The frequency of plasma is calculated using the following equation.

$$f_p = 8.98\sqrt{n_e}\ (\text{Hz}) \quad (3)$$

Plasma frequency is a fundamental property exclusively determined by density [26]. Plasma exhibits a high frequency due to the minuscule mass of electrons [27]. Debye shielding, also known as Debye length ($\lambda_D$), is a phenomenon in which charged particles in a plasma respond to an electric field in a way that diminishes its effect on the local fields [28, 29]. This results in the plasma exhibiting quasi-neutrality. The Debye length ($\lambda_D$) is defined as [21].

$$\lambda_D = \sqrt{\frac{\varepsilon_o K_B T_e}{n_e e^2}} = 743 \times \sqrt{\frac{T_e}{n_e}} \quad (cm) \ (4)$$

Hence, this study aims to diagnose and quantify the plasma parameters of the dielectric barrier discharge (DBD) system and illustrate the impact of gradually increasing the applied voltage and frequency on the plasma's properties.

## 2. Experimental part

Figure 1 shows a schematic of the dielectric barrier discharge (DBD) system manufactured in the laboratory, where copper was used to manufacture the dielectric barrier discharge electrodes and was insulated by a thermal insulator with the two electrodes of the system arranged vertically. The total diameter of the copper electrode is (5 mm), and the outer diameter of the thermal insulator inside which the copper electrode is placed is 60 mm. A high voltage (AC) power supply was used with a peak of 25 kV and worked on an increasing voltage starting from (5-9) kV with a fixed frequency at 7 kHz, and a

rising frequency was also used from (5-9) kHz with a fixed applied voltage at 8 kV to study the effect of increasing the applied voltage and increasing the frequency on the properties and parameters of the plasma. The upper cathode electrode of the dielectric barrier discharge was connected to the high voltage device as well as the anode electrode, and the distance between the two electrodes was 5 mm, with the use of a piece of glass with a thickness of 2 mm that was placed between the two electrodes during plasma generation. To diagnose the plasma and collect the resulting spectrum, a laboratory spectrometer (S3000-UV-NIR) operates between (250-1100) nm, with the optical fiber fixed by a metal holder and 1 cm away from the plasma-generating electrodes. These recorded data were analyzed and matched with the National Institute of Technology and Standards (NIST) data [30].

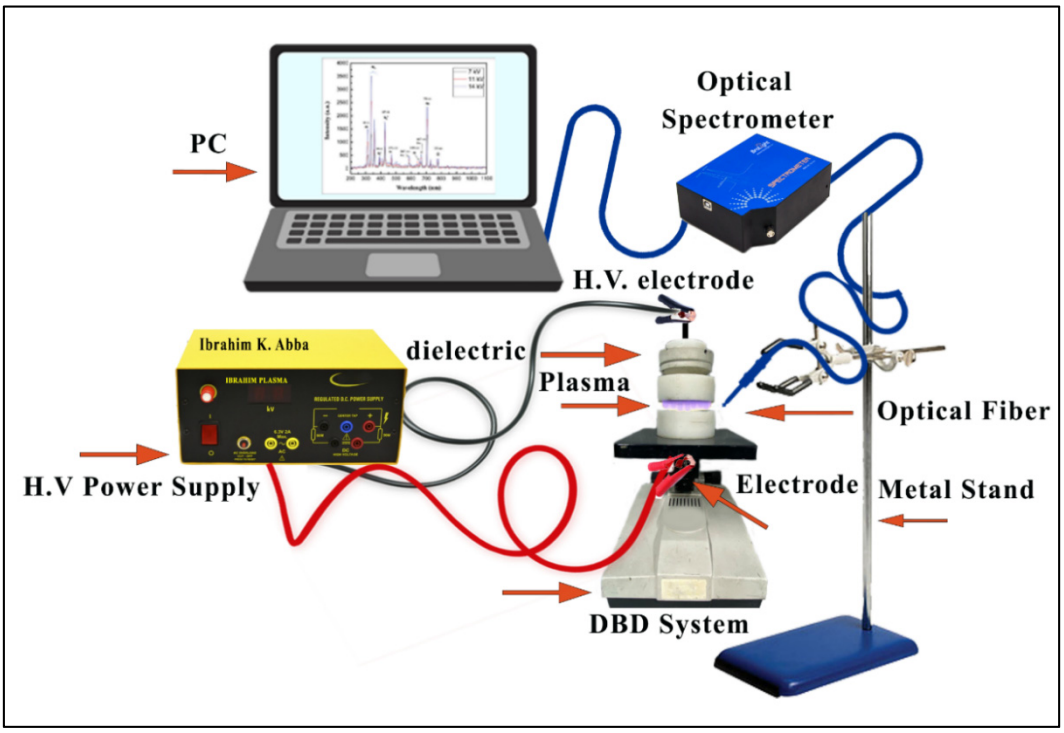



**Figure 1 –** Schematic diagram of the dielectric barrier discharge (DBD) system and setup of the optical spectrometer

## 3. Results and discussions

Analyzing the plasma spectrum produced by the dielectric barrier discharge is crucial for determining the remaining plasma parameters, making emission spectral diagnosis a highly significant technique. Under normal atmospheric pressure, an extensive and multi-peaked spectrum of nitrogen gas was acquired. The emission spectrum depicted in Fig. 2 exhibits many peaks spanning from 280 to 750 nm. These peaks were detected by the spectral diagnostic tool at a frequency of 7 kHz, while the applied voltage ranged from (5-9) kV, and the distance between the upper and lower electrodes was 5 mm. The emission spectrum analysis revealed many peaks corresponding to molecular nitrogen [31]. These peaks were observed at wavelengths ranging from 296.44 nm to 419.53 nm, with a prominent nitrogen peak at 336.38 nm. Additionally, nitrogen ionic peaks were detected at 672.94 nm and 715 nm. The spectral results indicate that increasing the applied voltage from 5 to 9 kV results in a proportional increase in the emitted intensity of the plasma spectrum. This increase in intensity is attributed to the higher energy supplied to the electrons, leading to a more significant number of collisions and the excitation of multiple molecules during the emission process [23].

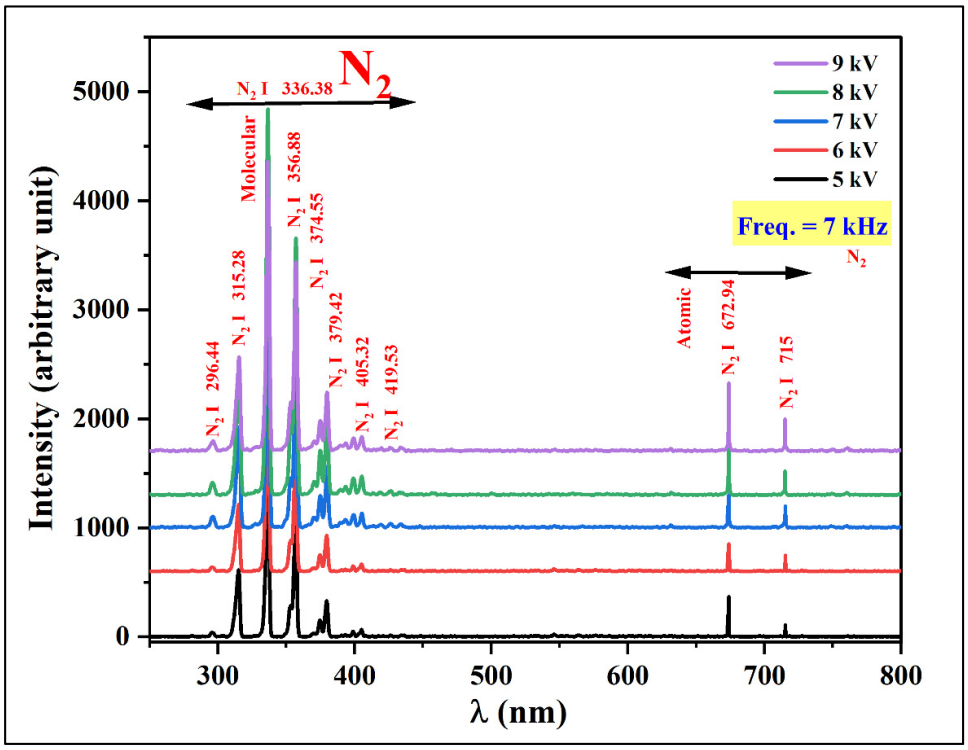



**Figure 2 –** The plasma spectrum from a dielectric barrier discharge at an increased applied voltage (5-9) kV and a fixed frequency of 7 kHz

Figure 3 displays the plasma spectrum produced by the dielectric barrier discharge under a fixed applied voltage of 8 kV. As the frequency value gradually increases from 5 to 9 kHz, the intensity of the emitted spectrum also increases. Additionally, the spectrum reveals the presence of multiple nitrogen peaks ($N_2I$) at specific wavelengths, namely 295.88, 314.64, 336.60, 374.55, 379.15, 398.87, 405.05, and 419.27 nm. The highest intensity of spectral emission occurs at 335.83 nm. When comparing the emitted spectra under increased applied voltage and frequency, we observe a consistent increase in the spectral emission intensity. Notably, the intensity is slightly higher when the frequency is increased. This can be attributed to the heightened collisions between molecules within the confined space between the electrodes, and these findings align closely with [20, 22].

To determine the plasma parameters and understand how they change in the dielectric barrier discharge (DBD) system with increasing applied voltage and frequency, the Boltzmann plots equations were employed to calculate the electron temperature ($T_e$), as shown in Eq. 1. The results demonstrated a progressive rise in the plasma electron temperature as the applied voltage increased, indicating a strong correlation between the two variables. The slope of the fitted line is represented by the fraction ($-1/T_e$), where ($T_e$) is a specific value. $R^2$ is a mathematical coefficient that quantifies the quality of a linear fit, with values ranging from 0 to 1. For each equation that fits inside the spectral range of the fitting line, as depicted in Fig. 4.

The findings demonstrated a progressive rise in the electron temperature values, ranging from 0.895 to 1.436 eV, as the applied voltage gradually increased. Similarly, the electron temperature was determined using Boltzmann plots equations when the frequency values rose within the range of (5-9) kHz, as shown in Fig. 5. The electron temperature varied within the range of (0.922 - 1.522) eV as the frequency increased gradually, with a modest rise observed in the first situation of applied voltage[32]. The electron temperature values in two cases increase due to the doubling of the discharge between the upper and lower electrodes, resulting from the increased energy supplied by the high voltage supply. This increase in energy leads to an increase in the discharge voltage; these findings are in agreement with the researchers' findings and are relatively near to them [31, 33].

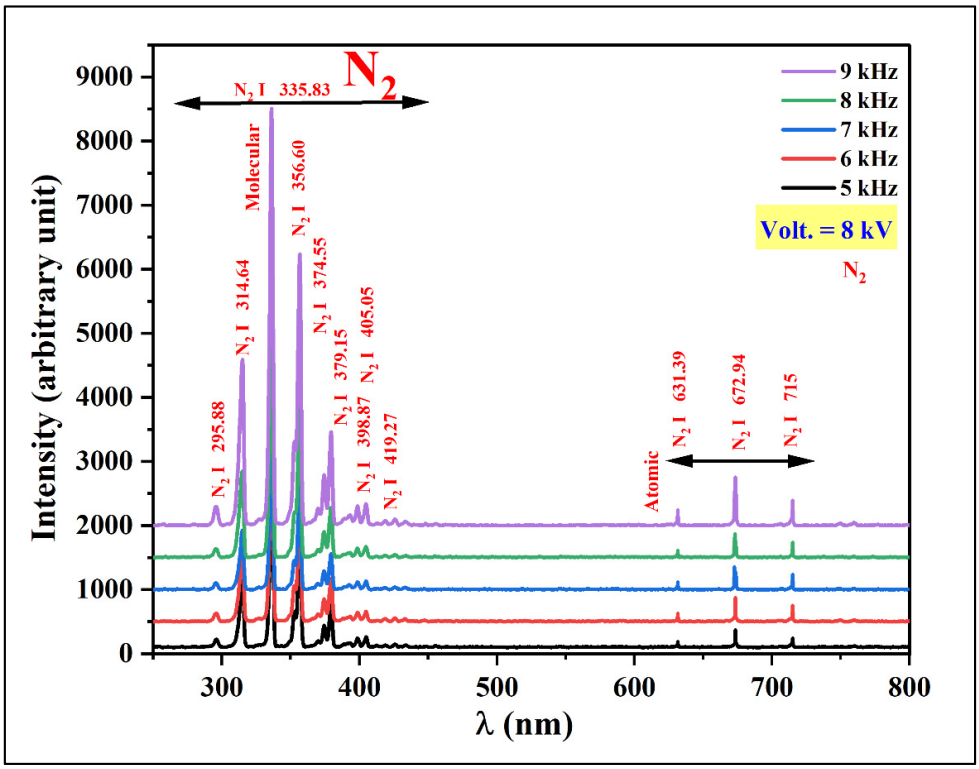



**Figure 3 –** The plasma spectrum from a dielectric barrier discharge at an increased frequency (5-9) kHz and a fixed applied voltage of 8 kV

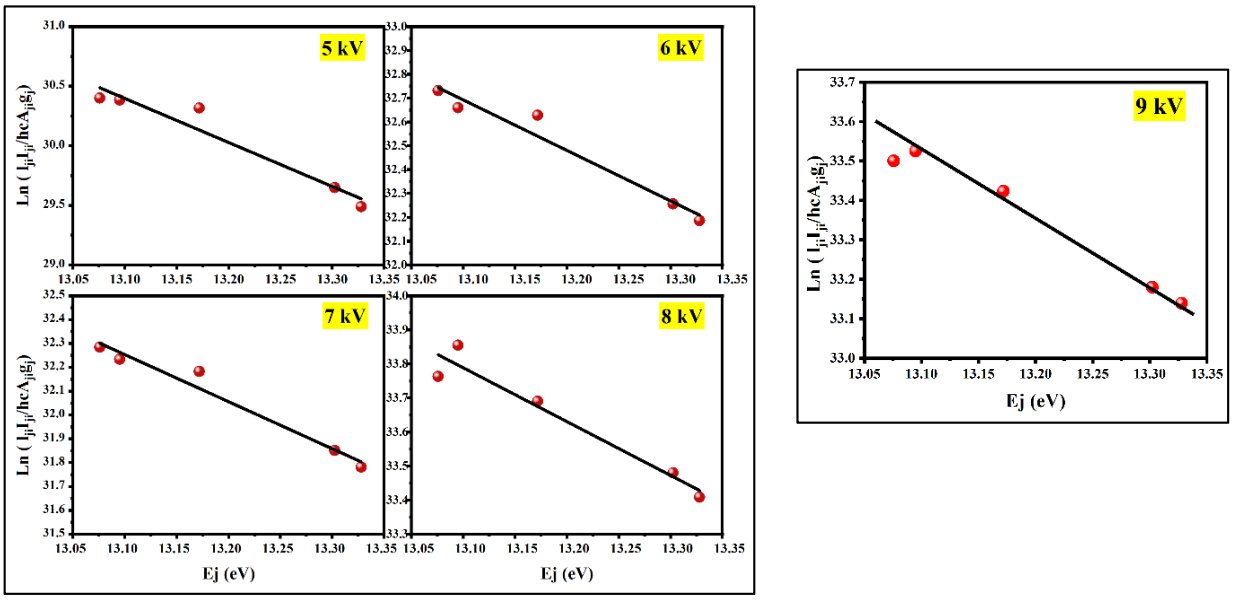



**Figure 4 –** Boltzmann plots at different applied voltage (5-9) kV to calculate the electron plasma temperature in dielectric barrier discharge (DBD)

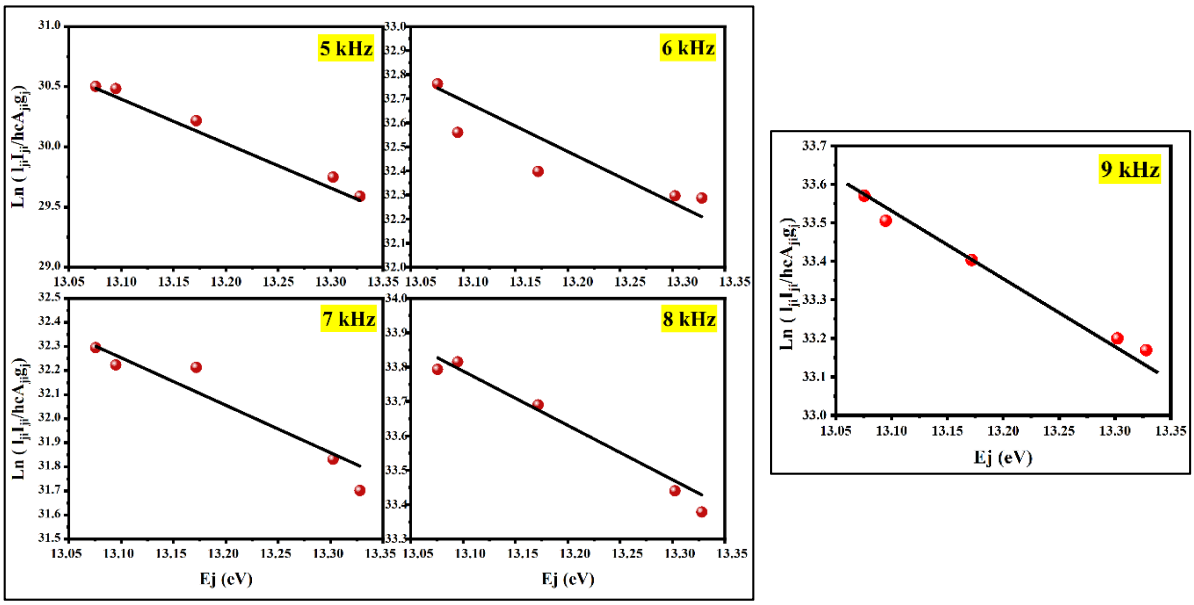



**Figure 5 –** Boltzmann plots at different frequencies (5-9) kHz to calculate the electron plasma temperature in dielectric barrier discharge (DBD)

We utilized Lorentzian fitting to calculate the full width at the mid-peak to determine the plasma electron density as in Eq. 2. This calculation was performed when the applied voltage and frequency were increased. The Stark effect was employed, considering the broadening values for 356.88 nm and 335.83 nm wavelengths, respectively. Tables 1 and 2 show the experimental data results for the full-width half-maximum parameters (FWHM) for the 356.88 and 335.83 nm wavelengths, where Fig. 6 also shows the gradual increase in wave intensity for each value of the applied voltage or frequency. Measuring the full-width half-maximum parameter (FWHM) is necessary to calculate the electron density in the resulting plasma in both cases. Fitting the observed profiles provides a very accurate total density, including spectral line broadening. It is noticeable that the electron density value increases (5.485-9.541) x $10^{16}$ ($cm^{-3}$) significantly when the full-width half maximum increases from (0.232-0.414) nm when the applied voltage increases, and in the same way when the frequency increases, the electron density value increases (4.856-8.090) x $10^{16}$ ($cm^{-3}$) at full-width half maximum range (0.211-0.344) nm, these results of electron density are aligned and coherent with the researchers' findings [20, 22]. Figure 6 illustrates these results, which indicate that both the applied voltage and frequency increase led to an expansion of the mid-peak width.

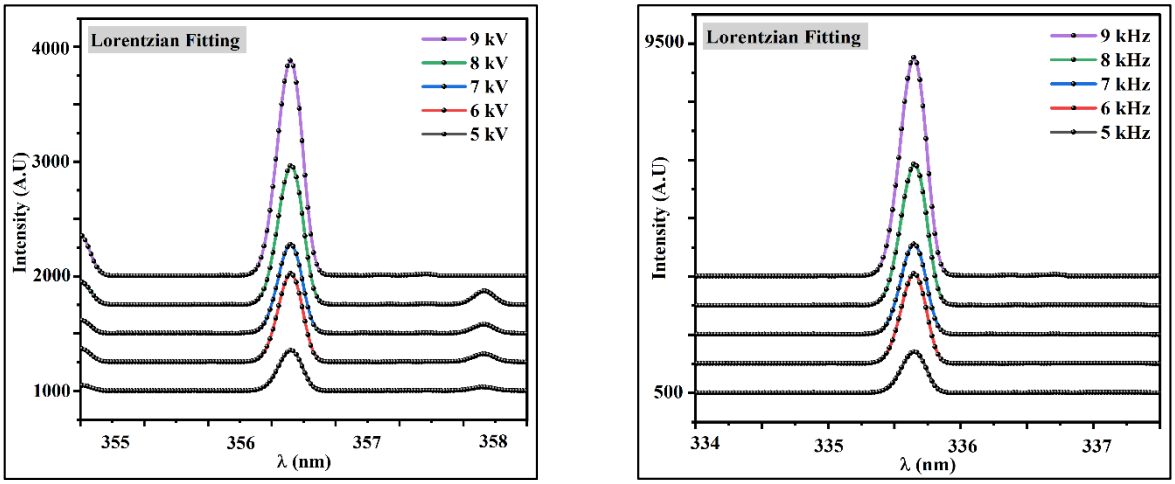



**Figure 6 –** Lorentzian fitting of line broadening for different applied voltage (5-9) kV and frequency (5-9) kHz

Figures 7 and 8 depict the variation in electron temperature and density as the applied voltage gradually increases while keeping the frequency fixed at 7 kHz. Additionally, they illustrate the increase in frequency ranging from 5 to 9 kHz while maintaining a fixed voltage of 8 kV in the dielectric barrier discharge (DBD) system. The two figures indicate that the plasma electron temperature ($T_e$) and electron density ($n_e$) progressively rise with increasing supplied voltage or frequency. This suggests an enhancement in the electric field intensity within the generated plasma, as the electric field increasingly accelerates free electrons, resulting in more frequent collisions with neutral gas atoms and molecules possessing higher energy. These collisions can ionize neutral particles, generating more free electrons and ions and resulting in a substantial rise in plasma electron temperature and electron density. This also applies when the frequency is incrementally raised while maintaining a constant applied voltage value. Augmenting the frequency will result in elevated collision rates since electrons acquire more incredible energy from the electric field prior to colliding with neutral particles, hence increasing their thermal energy due to the heightened frequency. Consequently, the plasma electron temperature and electron density will rise [20, 26].

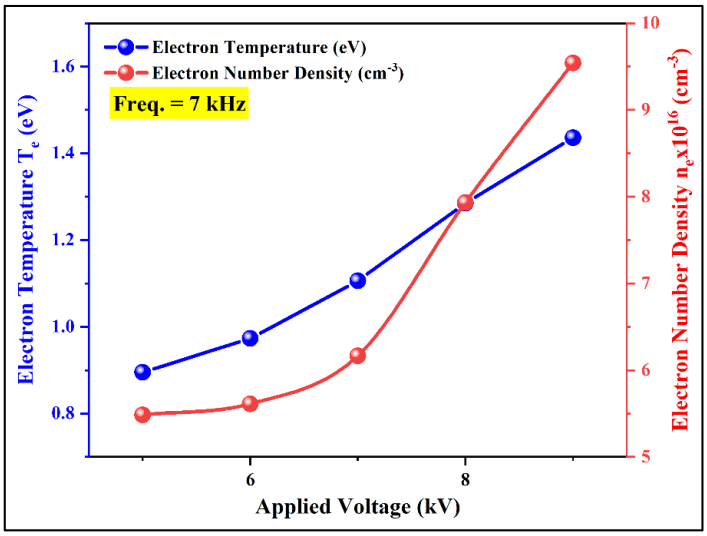



**Figure 7** – The electron temperature (Te) and electron density (ne) versus the increased applied voltage (5-9) kV at a constant frequency of 7 kHz

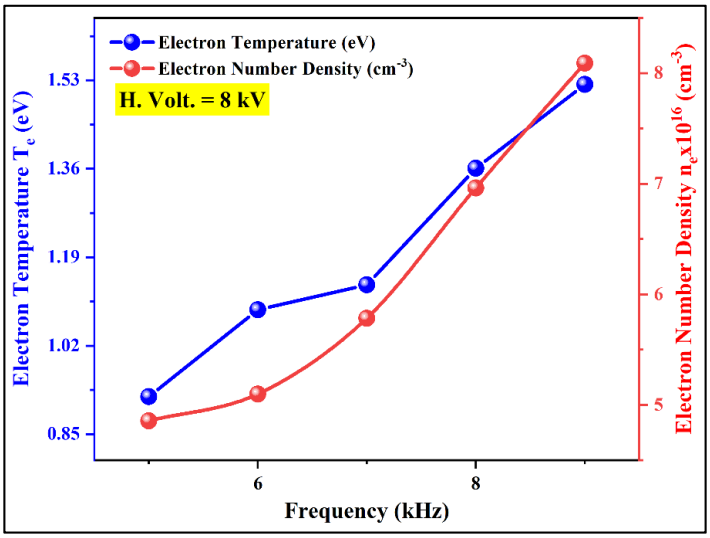



**Figure 8** – The electron temperature (Te) and electron density (ne) versus the increased frequency (5-9) kHz at a constant applied voltage of 8 kV

Tables 1 and 2 display the plasma properties obtained from the earlier equations (see Eq. 3 & 4) for both increasing applied voltage and frequency cases. The tables illustrate the direct correlation between the increased applied voltage and frequency, resulting in both scenarios' consistent rise in plasma frequency (fp) values. In contrast, there is a gradual drop in the Debye barrier ($\lambda_D$) values as the frequency increases.

**Table 1 –** DBD Plasma Parameter in case of Increasing Applied Voltage (5-9) kV

| Applied Voltage (kV) | Te (ev) | FWHM (nm) | ne x $10^{16}$ ($cm^{-3}$) | fp x $10^{12}$ (Hz) | $\lambda_D$ x $10^{-6}$ (cm) |
|---|---|---|---|---|---|
| 5 | 0.895 | 0.232 | 5.485 | 2.082 | 3.001 |
| 6 | 0.973 | 0.240 | 5.612 | 2.106 | 3.093 |
| 7 | 1.106 | 0.267 | 6.165 | 2.207 | 3.147 |
| 8 | 1.285 | 0.320 | 7.932 | 2.503 | 2.990 |
| 9 | 1.436 | 0.414 | 9.541 | 2.745 | 2.883 |

**Table 2 –** DBD Plasma Parameter in case of Increasing Frequency (5-9) kHz

| Frequency (kHz) | Te (ev) | FWHM (nm) | ne x $10^{16}$ ($cm^{-3}$) | fp x $10^{12}$ (Hz) | $\lambda_D$ x $10^{-6}$ (cm) |
|---|---|---|---|---|---|
| 5 | 0.922 | 0.211 | 4.856 | 1.983 | 3.237 |
| 6 | 1.089 | 0.226 | 5.098 | 2.032 | 3.434 |
| 7 | 1.137 | 0.252 | 5.783 | 2.164 | 3.294 |
| 8 | 1.361 | 0.290 | 6.962 | 2.374 | 3.285 |
| 9 | 1.522 | 0.344 | 8.090 | 2.559 | 3.223 |

An insulator is crucial to ensure the safety of the discharge between the electrodes. When ionization occurs between the two electrodes, charges build up on the insulator. The separation between the electrodes is a crucial factor significantly influencing the plasma parameters and its diagnosis[34, 35]. It directly impacts the characteristics of the plasma generated by the dielectric barrier discharge, such as the electron temperature ($T_e$), electron density ($n_e$), electron frequency ($f_p$), ($\lambda_D$), and the active species formed during the discharge between the electrodes. The results acquired for the plasma parameters assessed in the dielectric barrier discharge plasma system indicate their potential applicability across diverse fields, including medical, technological, industrial, and agricultural sectors, through the plasma electron temperature, electron density, Debye length, and plasma frequency, in conjunction with the other parameters measured from the system's plasma.

## 4. Conclusion

This study found a strong association between the applied voltage and frequency during the discharge process between the electrodes and the resulting plasma spectrum and plasma characteristics. The elevated voltage is crucial in influencing plasma electron temperature ($T_e$) and electron density ($n_e$) values in both scenarios. Specifically, the plasma electron temperature reached a maximum value of 1.436 eV, while the electron density reached $9.541x10^{16}$ $cm^{-3}$ at 9 kV. At the lowest voltage of 5 kV, the electron temperature ($T_e$) was 0.895 eV, and the electron density ($n_e$) was 5.485 $x10^{16}$ $cm^{-3}$. Similarly, increasing the frequency (5-9) kHz had a uniform effect on all plasma parameters, which closely resembled the effect of increasing the voltage. The findings also indicated that the spectrum emission strength rises proportionally with higher voltage and frequency. Additionally, many peaks were seen for nitrogen ($N_2$), encompassing both molecular and ionic forms. The spacing between the electrodes (5 mm) is a crucial factor in determining the production of the discharge and its uniform distribution throughout the electrode surface during the plasma generation process. Consequently, all plasma properties will be influenced.

## Acknowledgement

I want to thank the Plasma Laboratory at the University of Baghdad's Department of Physics and College of Science for motivating me to pursue a scientific career after completing my academic work.

**References**


1. Smirnov B. M. Theory of gas discharge plasma. Springer Cham. 2015. Vol. 84. 423 p. https://doi.org/10.1007/978-3-319-11065-3
2. Braithwaite N. S. J. Introduction to gas discharges // Plasma sources Sci. Technol. - 2000. - Vol. 9. - № 4. - P. 517. https://doi.org/10.1088/0963-0252/9/4/307
3. Wong C. S., Mongkolnavin R. Elements of Plasma Technology. Springer Singapore. 2016. 123 p. https://doi.org/10.1007/978-981-10-0117-8
4. Javanmard S., Pouryoussefi S. G. Comparison of characteristics of atmospheric pressure plasma jets using argon and helium working gases // Curr. Appl. Phys. - 2023 - Vol. 46. - P. 61–69. https://doi.org/10.1016/j.cap.2022.12.002
5. Kratzer J., Burhenn S. Chapter 12 - Dielectric barrier discharge devices A. D'Ulivo and R.E.B.T.-V.G.T. for T.E.A. Sturgeon // Eds. Elsevier - 2022. P. 403–442. https://doi.org/10.1016/B978-0-323-85834-2.00006-9
6. S. Dang Li X., Yu X., Abbas G., Zhang Q., Cao L. The application of dielectric barrier discharge non-thermal plasma in VOCs abatement: A review // Chem. Eng. J. - 2020. - Vol. 388. - P. 124275. https://doi.org/10.1016/j.cej.2020.124275.
7. Abbas I. K., Adim K. A. Synthesis and characterization of magnesium oxide nanoparticles by atmospheric non-thermal plasma jet, Kuwait // J. Sci. - 2023. - vol. 50. - № 3. - P. 223–230. https://doi.org/10.1016/j.kjs.2023.05.008
8. Haji A., Barani H. Chapter 1 - Introduction of plasma technology in The Textile Institute Book Series // S. Ul Islam and A. B. T.-A. in P. T. of T. S. Haji, Eds. Woodhead Publishing. 2024. - P. 1–12. https://doi.org/10.1016/B978-0-443-19079-7.00002-6
9. Laroussi M. The dielectric barrier discharge and the start of a beautiful friendship: Personal remembrance of Dr. Ulrich Kogelschatz // Plasma Chem. Plasma Process. - 2023. - Vol. 43. - №. 6. - P. 1287–1292. https://doi.org/10.1007/s11090-023-10313-2
10. Conrads R. A., Schmidt M. Plasma generation and plasma sources // Plasma Sources Sci. Technol. - 2000. - Vol. 9. - .№ 4. P. 441–454. https://doi.org/10.1088/0963-0252/9/4/301.
11. Kasa U., Juswono P., Santjojo D. J. D. H. Identification of reactive species produced by surfaces dielectric barrier discharge nonthermal plasma with gas sources variation (Air, N2, O2) to kill bacteria // J. Penelit. Pendidik. IPA - 2022. - vol. 8. - №. 4. P. 2371–2377. https://doi.org/ 10.29303/jppipa.v8i4.2167.
12. Kadhim A. A., Abbas B. K. Preparation of cobalt oxide nanoparticles by atmospheric plasma jet and investigation of their structural characteristics // Egypt. J. Chem. - 2022. https://doi.org/10.21608/ejchem.2022.146951.6414.
13. Rodrigues F., Pascoa J., Trancossi M. Heat generation mechanisms of DBD plasma actuators // Exp. Therm. Fluid Sci. - 2018. - Vol. 90. - P.55–65. https://doi.org/10.1016/j.expthermflusci.2017.09.005
14. Goldston R. J. Introduction to plasma physics // CRC Press - 2020. https://doi.org/10.1201/9780367806958.
15. Aadim K. A., Abbas I. K. Synthesis and Investigation of the structural characteristics of zinc nanoparticles produced by an atmospheric plasma // Jet. -2023. - Vol. 64. - №. 16. P. 10. https://doi.org/10.24996/ijs.2023.64.4.15.
16. Nguyen T. M., Kaushik N., Nguyen T. T., Choi E. H., Nguyen L. N., Kaushik N. K. The outlook of flexible DBD-plasma devices: Applications in food science and wound care solutions // Mater. Today Electron. - 2024. - Vol. 7. - P. 100087. https://doi.org/10.1016/j.mtelec.2023.100087.
17. Huo J. et al., Effects of chemically reactive species generated in plasma treatment on the physico-chemical properties and biological activities of polysaccharides: An overview // Carbohydr. Polym. - 2024. - Vol. 342 - P. 122361. https://doi.org/10.1016/j.carbpol.2024.122361.
18. Zaplotnik R., Primc G., Vesel A. Optical emission spectroscopy as a diagnostic tool for characterization of atmospheric plasma jets // Appl. Sci. - 2021. - Vol. 11. - №. 5. - P. 1–22. https://doi.org/10.3390/app11052275.
19. Asenjo-Castillo J., Vargas-Blanco I. Espectroscopia de Plasmas en condiciones de presión atmosférica // Rev. Tecnol. en Marcha - 2016. - Vol. 29. - № 6. - P. 47. https://doi.org/10.18845/tm.v29i6.2901.
20. Liu P., He L., Zhao B. Discharge and optical emission spectrum characteristics of a coaxial dielectric barrier discharge plasma-assisted combustion actuator // J. Spectrosc. - 2020. - Vol. 2020. - P. 6034848. https://doi.org/10.1155/2020/6034848.
21. Abbas I. K., Aadim K. A. Spectroscopic diagnosis of cobalt plasma produced by OES technique and influence of applied voltage on plasma parameters // Iraqi J. Sci. - Vol. 64. - №. 5. - P. 2271–2281. https://doi.org/10.24996/ijs.2023.64.5.15.
22. Kadhim M. M., Abbas Q. A., Abdulameer M. R. Study of some plasma characteristics in dielectric barrier discharge (DBD) system // Iraqi J. Sci. - 2022. - Vol. 63. - № 5. - P. 2048–2056. https://doi.org/ 10.24996/ijs.2022.63.5.20
23. Rosato J. Effect of collisions on motional Stark broadening of spectral lines // J. Quant. Spectrosc. Radiat. Transf. - 2023. - Vol. 306. - P. 108628. https://doi.org/10.1016/j.jqsrt.2023.108628.
24. Tapalaga I., Traparić I., Trklja N. Boca, J. Purić, Dojčinović I. P. Stark spectral line broadening modeling by machine learning algorithms // Neural Comput. Appl. - 2022. - Vol. 34. . №8. P. 6349–6358. https://doi.org/ 10.1007/s00521-021-06763-4.
25. Zenkhri D. E., Meftah M. T., Khelfaoui F. Screening and relativistic effects on the stark broadening of hydrogenic ion lines in a plasma // High Energy Density Phys - 2023. - Vol. 46. - P. 101035. https://doi.org/10.1016/j.hedp.2023.101035
26. Shrestha R., Subedi D. P., Gurung J. P., Wong C. S. Generation, characterization and application of atmospheric pressure plasma jet // Sains Malaysiana - 2016. - Vol. 45. - №. 11. - P. 1689–1696.
27. Shahrbabaki A. N., Bazazzadeh M., Khoshkhoo R. Investigation on supersonic flow control using nanosecond dielectric barrier discharge plasma actuators // Int. J. Aerosp. Eng - 2021. - Vol. 2021. - P. 2047162. https://doi.org/ 10.1155/2021/2047162
28. Lee S., Lim H. Debye shielding of an electron in various plasma distributions // J. Korean Phys. Soc -2022. - Vol. 80. - №. 2. - P. 153–160. https://doi.org/10.1007/s40042-021-00336-3
29. Orabi T. F., Aadim K. A. Spectroscopic diagnosis of nickel and zinc plasmas produced by plasma jet technique // J. Opt - 2024. https://doi.org/ 10.1007/s12596-024-01891-1.
30. Kramida A., Fuhr J.R. NIST DataBase // Physical Measurement Laboratory - 2023, https://doi.org/10.18434/T46C7N.

31. Khaleel S. F.,. Abbas Q. A. Influence of dielectric media on the plasma characteristics in DBD Discharge // Iraqi J. Sci.,-2022. -P. 2470–2481. https://doi.org/ 10.24996/ijs.2022.63.6.13.

32. Park S., Choe W., Moon S. Y. Yoo S. J. Electron characterization in weakly ionized collisional plasmas: from principles to techniques // Adv. Phys. X. - 2019. - Vol. 4. - № 1. https://doi.org/ 10.1080/23746149.2018.1526114.

33. Dilecce G., Ambrico P. F., Martini L. M., Tosi P. On the determination of the vibrational temperature by optical emission spectroscopy // Plasma Sources Sci. Technol. - 2022. - Vol. 31. - №. 7. - P. 77001. https://doi.org/ 10.1088/1361-6595/ac7f54.

34. Fikry M., Tawfik W., Omar M. Measurement of the electron temperature in a metallic copper using ultrafast laser-induced breakdown spectroscopy // J. Russ. Laser Res - 2020. - Vol. 41. - №. 5. P. 484–490. https://doi.org/ 10.1007/s10946-020-09901-w.

35. Jakob H., Kim M. K. Generation of non-thermal plasmas over large and complex surfaces // Plasma Res. Express. - 2020. - Vol. 2. - №. 3. https://doi.org/ 10.1088/2516-1067/abb2fd.

***Information about authors:***

*Abbas Ibrakhim Karim, associate professor at the University of Baghdad-College of Science-Dept. of Physics (Iraq) e-mail: Ibrahim.kareem1104a@sc.uobaghdad.edu.iq*

IRSTI 29.31.26 https://doi.org/10.26577/phst2024v11i2b010

# A new system to the spectroscopy analysis with multiple X-ray of free electron laser

Thair Abdulkareem Khalil Al-Aish[1*] and Hanady Amjed Kamil[2]

[1]Department of Physics, College of Education for Pure Sciences Ibn Al-Haitham, University of Baghdad, Baghdad, Iraq
[2]Directorate of Education of First Karkh, Ministry of Education, Baghdad, Iraq
*e-mail: thair.ak.i@ihcoedu.uobaghdad.edu.iq

*(Received August 22, 2024; received in revised form November 22, 2024; accepted December 2, 2024)*

The primary goal of this paper is the possibility of improving spectroscopy analysis using a new mechanism that has the ability to detect small crystalline defects and the fast transitions that occur within electronic states, which contributes significantly to the development of various fields and applications of scientific knowledge. The working mechanism is summed up by obtaining two laser pulses with specific specifications within the x-ray range, by creating an executive program (SAMXFEL) using the MATLAB program for the purpose of simulation. This system allows the investigation of rapid changes in the structure of matter. By analyzing the simulation results, two pulses of electron lasers were obtained with wavelengths ranging from (0.316535, 0.114399) nm and powers (927686, 927683) watts, in addition to pulse durations within (1.05512, 0.38133) atto-seconds that ensures that the target material is protected from damage. The proposed system in this paper is mainly based on the spectral and spatial separation of the two pulses to interpret the scattered and diffracted X-rays. The spatial separation allows multiple X-ray pulses to be emitted from different angles of the sample. X-ray diffractography using multiple simultaneous pulses from different angles becomes possible without loss of photon energy generated by the spectrometer.

**Key words:** Spectral analysis, pulses laser, pulse durations, undulator, diffraction.
**PACS number(s): 52. 70. La.**

## 1. Introduction

In general, spectral techniques rely mainly on three types of interactions of electromagnetic radiation with matter, which are emission, absorption and scattering. Because X-rays are of high energy, which are used to eject electrons from the inner shells of atoms to be replaced by electrons from the outer shells. Thus, energy will be emitted as distinct photons for each element, which allows to identify elements and understand how the atoms within various materials interact [1-7].

In the seventeenth century, the optical microscope was discovered, which had a great impact on the scientific revolution, as we were able to see things that were not visible to the naked eye. In 1667, Robert Hooke was able to improve the microscope and used it to examine snow and plants. While others were able to see very small things like hair, bones and skin [8]. William Henry Bragg and his son were the first to use X-ray spectroscopy in the 20th century to study how X-ray radiation interacts with atoms inside crystals, and they won the Nobel Prize in physics in 1915 [9].

In this work, it has been used a new system to the spectroscopy analysis with multiple x-ray of free electron laser (SAMXFEL). This system is characterized by its high ability to diagnose an important case represented by the very rapid transitions of the electronic states and structures of the sample. This is achieved only by using two laser pulses with wavelengths within the X-ray range and using free electron laser technology, which will have a great impact on scientific progress in the fields of physics and chemistry.

## 2. The Technique and mechanism

Analysis of the components of a sample based on irradiating it with a laser pulse based on X-ray free electron lasers (XFELs) technology is currently a very advanced technology for obtaining spectral

analysis of materials at the atomic and molecular levels with high-resolution imaging.

The most important feature of XFELs is that they provide us with very intense and coherent X-ray beams with very short pulse durations, which are essential conditions for studying and analyzing the structure and dynamics of the sample in unprecedented detail, which includes a number of steps such as X-ray Generation, X-ray-Matter Interaction, detection, data analysis, interpretation and visualization [10-15].

XFEL technology has made tremendous scientific progress in the field of materials science, allowing scientists and researchers to study and analyze the basic properties of a sample with exceptional accuracy, as well as explore dynamic processes at the atomic level, which has contributed to the advancement of many civil and military applications [8,9].

In this paper, a new system called SAMXFEL is proposed, based on the self-amplified spontaneous emission scheme (SASE) as shown in Figure (1). Where two laser pulses with different wavelengths within the X-ray range will be generated as a result of the technique of creating two undulators with different gaps instead of one undulator in the path of the accelerated electrons to obtain the best spectral analysis.

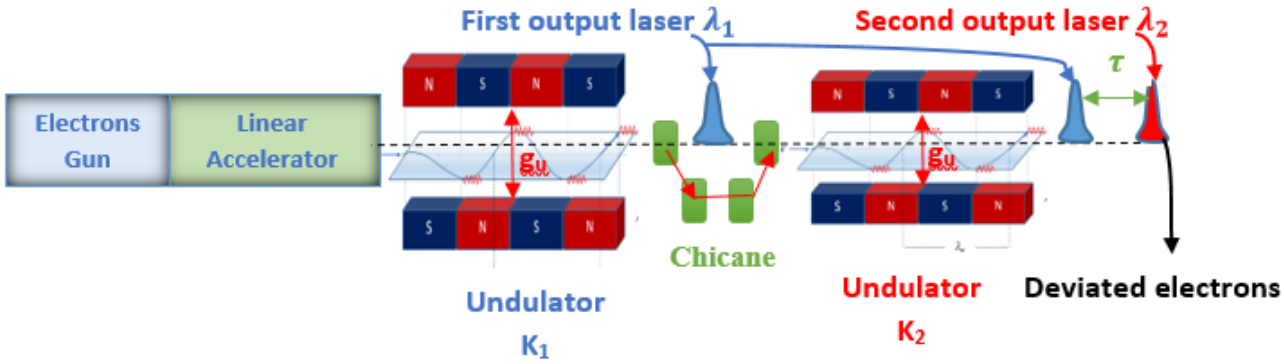



**Figure 1** – The SAMXFEL system with two undulators.

The two pulses are separated for a certain period of time (About a few femto-seconds) by magnets that separate the undulators to delay the electrons. In addition, these pulses have pulse duration in atto-seconds and powers in megawatt. Thus, the SAMXFEL system can explain the mechanism and dynamics of the ultrafast X ray transformations of structures and electronic states, which support greatly to progress of quantum x-ray optics, plasmas, astronomy, ultrafast chemistry [16,17].

The SAMXFEL system allows the investigation of rapid changes in the structure of matter, the two pulses are separated spectrally and spatially to interpret diffracted or scattered X-rays. Spatial separation allows multiple X-ray pulses to be irradiated from different angles of the sample. X-ray diffraction imaging with multiple simultaneous pulses from different angles becomes possible without loss of photon power generated by the spectrometer.

In a free electron laser FEL, any wavelength $\lambda$ of the output laser can be obtained according to equation (1) [18-21].

$$\lambda = \frac{\lambda_u}{2\gamma^2}\left(1 + \frac{k^2}{2}\right) \quad (1)$$

Where $\lambda_u$is the wavelength of electron in undulator, $k$ is the undulator parameter, and $\gamma$ is relativistic Lorentz-factor [21-23].

$$\gamma = \frac{E_e}{m_e c^2} \quad (2)$$

$$k = \frac{e\ \beta\ \lambda_u}{2\pi\ m_e c} \quad (3)$$

Where $E_e$is the electrons beam energy, $m_e$ is the electron mass. $\beta$ is the magnetic field [18,20,23].

$$\beta = 4.22 \exp\left[-\frac{g_u}{\lambda_u}\left(5.08 + 1.54\ \frac{g_u}{\lambda_u}\right)\right] \quad (4)$$

Where $g_u$is the distance between the two rows magnets of undulaor.

The power $P_u$ of output laser for two pulses is given by the equation(5): [18-20].

$$P_u = \left(\frac{\chi^2\ c\ E_e\ N_{PH}}{9\ \lambda}\right) e^{(21.57\ \rho\ L_u/\lambda_u)} \quad (5)$$

Where $\chi$ is Pierce parameter, $L_u$is the length of the undulator and $N_{PH}$ is the coherent photons [23-26]:

$$N_{PH} = 2\ \chi\ E_e\ \lambda/h\ c \quad (6)$$

## 3. Results and discussion of simulation

In order to obtain the two laser pulses proposed in this paper, an executive SAMXFEL program was created using MATLAB R2023b (see Figure 2). SAMXFEL contains many parameters to perform simulations and obtain the dimensions and specifications of the free-electron laser system suitable for producing the two proposed laser pulses as shown in Figure (1).

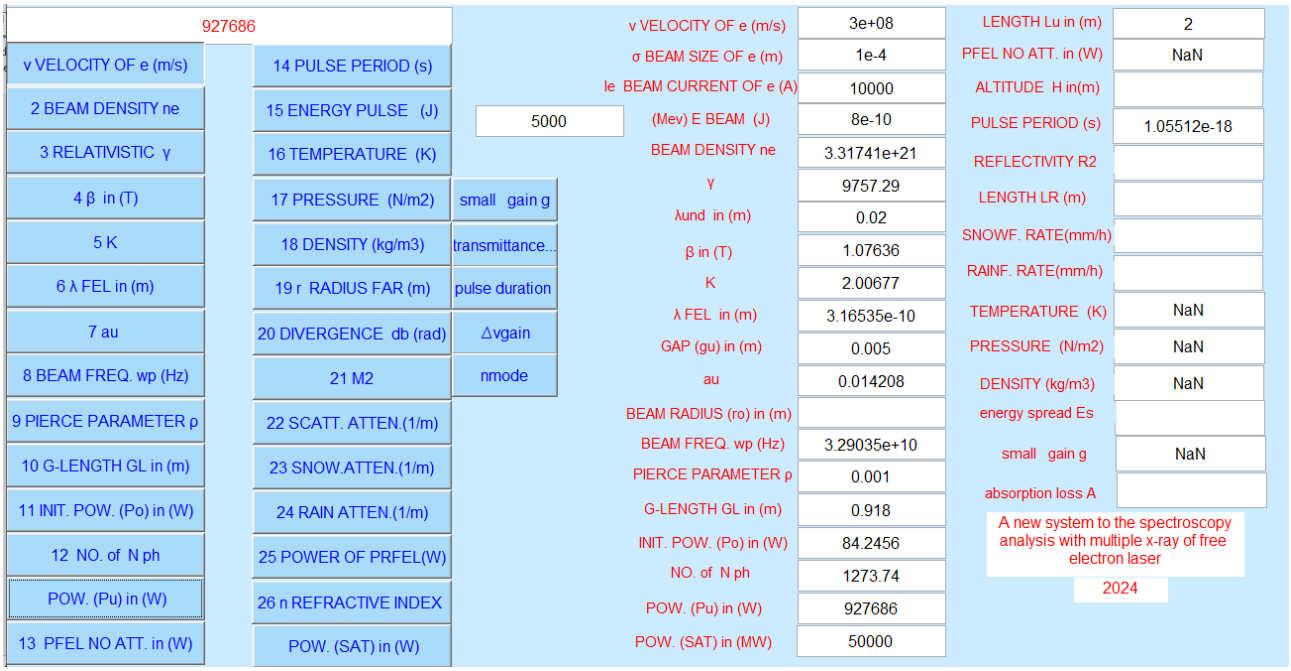



**Figure 2** – An executive SAMXFEL program interface.

Table 1 represents the results obtained, dimensions and specifications of the free electron laser system proposed for spectroscopy. Two laser pulses with wavelengths of 0.114399 nm and 0.114399 nm were obtained within the X-ray range by using Equation 1.

**Table 1** – The data of simulation for the dimensions and specifications of SAMXFEL system.

| $E_e$ (Mev) | $\lambda_u$ (m) | $\gamma$ | $\rho$ | $L_u$ (m) | | |
|---|---|---|---|---|---|---|
| 5000 | 0.02 | 9757.29 | 0.001 | 2 | | |
| $g_u$(m) | β(T) | K($Tm$) | $\lambda$(n$m$) | $N_{PH}$ | PP(as) | $P_u$ (w) |
| 0.005 | 1.07636 | 2.00677 | 0.316535 | 1273.74 | 1.05512 | 927686 |
| 0.01 | 0.226465 | 0.422221 | 0.114399 | 460.342 | 0.38133 | 927683 |

The basic idea for obtaining the two pulses is to fix the majority of the parameters in the system while changing one parameter, which is shown in Figure 2. Two undulaors were placed inside the free electron laser system, differing in the distance $g_u$ between the magnetic poles of the undulaors, which is shown in Figure 1.

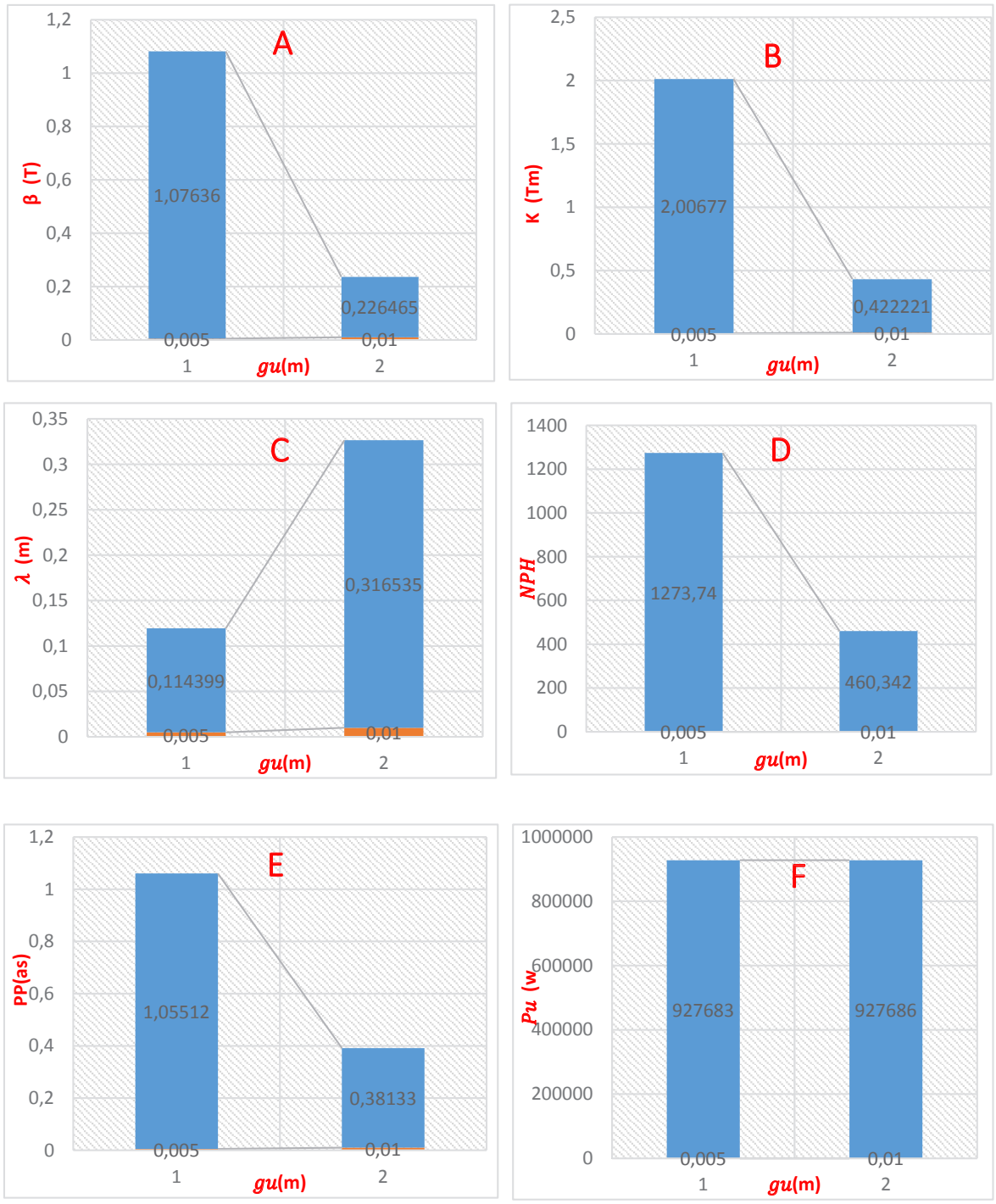



**Figure 3** – The relations between $g_u$ versus (β, K, λ, $N_{PH}$, PP , $P_u$ )

According to Equation 4, changing the distance $g_u$ necessarily leads to a change in the value of the magnetic field β arising between the magnets in an inverse relation as shown in Figure 3-A , this leads

to a change in the value of the parameter k according to Equation 3 in a direct relation. Figure 3-B, is clearly shows that reducing the distance $g_u$ between the rows of magnets necessarily leads to an increase in the parameter K as a result of a decrease in the strength of the magnetic field β responsible for the oscillatory movement of electrons inside the undulator. Thus, the wavelength $\lambda$ of the two resulting laser pulses was controlled and tuned according to Equation 1 as shown in Figure 3-C. By changing the chicane parameters, the time interval between the two pulses laser can be tuned with femtosecond precision. This is considered a very important feature of the SAMXFEL system to achieve better spectral analysis and reach the goal of the paper described in the previous paragraph.

## 4. Conclusion

This is a very important feature of the SAMXFEL system, as the two laser pulses, with close powers and a relatively large difference in wavelength, have a very large effect during interaction with the target material during spectroscopic analysis. Because two different bands of the X-ray band are absorbed with the same effective power. This leads to the generation of different peaks, which means obtaining the best possible spectroscopic analysis and detecting minor crystalline defects and rapid phase transitions. In addition, it can explain the mechanism and dynamics of electronic states and structures, which will greatly contribute to the progress of physical and chemical scientific fields.

From analyzing the simulation results obtained using the SAMXFEL system, it can be concluded that it is possible to obtain two laser pulses within the X-ray range with characteristics suitable for the

Figure 3-D, indicates an important fact in the free-electron laser system, represented by the increased influence of the magnetic field on the movement of the electrons passing through it. Photons are produced from the oscillation of the electrons, which increase significantly when the wavelength of the two resulting laser pulses is increased according to Equation 6.

Figures 3-E and 3-F, show the features and properties of the resulting laser pulses in terms of pulse duration, which changes significantly as a result of changing the wavelength of the laser pulses, while we note that the power of the two laser pulses is very close, on the order of a megawatt, due to the power depending on several variable parameters according to Equation 5.

spectroscopy process. So that the two pulses can be separated spatially and temporally to irradiate the target material at different angles to obtain a diffraction pattern without losing the power of the simultaneous photons resulting from the spectrometer, and to achieve a spectral analysis characterized by high accuracy. Obtaining ultra-short pulse durations for both laser pulses within a atto-seconds ensures that the target material is protected from damage.

## Acknowledgments

I would like to extend my sincere thanks and appreciation to the Department of Physics at the College of Education for Pure Sciences Ibn Al-Haitham / University of Baghdad for providing support and assistance in completing this research by providing scientific facilities in all areas of work to help overcome obstacles.

## References

1. Ignacio P., Nieto Faza O., Interaction of radiation with matter. Structure elucidation in organic chemistry. The Search for the Right Tools – 2015. – Vol.1-26. https://doi.org/10.1002/9783527664610.ch1

2. Band Y. Light and matter: electromagnetism, optics, spectroscopy and lasers. (Wiley & Sons, New York – 2006. P.656.

3. Warren D. B. The basics of spectroscopy, SPIE Press. Washington, USA. 2001. 142 p.

4. Bertin E.P. Principles and practice of X-ray spectrometric analysis. Springer Science & Business Media, University of Michigan, 1985, 1080 p. https://doi.org/10.1007/978-1-4613-4416-2

5. Marfunin A.S. Spectroscopy, luminescence and radiation centers in minerals. Springer Science & Business Media, Berlin. 1979. https://doi.org/10.1007/978-3-642-67112-8.

6. Grunter W., Klementiev K. X-ray absorption spectroscopy principles and practical use in materials analysis // Physical Sciences Reviews. – 2020. – Vol. 5. №.4. https://doi.org/10.1515/psr-2017-0181 .

7. Evans J. X-ray absorption spectroscopy for the chemical and materials sciences. John Wiley & Sons. 2018.- P.1-8. https://doi.org/10.1002/9781118676165

8. Mingos, D.M.P. Early History of X-Ray Crystallography. In: Mingos, D.M.P., Raithby, P.R. (eds) 21st Century Challenges in Chemical Crystallography I. Structure and Bonding, vol 185. Springer, Cham. 2020. https://doi.org/10.1007/430_2020_73

9. Brooks-Bartlett J.C., Garman E.F. The Nobel science: one hundred years of crystallography // Interdisciplinary Science Reviews. – 2015. – Vol.40(3). – P.44-264. https://doi.org/10.1179/0308018815Z.000000000116

10. Jakubowski, N. Freddy Adams, Carlo Barbante: Chemical imaging analysis // Anal Bioanal Chem. -2016. -Vol.408. -P. 4199–4201. https://doi.org/10.1007/s00216-016-9517-9

11. Bergman U., Yachandra V. K., Yano J. X-ray free electron lasers: applications in materials, chemistry and biology. Royal Society of Chemistry. 2017. Vol. 18. 463 p. https://doi.org/10.1039/9781782624097

12. Uwe B., Kern J., Robert W., Schoenlein, Wernet P., Yachandra V., Yano J. Using X-ray free-electron lasers for spectroscopy of molecular catalysts and metalloenzymes // Nature Reviews Physics. – 2021. Vol.3. – No. 4. – P.264-282. https://doi.org/10.1038/s42254-021-00289-3

13. Kirian R. A, Chapman H. N. Imaging of objects by coherent diffraction of X-ray free-electron laser pulses // Synchrotron light sources and free-electron lasers: Accelerator physics, instrumentation and science applications. – 2016. – P.1337-1397. https://doi.org/10.1007/978-3-319-04507-8_27-2

14. Huang N., Deng H., Liu B., Wang D., Zhao Z.,. Features and futures of X-ray free-electron lasers // The Innovation. – 2021. – Vol. 2(2). – P. 100097 https://doi.org/10.1016/j.xinn.2021.100097

15. Serkez S., Geloni G., Tomin S, Feng G., Gryzlova E., Grum-Grzhimailo A. N., Meyer M. Overview of options for generating high-brightness attosecond x-ray pulses at free-electron lasers and applications at the European XFEL // Journal of Optics. – 2018. – Vol. 20(2). – P. 024005. https://doi.org/10.1088/2040-8986/aa9f4f

16. Dunne M., Schoenlein R. W., Cryan J. P., Wolf T. J. A. Free electron lasers for X-ray scattering and diffraction // Theoretical and Computational Chemistry Series. – 2023. – P.301-343. https://doi.org/10.1039/9781837671564

17. Dunning D., Angal-Kalinin D., Clarke J. A., Henderson J. R., Mathisen S. L., Militsyn B. L., Marangos J. P. An introduction to the UK XFEL conceptual design and options analysis // 67th ICFA Advanced Beam Dynamics Workshop on Future Light Sources – 2023. – P.4. https://doi.org/10.18429/JACoW-FLS2023-TU4P13

18. Al-Aish T.A.K., Kamil H.A., Ultra-short pulses generation of free electron laser // The Scientific Journal of King Faisal University: Basic and Applied Sciences – 2022. Vol.23(2). – P. 28 – 32. https://doi.org/10.37575/b/sci/220045

19. Mitri S. Di., On the Importance of electron beam brightness in high gain free electron lasers // Photonics. – 2015. -Vol. 2. – P. 317–341. https://doi.org/10.3390/photonics2020317

20. Ali M. A., Al-Aish T. A. K., Kamil H. A., Analyzing and simulating the mechanism of laser medical therapy // AIP Conference Proceedings. – 2022. – Vol. 2437. -P. 020020. https://doi.org/10.1063/5.0092605

21. Yahaghi A., Fallahi A., Kärtner F., Free electron laser simulation tool based on FDTD/PIC in the Lorentz boosted frame // 7th International Particle Accelerator Conference (IPAC'16), Busan, Korea -2016.P. 3061–3063. https://doi.org/10.18429/JACoW-IPAC2016-WEPOY035

22. Al-Aish T.A.K., Kamil H.A. Design and establishment of an implementation to simulate and analyze the tertiary undulator of the FEL // The Scientific Journal of King Faisal University: Basic and Applied Sciences. – 2022. – Vol. 23(2). – P.39–42. https://doi.org/10.37575/b/sci/220036

23. Saleh M. K., Al-Aish T. A. K. Analyzing and simulate the near-mid field propagation for a Gaussian beam of x-ray laser // AIP Conference Proceedings. – 2023. – Vol. 3018. – No.1 https://doi.org/10.1063/5.0171743

24. Jaeschke E. J., Khan S., Schneider J. R., and Hastings J. Synchrotron light sources and free-electron lasers: Accelerator physics. Instrumentation and Science Applications. Switzerland: Springer Reference. 2016. 1400 p. https://doi.org/10.1007/978-3-030-23201-6

25. van Tilborg J., Barber S. K., Isono F., Schroeder C. B., Esarey E., Leemans W. P. Free-electron lasers driven by laser plasma accelerators // AIP Conference Proceedings. – 2017. -Vol. 1812. -P. 1–7. http://dx.doi.org/10.1063/1.4975838

26. Palma E. Di, Sabia E., Dattoli G., Licciardi S., Spassovsky I., Cyclotron auto resonance maser and free electron laser devices: a unified point of view // J. Plasma Phys. – 2017. – Vol. 83. – No. 1. – P. 1–15. https://doi.org/10.1017/S0022377816001239

***Information about authors:***

*Thair Abdulkareem Khalil Al-Aish, PhD, professor at the Department of Physics, College of Education for Pure Sciences Ibn Al-Haitham, University of Baghdad, Baghdad, Iraq, e-mail: thair.ak.i@ihcoedu.uobaghdad.edu.iq*

*Hanady Amjed Kamil, master of science, Directorate of Education of First Karkh, Ministry of Education, Baghdad, Iraq. e-mail:hanadyamjedkamil@gmail.com*

IRSTI 27.35.39 https://doi.org/10.26577/phst2024v11i2b011

# Cosmological model in modified f(R, G) Gauss-Bonnet gravity

I.K. Nurat[1*], S.R. Myrzakul[1] and F.B. Belisarova[2]

[1]L.N. Gumilyov Eurasian National University, Astana, Kazakhstan
[2]Al-Farabi Kazakh National University, Almaty, Kazakhstan
*e-mail: indira.nurat@mail.ru

*(Received October 20, 2024; received in revised form November 28, 2024; accepted December 2, 2024)*

In this work, the Gauss-Bonnet model of modified gravity is investigated, where some arbitrary function *G* is added to the Einstein-Hilbert action. This theory explains the accelerated expansion of the Universe. In this work. The article proposes *F(R, G) = f(R) + η(G)* modified gravity, which considers two gravities *f(R)* and *η(G)*, where *f(R)* is a function from the Ricci scalar, *η(G)* is a function from the Gauss-Bonnet invariant. The model is considered in a flat, isotropic and homogeneous Universe. As a result of some mathematical formalism, the dependence of the function *f(R)* on the scalar of curvature *R* and on *t* time is found. Geometric and dynamic parameters of the cosmological model *F(R, G) = f(R) + η(G)* were analyzed. Equations of motion and cosmological parameters, such as the Hubble parameter and scale factor, were obtained for the investigated model. Analyzing the obtained solutions of the scale factor, it was shown that the model describes the exponential acceleration of the Universe. Thus, it was found that the cosmological model under study has a similar interpretation to the de Sitter cosmological model.

**Key words:** Gauss-Bonnet gravity, *f(R, G)* gravity, Hubble parameter, acceleration of the Universe.
**PACS number(s):** 04.50.Kd.

## 1. Introduction

Many astronomical studies have shown that the Universe is currently expanding at an accelerated rate [1]-[5]. Most cases of general relativity (GR) are generalized by incorporating scalar curvatures, higher-order curvature terms, and also connections with dynamic scalar fields [6], [7]. Consequently, there is growing interest in studying modifications and generalizations of Einstein's theory. Various approaches and models exist for investigating the expansion of the Universe. Effective cosmological results can be obtained using modified theories of gravity. Various modified models and gravitational theories have been proposed, including *f(R)* gravity [8]-[10], $f(G)$ gravity [11] , scalar-tensor theory [12], $f(R,T)$ gravity [13] and $f(R,G)$ gravity [11], where $R$ is the Ricci scalar, $G$ is the Gauss-Bonnet invariant, $T$ is the torsion.

*f(R)* gravity, a kind of modified theory of gravity that generalizes Einstein's general theory of relativity. Over the past few decades, various forms of the $f(R)$ function have been investigated. Among these functions there are quite viable ones that correctly describe cosmological dynamics, a smooth transition between different cosmological epochs [14]. The cosmological interest in $f(R)$ gravity arises from the fact that these theories naturally demonstrate the late-time accelerated expansion of the Universe without the need for matter fields like dark energy. In a study by [15], a scheme for cosmological reconstruction of $f(R)$ gravity is presented. Among other existing theories, it can be shown that gravitational models based on $f(R)$ describe the transition from a matter-dominated phase to an accelerated phase [16]. However, it is well-known that $f(R)$ gravity has some imperfections. For instance, at the nonlinear level, issues related to curvature singularities arise [17]. As a result of the classical GRT tests obtained, most of the proposed $f(R)$ models are excluded in the limitations of the Solar System regime. In order to circumvent these imperfections, gravity $f(R)$ has been expanded to take into account additional scalars in the Einstein-Hilbert action. In this regard, an

optimistic alternative arises, such as $f(R,G)$ gravity [18-24]. The stability of cosmological solutions in $f(R,G)$ gravity is discussed in [25]. Theories like $f(R,G)$ satisfy the constraints of the Solar System [26].

In the Gauss-Bonnet theory of gravitation the Einstein action is modified by the function $f(G)$, where an arbitrary function $G$ is a quadratic invariant of the Gauss-Bonnet equation [11]. It is known that $G$ is a topological invariant in four dimensions, which participates in the formulation of quantum field theory in curved space. The invariant $G$ arises under gravitational influences containing second-order curvature invariants. The Gauss-Bonnet function $f(G)$ is added to the gravitational interaction to explain the accelerating expansion of the Universe at late times [27]. Moreover, such modified Gauss-Bonnet gravity can describe the transition from deceleration to acceleration as well as the phantom gap crossing. One can search for more serious restrictions on its form by comparing the theory with observational data. Models containing the Gauss-Bonnet invariant have attracted interest because of the ability of $G$ to simplify the dynamics of the system. In recent years, modified theories associated with the topological Gauss-Bonnet term have been studied in depth [28]. In [29], a class of Horndeski Lagrangian, with a scalar k-essence field associated to the Gauss-Bonnet term, is considered. A reconstruction method is proposed to derive viable models in accordance with cosmological data. The Gauss-Bonnet invariant is also considered in the $\Lambda$ CDM cosmological model [30]. It is shown that the $\Lambda$CDM model can be explained in such theories, where the problem of the cosmological constant is explained in the form of a modified of the cosmological constant.

In this paper, the evolution of the Universe is investigated by considering two gravity separated functions, gravity $f(R)$ and $\eta(G)$, where $f(R)$ is a function of the Ricci scalar R and $\eta(G)$ is a function of the Gauss-Bonnet invariant $G$ [31]-[35]. This theory without any cosmological constant can predict different phases of the evolution of the universe [36], [37]. The $G$ in the curvature invariant corresponds to the coevolution of the early Universe. Moreover, this theory describes accelerating waves of celestial objects. It also effectively explains the transition from the deceleration phase to the acceleration phase [38]. Thus, it is possible to construct feasible and consistent modified models using $f(G)$ [11], [39]. Section 2 presents the mathematical formalism of the cosmological model $F(R,G)$ of gravity. The equations of motion were derived and solutions of the unknown functions $f(R)$, $\eta(G)$ and the Hubble parameter, scale factor, were shown. In Sec. 3, cosmological parameters such as pressure, energy density, and state parameter are found and their graphical behavior is shown.

## 2. The cosmological model of $F(R,G)$ gravity

Consider the following action for $F(R,G)$ gravity

$$S=\int\sqrt{-g}\left[\frac{1}{2k^2}F(R,G)+L_m\right]d^4x, \qquad (1)$$

where $g$ is the metric determinant, $L_m$ – standard matter Lagrangian, $k^2=8\pi G_N$, $G_N$ is the Newtonian gravitational constant and the speed of light $c$ is assumed to be 1. Now it is necessary to bring Lagrangian into canonical form $L(a,\dot{a},R,\dot{R},G,\dot{G},t)$ from the action (1) to obtain the equation of motion. Here $a=a(t)$ is the scale factor, dependent on cosmological time $t$ and defined in the Friedman-Roberston-Walker metric (FRW)

$$ds^2=-dt^2+a(t)^2(dx^2+dy^2+dz^2), \qquad (2)$$

Next, using the Lagrange multiplier method (see for example [40]), we can set $R$ and $G$ as constraints on the dynamics. To eliminate high-order derivatives, we select a suitable Lagrange multiplier and integrate by parts. We rewrite action (1) for flat FRW metric as follows:

$$S=\int d^4xa^3\left[f(R)+\eta(G)-\alpha\left(R-6\left(\frac{\ddot{a}}{a}+\frac{\dot{a}^2}{a^2}\right)\right)-\beta\left(G-\frac{24\dot{a}^2\ddot{a}}{a^3}\right)\right], \qquad (3)$$

here the Ricci scalar $R$ and the Gauss-Bonnet invariant $G$ are defined as follows in terms of the Hubble parameter $H = \frac{\dot{a}}{a}$ for FRW metric:

$$R = 6\dot{H} + 12H^2, \tag{4}$$

$$G = 24H^2(\dot{H} + H^2). \tag{5}$$

At (4) $\alpha$ and $\beta$ are the Lagrangian multipliers that can be directly found by varying with respect to $R$ and $G$, giving $\alpha = f_R, \beta = \eta_G$, respectively. Where the indices denote derivatives with respect to the given variables $f_R = \frac{df(R)}{dR}, \eta_G = \frac{d\eta(G)}{dG}$.

The equation of action (4) is reduced to the following form

$$S = \int d^4x\left[a^3 f + a^3\eta^3 - a^3 R f_R + 6a^2\ddot{a}f_R + 6a\dot{a}^2 f_R - a^3 G\eta_G + 24\dot{a}^2\ddot{a}\eta_G\right] \tag{6}$$

According to the equation of action (4), we write the Lagrange function as

$$L = a^3 f + a^3\eta - a^3 R f_R - 6a^2\dot{a}\dot{R}f_{RR} - \\ -6a\dot{a}^2 f_R - a^3 G\eta_G - 8\dot{a}^3\dot{G}\eta_{GG}. \tag{7}$$

The Euler-Lagrange equation is written in the following form

$$\frac{\partial L}{\partial q} - \frac{d}{dt}\left(\frac{\partial L}{\partial \dot{q}}\right) = 0, \tag{8}$$

$$E_L = \left(\frac{\partial L}{\partial \dot{q}}\right)\dot{q} - L = 0, \tag{9}$$

where $q = a, R, G$ are generalized variables.

For the FRW metric the pressure $p$ and the density $\rho$ are defined as follows

$$p = -(3H^2 + 2\dot{H}), \tag{10}$$

$$\rho = 3H^2. \tag{11}$$

Also from energy condition

Using equation (5) and (7) we find

$$p = \frac{1}{2f_R}\left[f + \eta - Rf_R - G\eta_G + 4H\dot{R}f_{RR} + (2\dot{R}f_{RR})_t + 8H^2(\dot{G}\eta_{GG})_t + 16H\dot{G}\eta_{GG}(\dot{H} + H^2)\right], \tag{12}$$

$$\rho = 3H^2 = \frac{1}{2f_R}\left[-f - \eta + Rf_R + G\eta_G - 6H\dot{R}f_{RR} - 24H^3\dot{G}\eta_{GG}\right] \tag{13}$$

Adding up equations (13) and (14), we obtain the following equation

$$\dot{H} = \frac{1}{2f_R}\left[H\left(\dot{R}f_{RR} + 4H^2\dot{G}\eta_{GG}\right) - \left(\dot{R}^2 f_{RRR} + 4H^2\dot{G}^2\eta_{GG}\right) - \left(\ddot{R}f_{RR} + 4H^2\ddot{G}\eta_{GG}\right) - 8H\dot{H}\dot{G}\eta_{GG}\right] \tag{14}$$

Let's denote

$$A = \dot{R}f_{RR} + 4H^2\dot{G}\eta_{GG}, \tag{15}$$

then

$$\dot{A} = \left(\dot{R}^2 f_{RRR} + 4H^2\dot{G}^2\eta_{GG}\right) + \\ +(\ddot{R}f_{RR} + 4H^2\ddot{G}\eta_{GG}) + 8H\dot{H}\dot{G}\eta_{GG}. \tag{16}$$

Using (18) and (19) equations, we obtain equation (17) in a simplified form

$$\dot{H} = \frac{1}{2f_R}\left(HA - \dot{A}\right), \tag{17}$$

To solve (20) the differential equation, consider the following case

$$f_R = \frac{A}{2}. \tag{18}$$

Then equation (18) is reduced to a differential equation with separated variables

$$\dot{H} - H = -\frac{\dot{A}}{A} = C_1, \tag{19}$$

where $C_1 = const$.

The solution of the differential equation (22) can be found in the following form

$$H = e^{(t-t_0)} - C_1, \tag{20}$$

where $t_0$ - present current time and $t$ variable time, those $t_0 > t$,

$$A = e^{C_1(t-t_0)}. \tag{21}$$

According to (18) and (21) $f_R$ is written as

$$f_R = \frac{e^{-C_1(t-t_0)}}{2}. \tag{22}$$

Considering that $\left(f_R\right)_t = \dot{R}f_{RR}$ and $(\eta_G)_t = \dot{G}\eta_{GG}$, where $t$ in the index means the time derivative, then the equation (15) can be written in the following form

$$\frac{2f_R - (f_R)_t}{4H^2} = (\eta_G)_t. \tag{23}$$

Integrating equation (23), we obtain the following

$$\eta_G = -\int \frac{C_1 e^{-C_1(t-t_0)}}{8(e^{t-t_0} - C_1)^2}\,dt. \tag{24}$$

Next, consider the value of the equation for $f_R$. Substituting (20) into (2) we get the quadratic equation

$$12\left[\left(2f_R\right)^{-1/C_1} - C_1\right]^2 + 6\left(2f_R\right)^{-1/C_1} - R = 0. \tag{25}$$

Denoting $b = \left(2f_R\right)^{-1/C_1}$. we get the quadratic equation

$$b^2 - \left(2C_1 - \frac{1}{2}\right)b + (C_1)^2 - \frac{R}{12} = 0, \tag{26}$$

Solving this equation we get

$$b_{1,2} = 2\left(C_1 - \frac{1}{4}\right) \pm \sqrt{\frac{R}{3} - 2C_1 + \frac{1}{4}}. \tag{27}$$

Considering (22) and (27) we write the equation for $f_R$

$$f_R = \frac{1}{2}\left[C_1 - \frac{1}{4} \pm \frac{1}{2}\sqrt{\frac{R}{3} - 2C_1 + \frac{1}{4}}\right]^{-C_1}. \tag{28}$$

Since the solution of (24) and (28) equations is complex, consider a special case for $C_1 = -1$ and obtain solutions of integral equations in the following form

$$\eta_G = -\frac{1}{8\left(e^{(t-t_0)} + 1\right)} \tag{29}$$

and

$$f(R) = -\frac{5}{8} + \frac{1}{24}\sqrt{12R + 81}. \tag{30}$$

The derivatives of functions $\eta(G)$ and $f(R)$ on time $t$ are defined as

$$\dot{\eta} = \eta_G \dot{G}, \tag{31}$$

$$\dot{f} = f_R \dot{R}. \tag{32}$$

Then considering (20), we write the derivative of the function $G$ and $R$ in (4), (5) by time $t$

$$\dot{G} = 48\left(e^{2(t-t_0)} + e^{(t-t_0)}\right) \times$$

$$\times \left(e^{(t-t_0)} + \left(e^{(t-t_0)} + 1\right)^2\right) +$$

$$+24\left(e^{(t-t_0)} + 1\right)^2\left(3e^{(t-t_0)} + 2e^{2(t-t_0)}\right) \quad (33)$$

$$\dot{R} = 24e^{2(t-t_0)} + 30e^{(t-t_0)}. \quad (34)$$

Substituting equations (29) and (33) into (31) we obtain the function $\eta$ dependent on $t$

$$\eta(t) = -4e^{3(t-t_0)} - \frac{33}{2}e^{2(t-t_0)} - 15e^{(t-t_0)}. \quad (35)$$

Using equations (22) and (34) we obtain the function $f$ dependent on $t$

$$f(t) = 4e^{3(t-t_0)} + \frac{15}{2}e^{2(t-t_0)}. \quad (36)$$

## 3. Cosmological parameters

Cosmological parameters, global parameters of the Universe that characterize its composition and dynamics, are determined according to observational data or derived from them. The main cosmological parameters considered in this paper are the Hubble parameter, the scale factor, and the equation of state parameter relating its pressure and density. The most accurate measurements of the global parameters of the Universe are obtained from observed data on supernovae of type Ia stars and from the anisotropy characteristics of the relic radiation. In addition, data from the cosmic distance scale are used to measure the Hubble parameter.

Using equations (18) we can find the scale factor $a$ in the following form

$$a = e^{\exp(t-t_0)-C_1(t-t_0)+C_2}. \quad (37)$$

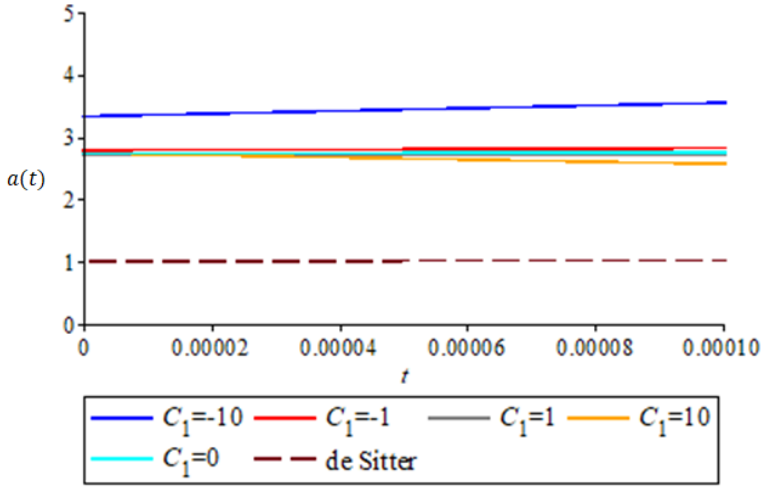



**Figure 1** – Variation of scale factor $a$ over time $t$ at $C_1 = -10$ (blue line), $C_1 = -1$ (red line), $C_1 = 0$ (blue line), $C_1 = 1$ (gray line), $C_1 = 10$ (yellow line), de Sitter model (dashed line)

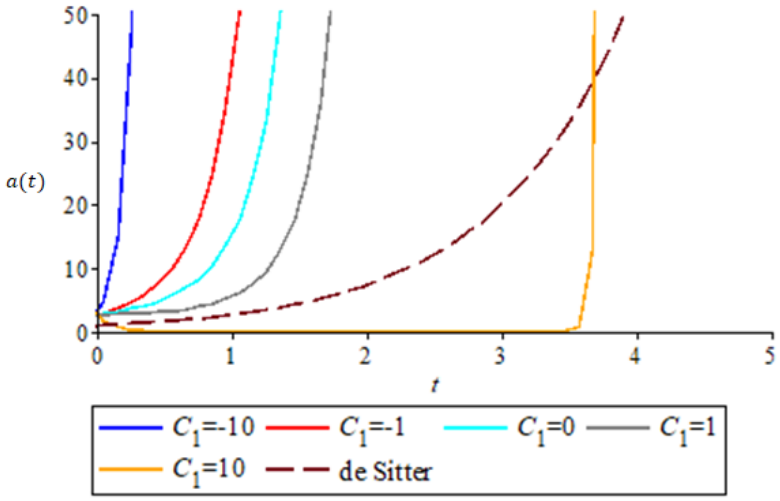



**Figure 2** – Variation of scale factor $a$ over time $t$ at $C_1 = -10$ (blue line), $C_1 = -1$ (red line), $C_1 = 0$ (blue line), $C_1 = 1$ (gray line), $C_1 = 10$ (yellow line), de Sitter model (dashed line)

The cosmographic evolution of the scale factor can be seen in Figure 1, at $C_2 = 0$. In Figure 1 we can observe the evolution of the scale factor at early times for the cosmological model under study. We also compare the behavior of these graphs with the behavior of the de Sitter model graph, since the de Sitter model also describes the exponential expansion of the Universe. Epochs from the Big Bang $10^{-43}$ s to the quark confinement $10^{-4}$ s, including the $10^{-36}$ s inflation stage, are considered. The graph showed that in this time interval all values are stationary and have larger values of the scale factor relative to the Einstein Universe. At large negative values of $C_1$ the values of the scale factor are larger.

Figure 2 shows the variation of the plots at later times. As can be seen, the scale factor of the Gauss-Bonnet model at $C_1 = -10;-1;0;1$ grows exponentially faster compared to the de Sitter model. Figure 2 shows that at large positive values of $C_1$ the stationary period is longer than at smaller and negative values.

The expansion of the Universe is classified using different phases of the $\omega$ state parameter. The state parameter $\omega$ is an immeasurable quantity and defined as

$$\omega = \frac{p}{\rho}, \tag{38}$$

where $p$ is the pressure and $\rho$ is the energy density of the matter distribution, equal to the ratio of the total average density of the Universe to the critical density.

$p$ and $\rho$ can be written in the following form

$$p = -3e^{2^{2(t-t_0)}} - 8e^{t-t_0} + \frac{3}{e^{t-t_0}} - 3 \tag{39}$$

and

$$\rho = 3e^{2(t-t_0)} + 6e^{t-t_0} - \frac{3}{e^{t-t_0}} + 3. \tag{40}$$

Substituting (39), (40) into the equation of state (38), we obtain $\omega$

$$\omega = -1 - \frac{2e^{t-t_0}}{3\left(e^{t-t_0}+1\right)^2 - \frac{3}{e^{t-t_0}}}. \tag{41}$$

The graphical result of $p$ and $\rho$ can be seen in the figures below

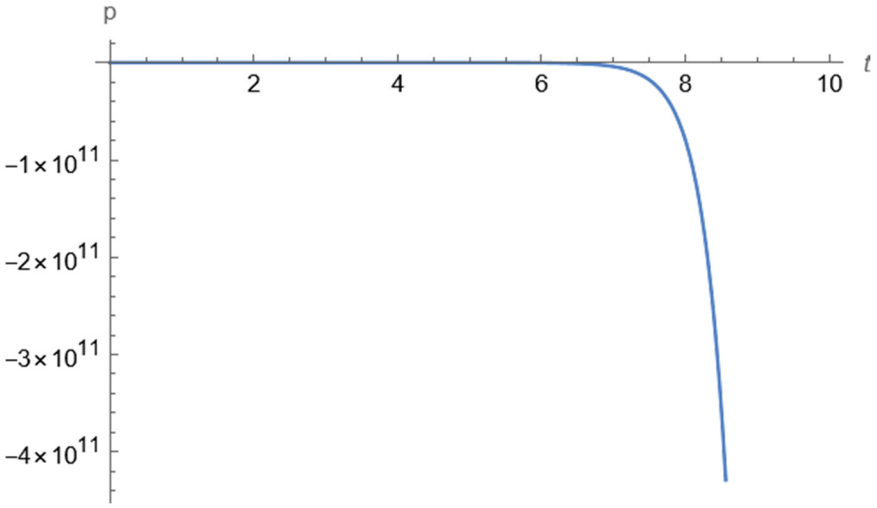



**Figure 3** – Change of pressure $p$ over time $t$

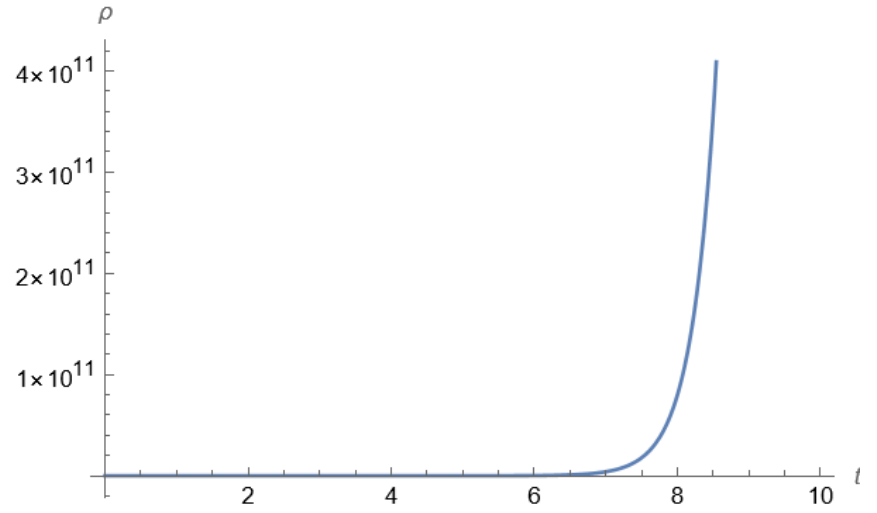



**Figure 4** – Change of energy density $\rho$ over time $t$

As can be seen in Figure 3, the pressure $p$ has a negative value, which indicates the expansion of the Universe. Figure 4 shows that the energy density has a positive value.

In the decelerated phase, when cold dark matter or dusty liquid dominates, the state parameter is defined as $\omega = 0$, and in the radiation epoch $0 < \omega < 1/3$ and in the rigid liquid $\omega = 1$. In the accelerated phase at the cosmological constant or in the vacuum era $\omega = -1$ , in the quintessence and quintom epoch $-1 < \omega < -1/3$

Figure 5 shows the graphical behavior of the state parameter of the investigated model of modified Gauss-Bonnet gravity. This figure clearly shows that the parameter of the equation of state changes tending to a negative value in the range $-1 \le \omega \le 0$, which shows good agreement with observational data of type Ia supernovae.

.

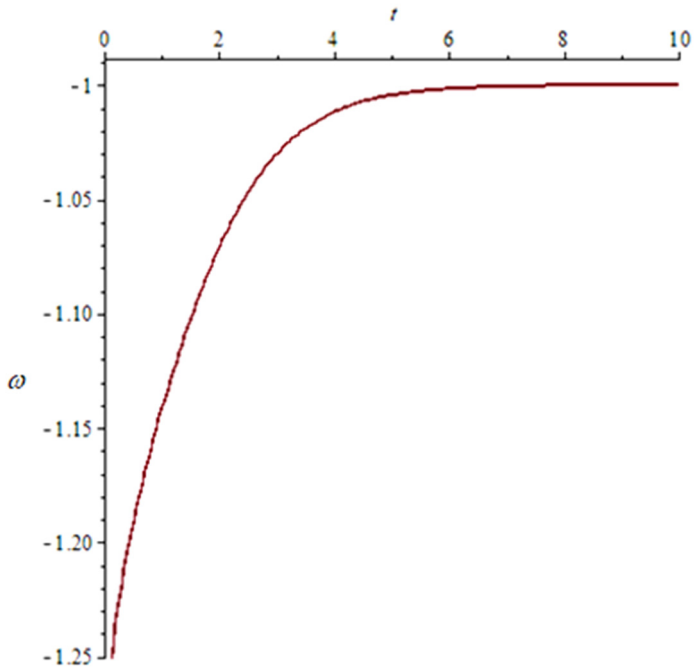



**Figure 5** – Change of state parameter $\omega$ over time $t$

## 4. Conclusion

In this paper the problem of cosmic acceleration in modified $f(R)$, $\eta(G)$ Gauss-Bonnet gravity is investigated. The dependences of the physical quantities $f(R)$, $\eta(G)$, the scale factor, and the Hubble parameter on the cosmological time $t$ are obtained. We found the function $f(R)$ dependent on the curvature scalar $R$. We also carried out a physical analysis of the obtained solution of the scale factor and found that this model has an adequate cosmological interpretation similar to the de Sitter cosmological model. The found values of the Hubble parameter and scale factor describe the exponential expansion of the Universe, which is shown in Figure 2. Figure 5 shows that the state parameter starts near zero at the beginning of cosmic time, i.e., the Universe is dominated by matter. Then at the end of cosmic time it progresses to a near negative value of -1, which exhibits a vacuum era-like behavior. As a result, our research model is realistic. Thus, it is shown that this modified Gauss-Bonnet gravity model describes the acceleration of the Universe.

**References**

1. Riess A. G. et al. Observational evidence from supernovae for an accelerating universe and a cosmological constant // The astronomical journal. – 1998. – Vol. 116. – №. 3. – https://doi.org/1009. 10.1086/300499

2. Perlmutter S., Schmidt B. P. Measuring cosmology with supernovae //Supernovae and Gamma-Ray Bursters. – 2003. – P. 195-217.

3. Bennett C. L. et al. The microwave anisotropy probe* mission //The Astrophysical Journal. – 2003. – Vol. 583. – №. 1. – P. 1. https://doi.org/10.1086/345346

4. Boughn S., Crittenden R. A correlation between the cosmic microwave background and large-scale structure in the Universe //Nature. – 2004. – Vol. 427. – №. 6969. – P. 45-47. https://doi.org/10.1038/nature02139

5. Eisenstein D. J. et al. Detection of the baryon acoustic peak in the large-scale correlation function of SDSS luminous red galaxies //The Astrophysical Journal. – 2005. – Vol. 633. – №. 2. – P. 560. https://doi.org/10.48550/arXiv.astro-ph/0501171

6. Aghanim N. et al. Planck 2018 results-VI. Cosmological parameters //Astronomy & Astrophysics. – 2020. – Vol. 641. – P. A6. https://doi.org/10.1051/0004-6361/201833910

7. Capozziello S., De Laurentis M. Extended theories of gravity //Physics Reports. – 2011. – Vol. 509. – №. 4-5. – P. 167-321. https://doi.org/10.1016/j.physrep.2011.09.003

8. Sotiriou T. P., Faraoni V. f (R) theories of gravity //Reviews of Modern Physics. – 2010. – Vol. 82. – №. 1. – P. 451-497. https://doi.org/10.1103/RevModPhys.82.451

9. Nojiri S., Odintsov S. D. Unified cosmic history in modified gravity: from F (R) theory to Lorentz non-invariant models // Physics Reports. – 2011. – Vol. 505. – №. 2-4. – P. 59-144. https://doi.org/10.1016/j.physrep.2011.04.001

10. Carroll S. M. et al. Is cosmic speed-up due to new gravitational physics? //Physical Review D. – 2004. – Vol. 70. – №. 4. – P.043528. https://doi.org/10.1103/PhysRevD.70.043528

11. Cognola G. et al. Dark energy in modified Gauss-Bonnet gravity: Late-time acceleration and the hierarchy problem // Physical Review D—Particles, Fields, Gravitation, and Cosmology. – 2006. – Vol. 73. – №. 8. – P. 084007. https://doi.org/10.1103/PhysRevD.73.084007

12. Fujii Y., Maeda K. The scalar-tensor theory of gravitation. – Cambridge University Press, 2003. https://doi.org/10.1017/CBO9780511535093

13. Harko T. et al. f (R, T) gravity //Physical Review D—Particles, Fields, Gravitation, and Cosmology. – 2011. – Vol. 84. – №2. – P. 024020. https://doi.org/10.1103/PhysRevD.84.024020

14. Faraoni V. R n gravity and the chameleon //Physical Review D—Particles, Fields, Gravitation, and Cosmology. – 2011. – Vol.83. – №. 12. – P. 124044. https://doi.org/10.1103/PhysRevD.83.124044

15. Nojiri S., Odintsov S. D., Sáez-Gómez D. Cosmological reconstruction of realistic modified F (R) gravities //Physics Letters B. – 2009. – Vol. 681. – №. 1. – P. 74-80. https://doi.org/10.1016/j.physletb.2009.09.045

16. Capozziello S. et al. Cosmological viability of f (R)-gravity as an ideal fluid and its compatibility with a matter dominated phase //Physics Letters B. – 2006. – Vol. 639. – №. 3-4. – P. 135-143.

17. Frolov A. V. Singularity problem with f (R) models for dark energy //Physical review letters. – 2008. – Vol. 101. – №. 6. – P.061103. http://dx.doi.org/10.1103/PhysRevLett.101.061103

18. De Laurentis M., Paolella M., Capozziello S. Cosmological inflation in F (R, G) gravity //Physical Review D. – 2015. – Vol.91. – №. 8. – P. 083531. http://dx.doi.org/10.1103/PhysRevD.91.083531

19. Wu B., Ma B. Q. Spherically symmetric solution of f (R, G) gravity at low energy//Physical Review D. – 2015. – Vol. 92. – №. 4. – P. 044012. http://dx.doi.org/10.1103/PhysRevD.92.044012

20. da Costa S. S. et al. Dynamical analysis on $ f (R,\mathcal {G}) $ cosmology //arXiv preprint arXiv:1802.02572. – 2018. http://dx.doi.org/10.1088/1361-6382/aaad80

21. Shamir M. F., Komal A. Energy bounds for static spherically symmetric spacetime in f (R, G) gravity //Communications in Theoretical Physics. – 2018. – Vol. 70. – №. 2. – P. 190. http://dx.doi.org/10.1088/0253-6102/70/2/190

22. Odintsov S. D., Oikonomou V. K., Banerjee S. Dynamics of inflation and dark energy from F (R, G) gravity //Nuclear Physics B. – 2019. – Vol. 938. – P. 935-956. https://doi.org/10.1016/j.nuclphysb.2018.07.013

23. Sanyal A. K., Sarkar C. The role of cosmological constant in f (R, G) gravity //Classical and Quantum Gravity. – 2020. – Vol.37. – №. 5. – P. 055010. https://doi.org/10.48550/arXiv.1908.05680

24. Singh R. Viability bounds in f (R, G) gravity with energy conditions //New Astronomy. – 2021. – Vol. 85. – P. 101513 https://doi.org/10.1016/j.newast.2020.101513

25. De la Cruz-Dombriz A., Sáez-Gómez D. On the stability of the cosmological solutions in f (R, G) gravity //Classical and Quantum Gravity. – 2012. – Vol. 29. – №. 24. – P. 245014. https://doi.org/10.1088/0264-9381/29/24/245014

26. De Laurentis M., Lopez-Revelles A. J. Newtonian, Post-Newtonian and Parametrized Post-Newtonian limits of f (R, $\mathcal{G}$) gravity //International Journal of Geometric Methods in Modern Physics. – 2014. – Vol. 11. – №. 10. – P. 1450082. https://doi.org/10.1142/S0219887814500820

27. Nojiri S., Odintsov S. D., Gorbunova O. G. Dark energy problem: from phantom theory to modified Gauss–Bonnet gravity //Journal of Physics A: Mathematical and General. – 2006. – Vol. 39. – №. 21. – P. 6627. http://dx.doi.org/10.1088/0305-4470/39/21/S62

28. Nojiri S., Odintsov S. D. Modified Gauss–Bonnet theory as gravitational alternative for dark energy //Physics Letters B. – 2005. – Vol. 631. – №. 1-2. – P. 1-6. https://doi.org/10.1016/j.physletb.2005.10.010

29. Sebastiani L., Myrzakul S., Myrzakulov R. Reconstruction of inflation from scalar field non-minimally coupled with the Gauss-Bonnet term //The European Physical Journal Plus. – 2017. – Vol. 132. – P. 1-9. https://doi.org/10.1140/epjp/i2017-11789-8

30. Nojiri S., Odintsov S. D. Modified gravity as an alternative for ΛCDM cosmology //Journal of Physics A: Mathematical and Theoretical. – 2007. – Vol. 40. – №. 25. – P. 6725. http://dx.doi.org/10.1088/1751-8113/40/25/S17

31. Li B., Barrow J. D., Mota D. F. Cosmology of modified Gauss-Bonnet gravity //Physical Review D—Particles, Fields, Gravitation, and Cosmology. – 2007. – Vol. 76. – №. 4. https://doi.org/10.1103/PhysRevD.76.044027

32. Lattimer J. M., Steiner A. W. Neutron star masses and radii from quiescent low-mass X-ray binaries //The Astrophysical Journal. – 2014. – Vol. 784. – №. 2. – P. 123. https://doi.org/10.1088/0004-637X/784/2/123

33. De Felice A., Tsujikawa S. Construction of cosmologically viable f (G) gravity models //Physics Letters B. – 2009. – Vol. 675. – №. 1. – P. 1-8. https://doi.org/10.1016/j.physletb.2009.03.060

34. Bajardi F., D'Agostino R. Late-time constraints on modified Gauss-Bonnet cosmology //General Relativity and Gravitation. – 2023. – Vol. 55. – №. 3. – P. 49. https://doi.org/10.1007/s10714-023-03092-w

35. Elizalde E. et al. ΛCDM epoch reconstruction from F (R, G) and modified Gauss–Bonnet gravities //Classical and Quantum Gravity. – 2010. – Vol. 27. – №. 9. – P. 095007. http://dx.doi.org/10.1088/0264-9381/27/9/095007

36. de Martino I., De Laurentis M., Capozziello S. Tracing the cosmic history by Gauss-Bonnet gravity //Physical Review D. – 2020. – Vol. 102. – №. 6. – P. 063508. https://doi.org/10.1103/PhysRevD.102.063508

37. Shah P., Samanta G. C. Stability analysis for cosmological models in f (R) gravity using dynamical system analysis //The European Physical Journal P. – 2019. – Vol. 79. – P. 1-9. https://doi.org/10.1140/epjc/s10052-019-6934-x

38. Myrzakulov R., Sáez-Gómez D., Tureanu A. On the Λ CDM universe in f (G) gravity //General Relativity and Gravitation. – 2011. – Vol. 43. – P. 1671-1684. https://doi.org/10.1007/s10714-011-1149-y

39. Capozziello S., De Laurentis M., Odintsov S. D. Noether symmetry approach in Gauss–Bonnet cosmology //Modern Physics Letters A. – 2014. – Vol. 29. – №. 30. – P. 1450164. https://doi.org/10.1142/S0217732314501648

***Information about authors:***

*Nurat Indira Kayratkyzy, PhD student at the Department of General and Theoretical Physics of the L.N.Gumilyov Eurasian National University, Astana, Kazakhstan, e-mail: indira.nurat@mail.ru*

*Myrzakul Shynaray Ratbayevna, PhD, Professor at the Department of General and Theoretical Physics, L.N.Gumilyov Eurasian National University, Astana, Kazakhstan, e-mail: myrzakul_shr@enu.kz*

*Belisarova Farida Beksultanovna, PhD, Associate Professor at the Department of Theoretical and Nuclear Physics at Al-Farabi Kazakh National University, Almaty, Kazakhstan, e-mail: farida.belisarova@kaznu.kz*

# CONTENTS

SCOPE AND AIM ..... 3

Yu. Zaripova, A. Yushkov, N. Amangeldiyeva, K. Dyussebayeva and A. Shaidollina
Monitoring the distribution of radon isotopes and their decay products in Almaty ..... 4

V.V. Dyachkov
Extraction of the radii of $^{9}$Be, $^{10}$B and $^{11}$B nuclei in the approximation of the strongly absorbing nucleus model in elastic scattering reactions of deuterons ..... 14

A. Temirzhanov, B. Sadykov, T. Zholdybayev, B. Duisebayev, G. Ussabayeva and Zh. Kerimkulov
STM32F407 microcontroller based multichannel analyzer for spectroscopy ..... 21

K. Samarkhanov and S. Askerbekov
Effect of Ca dopant concentration on the change in properties of ZrO2 ceramics ..... 29

J. Sh. Abdullayev and I. B. Sapaev
Modeling and calibration of electrical features of p-n junctions based on Si and GaAs ..... 39

K.S. Ayupov, H.F. Zikrillaev, E.B. Saitov, N.U. Abdullaeva, Z.N. Umarkhojayeva and M.M. Yakhyayev
Auto-oscillations of current in injection structures p+-p (Si<Mn>) based on heavily compensated silicon ..... 49

A.V. Dzhus, S.O. Subbotin, T.V. Pulina and G.V. Snizhnoi
Modeling the resistance of plate-like heat exchangers made of 06khn28mdt alloy (analogous to aisi904l steel) to crevice corrosion in recycled water enterprises ..... 58

A.Kh. Toremurat, A.I. Ashirbek, A.K. Akildinova and S.A. Orazbayev
Interaction of atmospheric pressure plasma with a liquid electrode ..... 67

Ibrahim K. Abbas
Effects of increasing applied voltage and frequency on plasma parameters in dielectric barrier discharge plasma ..... 76

Thair Abdulkareem Khalil Al-Aish and Hanady Amjed Kamil
A new system to the spectroscopy analysis with multiple x-ray of free electron laser ..... 80

I.K. Nurat, S.R. Myrzakul , F.B. Belisarova
Cosmological model in modified f(R, G) Gauss-Bonnet gravity ..... 92